Significant wave height variability and meso- and submesoscale current properties

Gwendal Maréchal

DOCTORAT SCIENCES BRETAGNE DE LA MER LOIRE ET DU LITTORAL

UBO
Université de Bretagne Occidentale

THÈSE DE DOCTORAT DE

L'UNIVERSITÉ
DE BRETAGNE OCCIDENTALE

ÉCOLE DOCTORALE N°598
Sciences de la Mer et du Littoral
Spécialité : *Océanographie physique et environnement*

Par
Gwendal MARECHAL

Variabilité des hauteurs significatives des vagues et propriétés des courants de méso- et de sousmésoéchelle

Thèse présentée et soutenue à Plouzané, le 17 janvier 2022
Unité de recherche : Laboratoire d'Océanographie Physique et Spatiale (UMR 6223)

Rapporteur.ice.s avant soutenance :

Anne-Claire BENNIS	Professeure des universités Université de Caen Normandie
Frédéric DIAS	Professeur des universités Collège Universitaire de Dublin

Composition du Jury :

Examinateur.ice.s :

Ana Beatriz VILLAS BÔAS	Chercheuse Institut de technologies de Californie
Christine GOMMENGINGER	Professeure NOC de Southampton
Marie-Hélène RIO	Chercheuse Agence Spatiale Européenne
Anne-Claire BENNIS	Professeure des universités Université de Caen Normandie
Frédéric DIAS	Professeur des universités Collège Universitaire de Dublin

Président du Jury :

Guillaume ROULLET	Professeur des universités Univ. de Bretagne Occidentale

Directeur de thèse :

Fabrice ARDHUIN	Directeur de recherche CNRS Univ. de Bretagne Occidentale

À mon ami Antonin Girardi ; engagé, humaniste et clairvoyant.
"On est ensemble où qu'on soit".

TABLE OF CONTENTS

Contexte et motivation en français

Les courants marins à la surface de l'océan sont naturellement turbulents, tout particulièrement aux échelles régionales (courants côtiers, courants de bord ouest, ondes internes, tourbillons océaniques et fronts). Les vagues, faisant office d'interface entre la basse atmosphère et les premiers mètres de l'océan, sont fortement modulées par la présence de tels courants. Les interactions entre les vagues et les courants de surface induisent des variabilités de cambrures, de directions, de longueurs d'ondes et d'amplitudes des vagues. Ces interactions ont grandement été étudiées durant le dernier siècle et sont, aujourd'hui, de plus en plus compréhensibles grâce à l'augmentation des puissances de calcul et aux nouvelles données in-situ et de télédétection dans l'océan global. Aux échelles océaniques de l'ordre de 10-100 km (*mésoéchelle*), et aux échelles inférieures à 10 km (*sousmésoéchelle*), la variabilité des caractéristiques des vagues semble être grandement proportionnelle aux propriétés des courants sous-jacents. La variabilité des hauteurs significatives des vagues induite par la présence de courant est provoquée par une superposition de mécanismes. Cette superposition est responsable, entre autres, du caractère non local des effets des courants sur les hauteurs de vagues. En effet, les courants redistribuent spatialement l'énergie des vagues aussi bien via la réfraction que par l'advection de l'action des vagues. La présence de courant induit également un décalage en fréquence des vagues pouvant résulter, localement, à un accroissement de leurs hauteurs.

Comprendre la variabilité du champ de vagues et de ses paramètres permet de réduire la contamination du signal de vagues dans certaines mesures de variables océaniques depuis l'espace (hauteurs des océans, vitesses des courants de surface ...). Aussi, comme la cambrure des vagues est modifiée par la présence des courants, les flux air-mer associés sont grandement modulés. Enfin, comme l'énergie des vagues est redistribuée spatialement par les courants sous-jacents (hautement turbulents et aléatoires), les effets des courants sur les vagues peuvent conduire à des zones d'amplifications anormalement fortes des hauteurs de vagues. Ce sont ces amplifications inhabituelles qui peuvent être à l'origine de catastrophes et de naufrages au large des côtes. Pour en citer un dans les alentours du courant des Aiguilles :

The SS Waratah, sometimes referred to as Australia's Titanic, was a 500-foot (150 m) long steamship that operated between Europe and Australia in the early 1900s. In July 1909, the ship, en route from Durban to Cape Town, disappeared with 211 passengers and crew aboard. To this day, no trace of the ship has been found...

The Times, p. 24 le 23 février 1911

Comme les courants marins sont, malheureusement, une variable océanique encore trop peu connue, les prévisions de telles catastrophes par les modèles maritimes sont fréquemment sous-estimées. En 2001, James Gardner, du centre américain de cartographie des côtes et de l'océan, affirmait que l'océan de surface serait moins connu que la surface de la lune. Ce manque de connaissance sur la dynamique superficielle de l'océan à des échelles inférieures à la centaine de kilomètres soulève la question : est-ce que la variabilité des hauteurs de vagues peut être utilisée pour retrouver cette dynamique des courants à la surface des océans ?

De cette question de l'inversion de la variabilité des paramètres de vagues pour déduire les courants sous-jacents, je me suis demandé, comment les gradients spatiaux des hauteurs significatives des vagues sont associés aux gradients des courants sous-jacents à la méso- et à la sousmésoéchelle. Cette courte introduction sera complétée dans le chapitre 1 par une introduction plus complète des vagues, des courants de surface et de leurs interactions. Le chapitre 2 montrera, dans un cadre théorique et idéalisé, comment les courants conduisent à une variabilité des hauteurs significatives de vagues à l'échelle régionale. Dans le chapitre 3 je proposerai une étude numérique et

idéalisée des effets d'un tourbillon océanique isolé de mésoéchelle sur le champ de vagues. Comme les tourbillons sont rarement isolés dans l'océan, j'étendrai l'étude numérique du chapitre 3 à un cadre réaliste dans le courant des Aiguilles où des données altimétriques viendront également valider nos résultats numériques (chapitre 4). Dans le chapitre 5, je complèterai les mesures altimétriques par les nouvelles mesures directionnelles et spectrales du satellite CFOSAT et de son antenne SWIM. Le chapitre 6 viendra clore ce manuscrit de thèse en proposant des perspectives d'études. En effet, je présenterai quelques résultats préliminaires sur la modulation des charactéristiques des vagues dans d'autres régimes de courants que ceux étudiés dans les chapitres précédents. Enfin, le chapitre 7 est un résumé de la thèse en français.

REMERCIEMENTS

Bien qu'il soit d'usage d'écrire quelques mots de remerciement en amont d'un mémoire, je leur accorde une place et une attention toutes particulières dans ce manuscrit synthétisant ces trois dernières années de doctorat.

Tout d'abord, j'aimerais remercier les instances qui ont financé mes trois ans de doctorat : le Centre National d'Etudes Spatiales et la région Bretagne. L'école universitaire de recherche ISblue a également financé une partie d'un séjour de 3 mois au Scripps à San-Diego, merci aux différents acteurs et actrices qui ont rendu cela possible.

Le manuscrit que vous avez entre les mains ou sur votre écran d'ordinateur, a très nettement gagné en qualité grâce au travail de relecture d'Anne Claire Bennis et de Frédéric Dias ainsi qu'aux examinatrices Ana Beatriz Villas Boas, Christine Gommenginger et Marie-Hélène Rio présentes lors de la soutenance de cette thèse de doctorat. Merci pour leurs retours.

Je souhaite également exprimer toute ma gratitude à Sergeï Badulin et Danièle Hauser pour leurs accompagnements, leurs précieux conseils et leurs encouragements lors des différents comités de suivi de thèse.

Une grande partie de ces travaux n'auraient pu voir le jour sans la littérature produite par Yves Quilfen, Guillaume Dodet et toute l'équipe du CCI-SeaStates (Centre Spatial Européen) sur les données altimétriques de hauteur significative des vagues.

Merci aussi à l'équipe CFOSAT-SWIM sans qui la valorisation des données du nouveau satellite n'aurait pas été possible. Merci donc à Danièle Hauser, Alexis Mouche, Antoine Grouazel, Alexei Mironov, Bertrand Chapron, Cédric Tourain, Dr. Fab et Gille Guitton.

Comme vous pourrez le lire, une grande partie des travaux a été menée dans l'environnement numérique WAVEWATCH III©, cela n'aurait pas été rendu possible sans l'expertise et la disponibilité de Mickael Accensi. Je le remercie également pour les temps de bidouillage à l'atelier sur notre système de Stéréo-Vidéo, son déploiement au Cap-Vert et sur la mission SUMOS dans le Golf de Gascogne.

J'envoie des remerciements tout particuliers à Bertrand Chapron et Ana Beatriz Villas Boas qui ont su éveillé ma curiosité sur plusieurs aspects de l'océanographie, éclairé certains résultats, poussé certains diagnostiques et qui m'ont fait gagner en confiance sur la qualité de mon travail.

Je tiens à exprimer toute ma gratitude à Alexis Mouche, Peter Sutherland et à Alvise Benetazzo pour la passion de la science des vagues qu'ils m'ont transmise pendant mes stages de fin d'étude. Un merci particulier à Peter qui m'a accordé sa confiance pour partir à ses côtés en mission terrain, en stage et en thèse.

L'enseignement de qualité de Guillaume Roullet et de Xavier Carton a fortement nourri ma passion pour l'océanographie ainsi que ma motivation, nécessaires pour se lancer dans ces 3 ans de thèse. Un grand merci à eux pour leurs encouragements.

Je me joins également à mes collègues doctorant.e.s et post-doctorant.e.s du laboratoire pour remercier notre cheffe d'équipe Fanny Girard-Ardhuin qui a grandement contribué à la maturation de nos travaux. Merci pour le cadre bienveillant et professionnel qu'elle installe dans l'équipe.

Bien que les remerciements destinés à l'encadrant soient naturels, j'aimerais insister sur l'importante contribution de Fabrice Ardhuin sur ces trois années de doctorat. Merci pour sa patience, sa qualité d'encadrement, les opportunités professionnelles qu'il m'a permis d'avoir durant ces trois ans. Merci aussi pour la liberté qu'il m'a accordée pour arpenter mes pistes de recherches. Merci également pour tout ce qu'il a apporté, apporte et apportera dans la communauté des vagues et de la télédétection. Enfin, merci à lui pour toutes les passions qu'il a initiées de par ses encadrements.

Merci également aux différentes équipes administratives qui, dans l'ombre, ont accompagné ce travail de thèse durant ces trois ans.

Ces travaux de thèse viennent clore huit années brestoises. Il est certain que les liens tissés durant cette petite décennie tiennent une grande place dans l'accomplissement de ce manuscrit. Merci aux ami.e.s de longue date rencontré.e.s sur les bancs de la fac : Guillaume, Jordan, Vincent, Eva, Maxime, Marine, Laurène, Shona, Yohan, Julie mais aussi aux ami.e.s rencontré.e.s plus récemment grâce au doctorat : Charly, Alex A, Edouard, Angelina, Arthur, Marine, Marie, Alex L.G, Sophia, Luc, Léo, Armand, Roy et Manuel. Je n'oublie pas les copain.ine.s rencontré.e.s au 36 : Salomé, Tom, Raph, Fanch, Francky, Elise, Esteban et les amis d'ailleurs, Adrien et Yanis qui ont su, à leur manière, contribuer à l'élaboration de ce manuscrit. Mes chère.s ami.e.s, merci de me compter parmi votre entourage.

Je voudrais exprimer toute ma reconnaissance à mes amies très proches Emma P.B et Emma C qui ont eu un rôle déterminant dans la finalisation de ce manuscrit. Toute ma gratitude également aux collègues et/ou ami.e.s formidables que sont Leïla, Ivane, et mes 3 compatriotes, Treden, William et Martin.

J'envoie un remerciement spécial à Kelly qui a grandement amélioré la forme de ce manuscrit.

Merci également à tout.e.s celles et ceux que j'oublie mais qui ont leur place dans ces remerciements.

CHAPTER 1

INTRODUCTION: WAVES, SURFACE CURRENTS, AND THEIR INTERACTIONS

There is no need to travel the global ocean or to be an oceanographer to observe surface gravity waves, walk to the closest beach or lake and observe them breaking on the foreshore.

1.1 Basic principles of surface gravity waves

1.1.1 Linear physics and statistics of surface gravity waves

I will hereafter call waves, when referring to the wind-generated surface gravity waves. Waves generation or wave growth is caused by the work of the wind forces above the ocean surface leading to an increase in wave energy. The key point in the wave growth by wind is that the air-sea interface (where waves are propagating) is a material surface so that wind energy cannot be transferred to the water by advection and thus must be driven by stresses. These stresses are highly modulated by the undulating surface with a pressure-surface slope correlation at the surface for the normal component of the stress. Those pressure-slope correlations are responsible for the wave-growth. Because the quantitative details of wind wave growth involve turbulence in the air and can be strongly modified by complex two-phase flows including aerosol and bubble formation, a full knowledge of this process still eludes a complete theory or numerical simulations (Ayet and Chapron, 2021; Deike et al., 2016).

In 1841 Sir George Biddell Airy developed a linear theory of waves. This theory is a good approximation of what happens at the air-sea interface for unidirectional, monochromatic and not too steep waves (Airy, 1841). Under the Airy approximation the dispersion relationship that links the wave intrinsic frequency $\sigma = 2\pi f$, where f is the inverse of the wave period T, and the magnitude of the wavenumber k is $\sigma = \sqrt{gk\tanh(kD)}$ with D is the water depth and g the gravity acceleration.

In deep water, $kD \gg 1$ and this relationship becomes,

$$\sigma = \sqrt{gk}. \tag{1.1}$$

From their generation area waves organized themselves into groups and propagate at the air-sea interface at the group speed $\mathbf{C}_g$,

$$\mathbf{C}_g = (\partial_{k_x}\sigma, \partial_{k_y}\sigma). \tag{1.2}$$

k_x,k_y are the two horizontal components of the wavenumber vector $\mathbf{k}$. Throughout the manuscript bold characters refer to vector notation. This group speed is also the average velocity at which the wave energy is radiated. As

the group speed depends on k, waves are dispersive in deep water, long-waves (small k) are propagating faster than short waves (large k). All the linear theory is given in detail by the pioneer works of Laplace (1776) and in Airy (1841).

Waves break where the orbital velocity, at the wave crest, approaches the phase velocity (Longuet-Higgins and Tanaka, 1997). The breaking is associated with an intense wave-energy dissipation and plays an important role in the fluxes between the ocean and the atmosphere. Wave breaking can be depth-induced (as we can see along our coastlines ; Divoky et al. (1970)) but also induced by the modulation of the short-waves by long-waves (Dulov et al., 2002; Guimaraes, 2018) or through their interactions with the currents (Phillips, 1984). During breaking events, waves generate sea spray, bubbles (Deane and Stokes, 2002), exchange momentum and heat between the atmosphere and the upper ocean (Melville and Rapp, 1985) and modify the surface drag (Reul et al., 2008).

It is evident that waves in the ocean cannot be considered as a solitary crest and trough but more as a superposition of sinusoidal wave trains, each with an amplitude (a), wavelength (λ) and direction (θ) (Fig. 1.1). Mathematically, the surface elevation η at a fixed position **x**=(x,y) and a specific time t, can be written as the following expression,

$$\eta(x,y,t) = \sum_{i=1}^{N}\sum_{j=1}^{M} a_{i,j}\cos\left[\sigma_i t - k_i\cos(\theta_j)x + k_i\sin(\theta_j)y + \phi_{0,i,j}\right], \tag{1.3}$$

with ϕ_0 an initial phase. The high frequency aspect of the wave signal results to consider a great number of cosine functions with relatively close frequencies to reproduce a wave field statistically realistic. The random and chaotic aspect of a wave field (Eq. (1.3), Fig. 1.1), make the *wave by wave analysis*, for instance, provided through surface elevation records, not the most efficient description of the wave field. A spectral description is a wiser choice, in other terms, studying how waves amplitude variance (or waves energy) is distributed with respect to frequencies and directions. This distribution defines the waves power spectrum, E(f,θ), this is a decomposition of the surface amplitude variance on Fourier modes. An accurate description of how wave spectrum is estimated from a random sea state is given in Peureux (2017). This application from $\mathcal{R} \rightarrow \mathcal{C}$ loses the phase of the wave field (the real position of crests and troughs), but is highly consistent with the wave field statistics. Moreover thanks to the spectral description one can separate waves systems according to their frequencies and directions. So, one can split waves generated from remote storms propagating faster than local wind, called swell (low frequency) and waves generated from local wind effect, called wind sea (high frequency). An example of an instantaneous E(f,θ) and its evolution over time is given in Fig.1.2 from light wave buoy (spotter) measurements in the Bay of Biscay. In this example, one can see sea-states highly bimodal in frequency (combination of wind sea and swell) between February 28^{th} 2021 and March 3^{rd} 2021 (Fig.1.2(b)). From March 3^{rd} 2021 wind sea decreases continuously to make room for swell exclusively on 4^{th} March. The dispersive properties of deep-water waves can also be observed in Fig.1.2(b), longer waves (low frequency) are measured before shorter waves (slight slope of E(f) signal in the swell band, from the 2^{sd} March 06:00-UTC to the 3^{sd} March 08:00-UTC).

The statistics of the sea-states can be described from E(f,θ) and its associated parameters, the resulting parameters are called bulk parameters. The parameters used throughout this thesis and their expressions are given below.

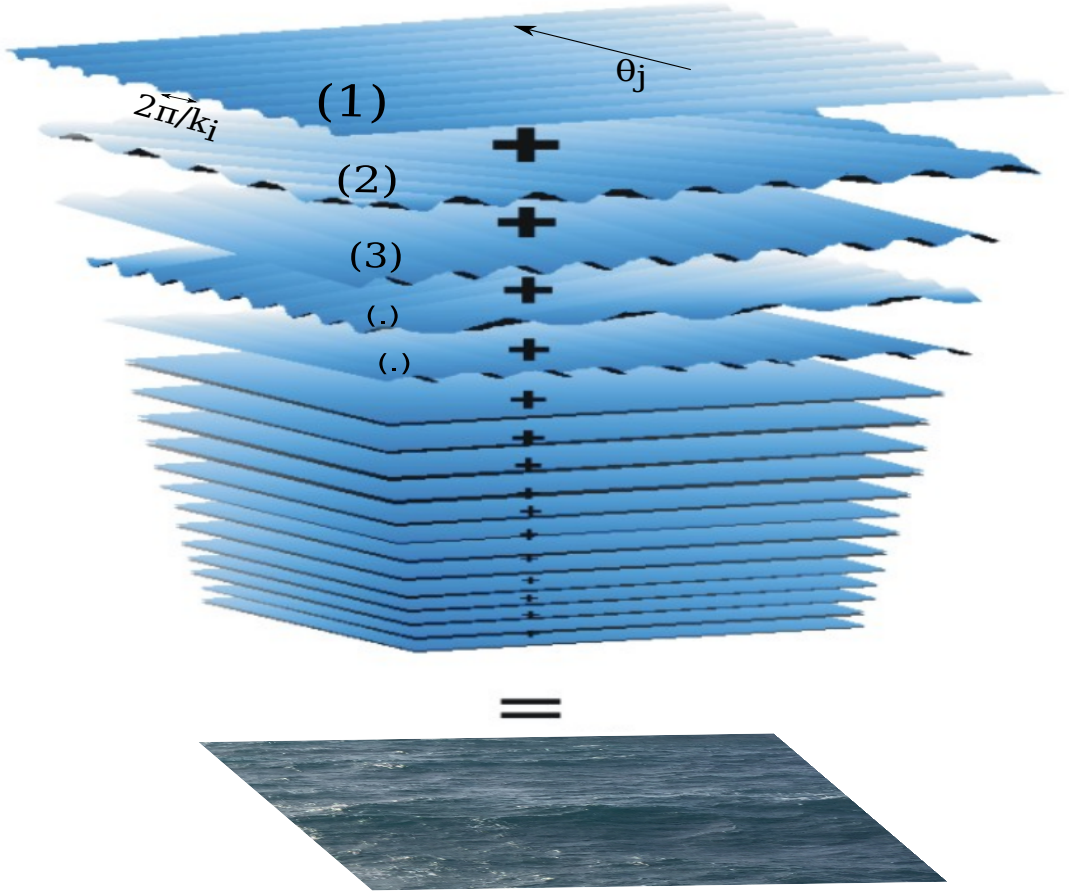

Figure 1.1: A given wave field decomposed into n monochromatic waves trains with specific wavelength and direction. (Adapted from Pierson et al. (1955).)

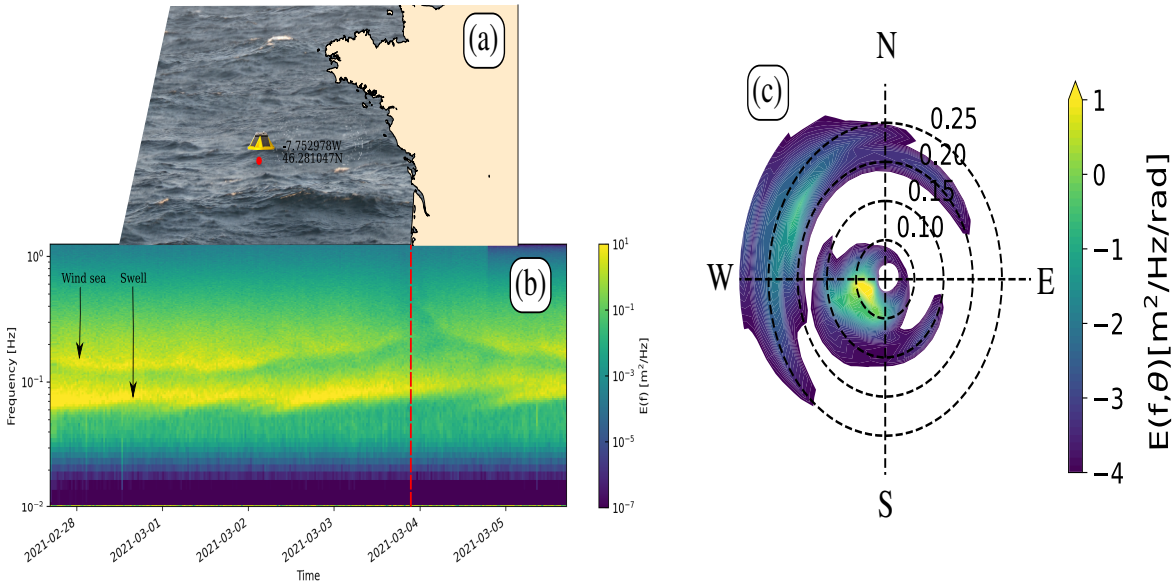

Figure 1.2: Wave periodogram (panel b) estimated from waves-spotter buoy measurements during the SUMOS field experiment (February 2021) in the Bay of Biscay (location of the spotter is given in panel a). An instantaneous two-dimensional spectrum is given on panel c (time highlighted by the dashed line on the periodogram), the significant wave height was 1,65m.

The significant wave height:

The most used wave height scale is the significant wave height (H_s or SWH), originally H_s was defined as the mean of the highest one third of all individual waves (Munk, 1944). Today H_s is defined as 4 times the standard deviation of the surface elevation. Both definitions give values within a few percent of one another in particular, assuming a Rayleigh distribution for the wave heights. Thus,

$$H_s = 4\sqrt{\int_{f=0}^{\infty}\int_{\theta=0}^{2\pi} E(f,\theta)d\theta df}. \tag{1.4}$$

The mean period $\mathbf{T}_{m0,-1}$:

The time to travel from one wave crest to another is called individual period, in a random wave field it is more desirable to deal with the mean period,

$$T_{m0,-1} = \frac{1}{\int_f\int_\theta E(f,\theta)d\theta df}\int_f\int_\theta f^{-1}E(f,\theta)d\theta df. \tag{1.5}$$

This definition of the mean period is not the only one, as the reader can see it is based on the negative first moment of the wave spectrum, other definitions exist and are based on higher moments of E(f,θ) which give more or less weight to high or low frequencies.

Directional mean parameters:

Wave field has a mean direction and a directional spreading. Following (Kuik et al., 1988) they are computed as follows,

$$
\begin{aligned}
a_1(f) &= \int_\theta E(f,\theta) cos(\theta) d\theta \\
a_2(f) &= \int_\theta E(f,\theta) cos(2\theta) d\theta \\
b_1(f) &= \int_\theta E(f,\theta) sin(\theta) d\theta \\
b_2(f) &= \int_\theta E(f,\theta) sin(2\theta) d\theta,
\end{aligned} \tag{1.6}
$$

Mean directions are,

$$\theta_1(f) = \arctan(\frac{b_1}{a_1}), \tag{1.7}$$

$$\theta_2(f) = \frac{1}{2}\arctan(\frac{b_2}{a_2}), \tag{1.8}$$

and directional spreadings,

$$\sigma_1(f) = 2\sqrt{1-(a_1^2+b_1^2)}, \tag{1.9}$$

$$\sigma_2(f) = \frac{1}{2}\sqrt{1-(a_2^2+b_2^2)}. \tag{1.10}$$

These mean parameters can be significantly different than waves peak parameters (peak direction -θ_p- or peak frequency -f_p-), their values are the direction and the frequency where E(f,θ) is the maximum. Let us notice that other wave parameters can be estimated from the wave spectrum as the mean square slope (mss, the variance of the slope), the waves-induced current called stocks drift and many others.

1.1.2 Measuring wave height from altimeters

All along the manuscript we will deal with H_s measured by altimeters, we should thus explain how these measurements are made. The altimeters monitor the ocean surface at the nadir (incidence angle = 0°, along the vertical). They emit radar pulses with a frequency around a fixed carrier frequency that is in a band for which atmospheric attenuation is minimal (Ku band, 13.6 GHz and Ka band 35 GHz for Saral-AltiKa). They record the time lag between the emitted pulse and the echo induced by the ocean surface which yields the position of the ocean knowing the position of the satellite. The significant wave height measurement is estimated from echoes induced by the wavy surface. The curve that gives the power of the echoes as a function of the travel time between the emission and the reception is called the waveform (Fig.1.3). Mathematically, for an ocean surface of uniform backscatter, the waveform is the convolution of the surface elevation cumulative Probability Density Function (PDF) and the instrument point target response (Brown, 1977). The waveform is composed of a leading edge and a trailing edge (Fig.1.3c). The calmer the sea-states, the sharper the leading edge sharp and vice versa (Fig.1.3a, b). Indeed, the higher the waves, the quicker the echo. The H_s estimation is performed by a fitting process of the leading edge called *retracking*. The value of H_s is taken to be the one for which the theoretical waveform described by the

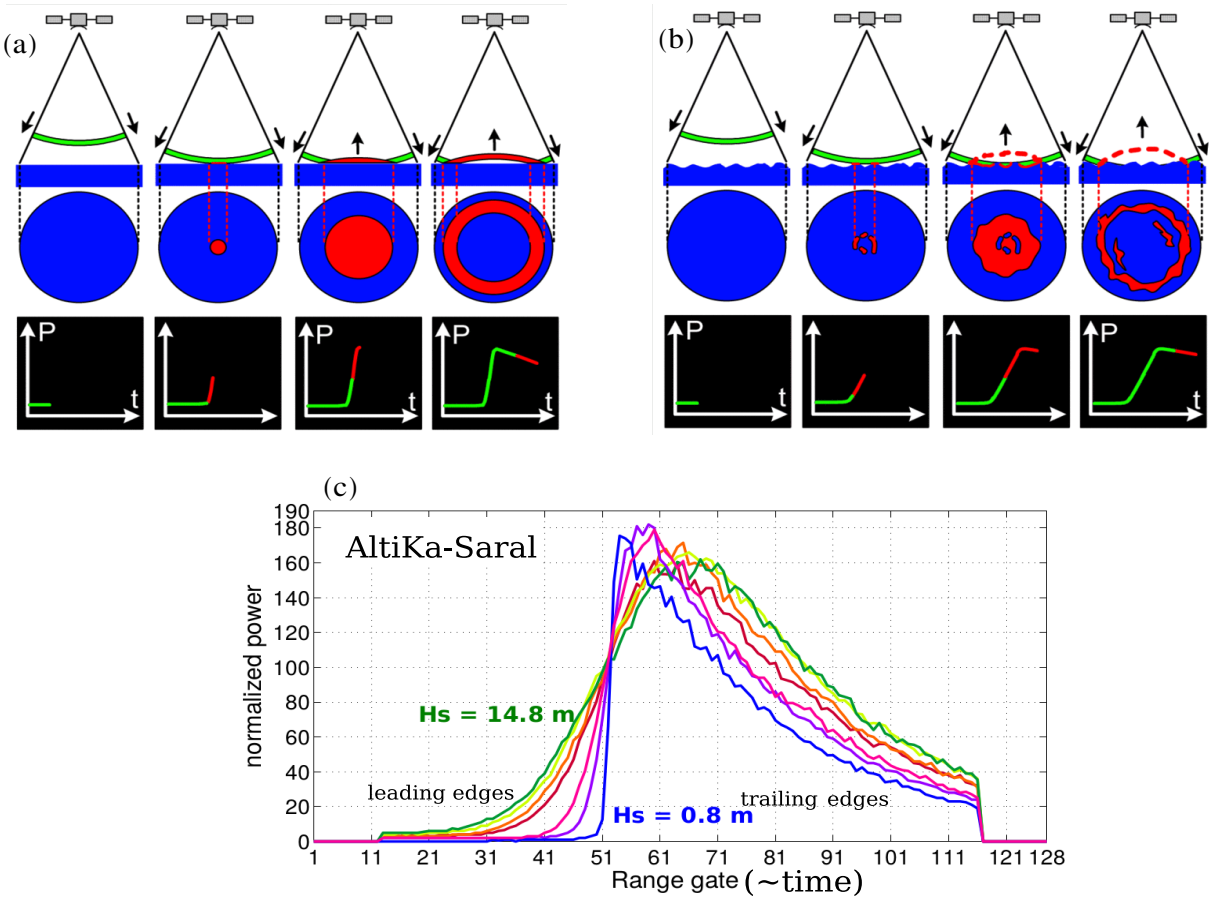

Figure 1.3: Significant wave height measurement from AltiKa-Saral altimeters. Each colored line is a different sea-state measurement. Panel (a) and (b) credit CNES (https://www.aviso.altimetry.fr/en/techniques/altimetry/principle/pulses-and-waveforms.html) and panel (c) from Ardhuin et al. (2019b)

.

Brown-Hayne model gives the best fit to the measured waveform (Brown, 1977; Hayne, 1980). The fit can be performed on the entire waveform, which is the usual MLE3 algorithm that uses a three parameters Maximum Likelihood Estimator (Thibaut et al., 2010) or can be partially applied in a range gates interval as in ALES (Adaptive Leading Edge Subwaveform Retracker) as described by Passaro et al. (2014). At present, with their $\sim$ 10 days revisiting time, altimeter constellation provides the largest database of wave height measurements at global scales from equator to polar areas (Ardhuin et al., 2019b).

1.2 The multiscale dynamics of ocean surfaces

Surface currents at global scale are generally described as basin-scale gyres with a temporal variability of decades. The surface currents as slow and large-scale movements is a very limited view of the actual ocean. For instance, in our coasts one can notice the quick and localized semidiurnal tides (Pouvreau et al., 2006). Beyond tides, surface currents are very dynamic both on and off our coasts with a wide spatiotemporal variability. One can refer to

Chelton (2001) for the different current regimes in the ocean and their associated spatiotemporal scales. We notice that the ocean is a "very flat" system, the effects of the currents have a much more horizontal extension than vertical extensions (horizontal extensions are 100 times bigger than vertical ones). Mathematically, surface current is a vector field composed of three components $\mathbf{u} = (u, v, w)$, which are the zonal, meridional and the vertical velocity respectively. Although the ocean currents have been firstly characterized as laminar flows (see: the first map of the Gulf-Stream drawn by Benjamin Franklin, Fig.1.4), the last twenty years have proven that the ocean surface is naturally turbulent at scales from several hundred kilometers to a few kilometers (Chelton et al., 2011; McWilliams, 2016) with a ubiquity of rotating (called eddies) or thin elongated structures (filaments, fronts).

Over the last 25 years, the most utilized system for the monitoring of the ocean surface is altimetry. At the first order, surface currents are in geostrophic balance (Coriolis acceleration and pressure gradients are in equilibrium).

$$-fv = -\frac{1}{\rho}\partial_x P, \tag{1.11}$$

$$+fu = -\frac{1}{\rho}\partial_y P, \tag{1.12}$$

u and v are the zonal and the meridional surface current component respectively, P is the pressure and ρ the ocean density. f is the Coriolis parameters, equal to 2Ω sin(lat) with Ω the Earth's rotation vector. Equations (1.11,1.12) are derived from the full Navier-Stokes equation in the stationary framework without non-linearity and without source and dissipation terms. The pressure gradient can be rewritten as a gradient of sea surface elevation by assuming that the ocean is hydrostatically balanced ($P = -\rho g h$), h is the height of the water column. Thanks to altimeters, surface geostrophic currents can be monitored at global scale to a spatial resolution of several hundred kilometers (Ballarotta et al., 2019) and allows one to capture the large eddies that cover the surface ocean[1] (Chelton et al., 2011).

By definition:

- flow is in geostrophic balance outside the equatorial band where (lat $\neq 0°$)
- currents are divergent free ($w_{z=z_\eta}$=0 m.s^{-1})

In each region of the ocean, the length scale of eddies are characterized by the Rossby deformation radius (R_D=NH/πf_0 ; where H is the total water column height, N the Brunt-Väisälä frequency which is a proxi of the ocean stratification and f_0 the local coriolis parameter). Surface turbulent features at a length scale (L) comparable to the deformation Rossby radius are called mesoscale. By definition, smaller scales are called submesoscale, at those scales the stratification plays a more major role than the earth rotation in the formation of surface coherent features (eddies, filaments). The map of the first Rossby deformation radius is given in Fig. 1.5a. The oceanic processes that drive the emergence of both meso- and submesoscale surface dynamic is beyond the scope of this manuscript, we only mention that instabilities that occur in the ocean (barotropic, baroclinic, mixed layer, Kelvin-Helmholtz, frontogenenesis,...) or flow over (against) seamounts (continental boundaries) can spontaneously create turbulent features at different scales (McWilliams, 1985; McWilliams, 2016). As the Rossby deformation radius is meridionally dependent, the submesoscales structures are smaller at high latitude and bigger close to the equator (Tulloch et al., 2011).

1. flows can be geostrophically balanced until few km

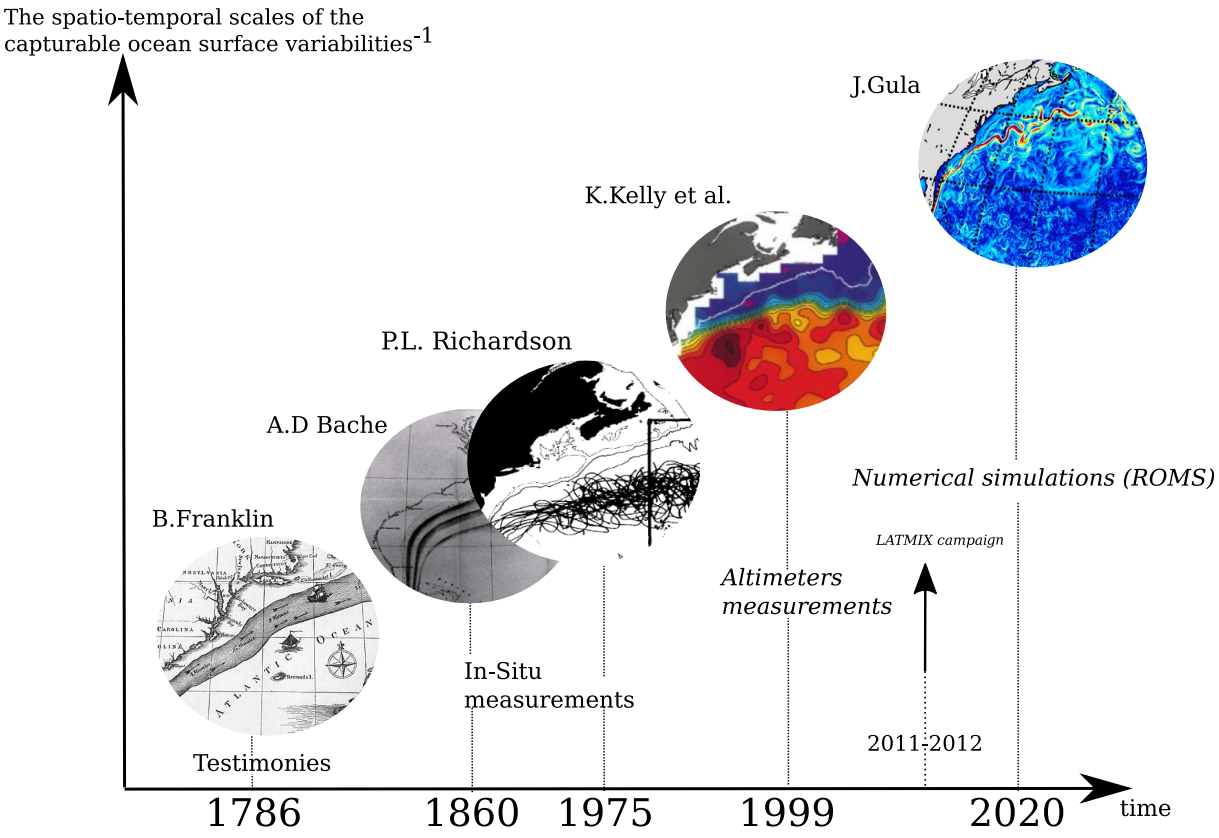

Figure 1.4: How the surface ocean dynamic has been seen through centuries, an example of the Gulf-Stream. The Gulf-Stream was first mapped by B.Franklin according to his cousin's testimonies in 1786. Then, from in-situ measurements, Bache (1860) proposed a survey of the Gulf-Stream meanders. During the Cold-War, Russian and American researchers started to study the *undersea storms* (commonly called eddies) in the Gulf-Stream by the use of multiple types of drifters (see Richardson (1985) among other). Kelly et al. (1999) studied seasonal variability of the Gulf-Stream by the use of altimeter data and were able to capture its large-scale variability. The LATMIX field campaign in the Gulf-Stream region has significantly increased our knowledge on oceanic small-scale processes through a ground truth (Shcherbina et al., 2015). At present, several numerical studies are performed to capture the very small-scale horizontal and vertical variabilities of the ocean. Here is a snapshot of instantaneous surface velocity via numerical CROCO oceanic model (J.Gula-LOPS (`10.5281/zenodo.4946133.`)).

Note that currents in a part of the mesoscale range and all currents at the submesoscale range are not captured by altimeter measurements, only large scale eddies or meanders can be monitored (Fig.1.4, see Fig.2 of Villas Bôas et al. (2019)). However, at the surface of the ocean, most of the lateral fluxes (momentum or heat) are driven by mesoscale eddy structures (Zhang et al., 2014). To assess these fluxes the growth and decay's processes of such eddies have to be well understandable and so their measurements are necessary. Also, due to the Kolmogorov inverse cascade of the 2D turbulence, surface processes at the submesoscale range have a large impact on these eddy fluxes (Klein et al., 2011). Finally, submesoscale currents also have strong associated vertical motions due to the incompressibility of the flow. Both mesoscale and submesoscale currents are key in the transport of geophysical tracers (temperature, salinity, chlorophyll), water mass and the biological activity. The sharp SST gradients associated with small mesoscale eddies and submesoscale currents are crucial in the estimation of heat fluxes between ocean and atmosphere. It would even seem that those vertical motions induced by submesoscale current are a source of heat exchange between the ocean and the atmosphere larger than the heating induced by the greenhouse effect (Su et al., 2018). Although kilometers-scale currents are key processes in the ocean and atmospheric systems, they are poorly known at global scale. The spatial resolution of altimetry-derived currents is too coarse to capture the small-scale and short-lifetime duration currents. The resolution limitation in the altimeters measurements triggered the necessity to monitor the ocean at higher resolution by the use of innovative remote sensing measurements (Gommenginger et al., 2018; Ardhuin et al., 2019a; Morrow et al., 2019; Wineteer et al., 2020). To cite the father of modern oceanography:

If I were to choose a single phrase to characterize the first century of modern oceanography, it would be a century of under-sampling. (Munk, 2002)

An idea to the readers: almost 60% of the ocean surface Kinetic Energy is missed by today altimeters measurements (ESA, 2019) and the state of the art of oceanic model reveals a large kinetic energy bias at global scale both at low and high frequency with respect to drogued drifters (Yu et al., 2019). It means that surface currents are still a variable partially understood albeit their global measurements are available (altimeters, Argo drifters, ...). In this manuscript we will highlight the drawback of working only with deduced-altimeters currents in the context of wave-current interactions.

1.3 Theories of how waves are modulated by surface currents

Now that surface gravity waves and currents have been introduced let us talk about how the two systems modulate each other. Waves respond differently to winds and currents. For example, in western boundary currents, the current-induced H_s variability occurs at much smaller scale ($\mathcal{O}(10^2\text{km})$) than the scale of storms ($\mathcal{O}(>10^3\text{km})$) that generate the waves (Ardhuin et al., 2017). At those scales different processes can be responsible for the inhomogeneity of the waves field and their associated H_s. Before discussing those processes in different numerical experiments and observations we propose to present them analytically in idealized frameworks.

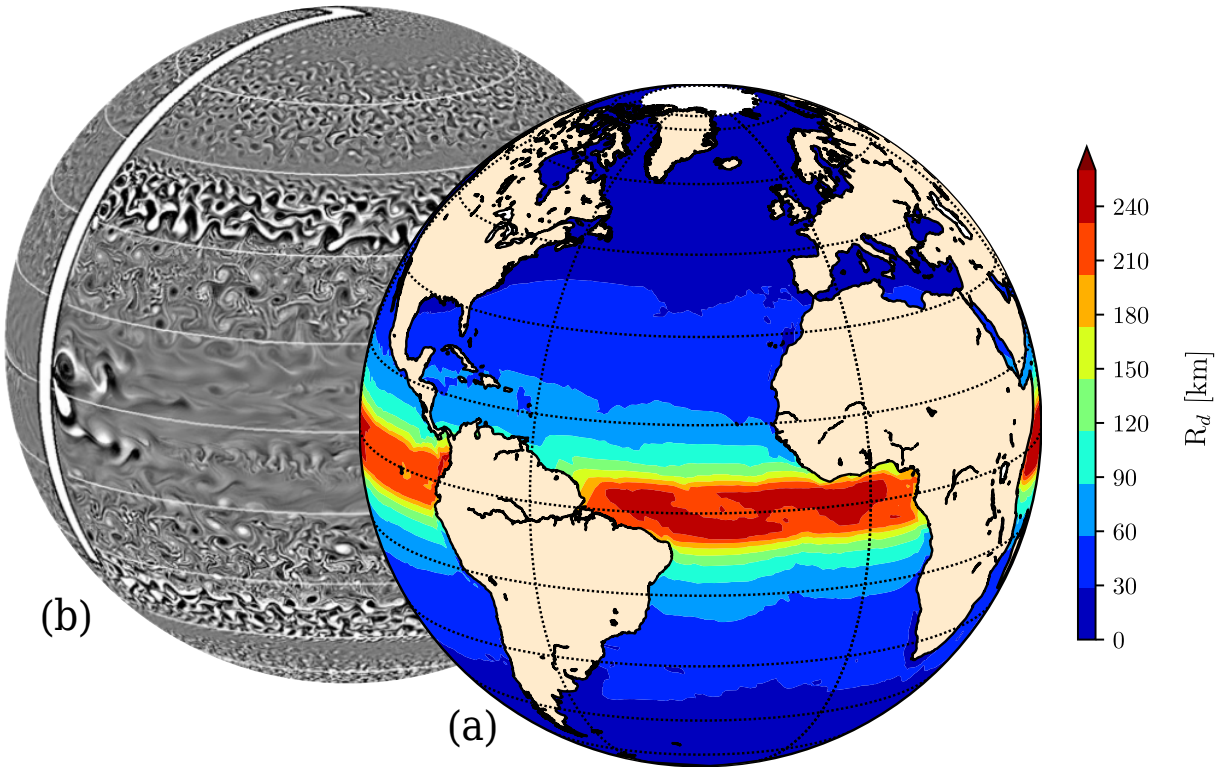

Figure 1.5: Panel (a) the first baroclinic deformation Rossby radius, adapted from Chelton et al. (1998). Panel (b), vertical surface vorticity from MITgcm oceanic model with no continent, the thick white strip is a land barrier that serves as the eastern (western) boundary of the small (large) basin. Taken from Tulloch et al. (2011).

Preamble: geometrical optic approximation

In a current field the dispersion relationship in deep-water (Eq.1.1) is rewritten as such that the dispersion of the waves is in the frame of reference of the currents:

$$\omega = \sqrt{gk} + \mathbf{k}.\mathbf{u}, \tag{1.13}$$

ω is called the absolute frequency. One can see that the currents induce a Doppler shift on the waves, i.e, waves can be extended and shortened. Throughout the manuscript, we will explore the effect of currents on the waves assuming the geometrical optic approximation. This approximation relies on the fact that currents are slowly varying with respect to the waves,

$$\omega >> \max\left|\frac{1}{|\mathbf{u}|}\partial_{t_{curr}}u\right|, \tag{1.14}$$

and that their spatial scales are larger than the wave wavelength,

$$k >> \max\left|\frac{1}{|\mathbf{u}|}\partial_{x_{curr}}u\right|. \tag{1.15}$$

$\partial_{x_{curr}u}$ and $\partial_{t_{curr}u}$ are the characteristic spatial and temporal scales of the current (Peregrine, 1976). Also the surface current velocity will be considered as much slower than the wave group velocity,

$$\frac{|\mathbf{u}|}{C_g} << 1. \tag{1.16}$$

From the geometrical optics approximation framework, the effects of currents on the kinematics of the waves can be described by the ray equations, applying Eq.1.16 and considering that $\partial_t k + \partial_x \omega = 0$, Phillips (1977); Mei (1989) derived the following expressions:

$$\begin{cases} \dot{\omega} = d_t(\mathbf{k}.\mathbf{u}), & (1.17)\\ \dot{\mathbf{x}} = \mathbf{C}_g + \mathbf{u}, & (1.18)\\ \dot{k} = -\hat{k}.\nabla(\mathbf{k}.\mathbf{u}), & (1.19)\\ \dot{\theta} = -\frac{1}{k}\hat{n}.\nabla(\mathbf{k}.\mathbf{u}). & (1.20) \end{cases}$$

The $\dot{}$ denotes the total time derivative and is equal to $\partial_t + (\mathbf{C}_g)\nabla$. The equations in the system above describe the conservation of the absolute frequency, the advection velocity, the change in wavenumber (or Doppler shift), and the change in direction (or refraction) induced by the presence of the current respectively. $\hat{n}.\nabla$ is the perpendicular gradient $(-\sin\theta\partial_x + \cos\theta\partial_y)$. One can see that the refraction is the strongest where wave and current are perpendicular and the strongest Doppler shift where waves and current are aligned.

The dynamic of the waves is governed by the wave action transport equation (in its Eulerian form),

$$\partial_t A(f,\theta) + \dot{\mathbf{x}}.\nabla(A(f,\theta)) + \partial_k(\dot{k}A(f,\theta)) + \partial_\theta(\dot{\theta}A(f,\theta)) = \frac{S(f,\theta)}{\sigma}, \tag{1.21}$$

with the wave action defined as

$$A(f,\theta) = \frac{E(f,\theta)}{2\pi f}. \tag{1.22}$$

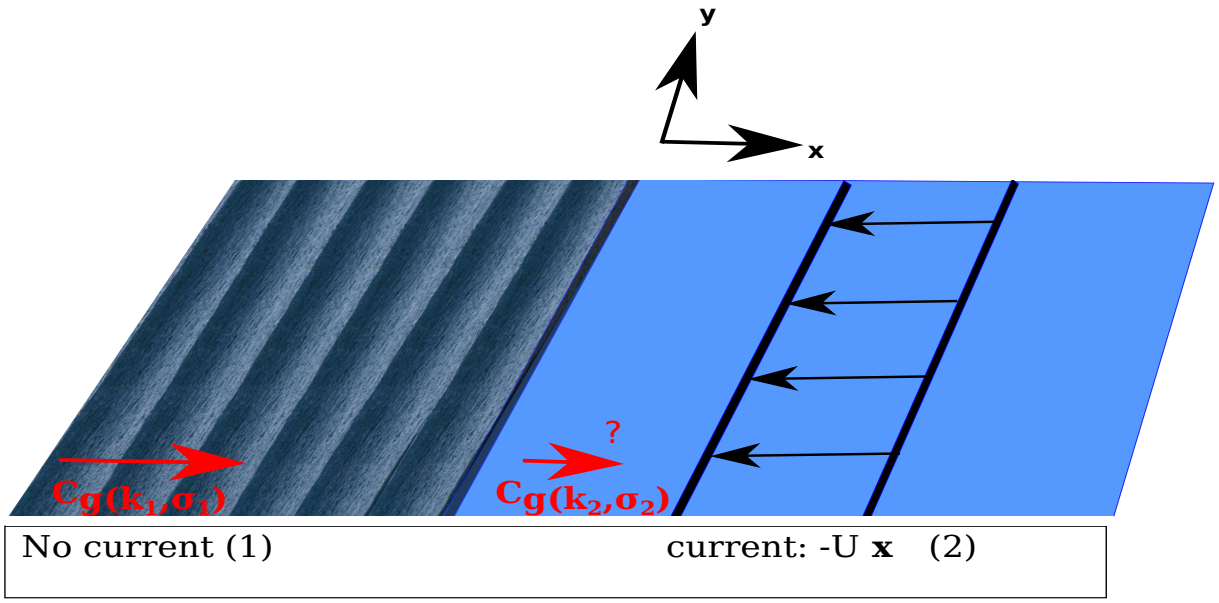

Figure 1.6: Ocean surface split in two areas, one without current and one with current. Waves are propagating eastward (x positive). In the domain (2) waves and current are opposite.

The left-hand side of Eq.1.21 describes the dynamic of the wave action (rate of change over time, advection in physical and spectral space). The right-hand side of Eq.1.21 is the sum of the source and dissipation terms (S_{in}, S_{nl}, S_{dis}) where the terms denote, respectively, wave growth by the wind, nonlinear wave-wave interactions of wave energy through four-wave interactions, wave dissipation due to whitecapping, bottom friction and depth-induced wave breaking. One can notice that Eq.1.21 captures the current-induced refraction, the Doppler shift, and the advection of the wave action. In this manuscript, the current-induced scattering on the waves will be neglected, which is true in general at scale larger than $\mathcal{O}$(1 km).

1.3.1 How wave amplitude is modulated by the effect of the current-induced doppler shift?

We propose a very simple model to highlight how the changes of frequency can result in a change of wave amplitude. We take the framework described in p.57 of Phillips (1977). Let us consider a domain split in two distinct areas, one without current and one with currents propagating in opposite direction of the incident waves. The current is meridionally homogeneous and much slower than the wave group velocity $\mathbf{C}_g$. As the number of crest is conserved between **(1)** and **(2)** we can write,

$$\sigma_1 = \sigma_2 + \mathbf{k}_2.\mathbf{U}, \tag{1.23}$$

In deep water: $\sigma^2 = gk$, so,

$$\sigma_1 = \sigma_2 - \frac{\sigma_2^2}{g}U. \tag{1.24}$$

Figure 1.7: How wave amplitude is changed according to the current intensity (negative values are for opposite current) and wave period.

In **(2)** waves become shorter, and the wavenumber in (2) can be written as a function of the current velocity and the incidence wavenumber. The reader is referred to Phillips (1977) for details.

$$k_2 \quad \sim \quad k_1(1+2\alpha),$$

$\alpha = k_1 U/\sigma_1$ is the ratio of the current intensity at location **(2)** and the phase velocity at location **(1)**. In term of amplitude, considering the conservation of wave action between (1) and (2), ($A \propto a^2$) yields

$$a_2^2 \quad \sim \quad a_1^2(1+4\alpha+4\alpha^2). \tag{1.25}$$

One can see that the modification of the wave amplitude induced by the current in **(2)** is a function of the wavelength (or period) of the incident waves and the intensity of the current. We give the diagram of wave amplitude according to the two variables in Fig.1.7. One can see that where waves and currents are aligned, wave amplitude decreases and vice versa. The shorter incident waves, the more they feel the current and are amplified (decreased) for opposite (aligned) current. These results can be linked with wave steepness ak. From this result one can see a clear reciprocal energy exchange between waves and the underlying current. This energy flux is under the form of radiation stress. To apply this case to a real ocean we refer to Phillips (1977) (p. 60). For a very choppy sea (continuously energized by the wind and balanced with breaking), propagating in a diverging current (first opposed and then aligned with the wave direction), waves become steeper and steeper leading to a vigorous local wave breaking with an intense turbulence at the water surface. Then when waves are entering in the current that flows in the same direction, energy is extracted from the waves to the current. As waves have lost a large part of their energy in breaking upstream, it leads to a much calmer sea surface in the second part of the current. This effect often occurs in strongly varying tidal currents as along our Brittany coasts (at Pointe du Raz -Brittany- for example).

1.3.2 How wave amplitude is modulated by current-induced refraction?

To illustrate the concept of current-induced refraction on waves we propose to the reader the very simple case studied by Johnson (1947) based on the optical geometric framework. Let us consider an area split in two, one with current and one without current as shown in Fig.1.8. A monochromatic wave enters in the current with a certain incidence α. Following the Snell-Descartes law, we can write the following equality,

$$\frac{C_{\phi_0}}{\sin\alpha} = U + \frac{C_\phi}{sin\beta}. \tag{1.26}$$

We recall thanks to the Airy theory that, in deep water, $C_g = \frac{1}{2}C_\phi$ with $C_\phi = \sqrt{\frac{g\lambda}{2\pi}}$. We can write the wavelength as $\lambda = \frac{C_\phi^2 2\pi}{g}$.The link between the angle β and α is

$$\sin\beta = \frac{\lambda}{\lambda_0}\sin\alpha. \tag{1.27}$$

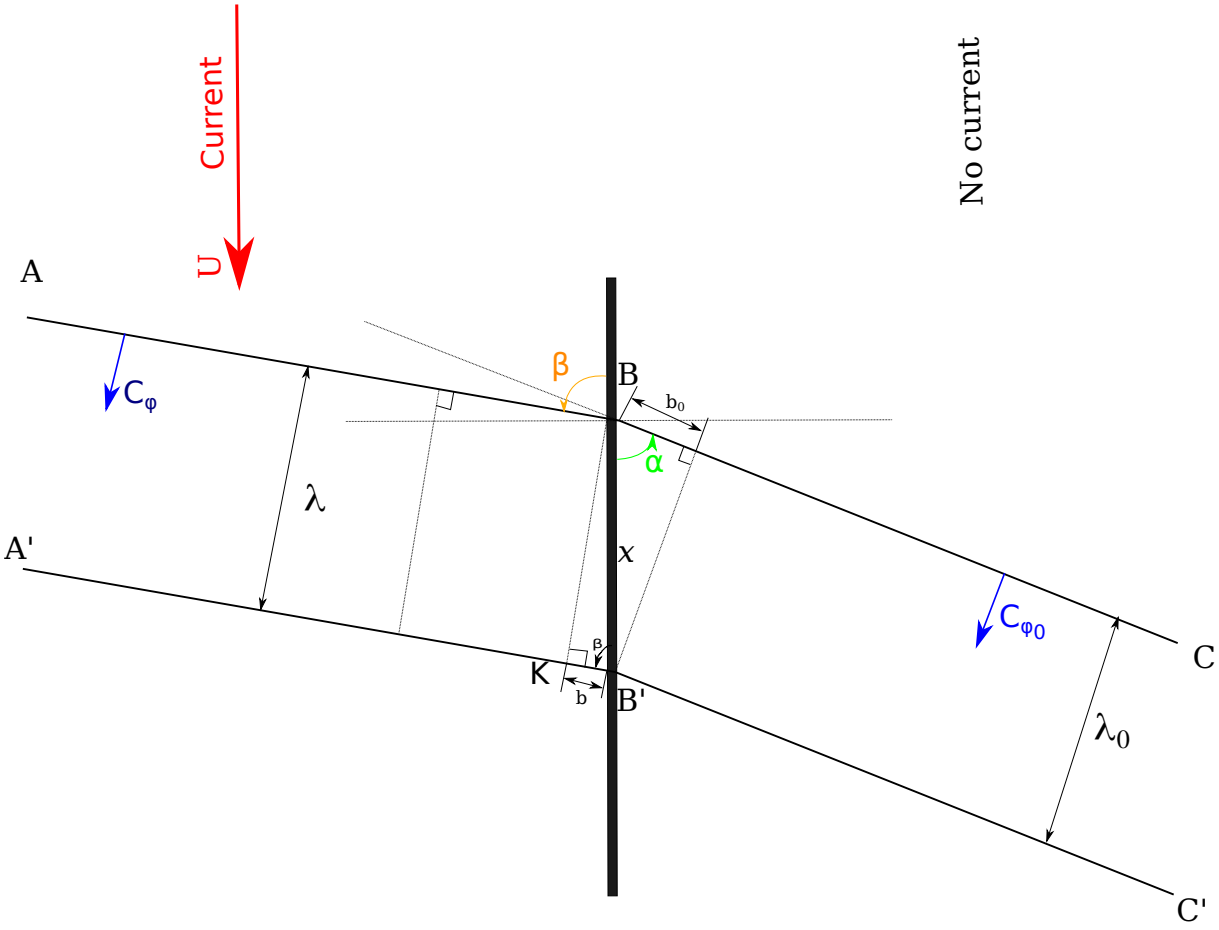

Figure 1.8: Two-wave crests (C,C′) refracted (A,A′) by the presence of a southward surface currents. The reader can recognize the very academic framework of geometric optics with a surface current instead of a change of refracted index *n*. C_{ϕ_0} and C_ϕ are the phase speed in the media without and with current forcings.

Combining Eq.(1.26) and Eq.(1.27) one can write,

$$\sin\beta = \frac{\sin\alpha C_{\phi 0}^2}{(C_{\phi 0} - U sin\alpha)^2}. \tag{1.28}$$

As considered for the previous section, we can consider a undimensional factor function of the underlying current velocity and the incident waves phase velocity,

$$m = \frac{U}{C_{\phi_0}}. \tag{1.29}$$

We write the ratio of the incident and refracted wavelength as a function of m.

$$\frac{\lambda}{\lambda_0} = \frac{1}{(1 - m\sin\alpha)^4}. \tag{1.30}$$

Now that the refraction angle and the evolution of the wavelength have been written exclusively as a function of the initial conditions of the problem, we focus on the evolution of the energy fluxes for one wavelength. The energy is advected by the group velocity. For a length of crest b and b_0 in media with and without current respectively, with b_0=$\overline{BB'}sin\alpha$ and b=$\overline{BB'}$cosβ we have the equality of the fluxes:

$$\frac{1}{2}C_{\phi_0}b_0a_0^2 = \frac{1}{2}C_\phi ba^2 + U sin\beta ba^2, \tag{1.31}$$

with a the amplitude of the waves. Knowing the values of b and b_0 one can write (after some algebra),

$$\left(\frac{a}{\lambda}\right)^2 = \left(\frac{a_0}{\lambda_0}\right)^2 \frac{(1 - msin\alpha)^6}{(1 + msin\alpha)} \frac{cos\alpha}{cos\beta}. \tag{1.32}$$

This relation of the new wave steepness resulting from the current-induced refraction shows a dependency of the incident angle, the refracted angle, current intensity and the phase speed of the waves (directly linked to the incident wavelength). One can see that the refraction induced by the homogeneous current leads to a change of wavelength and a compression/stretching of the wave crest.

We propose to plot the Eq.1.32, i.e., the Δsteepness as a function of the incident angle α for different m, (Δsteepness=M(α,m)). Results are shown in Fig.1.9. $\alpha = 0$, (α=90°) means that wave and current are perpendicular (aligned/opposite). Positive (negative) m means that current is flowing northward (southward). One can see that, for positive m, the wave becomes smoother for small angles and then becomes very steep when waves approach the orthogonality with the current (M$\rightarrow \infty$). The more waves and current perpendicular, the faster the wave steepness increase. Of course M$\rightarrow \infty$ is a no-sense physically, this vertical asymptote is broken because the waves tend to break when wave steepness reaches a certain threshold. For negative m, waves become steeper and steeper for α smaller than a certain incidence (we call it, α_{max}) and becomes rapidly smoother where $\alpha > \alpha_{max}$. The stronger the current (or wave shorts) ($|m| > 0,3$), the greater the wave steepness increases due to refraction and without needing to be strictly perpendicular to the current.

Thanks to this very simple example, we showed that wave amplitude (or steepness) can be enhanced due to the presence of the current through the refraction process. Mei (1989) proposed a similar example by studying the refraction induced by a gaussian surface current (similar to the main structure of western boundary currents). The author proved that waves follow the Fermat's principle, i.e: *wave propagates one location to another such that the*

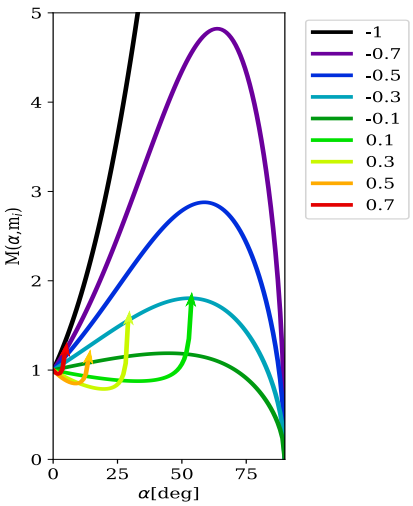

Figure 1.9: Steepness factor (M) with respect to the incidence angle of waves. Each color is a value of m (Eq.1.29) given in the legend. This figure is adpated from the Fig. 4 of Johnson (1947).

path duration is locally the shortest ; and that their trajectories follow the following equation based on Eq.1.13,

$$y - y_0 = \pm \int_{x_0}^{x} \frac{K dx}{(k^2(x) - k_y^2)^{1/2}}, \tag{1.33}$$

y and y_0 are the position of the arrival point and starting point respectively. The framework of Mei (1989)'s studies is given in Fig.1.10. K is the projected wavenumber from the Snell-Descartes equality (ksin(α)=k$_0$sin(α_0)=k$_y$). We do not perform the demonstration of Eq.1.33 in this manuscript but we use it to describe three different wave regimes resulting from current-induced refraction:

1. Waves enter in the Gaussian current with a certain incident angle, waves are refracted inside the current, toward the normal where current intensity increases and toward its initial direction where current intensity decreases. Waves leave the current with the same initial angle. Mathematically, in Eq.(1.33), 0<k_y<min(k) everywhere in the domain.

2. For waves sufficiently short (k larger than a wavenumber threshold) waves cannot enter in the current (mathematically, where the denominator of Eq.(1.33) $\notin \mathcal{R}$), thus waves are reflected by the current.

3. Waves are propagating against the current with an initial propagation inside the Gaussian current. Mathematically the denominator is defined only in $|k_y|$ <k_c^2 thus $-k(x_c)$<k<$k(x_c)$. In this last case waves are trapped inside the current as light waves can be trapped in an optic fiber between two specific refractive indexes or for electron waves in a special class of semiconductor.

If we draw the three regimes: We wanted to highlight the refraction processes in a real ocean. We show in Fig.1.12 two sun-glitter images acquired by the Multi-Spectral Sentinel-2 ESA satellite in the Agulhas current region (panel (a)) and in the Mediterranean Sea, offshore the city of Barcelona (panel (b)). Short crested waves are visible thanks to the contrast of the sun reflection at the wave crests and the wave troughs. We highlight the current fronts by

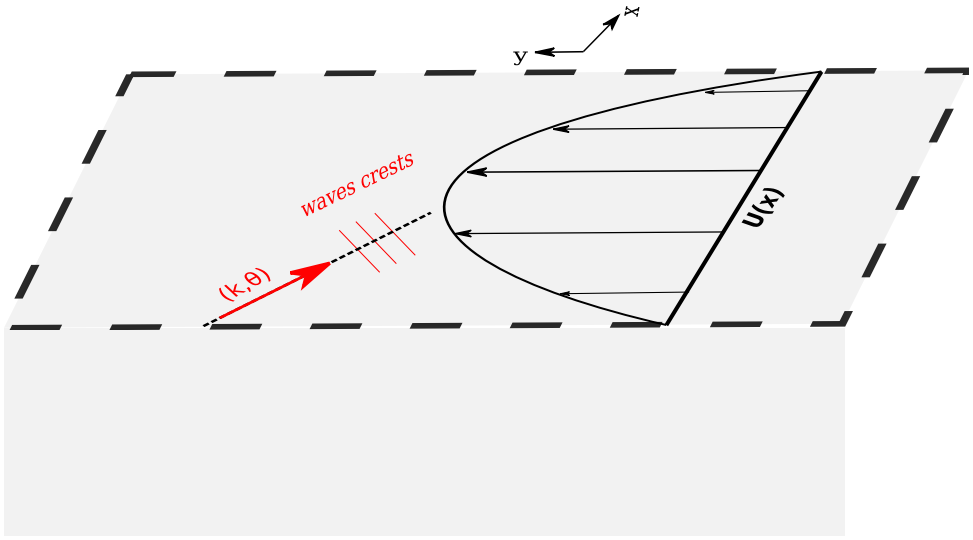

Figure 1.10: Waves propagating inside a surface current field with a gaussian shape (Adapted from Mei (1989)) .

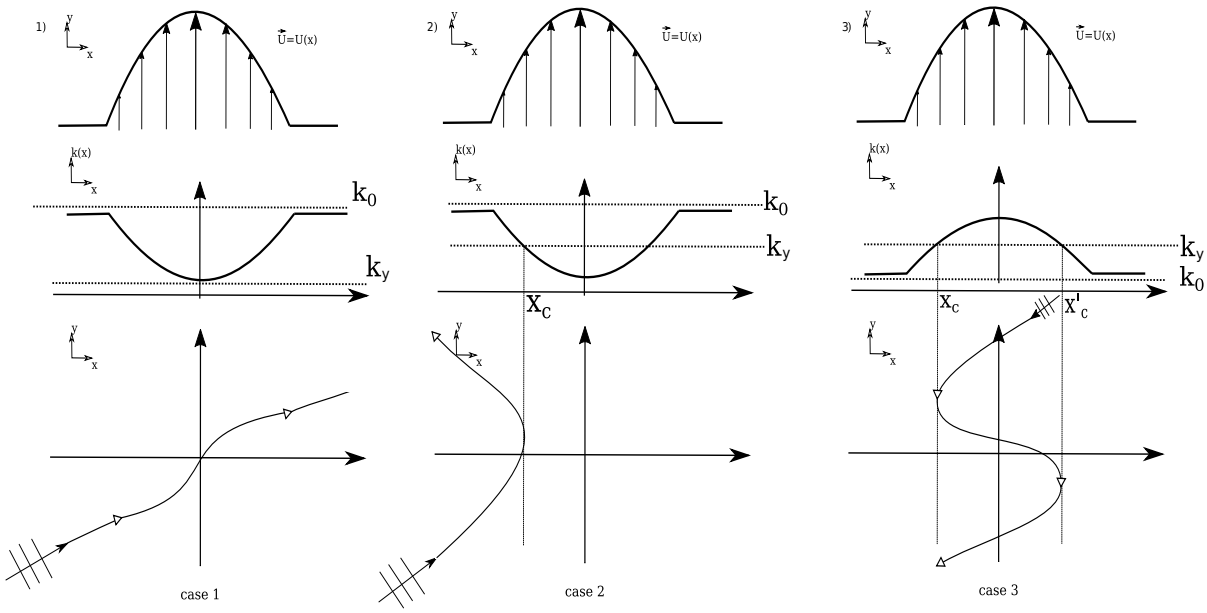

Figure 1.11: Each figure is organized as follows: the top row is the shape of the current, the second row is the evolution of the wavenumber module and the last row gives the trajectory of one wave-ray assuming that the wave action is conserved along its trajectory. Panels (1), (2), and (3) are for the three regimes (1,2, and 3) described above.

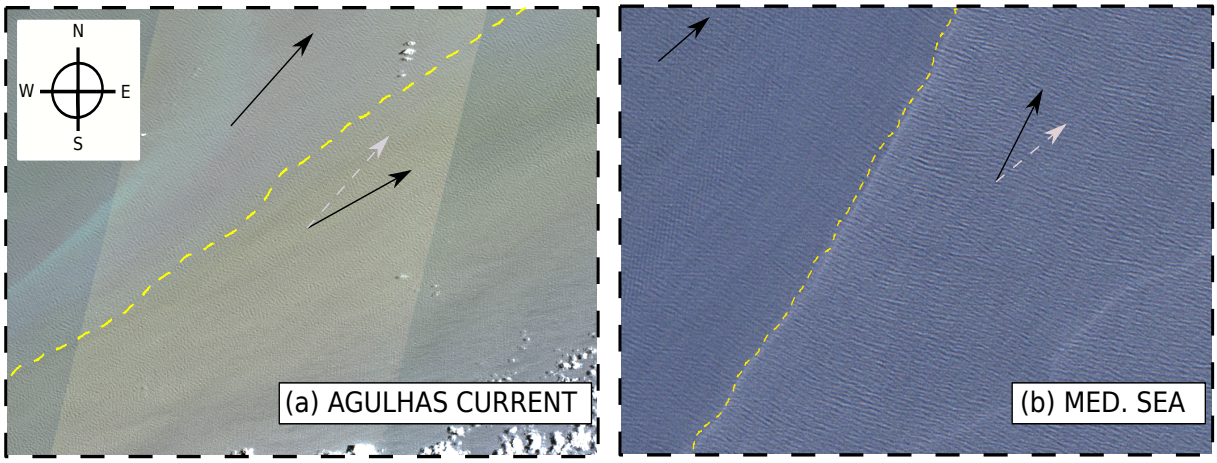

Figure 1.12: Two instantaneous optic images acquired from the Multi-Spectral Sentinel-2 ESA satellite. (a) Acquisition in the Agulhas current region on January 09, 2022. The grey stripes are due to the change of Sentinel-2 sensors during the scanning of the sea. (b) Acquisition in the Mediterranean Sea offshore the city of Barcelona on July 31, 2021. Two current front are highlighted in yellow dashed lines. The black arrows give the mean direction of the waves on both side of fronts. The grey lines are the directions of the waves on the west side of the front projected on the east side of the front.

dashed yellow lines. On both side of the fronts, the wave directions are given by the solid black arrows. The grey arrows represent the direction of the waves at the the west side of the front projected on the east side of the front. Waves are turning due to the current. The intensity of the current-induced refraction can be quantify thanks to a spectral analysis of the image (Kudryavtsev et al., 2017b). In Fig.1.12a, one can see that, at the east side of the front, waves are aligned with the Agulhas current. This has already been discussed by (Kudryavtsev et al., 2017b) and previously in this manuscript. Waves are trapped by the Agulhas current in a same manner that optic fiber traps light between two refraction index. In the Fig.1.12b, waves at the west of the current front are less visible than waves at the east side of the current front. It seems that the current induces a change of the wave steepness leading to an increase of the contrast between wave crests and troughs. The evolution of wave direction by the current-induced refraction is highly visible in this optical image acquired by the Sentinel-2 satellite. Let's note that one can estimate the wave elevation from this image following the method described in Kudryavtsev et al. (2017a).

1.3.3 How the wind work on ocean surface is modulated by the presence of surface currents?

Waves are generated by the work of the wind above the ocean. The interactions between wind and waves are detailed in Janssen (2004). The effective action of wind on the ocean surface (called wind stress-τ-) is relative to the shear flow between the ocean and the wind,

$$\tau = \rho C_D |\mathbf{U}_{atm} - \mathbf{U}_{cur}|(\mathbf{U}_{atm} - \mathbf{U}_{cur}) \tag{1.34}$$

C_D is the drag coefficient, $\mathbf{U}_{atm}$ and $\mathbf{U}_{cur}$ are the wind and current vector velocity and ρ the air density. Thus surface currents modulate the wind force and so indirectly the waves. The H_s decrease induced by the destructive

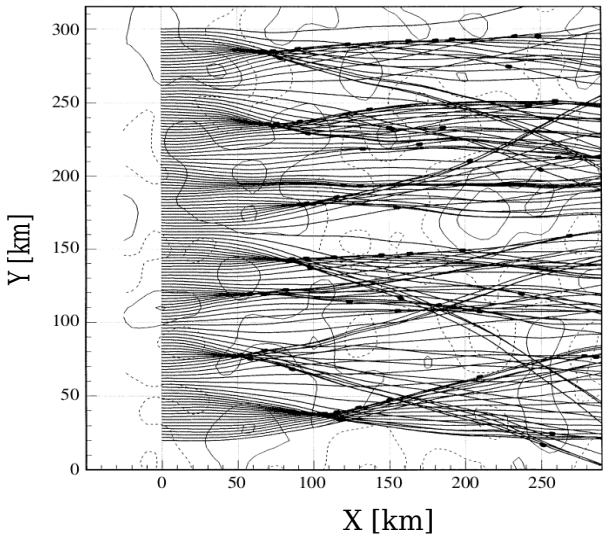

Figure 1.13: From White and Fornberg (1998). Waves rays over a synthetic and chaotic eddies field.

shear between wind and current is well captured by global waves simulation in the circumpolar current where winds and currents are opposed (Echevarria et al., 2021).

1.3.4 Modulation of the wave field in realistic current

From the theoretical works of Mei (1989) and Johnson (1947) we have seen that monochromatic wave trains are deflected and enhanced (or decreased) by the presence of a very simple and deterministic current. In the ocean, the wave field and surface currents are much more random and chaotic. In a more realistic current field, i.e., more stochastic, the effects of a multi-scale surface current field on the wave propagation can be studied with a ray-tracing method. One result is given in Fig.1.13 for wave trains initialized at T=10sec and θ=270° (eastward). The amplitude of the ray curvature (χ), or curvature radius, is a function of the wavelength of incident waves and the vorticity of the flow (Kenyon, 1971; Dysthe, 2001),

$$\chi = \frac{\zeta}{C_g}. \tag{1.35}$$

The relation Eq.(1.35) can be demonstrated by the ray equations. One can see, in Fig.1.13, areas where rays diverge and converge. The location where rays cross is called a caustic. At a caustic location, for monochromatic waves, the theory states that wave action tends to infinity leading to an infinite wave height (Eq.(1.4)). In reality this infinite action is washed away because of the polychromatic nature of the wave field, i.e., wave variance density is not distributed on one discrete frequency but on an interval of frequencies, thus caustic does not emerge. To illustrate the current-induced refraction and the finite amplitude of significant wave height, reader can refer to the works of Ardhuin et al. (2012); Ardhuin et al. (2017); Villas Bôas et al. (2020) where the authors studied the H_s in different current regimes (tidal currents, western boundary currents and seasonal coastal currents). One can notice that H_s lumps and streaks follow the spatial distribution of wave rays which are dependent on the underlying current statistic (Fig.1.14). The combination of the current effects on waves: refraction, wave action advection and the Doppler shift, lead to a spatial redistribution of the wave energy at the meso- and submesoscale range. Please note

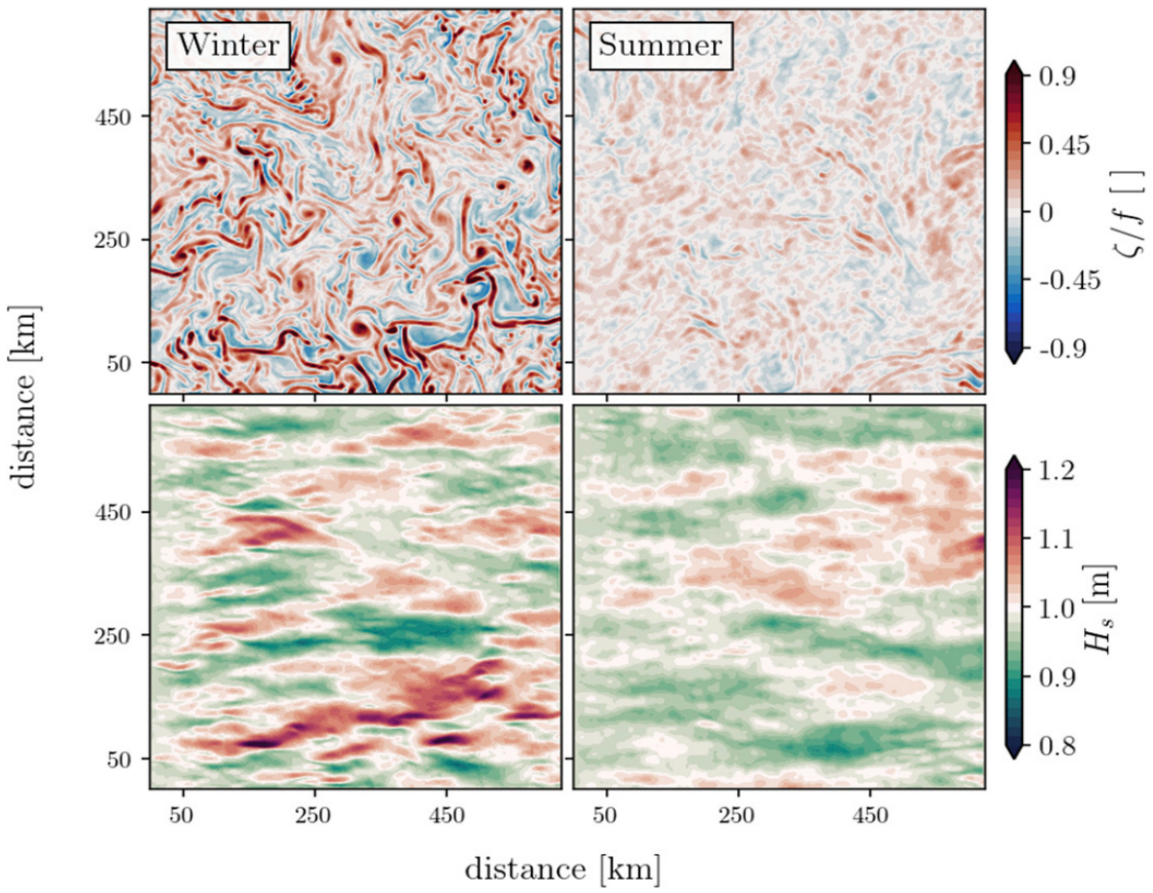

Figure 1.14: From Villas Bôas et al. (2020). Up panels show two surface current vorticity fields in the Coastal California Current simulated with the MITgcm model, one field in winter and one in summer. The two bottom panels are the Significant wave height (H_s) fields modulated by the current presented above (without current H_s is homogeneous and equal to 1m).

that from Fig.1.14, we confirm that the spatial scale of wave height variability induced by current ($\mathcal{O}$(10-100)km) is small relative to the spatial scale of the wind stress force ($\mathcal{O}$(100-1000)km).

1.4 Out of the scope of this Manuscript

In this thesis we focus on wave-current interaction and more specifically on some effects of surface currents on surface gravity waves. A few other effects that will not be further studied are summarized below.

1.4.1 Effect of surface gravity waves on surface currents

Just like surface currents have effects on wave dynamics and their properties, a reciprocal interaction exists, i.e., the effects of waves on the surface current. The Stokes drift induced by surface gravity waves or the mixing in the first meters of the water column resulting from wave breaking are two examples of how waves can modulate the surface

currents. For the theoretic aspects we advise the reader to refer to Rascle (2007) works and for applications in specific current regimes to Suzuki et al. (2016), McWilliams (2018), D.Hypolite et al. (2021). The full interactions between waves and currents can be diagnosed in different current regimes by the use of fully coupled wave-current simulations as demonstrated by Bennis et al. (2011) or Brumer et al. (2020).

1.4.2 Vertical sheared current effect on surface gravity waves

Throughout this manuscript, we refer to surface currents. But what are surface currents? On which range of heights, can we consider the current as at the surface? We showed that we are able to retrieve surface currents from altimeter measurements but what is the meaning of this kind of current in a three-dimensional ocean? One solution is to consider the current as barotropic (same current along the first meters of the ocean), in this framework we can avoid the necessity to define the range of the height of the surface current. However, it is well known that current can be highly baroclinic in the first meter of the ocean (strong shear in the current vertical profile). In a vertical sheared current, the modulation of the wave field by current becomes depth dependent. Thus, the linear dispersion relationship given by Eq. (1.13) has to be modified (Stewart and Joy, 1974),

$$\omega = \sigma + \mathbf{k}.2k \int_{-\infty}^{0} \mathbf{U}(x, y, z, t) e^{2kz} dz \tag{1.36}$$

Considering that waves modulation is highly sensitive to the vertical shear, long waves can "feel" deeper current than shorter waves. Thanks to the Doppler shift of wave frequency induced by the underlying current, the shear of the current can be estimated (Stewart and Joy, 1974). The sensibility of the shift in frequency induced by vertical sheared current is strong for the first 10 meters of the ocean and becomes negligible at higher depth (assuming a linear velocity profile along the vertical, see Fig.1 of Ardhuin et al. (2021)).

An important assumption in this thesis is that the surface currents are assumed uniform over the large enough fraction of the wavelength that the dispersion effect given by eq. (1.36) is practically independent of k. We have shown that the change of wave dispersion induced by current lead to a change of wave amplitude (see Fig.1.7) thus the shear of the current along the vertical will certainly lead to a change of the H_s as well. For a more complete study the considered current should be depth dependent.

1.5 Application of waves-current interactions

1.5.1 Waves forecast

The celebrated works of Munk et al. (1963) or Snodgrass et al. (1966), where authors tracked the swell from its generation in the Indian and Southern Ocean all the way to coasts in California and Alaska, have shown the robustness of the backtracking method. However, there are persistent puzzling failures. Indeed, spatiotemporal biases in swell arrival are often noticed as well as the spatial shift of the location of storm source after back propagation of the swell with respect to the real location. The main reason is the presence of strong current in the swell trajectory. Gallet and Young (2014) proved that, for a storm occurring in the Southern Ocean, strong and large-scale currents in the circumpolar current and at the equator explain the several hundreds of kilometers shift of storm sources. Smit and Janssen (2019) complete the previous study by focusing on submesoscale currents. Authors showed that even if submesoscale currents are weaker than larger mesoscale scale currents, the accumulation of such small-scale

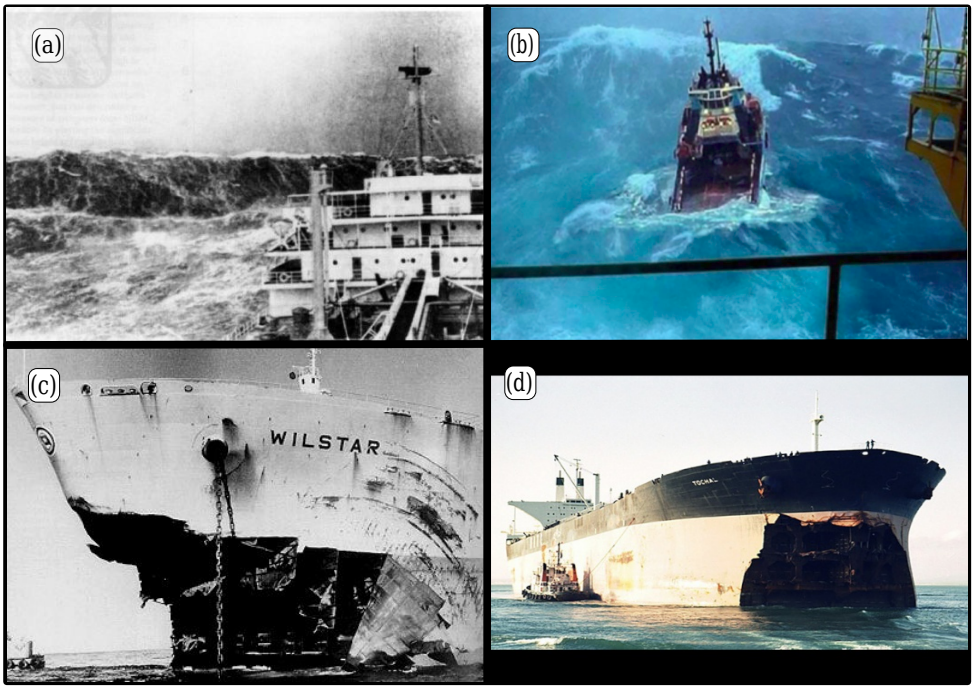

Figure 1.15: Vessels and abnormal high waves. (a) Rare photographs showing the wall of water approaching a vessel and the submersion of a ship at sea (b). High damages induced by the shock of vessels and giant waves: the Norwegian vessel Wilstar in 1974 offshore Durban (c), the Iranian Tochal vessel in 1994 offshore Cape Town (d).

patterns can be responsible for a large uncertainty on wave directionality and thus responsible for a bias in the swell arrival as well.

Albeit this spatiotemporal bias in the swell arrival or the lack of accuracy of the storm source seems to be more a matter of scientific questions or recreational drawbacks, it is crucial to notice that a erroneous forecast of the waves can also induce disastrous consequences on human lives, especially for professionals of the sea. Although today significant wave height forecast are of good quality (with respect to the satellite and buoy measurements among others, Stopa et al. (2016)), operational wave model underestimate the intensity of ∇H_s in strong current fields (Quilfen et al., 2018). It is certain that at regional scale, in coastal boundary current, an underestimation of ∇H_s can result in dramatic consequences (Fig.1.15, Pierson (1972), Mallory (1974),Lavrenov (1998)).[2]

1.5.2 Remote sensing

As waves are at the air-sea interface, this is the first water system seen by remote-sensing satellite for a transparent atmosphere. The contribution of waves on Sea-Level-Anomaly measurements from altimeters is a source of bias, called the Sea-States-Bias (SSB). For instance, SSB resulting from waves have been quantified to be around 3% of the local H_s (Vandemark et al., 2005) for Ka-band measurement, this percentage changed under changing wave conditions: fetch, mean period, etc. Gommenginger et al. (2003) showed that SSB seems to be principally governed by the slope of the long waves more than the H_s. Villas Bôas et al. (2017) showed that the layover effect

2. Abnormal high waves are not exclusively due to the interaction between waves and a strong current but can also emerge from hydrodynamic nonlinear instabilities (Heller, 2005; Ruban, 2010).

induced by the short waves is also a source of the error for the upcoming SWOT satellites. As currents induce a change of wave steepness (and H_s), it is crucial to understand these interactions well to correct the wave-induced biases in the level of the sea measurements. Sandwell and Smith (2005) proposed a correction of waves in the level of the sea measurement assuming H_s very smooth over a scale of $\sim$90 km. Recent study shows that H_s are strongly modulated around 90 km (Ardhuin et al., 2017; Quilfen et al., 2018; Quilfen and Chapron, 2019) thus this correction cannot be applied in strong mesoscale currents.

Beyond altimeter measurements, wave-current interactions have an impact on other remote sensing surface current measurements. The proposed SKIM mission (Ardhuin et al., 2019a) has been imagined to measure directly both surface currents and wave spectrum at an unprecedented spatial resolution from space. The measurement is based on the same processes as a coastal HF radar which measure the Doppler shift of the emitted signal induced by currents. The SKIM Team et al. (2017) highlighted a source of uncertainty in the retrieved current due to the fact that waves and current are closely correlated at scale $<$100 km, waves induce a bias in the Doppler centroid measurement which is dependent on the wave-induced current (Stokes drift). An accurate measurement of the wave spectrum is thus necessary to remove the contribution of the waves in the current signal.

As currents strongly modulate the wave field (Eq.1.21), understanding accurately those modulations can be of benefit to capture surface currents by inverting their effects on waves. Rascle et al. (2014); Rascle et al. (2018) by involving remote sensing images (SAR and optical), showed a strong modulation of the backscattered signal at small scales. Those modulations exhibited structured features as filament or submesoscale eddies. Under assumptions more or less robust, they proposed a first guess of the current gradients (divergent or horizontally sheared currents) by inverting the modulation of the mean square slope induced by the underlying current.

1.5.3 Air-sea fluxes

Recent works performed by Romero et al. (2017), Romero et al. (2020) have shown that submesoscale currents drive inhomogeneity in the wave fields and trigger wave breaking. Because atmosphere-ocean gas exchange is primarily driven by the surface turbulence (Villas Bôas et al., 2019), wave-current interactions are crucial in heat, momentum and aerosols fluxes emission both in the ocean and the atmosphere. As ocean and atmospheric models are conditioned by these fluxes, the better the interactions between waves and currents are understandable, the truer are both oceanic and atmospheric models.

1.6 Abstract of the introduction and Manuscript's structure

Due to the ubiquity of meso- and submesoscale oceanic surface features (eddies, fronts, filaments), wave field is strongly modulated at scales similar to the current features scales from 1 to 200 km (Ardhuin et al., 2017; Romero et al., 2020; Villas Bôas et al., 2020). The modulation of the wave field by current results from the refraction process (change in waves direction), the Doppler shift (change in wave frequency) and the advection of the action fluxes. In the case of strong and well-known tidal currents, wave models are able to capture the spatiotemporal inhomogeneity of the wave field (Ardhuin et al., 2012) even under extreme conditions (Bertin et al., 2012). Evolution of wave height field during high and low tides offshore Brittany coast is given in Fig.1.16. One can see the two spatial variability regimes, one due to the presence of the archipelago and one due to the presence of the strong semidiurnal currents. One can see the maximum values of the wave height offshore. Ouessant Island is only captured by models

forced with tidal currents. The H_s time series in Fig.1.16g shows that all the semidiurnal variability is lost when currents are not taken into account in the wave model. The interactions with other current regimes (mesoscale and submesoscale eddies, fronts, inertial currents, internal waves-induced currents, ...) are definitely less predictable and understandable due to the complexity and the random aspect of such current fields. Although the effects of current on waves kinematic are well documented all along the twentieth century, the documentation of current effects on wave parameters such as H_s are rarer in the realistic current field. It might be because those variations occur at very short spatial-scale whereas H_s measurements at those scales were still anecdotal since the works of Kudryavtsev et al. (2017a), Quilfen and Chapron (2019), or Romero et al. (2017). From a geometrical optics approximation framework, the new high-resolution wave measurements from space and the states of the art of wave modeling in surface current fields, we tried to answer in what way the spatial wave variabilities induced by surface current gradient are related to the underlying currents at meso- and submesoscale? We principally focus on the significant wave height of the waves.

The manuscript is built as follows: first, in chapter 2, thanks to a very idealized framework, we explain and quantify how H_s is modified for a given surface current. Then, in chapter 3, we evaluate and quantify the effects of an idealized and of a realistic oceanic eddy on H_s, $T_{m0,-1}$, and the peak wave direction. The experiment will be done with idealized wave numerical simulations. In chapter 4, we extended chapter 3 to a realistic framework in the Agulhas currents. In this chapter the numerical outputs are validated with high resolved altimeter data and the statistics of spatial gradients of both significant wave height and surface currents are discussed. In chapter 5 we tried to go beyond the one dimensional study provided by altimeter data by the use of the new French-Chinese spectrometer CFOSAT (Hauser et al., 2020) allowing both a directional and a wavelength description of waves variability. In Chapter 6 we propose an aperture of how waves are modulated in very spatially and temporally current regimes as in surface signatures of internal waves and in (near)inertial oscillations. Chapter 7 is a summary of the thesis in French.

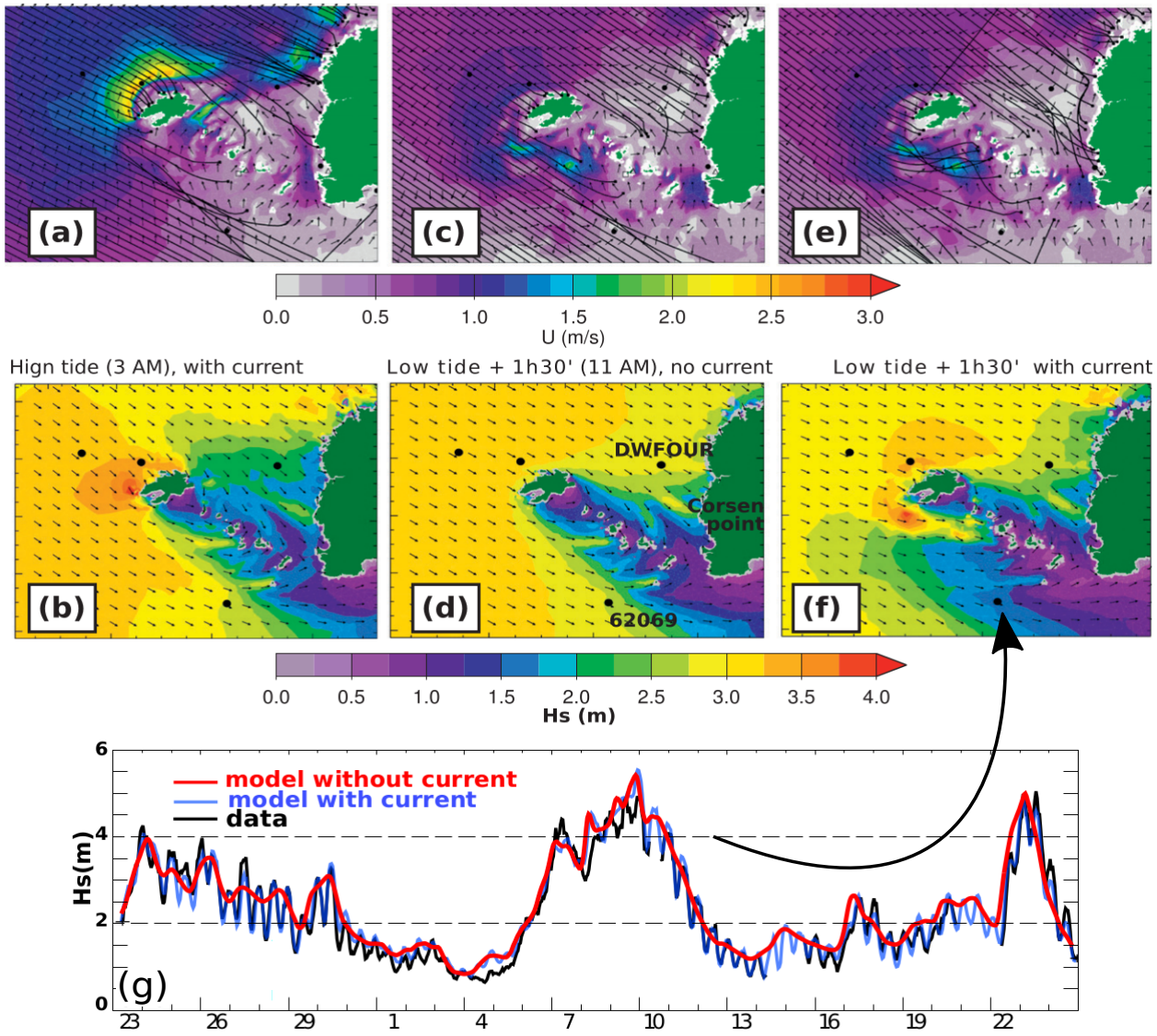

Figure 1.16: Tidal currents and simulated significant wave height field offshore Brittany coast during high (panel a,b) and low tide events without current (panel c,d) and with current (panel e,f). Panel (g) shows measurements at the Pierres Noires buoy (62069) in solid black line. Solid red and blue lines show colocalized H_s simulated without and with currents forcing. From Ardhuin et al. (2012)

CHAPTER 2

WAVE HEIGHT AMPLIFICATION AND ANALOGY WITH OTHER REFRACTION EFFECTS AND SAR IMAGERY

2.1 Conservation of wave energy flux

Villas Bôas et al. (2020) showed numerically that the spatial significant wave height gradients (∇H_s) at the mesoscale and the submesoscale range are driven by the intensity and the nature of the underlying flow. In this chapter we show qualitatively and quantitatively how current-induced refraction enhances significant wave height via a very simplified theoretical model. We consider a semi-open domain with an open right boundary and a wave generator at the left boundary. The wave trains are assumed to be monochromatic. From the left to the right boundary, the wave action flux is assumed to be conserved such that,

$$\nabla.(\mathbf{C}_g \frac{A}{\sigma}) = 0, \tag{2.1}$$

with A the action density, σ the incident wave frequency and C_g the associated group speed. In the domain we impose a very simplified current profile which can be described analytically. The current-induced refraction will be highlighted by a ray tracing method, in the same manner of White and Fornberg (1998) (Fig.1.13). At the left boundary, we consider a tubes of rays with a width equal to the distant between two successive rays (diameter of dl_0 at the left boundary and dl(x) at a distance x from the left boundary). We follow the energy inside these tube of rays throughout the domain. Assuming that the energy flux is conserved throughout one tube of ray, and neglect variations of C_g along the wave path line, the change of energy induced by refraction is simply given by the change of the ray tube diameter. A sketch in Fig.2.1 describes the framework. We consider a current of the form: $u(x, y)$=$(u(y), 0)$. The question that we want to answer here is, for a given current field and an initial H_s, what is the value of H_s at a distance x from the left boundary after that refraction occurs?

We focus on one tube of rays. From the conservation of the wave action, we can write:

$$C_{g0} \frac{A(x_0, y_0)}{\sigma_0} dl_0 = C_g \frac{A(x, y)}{\sigma} dl(x), \tag{2.2}$$

x_0 and y_0 are the position of the ray at the west boundary and y its position at a distance x. The position y is equal to,

$$y = y_0 + dy, \tag{2.3}$$

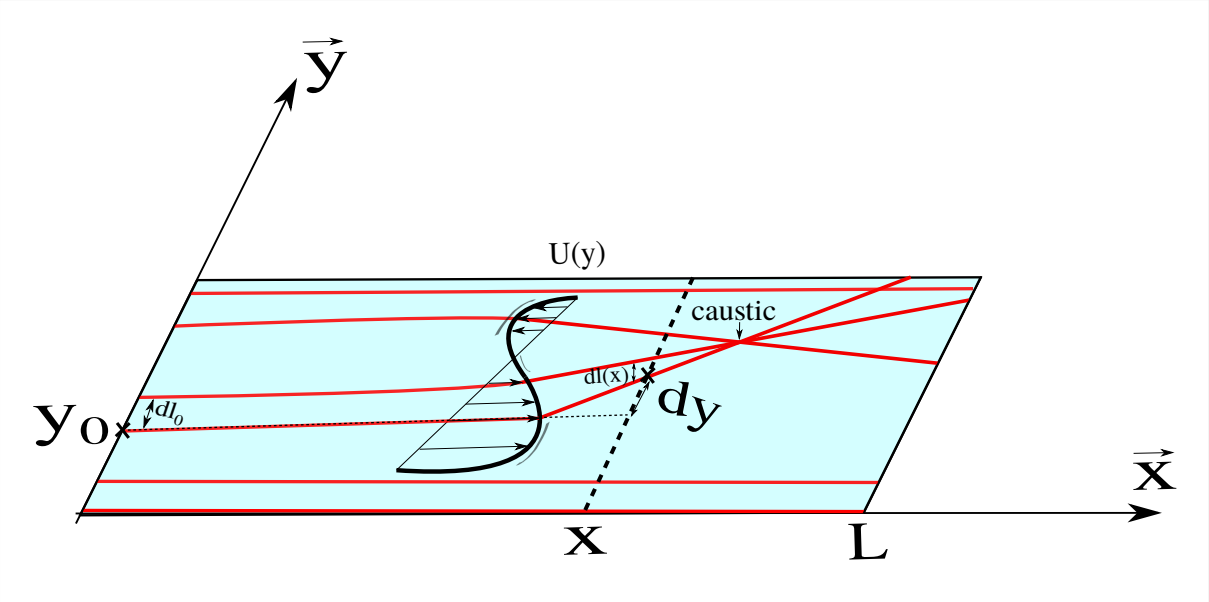

Figure 2.1: Sketch of ray tracing over an isolated zonal current (y-axis dependent). Wave rays are deflected from their initial direction because of refraction. The original width of ray tubes is dl_0, this width is equal to dl(x) in x.

with dy the deviation induced by the current shear. From Eq.1.35 one can write,

$$y = y_0 + \int_x \int_{x'} \frac{\zeta}{C_g} dx dx'. \tag{2.4}$$

One can recognize the curvature of the wave ray due to refraction in Eq.(2.4). The double integral is because the curvature of a function is linked to the second derivative of the function. For the simplified problem of a velocity field $u(y)$ over a strip from $x = 0$ to $x = L$, the Eq.(2.4) above can be rewritten in a more general form to give the location of y of a ray as a function of the velocity field u,

$$Y(x, y_0) = y_0 + \int\int \frac{1}{C_g(x'', Y(x'', y_0))} \frac{\partial u(x'', Y(x, y_0))}{\partial y} \mathrm{d}x' \mathrm{d}x''. \tag{2.5}$$

As a result, the conservation of wave action ($A = \frac{E}{\sigma}$) in a tube of rays that start parallel at $Y(x, y_0)$ and $Y(x, y_0 + dy)$ is

$$C_g(x, Y)E(x)[Y(x, y_0 + dy) - Y(x, y_0)]/\sigma(x) = C_g(0)E(0)dy/\sigma_0, \tag{2.6}$$

and, neglecting variations of C_g and σ for a start, it can be rewritten as

$$E(x, Y) = \frac{C_g(0)E(0)}{C_g(x, Y)} \frac{1}{\partial Y/\partial dy_0} = \frac{1}{1 + \frac{1}{C_g(0)} \int\int \frac{\partial^2 U}{\partial y^2} \mathrm{d}x' \mathrm{d}x''} E(0). \tag{2.7}$$

In other words, for any given x the energy distribution along the y axis, perpendicular to the direction of propagation and to the current u is given by a mapping from 0 to x, with an initially uniform distribution (we could also

start from a non-uniform distribution), is transformed by the Jacobian of the mapping, $1/1 + \int\int \frac{\partial^2 U}{\partial y^2}/C_g \mathrm{d}x'\mathrm{d}x''$.

2.2 Numerical application of Eq.2.7

2.2.1 Note on spectral wave model

Structure of wave model

Although the setups of a wave model are described in this chapter and in chapters 3 and 4, we consider it wise to quickly introduce how the wave model is built. Our numerical investigations are based on the WAVEWATCH-III framework which solves the wave action equation (Eq.1.21). Because we only consider the spectral density and not the relative phases of the different components WAVEWATCH III is called a **phase-averaged** model in opposition with other wave models that at least solve for the bispectrum, complex amplitudes, or solve for the wave field in the space or time domain (Herbers and Burton, 1997; Janssen and Herbers, 2009; Kirby, 1984; Belibassakis, 2007). WAVEWATCH-III describes how the wave action spectrum evolves both in spatial and spectral space. The model computes at each grid point the evolution of the wave spectrum (see spectra in Fig.1.2) following a chosen numerical scheme. The computed spectra can be extracted at specific points (which is numerically costly) or integrated to retrieve wave parameters, namely H_s, mean period, mean direction, mean square slope .... The details of how the waves are modeled (forcing, initialization, boundary conditions, sources terms, ...) are given in the user manual (The WAVEWATCH III ® Development Group, 2019).

Performance and drawback of wave model

Wave models have been improved a lot until today. The oldest one reported was the works of Montagne (1922) where the author proposed a 18 to 36 hours swell forecast for commercial traffic offshore Morocco coasts. Then, during World War II, allies took advantage of W.Munk wave forecast work for the military troops landing in Normandy. [1] Finally, wave models have been continuously developed and parametrized in agreement with field measurements and theories to describe waves generation, propagation and dissipation as much coherence as possible. The performance of present spectral wave models with respect to buoys and altimeters measurements are described in Stopa et al. (2016), authors showed that both high and low moments of the wave spectrum are well simulated except for the directional spreading which needs improvement. Today we are able to simulate both in direction and wavenumber wave systems from several hundred meters to a few meter wavelength. Nevertheless, the dynamic of short waves (meter to centimeter meters scale) is still questioned due to their own dynamics, it seems that short-wave formation does not seem inline with the theory of the long wave formation (Munk, 2009; Peureux, 2017)). In this thesis we will only focus on waves from several hundred meters to $\sim$ 10 m wavelengths.

2.2.2 Wave model set up

We considered two current profiles,

1. **u**(x,y)=(U_0y $\vec{x}$, 0 $\vec{y}$),
2. **u**(x,y)=(U_0cos(y) $\vec{x}$, 0 $\vec{y}$),

1. Thanks to the declassification of thus works, the performance of Munk works have been described in Bates (1949).

with U_0=1.5 ms^{-1}. One can see that both flows are rotational ($\zeta = \partial_x v - \partial_y u$) so the waves will be refracted for both cases and their associated deviation will be equal to $\frac{\zeta}{C_g}$. However the profile (1) has a second derivative that is equal to 0 so according to the Eq.2.7, the wave energy at a distance x along the y-axis will be equal to the initial energy. For the current profile (2) we expect that the distribution of the energy at the distance x along the y-axis will have the form of cosine function. We verify it with idealized numerical experiments. We based the experiments on the WAVEWATCH-III framework that solves the wave action equation (Eq.1.21) with incidence waves of 10 sec peak period. Waves are initialized with $H_s = 1$ m with a direction equal to 270°. Waves are generated at the left boundary every hour from narrow wave spectra gaussian in frequency.

2.2.3 Results: curvature of wave rays and H_s enhancement

We try to explain how the H_s is modified by the current-induced refraction. We propose to compare the theoretical result obtained from Eq.2.7 and the numerical output from the simulation based on the WAVEWATCH-III framework for the current profile (2). The Eq.2.7 is rewritten in terms of H_s considering H_s=4$\sqrt{E}$. Theoretical and numerical results when waves reach the stationary state are shown in Fig.2.2. At large scale the H_s structures show similar patterns for both results with two areas of H_s enhancement centered around Y=30km and Y=90km separated by one area of H_s reduction. Nevertheless, the structures of H_s enhancement do not coincide for both results. Numerical simulations show cusp structures whereas theoretical results shows two large patches. In those large patches of H_s enhancement, the maximum of H_s reaches 4 m (saturated range of the color scale in Fig.2.2) whereas the simulated H_s does not exceed 2.2 m. Where the width of ray tubes becomes too narrow the analytical model overestimates the H_s. Perhaps integrating the second derivative of the current only along the x-direction is a too strong assumption. Integrating the current along the rays could yield a result closer to the numerical simulation. Also we guess that the limit with this analytical study is that we considered the width of the ray tube as the only contributor of the change in energy in the current field. We thought to extend this analytical study by taking into account the contribution of all wave rays initially horizontal (not bent) and homogeneously distributed at the left boundary, as done in White and Fornberg (1998). Each wave ray carries a certain quantity of wave action. At a distance x from the left boundary the distribution of the rays is strongly different from the initial distribution at the left boundary (Fig.2.1). The new questions will therefore be: is the evolution of H_s induced by the current-induced refraction related to the new distribution of the wave rays? By how much is related?

Although that the Eq.2.7 does not provide an accurate estimation of the H_s if the integral is performed only along the x-direction, it provides a qualitative information of the ∇H_s and both a qualitative and quantitative information of the current-induced refraction. Numerical results, when waves reach the stationary states for current forcing fields (1) and (2) are shown in Fig.2.3. Thanks to a Monte Carlo ray tracing method, we see that waves are deflected from their initial direction due to the presence of the current. For the current profile (1), wave rays are bent toward the bottom part of the domain whereas current profile (2) shows trapped ray structures with 2 caustics at X=37 km in the areas where currents are flowing toward the left. One can see that the rays that are aligned with the current direction at Y$\sim$65 km remain straight. The associated H_s fields show a constant H_s equal to the initial H_s (1 m). For current forcing (1), H_s remains constant and equal to the initial H_s. For current forcing (2), the two areas of H_s enhancements are explained previously (cf Fig.2.2). One can see that where wave rays converge the model yields H_s enhancement areas with a maximum where caustics occur. The distance where caustics occur has been computed from Eq.2.7 by finding the value of x where the denominator is equal to 0. For current profile (2)

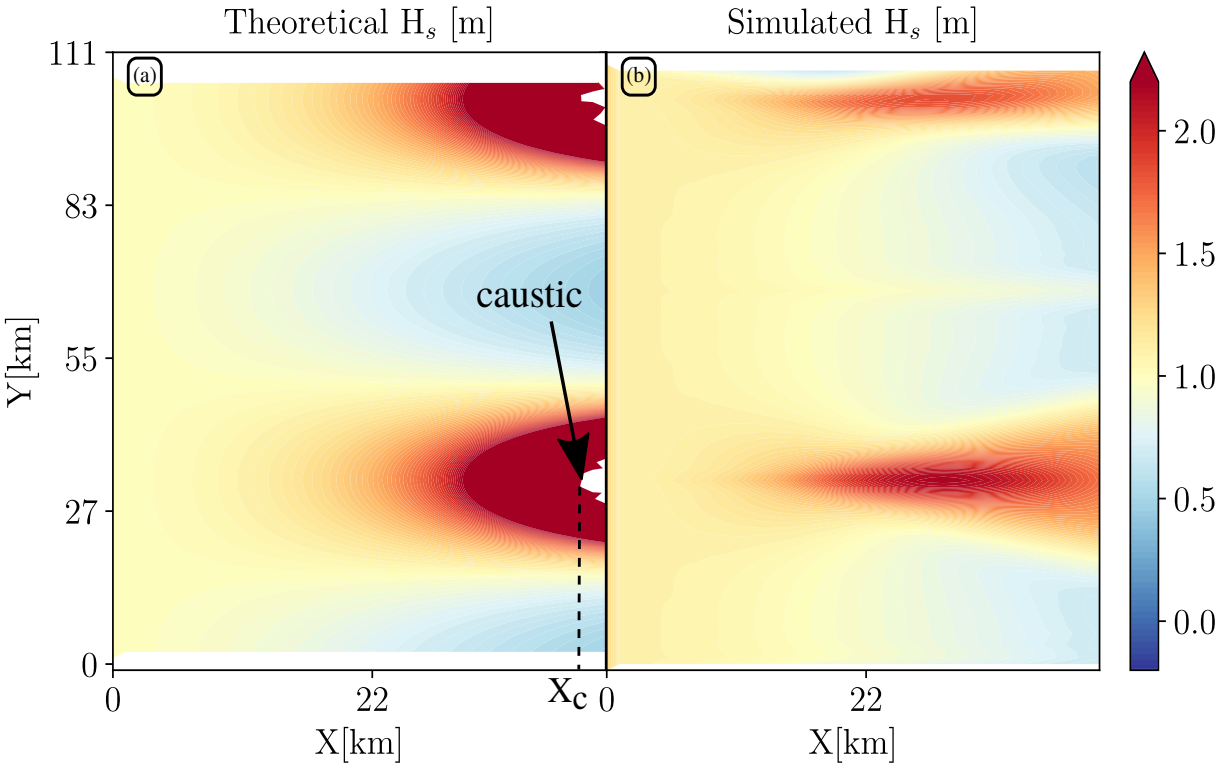

Figure 2.2: Significant wave height fields from (a) Eq.2.7 and (b) WAVEWATCH-III simulation. X_c is the distance from the left boundary where caustic occures. Without current H_s is equal to 1m in the entire domain.

the analytical application yields $x = 37.288$ m which confirms the first result yielded by the ray tracing method. Surface current profiles with a non null second derivative lead to the modification of the width of the ray tubes and create ∇H_s. Upstream from the wave caustic, one can notice that the directional spreading (σ_θ) of the wave system is the highest because waves are coming from all directions. Downstream the caustic, σ_θ decreases which can be noticed by the fact that wave rays are scattered.

2.2.4 Discussions: surface current gradients and cusp singularity

Current induced-refraction bends wave rays. In the case where the current profile shows a non-null second derivative, wave rays can create caustics (Fig.2.3c). For a sufficiently large number of wave rays, slightly upward the caustic one can see a cusp shape of the rays correlated to the patches of H_s enhancement (Fig.2.3d). In the works of White and Fornberg (1998); Heller et al. (2008), the authors assimilated these regions in the ocean where giant waves are produced which corroborate with our numerical findings (cf. the strong enhancement of H_s beneath the rays in Fig.2.3). Downstream from the first cusp singularity one can see that wave rays are scattered. The focalization regime of the wave rays switches to a dispersive regime and the H_s signal is spread out. This agrees with our Eq.2.7 and results of White and Fornberg (1998); Heller et al. (2008). The distance of the first cusp singularity appears from the left boundary was established in White and Fornberg (1998) and equal to,

$$L \sim \Upsilon(\tilde{u_0}/C_g)^{-2/3}, \tag{2.8}$$

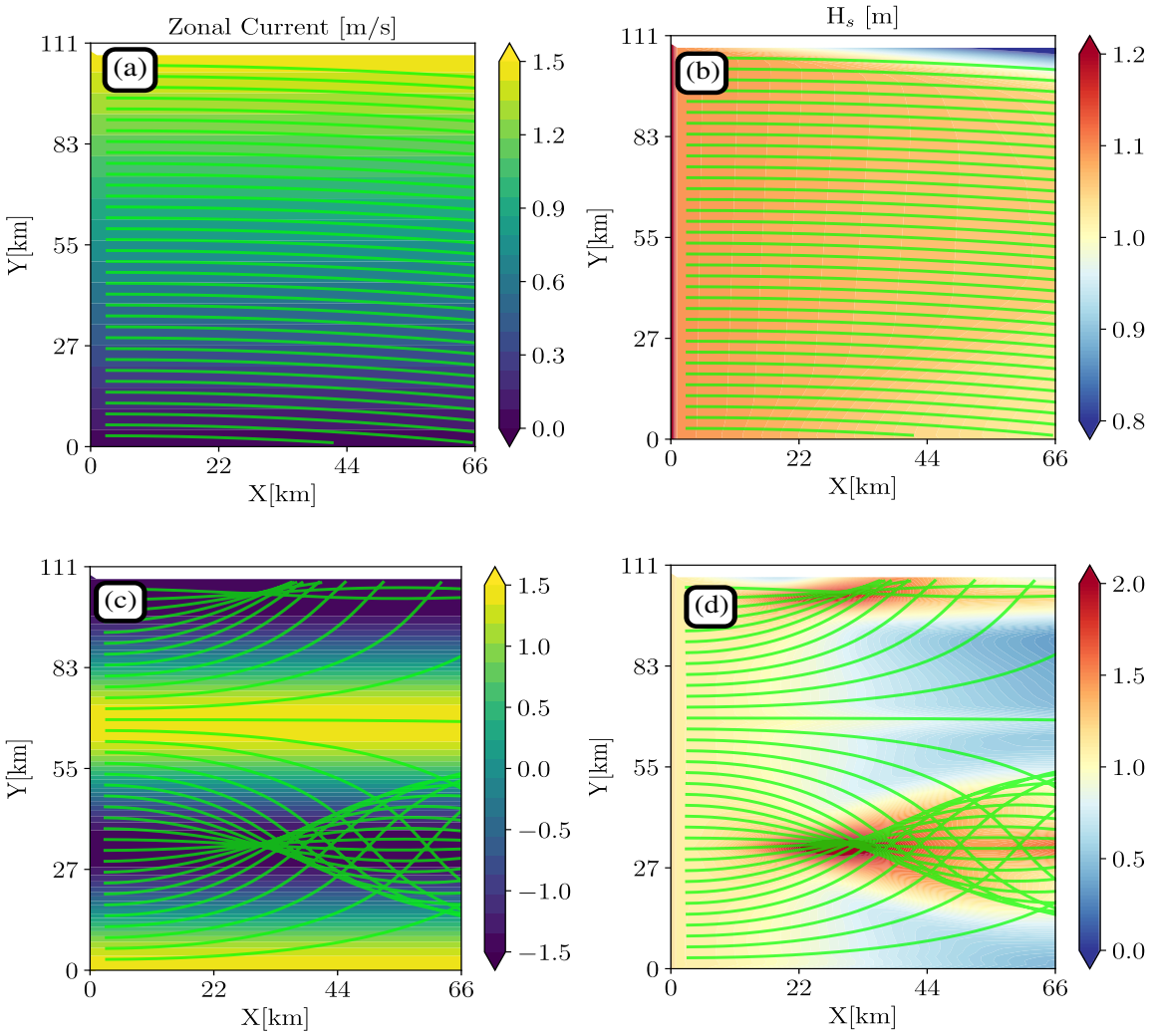

Figure 2.3: Very idealized numerical simulations of current-induced variability on the significant wave height field. Panels (a) and (c) show the current profiles where waves are propagating, the current is stationary. Panels (b) and (d) show the simulated H_s fields when the wave fields reach the stationary state. Solid green lines are wave rays which highlight the current-induced refraction by following the trajectory where wave action is conserved.

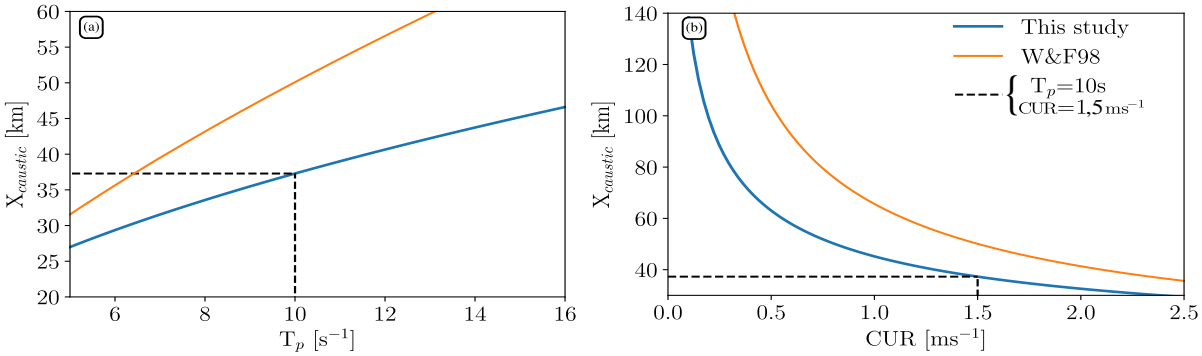

Figure 2.4: Panel (a): The distance from the left boundary of the first caustic as a function of the current intensity, for 10 sec incident waves. Panel (b) The distance from the left boundary of the first caustic as a function of the incident wave period for current intensity equal to 1.5 ms^{-1}. The intersection of blue and dashed black lines highlight the example of Fig.2.3 ($X_{caustic}$=37.288 km). Both panels are for current profile of **u**(x,y)=(U_0cos(y)$\vec{x}$,0$\vec{y}$). The theoretical solution of White and Fornberg (1998) is given in orange.

with Υ the correlation length of the current and $\tilde{u_0}$ the velocity fluctuations over the correlation length. We computed the distance of the first caustics from Eq.(2.8), for incidence waves of 10 sec of period, an underlying current velocity fluctuation of 1.5 ms^{-1} and a correlation length of 1/4 of the current's wavelength. For the surface current profile (2) the distance obtained from Eq.2.7 perfectly matches with the caustic obtained from the ray tracing method. The result of Eq.(2.8) expects that the caustic occurs 10 km further to the right with respect to the ray tracing results. This shift could be due to the fact that the Eq.(2.8) is based on the assumption that the first caustic occurs at a distance L much larger than $\tilde{u_0}$ which is not the case here (L = 37 km and $\tilde{u_0}$ = 18 km). It would be interesting to verify the Eq.(2.8) in realistic oceanic current patterns. Nevertheless, one can notice that for variable currents intensity and incident wave periods, our analytical finding is qualitatively in agreement with results of White and Fornberg (1998).

Heller (2005) introduced the freak index (γ) that is a measure of the danger or the "chance to meet an abnormal high wave" at sea. This index is equal to,

$$\gamma = \chi'/\sigma_\theta, \tag{2.9}$$

with χ' the angle of deflection of the wave ray (equal to the ray curvature over a given distance) and σ_θ the directional spreading of the incident waves. From Eq.2.9 one can see that the more the waves are directional, the more the freak index increases. This means that in a strong current during a storm with a very strong wind sea with incoming waves from a lot of directions, the chance to meet abnormal high waves is less than for well-directional wave trains. In the same context, the intensity of how wave rays are bent is therefore a proxy of the occurrence of waves with extreme height. We do not make the application here because the currents are not realistic.

2.2.5 Discussions: Ray tracing and H_s in other current gradient fields

In the case of very idealized framework, we have seen that ∇H_s appear for current profile with a non-null second derivative. We propose to extend the previous results in other idealized current profile with the same Υ and $U_0 = 0.5 ms^{-1}$:

3. **u**(x,y)=($U_0 \sin(x)\ \vec{x}$,0 $\vec{y}$),
4. **u**(x,y)=(0 $\vec{x}$,$U_0 \sin(x)\ \vec{y}$),
5. **u**(x,y)=(0 $\vec{x}$,$U_0 \sin(y)\ \vec{y}$).
6. **u**(x,y)=($U_0 \sin(y)\ \vec{x}$,0 $\vec{y}$) $\rightarrow$ very similar to the current profile (2).

We consider the new current profiles (3, 4, 5, 6) to study all the components of the deformation tensor, $\partial_{x_i} u_j$, repeated indices i,j = 1 to 2 indicate summation over x and y dimension. The wave field propagates from the left boundary to the right boundary. We rerun our wave model with T_p =7 sec and H_s =1.2m incident waves. We plot the numerical results when the wave fields reach the stationary state, results are given in Fig.2.5. The Eq.2.7 should be modified to take into account the y-component of the flow vorticity responsible for the wave ray curvature. Without rewriting the equation explicitly, we expect that flows with no vorticity (profile (3) and (5)) cannot modify the width of the ray tubes and therefore cannot modify the H_s field.

For current profile (3, Fig. 2.5a), 7 sec incident waves becomes longer where current and waves are aligned ($\sim +0.5$s) and shorter where waves and current are opposite (~ -1.5s). The change of wave period is not shown here. Where waves and current are opposite, H_s increases from 1.2 m to 1.5 m according to the calculus performed in chapter 1 section (see Fig.1.7). We see the opposite where waves and current are opposed with a decrease of H_s from 1.2 m to 1m. For current profile (4, Fig. 2.5b) one can see that H_s are not enhanced in the domain. The width of the ray tubes remains constant. However, rays are curved due to the vorticity of the flow. One can see that the curvature of the rays does not match perfectly with the current profile, indeed, the maximum of curvature is slightly downstream from the maximum of the current intensity. For current profile purely divergent (5, Fig. 2.5c), the strain of the current induce a slight modification of the ray-tube width with a slight increase of H_s (from 1.2 m to 1.5 m) where rays converge. We see the opposite where rays diverge (from 1.2 to 0.9m). In this current there is no caustic in the first 88 km. This slight deviation of the rays with this increase of H_s for purely diverging flow corroborates with Villas Bôas and Young (2020); Villas Bôas et al. (2020). The current profile (6,Fig. 2.5b) provides a non-null vorticity and inflection points (a non null second derivative) perpendicular to the incident direction of the waves. Waves (rays) are strongly refracted with the appearance of a caustic around $X = 66$ km and $Y = 55$ km. At this location H_s reach values higher than 1.8 m. One can see the decrease of H_s by a factor of two (from 1.2 m to 0.6m) where rays diverge (ray tubes become wider).

2.3 Synthetic Aperture Radar imagery analogy

The Eq.2.7 is very similar to the distribution of acoustic power in sound propagation. If one is interested in the spatial properties of $E(x, y)$, as defined by a power spectral density in y, we can also use the analogy with the synthetic aperture radar processing that shifts the position of pixels in a SAR image relative to their positions in a real aperture image (Hasselmann et al., 1985a). We note that E is proportional to H_s^2, and thus the spectrum of E is related to the spectrum of H_s that was investigated by Ardhuin et al. (2017) andVillas Bôas et al. (2020). In the case of the SAR transformation, the y direction corresponds to the azimuth direction, and the mapping is $Y = y_0 + wZ/V$ where Z is the vertical distance between the radar and target and V is the velocity of the radar. The vertical orbital velocity of the waves, w, is here replaced by a transformation of the current field as given by eq. (2.5). From this analogy, we expect that the spatial variation of the energy E has both a quasi-linear regime in which it is

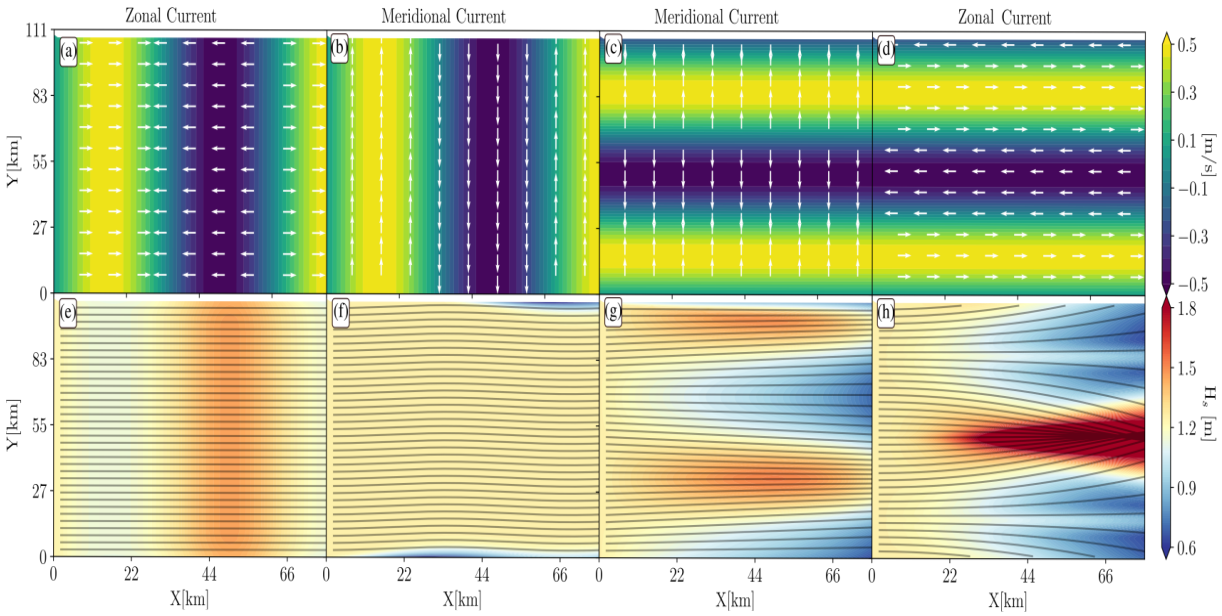

Figure 2.5: Upper row (panels a, b,c, and d), current profiles and their associated direction in white arrows. Bottom row, the associated simulated H_s (panels e, f, g, and h). The expressions of the current profiles are given above, in the core of the manuscript, as items (3), (4), (5), and (6) for panel a, b, c, and d respectively. Wave rays from a Monte-Carlo ray tracing are superimposed to the H_s field.

proportional to the spatial variation of the current, and a cut-off effect that effectively removes all small scales for wave numbers larger than the root mean square ray displacement Y. This can be computed explicitly for $Y \ll 1/k_y$ where k_y is the typical wavenumber of the current field, as we can approximately use $U(Y(x'', Y(x, y_0)) \simeq U(y_0)$. It would be interesting to verify how currents act as waves act on the SAR transformation for multi-scale current fields (more realistic than the currents presented in this chapter). It would be a good approach to study, among others, the respective effects of meso- and submesoscales currents on the H_s field.

2.4 Summary of the chapter

In this chapter we showed how the H_s are modulated by the presence of surface currents from an analytical and idealized framework based on the conservation of the action flux in the current field. From this analytical model, we have shown that current profiles without a non-null second derivative in the direction perpendicular to the wave direction, cannot redistribute the initial wave energy. We performed numerical simulations to verify the robustness of the developed model. Although the analytical model reproduced solely qualitatively the numerical outputs upward from the first wave ray caustic, i.e., only the good localization of the H_s enhancement and the position of the first wave rays caustics with a remarkable precision. The distance of the first caustic given in White and Fornberg (1998) does not coincide with the Monte Carlo ray tracing experiments presented in the chapter. This might be due to the fact that the distance from the left boundary and the first caustic has a similar length scale with respect to the correlation length of the currents used. In White and Fornberg (1998), the authors worked with much more realistic and turbulent flows and showed that most of the first caustic occurs at distance

three times the correlation length of the current patterns (as shown in the example in Fig.1.13). The wave action concentration into a lens shape, or caustics, have been assimilated to the location of the formation of abnormal high waves (Lavrenov, 1998; White and Fornberg, 1998; Heller, 2005; Heller et al., 2008). Numerical simulations reveal strong H_s maximums with a cusp shape where wave rays converge and form lenses. Finally, we have shown that the current-induced ray curvatures are comparable to the SAR transformation induced by the wavy surface. The superposition of current features deviates the wave rays and creates zones of focalization and defocalization of the rays as the velocity bunching induced by the waves in the SAR transformation. From the numerical outputs presented in this chapter and the analogy of the SAR transformation, we propose to extend this very idealized study to focus on the H_s variability in more realistic current patterns. We will try to quantify the H_s modifications in terms of amplitude and spatial scales with respect to the intensity and the scales of the current.

CHAPTER 3

IDEALIZED WAVE SIMULATIONS IN AN ISOLATED MESOSCALE OCEANIC EDDY

We showed in the introduction that the ocean surface is strongly turbulent, much more than described by Benjamin Franklin in 1786. The characterization of ocean variability at mesoscale has been significantly improved thanks to two decades of nadir altimetry (Chelton et al., 2011). From the first mesoscale oceanic eddies observed in detail in the Gulf-Stream rings in 1951 by Fuglister and Worthington (Fuglister and Worthington, 1951) to the recent advances in ocean modeling and eddy-resolving simulations (Capet et al., 2016; Klein et al., 2008; Gula et al., 2015), the turbulence of the ocean at meso- and submesoscale has been increasingly well documented since the last century. The energy cascade from very large scale to microscale through meso- and submesoscale oceanic processes significantly affects ocean biodiversity via physical-biological interactions. As waves are strongly modified at the mesoscale range and because eddies populate the entire ocean surface, we proposed to study how the wave field is modified by such oceanic patterns. We proposed an idealized numerical study based on the WAVEWATCH-III framework forced by both a simplified eddy field and a more realistic eddy field. The aim of this section is firstly, to quantify the effect of a realistic oceanic current pattern on the wave characteristic and secondly, how the spatial surface current gradients are related to spatial wave characteristic gradients. We will principally focus on the H_s.

The major part of the results presented in this chapter have been submitted to the journal Ocean Science on June 3, 2021. There is some overlapping with the introduction. Also the reference Marechal and Ardhuin (2021) was mentioned, this paper is given in the next chapter.

3.1 Introduction

The ubiquity of mesoscale (10-100 km) and submesoscale (1-10 km) eddies, fronts, and filaments at the superficial layer of the ocean induces a strong variability in the wave field: waves-current interactions result in a change of significant wave height (H_s), frequency, and direction (Phillips (1977) and Mei (1989)). From these modulations, it has been proved recently, thanks to both field measurements and numerical simulations, that the effects of currents on waves induce strong regional inhomogeneity of the wave field (Romero et al., 2017; Romero et al., 2020). In particular, Ardhuin et al. (2017) showed, thanks to realistic numerical simulations that the H_s variability is closely linked to surface Kinetic Energy (KE) at the mesoscale range. Quilfen et al. (2018); Quilfen and Chapron (2019) used high resolution H_s measurements from altimetry to highlight the close link between current gradients (∇U) and significant wave height gradients (∇H_s). Villas Bôas and Young (2020) proved, in the absence of wave dissipation and wind momentum input, that the gradient of the wave direction induced by current is necessarily induced by the solenoidal component of the surface currents (vorticity). Finally, Villas Bôas et al. (2020), under the same

assumptions, emphasized the narrow link between the vorticity of the flow and the ∇H_s. Surface currents seem to increase the deep-water breaking wave probability (Romero et al., 2017; Romero et al., 2020). Wave breaking at the air-sea interface is the major source of momentum and heat exchange between waves and currents (Melville and Rapp, 1985; Cavaleri et al., 2012) or gas and sea spray production (Monahan et al., 1986; Veron, 2015). That is why surface mesoscale and submesoscale currents, through their interactions with the wave field, have a significant impact on air-sea fluxes (momentum, gas, heat, sea-spray, ...).

In the ocean and particularly in western boundary currents, eddies are ubiquitous from the mesoscale to the submesoscale range Chelton et al. (2007); Chelton et al. (2011); Gula et al. (2015); McWilliams (2016); Rocha et al. (2016a). The interaction between eddy field and waves is thus of primary importance for the global distribution of wave properties. In the present study, we analyze numerically the effect of an isolated and large realistic eddy on the wave properties (H_s, $\mathrm{T}_{m0,-1}$, and direction). Former similar works have been already performed, but only for idealized eddy cases (i.e. Gaussian profiles, see Mapp et al. (1985); Mathiesen (1987); Holthuijsen and Tolman (1991); White and Fornberg (1998); Gallet and Young (2014)). However, the structure of eddies in the ocean can strongly differ from textbook analytical idealized profiles (Le Vu et al., 2018; de Marez et al., 2019), making the study of waves-Gaussian eddies an unrealistic framework. Indeed, the instabilities occurring in a large and isolated eddy result in the strong production of energy in the ocean submesoscale range (Hua et al., 2013; de Marez et al., 2020b) which would interact strongly with waves. Furthermore, most of the previous studies solely focused on the refraction induced by an eddy without discussing on the modulation of wave parameters (H_s or mean wave period, Mapp et al. (1985); White and Fornberg (1998); Gallet and Young (2014)). Here, our goal is to investigate the long-term mean effects of an isolated cyclonic eddy with a realistic shape (highly dynamic at the meso- and submesoscale) on the wave properties. We demonstrate that wave field characteristics are strongly modified by the presence of the eddy and that the wave variability is more important as the eddy field is multi-scale dynamic.

In a actual ocean, it has been shown that the propagation of ocean swells is affected by the presence of currents. The resulting deviation of the waves from the great circle path due to current-induced refraction is affected by both mesoscale currents (Gallet and Young, 2014) and submesoscale turbulences (Smit and Janssen, 2019). In this chapter we show the cumulative effects of both mesoscale eddy and submesoscale currents on the wave propagation and their characteristics. Also the extreme values of wave properties will be investigated. This study is relevant for remote sensing application. The estimated ocean circulation from altimeter measurements are affected by noise correlated to the H_s. Some proposed methods to remove the contribution of waves in altimeter measurements assume that the wave field is sufficiently smooth (homogeneous) under 200 km (Sandwell and Smith, 2005). Focus on H_s variability over a realistic eddy field pattern (more realistic than a Gaussian eddy) will reveal very sharp H_s gradients at scale smaller than 200 km. Thus, it results that the assumption that the wave field is homogeneous at the scale of hundred kilometers erroneous. Quantify the heterogeneity in the wave field at the mesoscale range would allow improving denoising methods in the measurement of Sea-Level-Anomaly. Finally, previous works showed that wave characteristics can be inverted to infer surface currents intensity (Huang et al., 1972; Sheres et al., 1985), more recently Villas Bôas et al. (2020) showed that ∇H_s can be inverted to infer the statistics of the underlying ∇U. The phases of these ∇U are difficult to infer due to the non-local effect of the current on the H_s. In the same framework of Villas Bôas et al. (2020) we will show that the amplitude of ∇U could be estimated by inverting the variability of the wave field induced by the eddy field. Reconstructing such ∇U field would be fruitful for a wide range of applications (search and rescue, plastic debris monitoring, biological activities or short-term

wave forecast) but we will see that such reconstruction is limited due to the nonlocal effects of the current on H_s. Please note that the studied eddy, dynamic both at the meso- and the submesoscale range, is typically the current structures that can be found in the vicinity of main branches of western boundary currents, e.g., in the Gulf-Stream (see Fig.9a of Gula et al. (2016) among other).

This chapter is organized as follows. First, we introduce the eddy structure used in the study, based on the work of de Marez et al. (2020b), and the numerical framework WAVEWATCH III (The WAVEWATCH III ® Development Group, 2019) without source term. Then, we present the results of the numerical experiments. We discuss how significant wave height and current gradients are coupled in the optical geometry approximation both in and downstream from the realistic eddy. A quick investigation of how the effects of nonlinear wave-wave interactions on the intensity of the wave parameter gradients is given in Appendix 2. Limits and perspectives of this present work close this chapter.

3.2 Method

3.2.1 A cyclonic eddy from in-situ measurements

To study the wave propagation through an eddy field, we used the current outputs of the simulation performed by de Marez et al. (2020b). In this study, authors performed idealized simulations, using the Coastal and Regional Ocean COmmunity model, CROCO (Shchepetkin and McWilliams, 2005), that solves the hydrostatic primitive equations (PE) for the velocity $\mathbf{u} = (u, v, w)$, temperature T, and salinity S, using the full equation of state for seawater (Shchepetkin and McWilliams, 2011). The spatial resolutions are chosen to accurately resolve both the frontal dynamics and the forward energy cascade at the surface. The simulation is initialized with a composite cyclonic eddy as revealed by Argo floats in the northern Arabian Sea (details of the composite extraction are fully described in de Marez et al. (2019)). The eddy is intensified at the surface, but has a deep-reaching influence down to about 1000 m depth. Its initial horizontal shape corresponds to a shielded vorticity monopole: a positive core of vorticity and a shield of negative vorticity (Fig. 3.1(c)). Its radius, $R = 100$ km, is large compared to the mean regional Rossby radius R_D (47 km, see Chelton et al. (1998)). It is a mesoscale eddy. In the following, mentions of "submesoscale" refers to features and processes occurring at scales that are small compared to Rossby deformation radius (*i.e.* $Bu > 1$ with $Bu = \frac{R_D^2}{L^2}$). de Marez et al. (2020b) observed that the eddy is unstable with respect to a mixed barotropic/baroclinic instability. The latter deforms the eddy, which eventually evolves into a tripole after about 4 months of simulation. Sharp fronts are subsequently generated in the surface mixed layer at the edge of the tripole. These fronts then become unstable, and this generates submesoscale cyclones and filaments. Near these fronts, diapycnal mixing occurs, causing the potential vorticity to change sign locally, and symmetric instability to develop in the core of the cyclonic eddy. Despite the instabilities, the eddy is not destroyed and remains a large-scale coherent structure for one year of simulation. A full description of instability processes can be found in de Marez et al. (2020b). Snapshots of the current velocity and vorticity of the fully developed eddy field after 210 days of simulation are represented in Fig. 3.1b and d respectively. The main core of the cyclone is surrounded by filaments, submesoscale eddies and fronts, that lead to sharp vorticity gradients. This vorticity field is far from the usual idealized representation of eddies often considered in the literature, and is closer to reality (see *e.g.* Fig. 1 in Lévy et al. (2018) for an example of a realistic turbulent field above mesoscale eddies).

For the purpose of the present study, we consider the surface velocity fields (the simulated level closest to

the ocean surface) from the simulation outputs described above. We use the initial state that represents the eddy before instabilities occur (Fig. 3.1(a)), and the state after 210 days of simulation, in which submesoscale features have been generated by the spontaneous destabilization of the eddy (Fig. 3.1(b)). At 210 days all instabilities have occurred (mixed barotropic/baroclinic instabilities). After 210 days, the eddy field starts to dissipate making some small-scales features disappear (de Marez et al., 2020b)[1]. We note that the use of strictly 2D surface current is an approximation of what happens in nature. In reality, waves feel the effects of an "average current" integrated over a certain depth along the first meters of the water column. This depth depends on the wavelength of the waves (Kirby and Chen, 1989). We discuss this approximation at the end of the chapter.

3.2.2 The wave model

To describe the dynamic of waves over the eddy described above, we use the WAVEWATCH III framework (The WAVEWATCH III ® Development Group, 2019) forced both with the initial state of the eddy (Gaussian shape, Fig.3.1a,c) and the fully developed eddy (Fig.3.1b,d). The model integrates the wave action equation (Eq.1.21). For this study we consider swell, far from their generation areas, propagating in the current field without any source term (no dissipation, no nonlinear exchange between waves, and no wind input, i.e. the right-hand side of Eq.(1.21) is equal to 0). The aim of the current study is to investigate, in a very idealized case, how long wave properties can be modified by an eddy field more realistic than an isolated Gaussian eddy.

Throughout this chapter we discuss the evolution of the amplitude, the wavelength and the direction of the wave field through the H_s, the mean wave period weighted on the low frequency part of the wave spectrum ($T_{m0,-1}$), and the peak direction respectively. H_s and $T_{m0,-1}$ are called "bulk parameter" because they are integrated over the wave energy spectrum $E(\sigma, \theta)$. They are defined by the Eq.1.4 and Eq.1.5. The performance of the wave model used in this chapter has already been discussed in boundary current systems such as in the Gulf Stream, the Drake Passage and the Agulhas current, especially concerning the H_s estimation (Ardhuin et al., 2017; Marechal and Ardhuin, 2021). In those previous studies, wind forcing, waves dissipation, and nonlinear wave-wave interactions have been taken into account.

We initialized simulations with waves that are propagating from the left boundary of a 500×500 km Cartesian domain, with a resolution of 500 m both in horizontal (X-dimension) and vertical directions (Y-dimension). The right boundary is open. The initialization is done with narrow-banded wave spectra gaussian in frequency centered at varying peak frequencies, f_p=0.1428 Hz, 0.097 Hz, and 0.0602 Hz. The energy spectrum has a frequency spreading of 0.03 Hz around the peak frequency and the initial H_s is equal to 1 m. The frequencies have been chosen to correspond to the mean periods used in the work of Villas Bôas et al. (2020) (7 s, 10.3 s, and 16.6 s). Waves are generated every hour at the left boundary, from spectra described above. The initial direction of waves is 270°. The direction convention follows the meteorological convention such that 270° waves are coming from the left and 0° waves are coming from the top of the domain. The wave field reaches a stationary state after 09:15, 08:45, and 07:30 of simulations for initializations of T_p=7 s, T_p=10.3 s, and T_p=16.6 s, respectively. We recall that source terms have been set to zero and the current field is assumed stationary. The wave model global time step is 12 s, the spatial advection time step is 4 s, and the spectral advection time step is 1 s. The model provides outputs every fifteen minutes. Wave spectra are computed at each grid point, discretized into 32 frequencies and 48 directions. High directional resolution is required for a better description of wave refraction, especially in the strong rotational

1. The cyclonic vortex field is available at https://data.mendeley.com/datasets/bwkctkk5bn/1

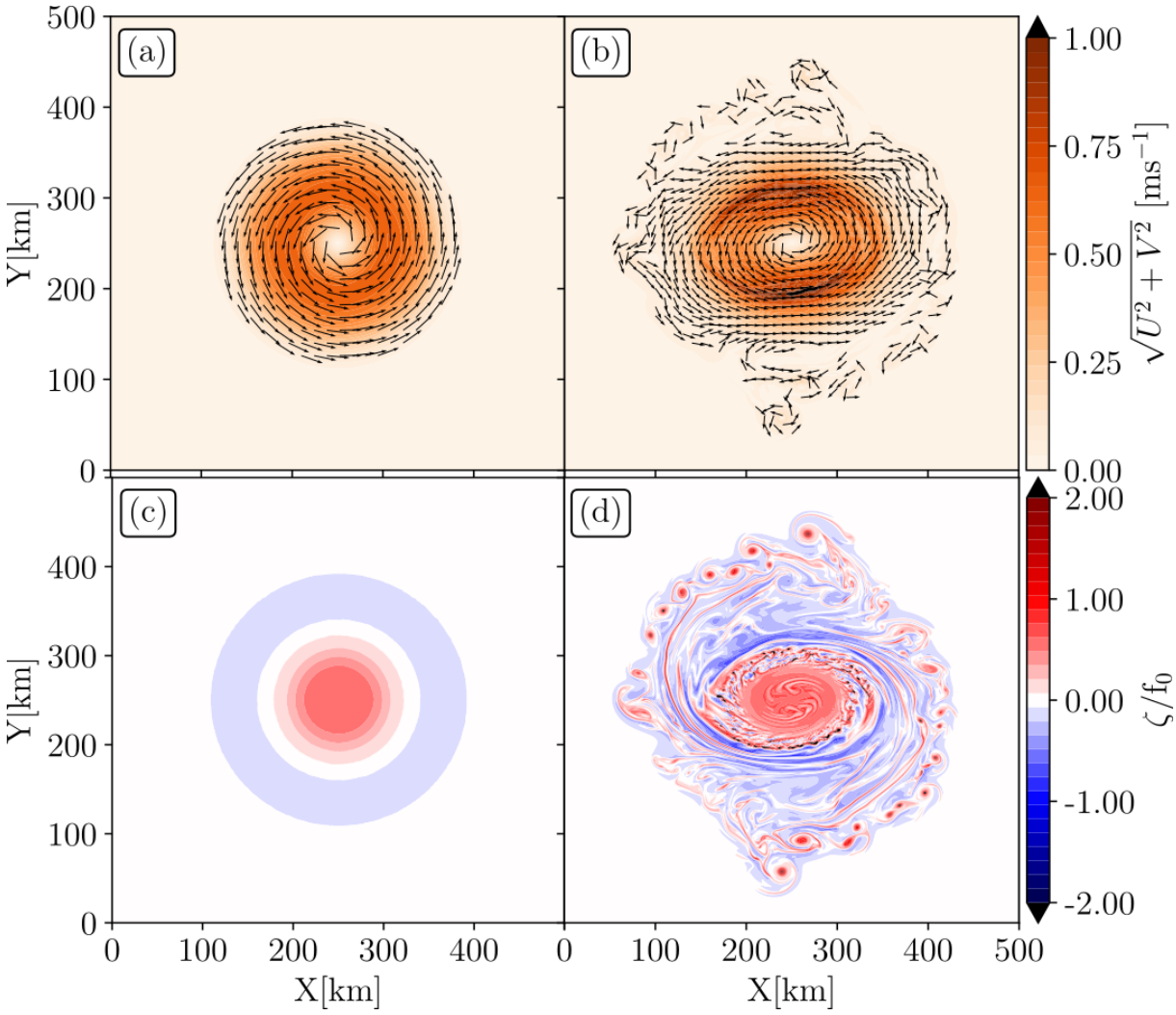

Figure 3.1: Surface currents velocity and direction for the initial/Gaussian eddy (panel a) and after 210 days of destabilization (panel b). Their associated normalized relative vorticity (ζ=$\partial_x V - \partial_y U$) is given in panel (c) and (d). The Coriolis parameter is kept constant in the simulations: $f_0 = 5.2\,10^{-5}\,\mathrm{s}^{-1}$. The original zonal and meridional velocities (de Marez et al., 2020b) have been multiplied by two here.

currents (Ardhuin et al., 2017; Marechal and Ardhuin, 2021). The surface current forcing fields are from de Marez et al. (2020b)'s simulations outputs. In one case we consider the initial shape of the cyclonic eddy (Fig. 3.1(a,c)). In the other case, we consider the fully developed state of the cyclonic eddy (Fig. 3.1(b,d)). In the following, these cases are called the initial and the fully developed cases, respectively. The initial eddy case is similar to the former works performed over analytical eddy (Mathiesen, 1987; Holthuijsen and Tolman, 1991; White and Fornberg, 1998; Gallet and Young, 2014). The variation timescale of the current is much longer ($\mathcal{O}(1)$ week) than the waves (($\mathcal{O}(1)$ minute). So it respects the steady current assumption during one wave train propagation. The eddy described in the previous section and in de Marez et al. (2020b) is an averaged composite eddy reconstructed from measurements in the Arabian Sea (de Marez et al., 2019). The method of reconstruction tends to an underestimation of the eddy intensity, that is why the intensity of the current has been multiplied by two to increase the effects of the currents on wave properties. The eddy is staying geophysically realistic (current velocity remains around 1 m.s^{-1} and normalized vorticity lower than 2, Fig.3.1). Those values are comparable with surface vorticity measured in the first hundred meters of the Arabian sea (de Marez et al., 2020a) and simulated in other current regimes as in the western boundary currents (Gula et al., 2015; Tedesco et al., 2019). Although the eddy field represented in Fig.3.1 is from an averaged composite eddy (solely estimated using in-situ data), it has been considered, in this study, as realistic because it differs from an analytical vortex. Also, it has been compared with altimeter and drifter data in the region where it has been estimated. The cyclonic eddy is coherent with those measurements (see Fig.12, 13, and 14 of de Marez et al. (2019)).

3.3 Wave field variability in a cyclonic and realistic eddy

The frequency sensibility of the incident waves is studied both in the initial and in the fully developed eddy. Waves are dispersive in deep water, their group and their energy propagates at the group velocity (C_g). For T_p=7 sec, T_p=10.3 sec and T_p=16.6 s, group velocity are 5, 8, and 13 m.s^{-1}. To reach X=X$_0$ (a given value of the horizontal axis) shorter waves take more time than longer waves. As waves are generated continuously from the left boundary, a stationary state is reached after a sufficiently long simulation time. In Figs. 3.2, 3.5, and 3.6 fields are taken once the stationary state is reached. Surface currents modulate the wave amplitude, the wave frequency and the waves direction. The variability of those quantities is highlighted through H_s, T$_{m0,-1}$, and θ_p fields. The response of other waves variability for these underlying current, as the directional spreading or the mean direction, is not described in this chapter.

3.3.1 Modulation of wave parameters

We presented in the first chapter that the wave action is redistributed by the surface current revealing spatial H_s gradients. Here we present how both an idealized and a realistic eddy field redistributes spatially the wave action. The size and the intensity of spatial gradients of wave parameters will be discussed according to the current forcing field and the incident frequency of the waves.

Significant wave height

Surface currents induce a strong regional H_s variability, especially in a highly solenoidal field (Ardhuin et al., 2017; Villas Bôas et al., 2020). Outputs of wave simulations forced with the initial and with the fully developed eddy are

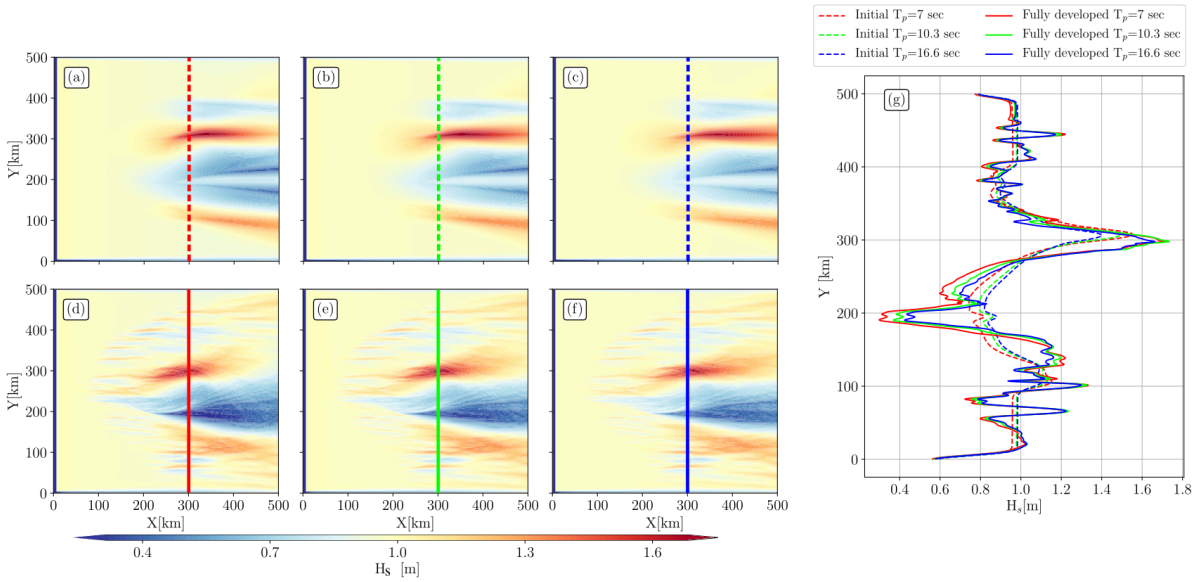

Figure 3.2: Significant wave height (H_s) fields for (a,d) T_p=7 sec, (b,e) 10.3 sec, and (c,f) 16.6 sec incident waves. Without current forcing the entire domain is equal to the initial H_s (1 m). The first row (a,b,c) shows H_s fields for simulations forced with the initial eddy (Fig. 3.1(a,c)); the second row (d,e,f) shows the same fields but for simulations forced with the fully developed eddy (Fig3.1(b,d)). Panel (g) shows H_s along X = 300 km (colored dashed/solid lines in left panels) for all simulations.

given in Fig. 3.2. The presence of the vortex induces strong ∇H_s, inside and outside the eddy fields. Simulations forced with the initial eddy (3.2a,b,c) show large scale and alternate signs of H_s structures along meridians (fixed X−axis). The increase and decrease structures have a lens shape. H_s reaches a maximum of 1.62 m at X=333 km and Y=311 km for simulation initialized at T_p=7 sec, 1.62 m at X=349 km and Y=310 km for simulation initialized at T_p=10.3 sec, and 1.57 m X=365 km and Y=310 km for simulation initialized at T_p=16.6 sec. A transect at X=300 km is given for each initialization in Fig. 3.2g. Two maximums are noticeable, the main one at Y=310 km and a secondary at Y=125 km. Two minima are noticeable, one at Y=200 km (H_s= 0.8 m) and a secondary around Y=380 km (H_s=0.85 m). One can see the shorter the waves, the stronger the extremes H_s. Globally, H_s follows the current vorticity signal (Fig.3.1c). The enhanced H_s areas are associated with the boundary of the inner eddy core ($\zeta > 0$) where waves are propagating against the current and in the bottom part of the vorticity ring ($\zeta < 0$) that surround the eddy core. The areas where H_s are enhanced are consistent with waves-eddies interactions simulated in realistic fields ; (see Fig. 6 of Romero et al. (2020) and Fig.1 of Ardhuin et al. (2017)).

The simulations forced with fully developed eddy show stronger spatial inhomogeneities in the wave field (Fig. 3.2d,e,f). As noticed for simulations forced with the initial eddy (3.2a,b,c), the H_s field is matching with the current forcing (Fig. 3.1b), in other words, where surface current gradients are important, strong ∇H_s are noticed. H_s values are mostly modulated by the fully developed eddy core. The ellipsoid shape of the fully developed eddy leads to a modulation of the H_s values $\sim$ 50 km more upstream (smaller X values) than for simulations forced with the initial eddy. Let us note that ∇ H_s are apparent in the submesoscale eddies that have been emerged spontaneously all around the eddy core. In the submesoscale eddy field, wave field shows alternate signs of H_s variability, with globally the same intensity whatever the incidence frequency. It is explicitly shown at X= 300 km,

at Y<180 km and Y> 350 km (Fig. 3.2g) for each initialization. In the same transect, at Y=200 km, we can do the same remark as previously, the more short are incident waves, the more sharp are ∇H_s. However, at X=300 km and at Y corresponding to submesoscale eddies, the $\nabla\ H_s$ are identical whatever the frequency of the incident waves. The H_s patterns in the fully developed eddy are more scattered (mostly zonally due to the initial direction of the incident wave packet) than in the initial eddy. ∇H_s are sharper for simulations forced with the fully developed eddy and higher extreme values are noticeable. One can see that ∇H_s are important downstream from the eddy field. The horizontal size of H_s patches (intensified or decreased H_s structures) are comparable to the width of the eddy (Fig.3.2a-f). Finally, one can see that for all simulations the signature of the eddy in the H_s field is not totally symmetric with respect to the center of the domain whereas the two forcing current field are. We propose to follow the extremes values of H_s along the X-axis to quantify this non-symmetry of H_s.

We perform the histograms and the Cumulative Density Function (CDF) of H_s at different distances from the left boundary (200 km,250 km, 300 km, 400 km, and 450 km) for simulation forced with the initial (Fig.3.3) and the fully developed eddy (Fig.3.4) with waves initialized at 7 sec, 10.3 sec, and 16.6 sec. The extreme values are computed from the 99^{th} centils for all simulations. For simulations forced with the initial eddy with a gaussian shape, (Fig.3.3), the histogram is very narrow at 200 km from the left boundary. The extreme values are equal to the initial H_s (1 m). The distributions are increasingly wider from $X = 250$ km to $X =$400 km. The extremes H_s values are the largest for waves initialized at 7 sec at $X = 250$ km to $X =$300 km where extreme values of H_s increase by more than 20% and 50% respectively. Downstream from $X = 300km$, the highest extreme values are for simulation initialized with 16.6 sec waves with a maximum at 400 km where H_s increase by more than 50%. Note that, the lowest values of H_s at X>400 km from the left boundary are for the simulation initialized with 7 sec waves.

Simulations forced with the fully developed eddy are much wider than simulation forced with the initial eddy from $X = 200$ km to $X = 300$ km. The extreme values of H_s at $X =$200 km and $X =$250 are the highest for simulation initialized with 7 sec waves where H_s extreme values increase by 26% and 54%. At 300 km the maximum H_s extreme values are for simulation initialized with 10.3 sec waves as shown in the H_s transect in Fig.3.2g. Downstream from $X = 300$ km the maximum H_s extreme values are for simulation initialized with 16.6 sec waves. The highest H_s extreme values are at $X =$300 for all the initializations where the H_s extreme values increase by more than 60%. Let us note that, we do not see the maximum of the extreme values of H_s in the center of the domain.

Peak direction

The effect of currents on wave directions can be captured to the first order by the θ_p field. Waves are turning in the current field due to refraction, globally toward the South (θ_p increase) in the bottom part of the domain and toward the North (θ_p decreases) in the upper part. When waves pass through the eddy, θ_p changes due to the vorticity field, at X=125 km for the initial eddy (Fig.3.5a,b,c), and slightly upstream, at X=79 km, for the fully developed eddy (Fig.3.5d,e,f). Patterns shown in Fig. 3.5 are similar to the H_s gradient patterns shown in Fig. 3.2 with a large-scale dipole for simulations forced with the initial eddy and both large-scale and small-scales signal gradients for simulations forced with the fully developed eddy. Narrow yellow bands in the left part of each panel are spurious. They marked the boundary where waves are generated at the left boundary. The peak direction gradient ($\nabla\theta_p$) intensity depends both on the incident wave frequency and the underlying vorticity field (Dysthe, 2001; Kenyon, 1971). $\nabla\theta_p$ is stronger for simulations initialized with T_p=7 sec (Fig. 3.5a,d) than for

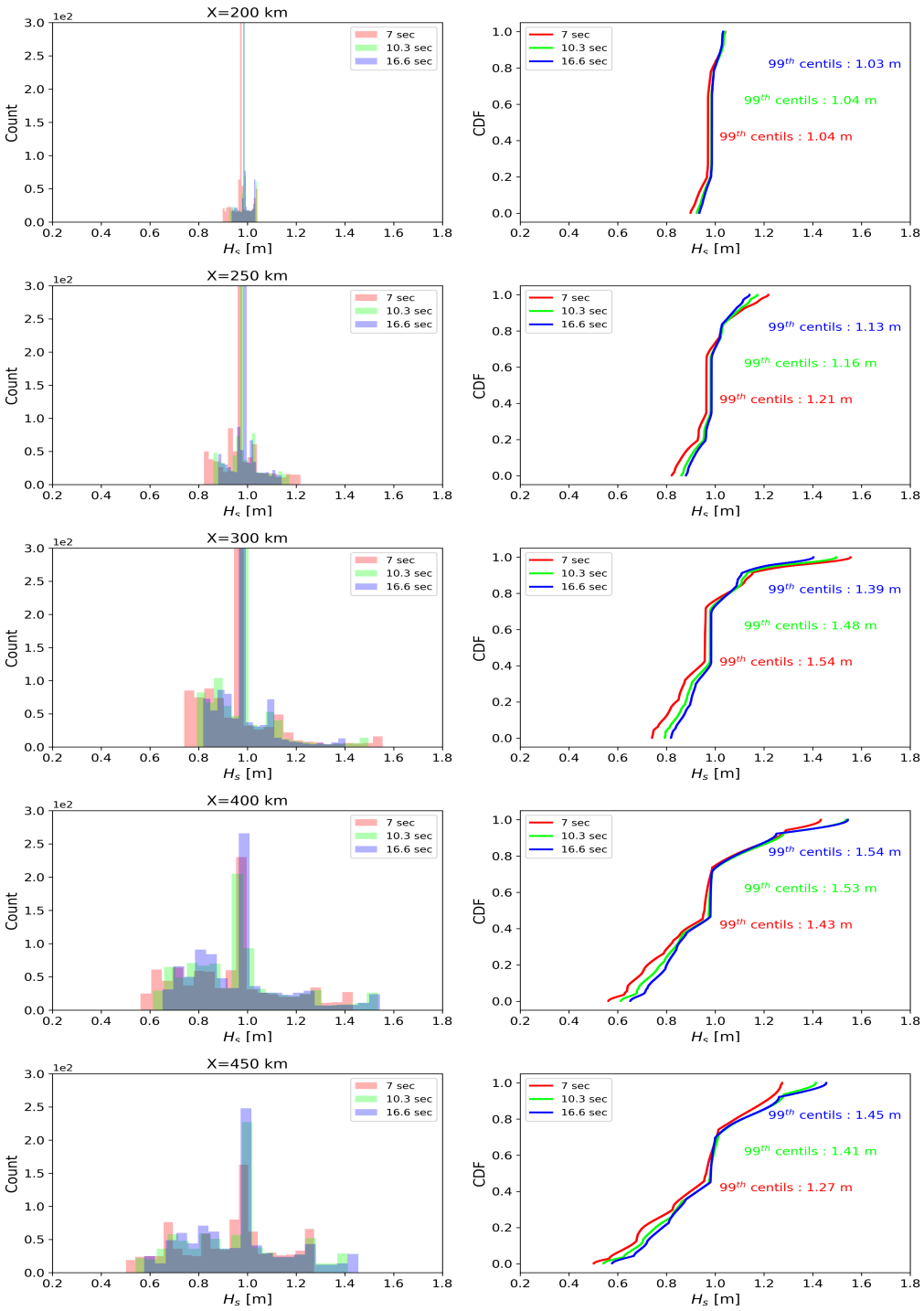

Figure 3.3: The figure is organized as follows: left panels are histograms of H_s at specific distance from the left boundary from 200 km to 450 km (the distances are given in title of each panel). The right panels are the cumulative density function (CDF) at specific distance from the left boundary, the distances are given in the associated left panel. Those plots are for H_s simulated in the initial eddy with waves initialized at 7 sec, 10.3 sec, and 16.6 sec period.

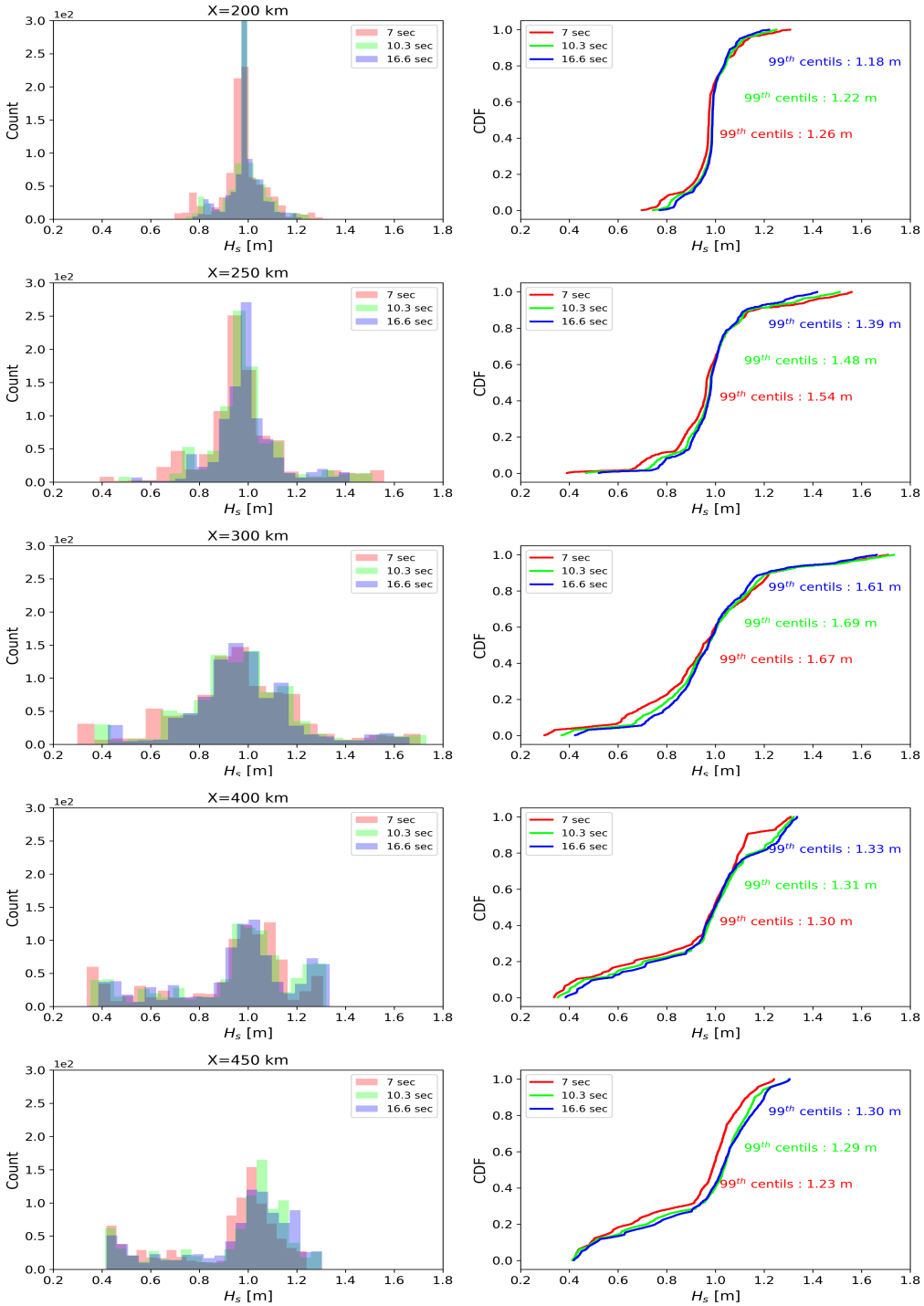

Figure 3.4: Same as Fig.3.3 for H_s simulated in the fully developed eddy.

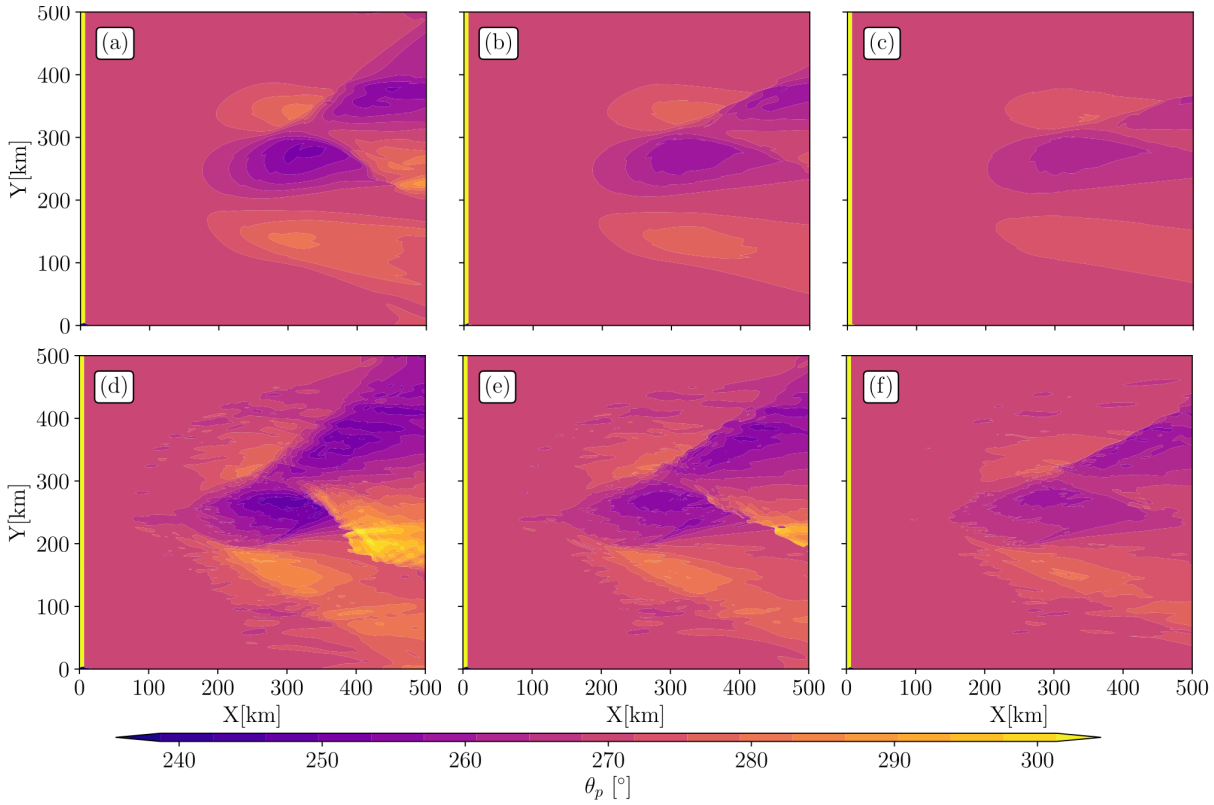

Figure 3.5: Peak direction (θ_p) field for (a,d) T_p=7 s, (b,e) 10.3 s, and (c,f) 16.6 sec incident waves. Without current forcing the entire domain is equal to the initial θ_p (270°). The first row (a,b,c) shows fields for simulations forced with the initial eddy (Fig. 3.1(a,c)); the second row (d,e,f) shows the same fields but for simulations forced with the fully developed eddy (Fig. 3.1(b,d)).)

simulations initialized with T_p=10.3 sec and 16.6 sec. In the same way, $\nabla\theta_p$ is enhanced for simulations forced with the fully developed eddy (Fig. 3.5d,e,f)) where current field shows more smaller current features. The result corroborates Villas Bôas et al. (2020)'s findings where authors forced the wave model with synthetic surface currents inverted from Kinetic Energy spectrum (with a random phase). The more turbulent the current is, the more the waves are refracted. Refraction can induce a change of θ_p that can reach $\pm$ 30° for simulation initialized with T_p=7 sec and forced with the fully developed eddy (Fig.3.5d). Very long wave trains (T_p=16.6 sec) hardly reach a deviation of wave direction higher than 10°, both in the fully developed and initial eddy. Finally, one can see that θ_p differs downstream from the eddy with respect to the initial direction (270°), waves keep in memory the current-induced refraction downstream from the isolated eddy.

Mean wave period

Surface currents have an effect on the wave frequency (Phillips, 1977) due to the conservation of the absolute frequency (Eq.(1.13). Surface currents modify the $T_{m0,-1}$ field. Also, because the wave action is redistributed by the refraction process, shown in chapter 2, and that Eq.(1.5) depends both on the waves energy and the wave intrinsic frequency, one can expect that the current-induced refraction and Doppler shift have an effect on $T_{m0,-1}$

signal.

Wave simulations are initialized with different wave peak frequencies, so it leads to changes of $T_{m0,-1}$ in the entire domain which is not current-induced. The different initializations of the wave field justify the representation of the relative difference of $T_{m0,-1}$ ($\Delta T_{m0,-1}$) rather than the raw outputs. This $\Delta T_{m0,-1}$ is the difference between outputs of simulations performed with and without surface current forcing (Fig.3.6). The spatial inhomogeneities are more striking for simulations forced with the fully developed eddy, similar to the H_s and θ_p fields (Fig. 3.2, 3.5). For a fully developed eddy, Δ $T_{m0,-1}$ exceeds 3 sec in the eddy core for X between 200 km and 400 km. For simulations forced with the initial eddy, Δ $T_{m0,-1}$ does not exceed 2 sec at the same location (Fig 3.6g). The Δ $T_{m0,-1}$ does not depend much on the frequency of the incident waves, or at least, not as much as θ_p field studied above. Slight differences are, however, noticeable for simulations forced with the fully developed eddy. This is not clear if there is a link between the incident wave frequency and the slight differences in the $\Delta T_{m0,-1}$ signal especially in the submesoscale eddies where Δ $T_{m0,-1}$ are stronger for long incident waves whereas we see the opposite in the core of the fully developed eddy. Δ $T_{m0,-1}$ are positive where waves and current are propagating in the same direction and vice versa. This change of Δ $T_{m0,-1}$ seems to be due to the current-induced Doppler shift on the wave frequency (Eq.(1.13)) and that the absolute frequency is conserved. Where waves and current are opposite we see that H_s are enhanced (Fig.3.2) and wave wavelengths are shortened. It could be explained by the conservation of wave action ($D_t N = 0$, Eq. (1.21)). If we focus on the maximum of Δ $T_{m0,-1}$ at Y=200 km, waves are extended about 153 m and H_s decreased about 0.65 cm. One can see that wave stripes induced by refraction (Fig. 3.5) are also captured in the Δ $T_{m0,-1}$ fields and that waves are shorter (smaller $T_{m0,-1}$) where H_s were enhanced (Fig. 3.2). We show again that the change of H_s induced by current is due to a superposition of processes.

The histograms and the CDF of the absolute value of $\Delta T_{m0,-1}$ are performed in the same manner of the histograms and the CDF of the H_s values presented before. The statistical results are given Fig.3.7 for the simulations forced with the initial eddy and Fig.3.7 for the simulations forced with the fully developed eddy. For X =200 km, in the initial eddy, the changes of $\Delta T_{m0,-1}$ do not exceed 0.5 sec for all the initializations. Downstream from X =200 km, the variability of $\Delta T_{m0,-1}$ and the extreme values are strongly increasing with a maximum of +1.74 sec at X =300 km for waves initialized at 16.6 sec. There is not a clear link between the extreme values of $\Delta T_{m0,-1}$, the distance from the left boundary and the period of the incident waves. Indeed, at X =250 km the extreme values of $\Delta T_{m0,-1}$ are for 7 sec incident waves whereas, downstream from X =250 km the extreme values are for simulations initialized with 16.6 sec waves. The histograms performed for simulation with the fully developed eddy show higher variability of $\Delta T_{m0,-1}$ with the highest extremes values at X =300 km for simulations initialized with 10.3 waves ($\Delta T_{m0,-1}$=3.78 sec). Downstream from the core of the eddy the change of $\Delta T_{m0,-1}$ is still significant for both simulation forced with the initial and the fully developed eddy.

For all the variables studied here (Fig.3.2,3.5, 3.6), waves are continuously generated at the left boundary, a solitary incident wave train strongly affect the results presented above, for instance the nonlocal effect of refraction on the wave field is strongly less pronounced (not shown).

3.3.2 Ray tracing

In a rotational current field, wave rays are bent because of refraction. In a strong rotational current field, the change of H_s is mostly driven by refraction from mesoscale and submesoscale currents (Irvine and Tilley, 1988;

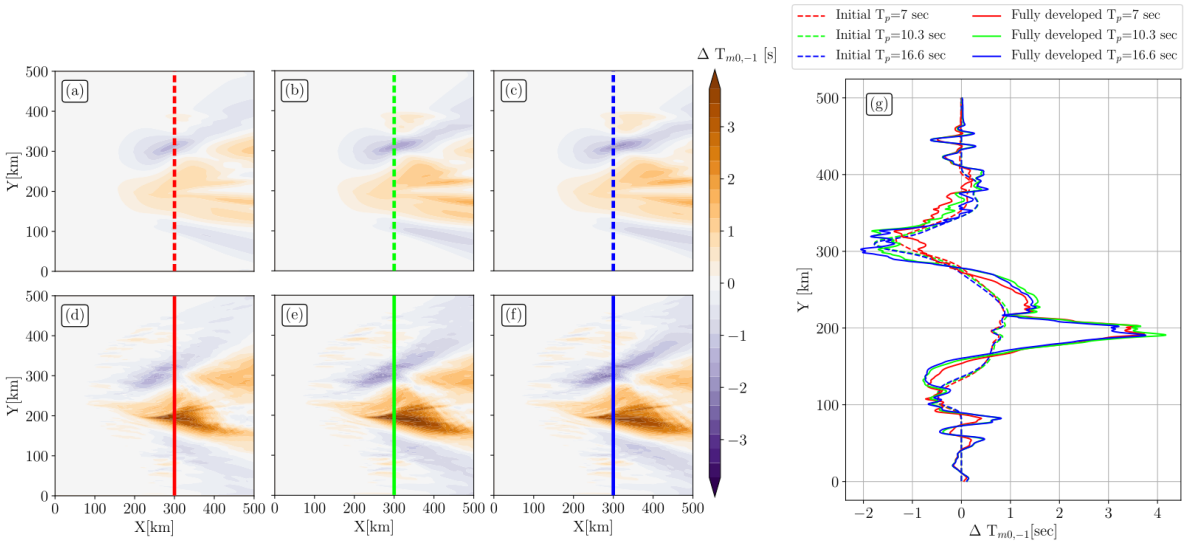

Figure 3.6: Mean wave period difference ($\Delta T_{m0,-1}$) between simulations forced with and without current ($\Delta T_{m0,-1}$=$T_{m0,-1}$(curr)-$T_{m0,-1}$(Nocurr)). Panels (a,d) show $\Delta T_{m0,-1}$ fields initialized with T_p=7 sec wave group. Panels (b,e) show $\Delta T_{m0,-1}$ fields initialized with T_p=10.3 s. Panels (c,f) show $\Delta T_{m0,-1}$ fields initialized with T_p=16.6 s. The first row (a,b,c) shows instantaneous fields for simulations forced with the initial eddy (Fig.3.1(a,c)); the second row (d,e,f) shows the same fields but for simulations forced with the fully developed eddy (Fig.3.1(b,d)). Panel (g) shows $\Delta T_{m0,-1}$ along X = 300 km (colored dashed/solid lines in left panels) for all simulations.

Ardhuin et al., 2017; Romero et al., 2020). In the present study, the isolated vortex modifies wave fields which results in a strong inhomogeneity in the H_s and $T_{m0,-1}$ fields (Fig. 3.2, 3.6). This current-induced refraction is highlighted here thanks to a Monte Carlo ray tracing simulation which follow the wave action trajectory. The wave energy spectrum, $E(\sigma,\theta)$, is not conserved in surface current fields. Indeed waves and currents exchange energy. Nevertheless wave action ($A(\sigma,\theta)$) is conserved (Bretherton and Garrett, 1968). The ray tracing assumes that surface currents are stationary ($\frac{|u|}{C_g} \ll 1$) and that incident waves are monochromatic. In a real ocean, wave field is a superposition of wave trains with specific directions and frequencies, thus ray tracing is only a very simplified view of how the direction of the waves is modified by the presence of currents. Thanks to the wave-ray kinetic equations (see introduction), we expect that refraction is more important where waves and currents vectors are perpendicular (see the $\dot{\theta}$ in introduction). Examples of ray tracing are shown in Fig. 3.9 in both the initial and fully developed eddy.

The initial direction is 270° (waves are coming from the left boundary) and the initial periods are the same as the ones discussed above (T_p =7 sec, 10.3 sec, and 16.6 sec peak periods). We see that the current-induced refraction is sensitive to both the nature of underlying current and the frequency (or wavelength) of the incident waves. The radius of curvature of wave rays is larger where the current field is highly rotational (Fig. 3.9d,e,f) and when simulations are initialized with T_p=7 sec waves (Fig. 3.9a,d) (Kenyon, 1971; Dysthe, 2001). In the initial eddy case, the wave train is refracted both by the eddy's edge (toward the South) and the core of the eddy (toward the North) (Fig. 3.9a,b,c). It leads to two wave rays focalization areas downstream from the initial eddy. These focalization areas, or caustics, are slightly shifted zonally toward the right boundary when the incident waves are longer (see Fig.2.4 of the introduction). The caustic in the upper part of Fig.3.9 (a,b,c) appears at X=330 km,

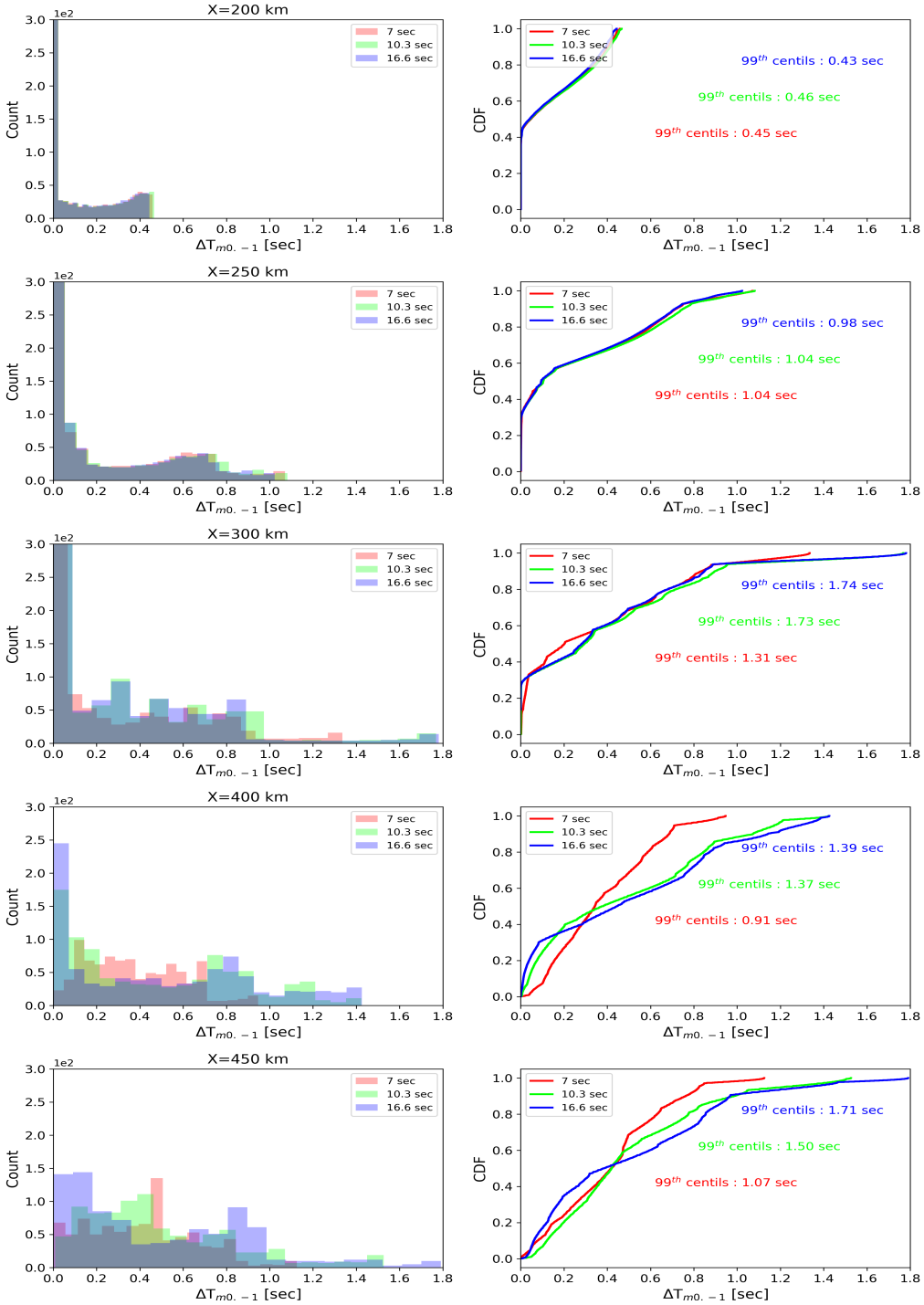

Figure 3.7: Same as Fig.3.3 for the absolute value of $\Delta T_{m0,-1}$ (difference between simulations forced with and without current).

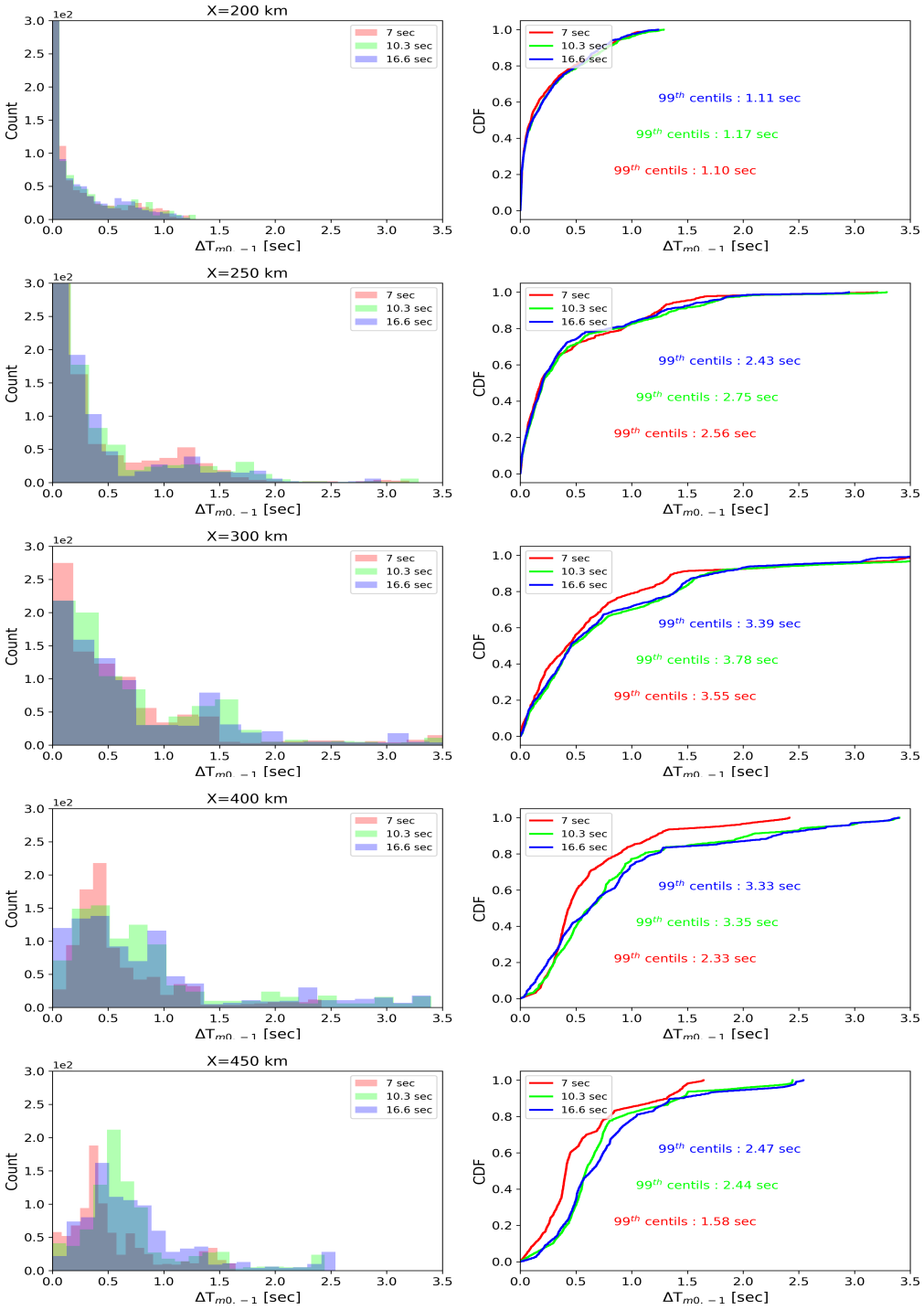

Figure 3.8: Same as Fig.3.7 for simulations in the fully developed eddy.

X=370 km, and X=445 km for simulations initialized with 7 sec, 10.3 sec and 16.6 sec respectively. In the fully developed field, both mesoscale and submesoscale features bend wave rays. One can see that the number of caustic increases in the fully developed eddy with a maximum of caustics for T_p= 7 sec incident waves (Fig. 3.9d). Even if isolated submesoscale eddies have a vorticity comparable with the eddy core ($\frac{\zeta}{f_0} \sim$1.5), they do not refract waves as much as the center structure does. Indeed, if we look at the southernmost submesoscale eddy we see that one wave ray is deviated by about 30 km from the left boundary to the right boundary whereas one wave ray at the center of the domain is deviated by more than 200 km. The frontal dynamic at the boundary of the main structure of the fully developed eddy induce the strongest wave-ray deviation whereas their scale and their relative vorticity is comparable to submesoscale eddies structures. So, the shape of vorticity patterns is key in the intensity of the refraction. One can notice that ray convergent areas are located where H_s reaches peaks (Fig. 3.2), especially at the edge of the positive vorticity core. The longer the incident waves, the further from the left boundary the H_s enhancement areas. Through idealized numerical studies given in chapter 2 of this manuscript and realistic numerical studies in strong current fields, Ardhuin et al. (2012) and Kudryavtsev et al. (2017b), the link between ray caustics and H_s enhancement has been shown qualitatively. One can notice that from the work of Heller (2005) and because the initial directional spreading is the same for each numerical realization, the freak index (Eq.2.9) is much more important for fully developed eddy than for the initial eddy. This index is even more important when incident waves are short and very directional, for instance the case shown in Fig.3.9d).

The strong vorticity field both for initial and fully developed cyclonic eddy induces a wave-ray scattering which can reach a deviation of several hundred kilometers with respect to propagation without background current. This deviation is more important for short waves incidence (Fig. 3.9a,d). The current-induced wave-scattering can be responsible for the space-time bias in the forecast of waves arrival (Gallet and Young, 2014; Smit and Janssen, 2019). The ray tracing study shows that refraction has a local effect on wave direction, strong ray deviations appear where ∇U are strong. However, refraction effects on wave parameters are nonlocal. We saw that H_s enhancement and changes of $\Delta T_{m0,-1}$ can appear both inside and outside the eddy (Fig.3.2,3.9). In other words, strong ∇H_s are not necessarily at strong ∇U locations. The location of H_s enhancement areas are significant where wave-caustic occurs, more or less distant from the left boundary according to the period of the incident waves. The structures of H_s (Fig.3.2) and $\Delta T_{m0,-1}$ (Fig.3.6) seem to follow the distribution of the wave ray (Fig.3.9).

3.4 Separating the effects of the currents on the variability of wave height and the mean period

The eddy-induced current lead to a variability in the wave field at the meso- and the submesoscale range. Because the combination of current effects on the wave field is not linear, it is difficult to attribute one effect more than another one as the cause of the spatial inhomogeneities in the wave field. Thus, we want to highlight and to quantify the effects of the current-induced Doppler shift and the current-induced refraction on the spatial patterns of the H_s and $\Delta T_{m0,-1}$.

3.4.1 The new wave model setup

The refraction (change in wave direction) and the Doppler shift (change in wavenumber) have been activated and deactivated for two new wave simulations. We have, on one hand, one simulation without Doppler shift and

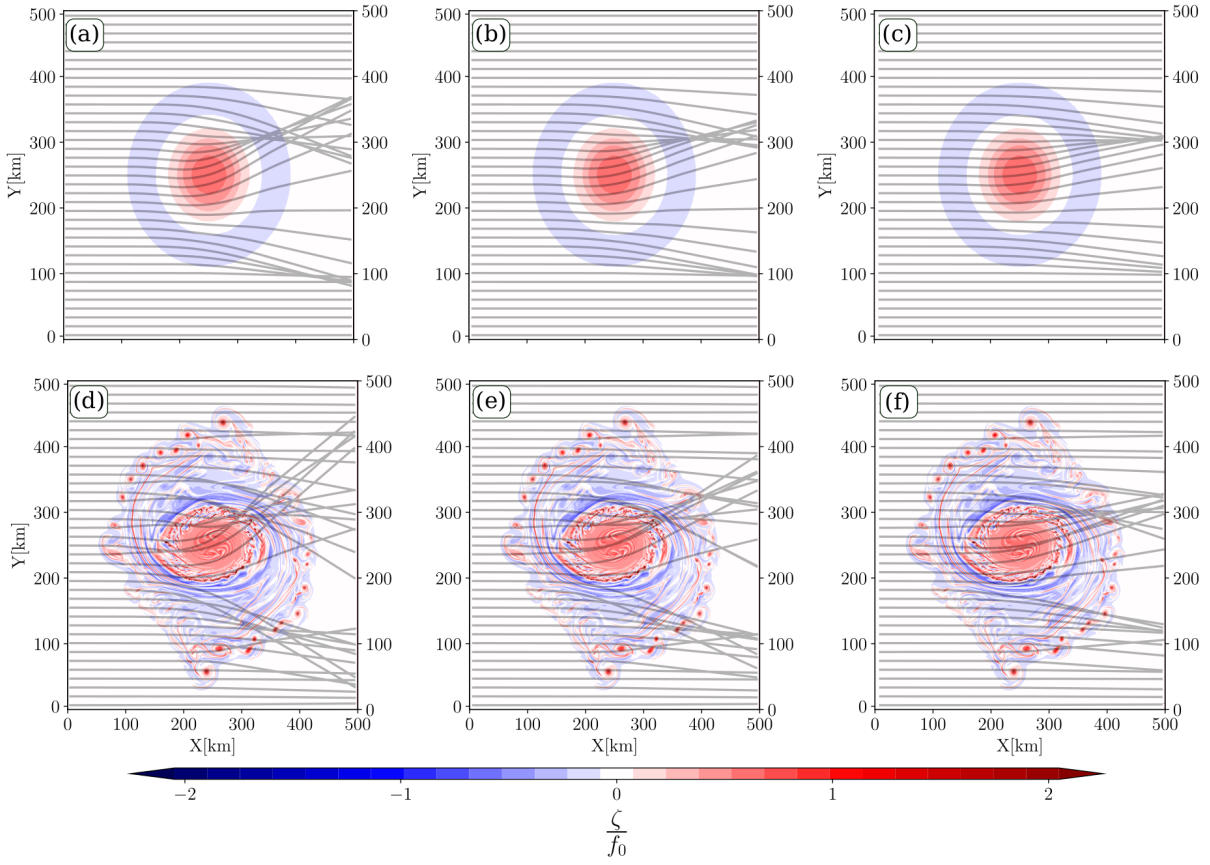

Figure 3.9: (a,b,c) Ray tracing for waves traveling in the initial eddy with T_p =7 s, (a) 10.3 sec (b), and 16.6 sec (c) peak period. Same for panels (d,e,f) but for waves traveling in the fully developed eddy. The vorticity fields are given in the background.

		Initial eddy		
Initial T_p	**Centils**	**Reference [m]**	**Only Doppler [m]**	**Only Refraction [m]**
7 sec	50th centil	0.976	0.999	1.003
	95th centil	1.196	1.103	1.352
	99th centil	1.422	1.227	1.606
10.3 sec	50th centil	0.987	0.996	0.997
	95th centil	1.203	1.069	1.315
	99th centil	1.459	1.146	1.539
16.6 sec	50th centil	0.988	0.992	0.993
	95th centil	1.182	1.049	1.208
	99th centil	1.459	1.106	1.523

Table 3.1: The median, the 95^{th}, and the 99^{th} centils of the simulated H_s with the initial eddy forcing with waves initialized at 7 sec, 10.3 sec, and 16.6 sec.

one simulation without refraction on the other hand. For the new simulations, the current forcing are still from the initial and the fully developed eddy and waves are continuously generated from the left boundary from wave spectra gaussian in frequency. The incident periods are still equal to 7 sec, 10.3 sec and 16.6 sec. The source terms are still deactivated and the advection of the wave action driven by the sum of the current and the group velocity is still activated.

3.4.2 The spatial patterns of H_s

Simulation outputs for the initial eddy

Simulation forced with the initial eddy induces large scale H_s gradients (Fig.3.2a,b,c) with areas where H_s can be enhanced by more than 50% (Fig.3.3). Simulations where the Doppler shift is deactivated (center column of Fig.3.10), show similar patterns than the reference simulation ((left column of Fig.3.10)) with an area of H_s enhancement but more localized and with higher extreme values (see associated values on Table 3.1). Also, the extreme values of H_s are much higher. The 99^{th} centil of H_s increases by a factor between 50% and 60%, whereas, for the reference simulation, outputs show an increase of the 99^{th} centil of H_s by a factor between 42% and 45% for 16.6 sec and 7 sec incident waves respectively. One can see in table 3.1 that, the extreme values of H_s are very similar for the reference simulation regardless of the period of the incident waves. Simulations without refraction (right column of Fig.3.10) show a local enhancement (decrease) of the H_s values in the core of the eddy where waves and current are opposed (aligned). The increase (decrease) of the H_s does not exceed 20% and is maximum for 7 sec incident waves and minimum for 16.6 sec incident waves (see table. 3.1).

Simulation outputs for the fully developed eddy

Simulation forced with the fully developed eddy induces H_s gradients at the meso- and submesoscale range (Fig.3.2d,e,f) with areas where H_s values can be enhanced by more than 60% (Fig.3.4). Simulations where the Doppler shift is deactivated (center column of Fig.3.12), show similar patterns than the reference simulation (left column of Fig.3.12) with several areas of H_s enhancement in the eddy core and in the submesoscale eddies. The

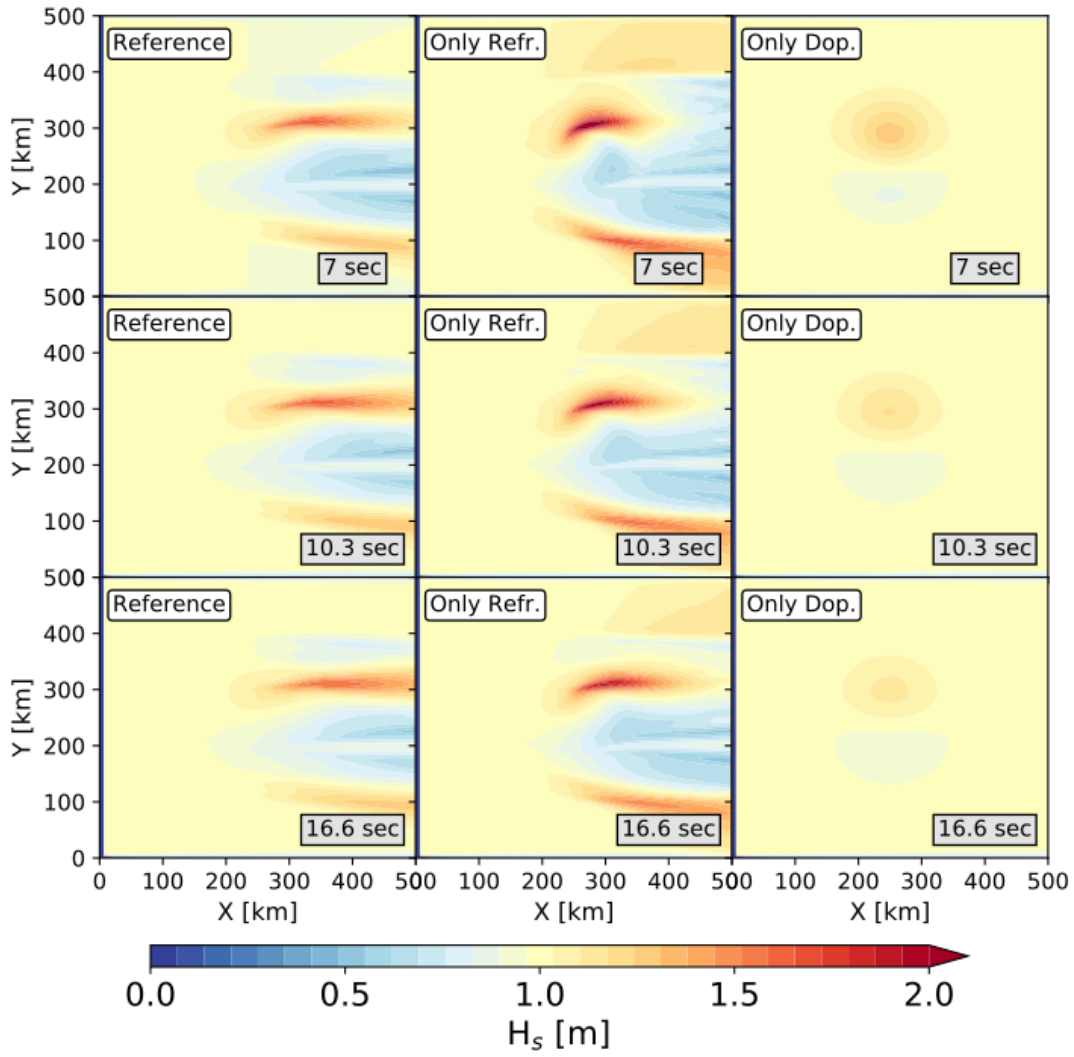

Figure 3.10: Significant wave height simulated in the initial eddy without current-induced Doppler shift (with refraction) and without current-induced refraction (with Doppler shift). The figure is organized as follow. The first raw is for simulations initialized with 7 sec wave period, the second raw is for simulations initialized with 10.3 sec wave period, and the third raw is for simulations initialized with 16.6 sec wave period. Labels "Reference" refer to the simulation where both Doppler shift and refraction are taken into account. Labels "Only Refr." refer to simulations without the Doppler shift and "Only Dop." for simulations without the refraction. Without current the H_s is equal to 1 m in the entire domain.

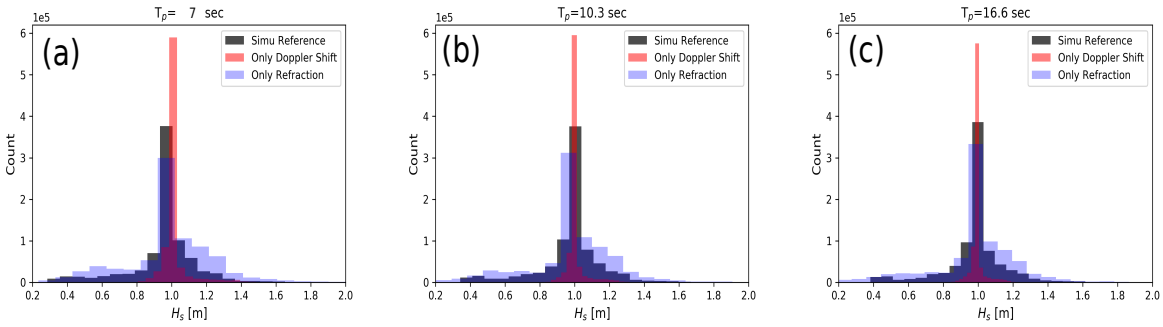

Figure 3.11: The figure shows the histogram of H_s in the entire simulated domain for simulation forced with initial eddy. The black histograms refer to the reference simulations, the red histograms for simulations where the refraction has been deactivated and the blue histograms refer to the simulations where the Doppler shift has been deactivated. Panel (a), (b) and (c) are for simulations initialized with 7 sec, 10.3 sec, and 16.6 sec waves

		Fully Developed Eddy		
Initial T_p	**Centils**	**Reference [m]**	**Only Doppler [m]**	**Only Refraction [m]**
7 sec	50^{th} centil	0.988	0.999	1.002
	95^{th} centil	1.182	1.149	1.568
	99^{th} centil	1.448	1.366	1.706
10.3 sec	50^{th} centil	0.991	0.996	0.997
	95^{th} centil	1.245	1.093	1.534
	99^{th} centil	1.465	1.226	1.612
16.6 sec	50^{th} centil	0.990	0.992	0.993
	95^{th} centil	1.236	1.063	1.314
	99^{th} centil	1.439	1.157	1.560

Table 3.2: Same as Table.3.1 but for simulations forced by the fully developed eddy.

main patch of H_s enhancement in the core of the eddy is more localized with higher extreme values for simulation without Doppler shift as described in the previous section. Also, for the simulation without Doppler shift, the more the incident waves are short, the more the extreme values are strong (see associated values on Table **??**) and the more are localized the location of H_s enhancement. The extreme values of H_s are much higher for simulations with only the current-induced refraction, where the 99^{th} centil of H_s increases by a factor between 50% and 70%, than for the reference simulation where the 99^{th} centil of H_s increases by a factor between 43% and 46%. Thus, simulations with only refraction show higher extreme values for the fully developed eddy than for the initial eddy. Simulations without refraction (right column of Fig.3.12) show a local enhancement (decrease) of the H_s values in the core of the eddy where waves and current are opposed (aligned). The increase (decrease) of the H_s reach 36% for 7 sec incident waves which is higher than simulation forced by the initial eddy. One can see that, the effect of the Doppler shift induced by the presence of submesoscale eddies seems inducing negligible variability in the H_s field. Still for simulation where the refraction is deactivated, downstream from the core pf the eddy, one can see a very slight increase of H_s.

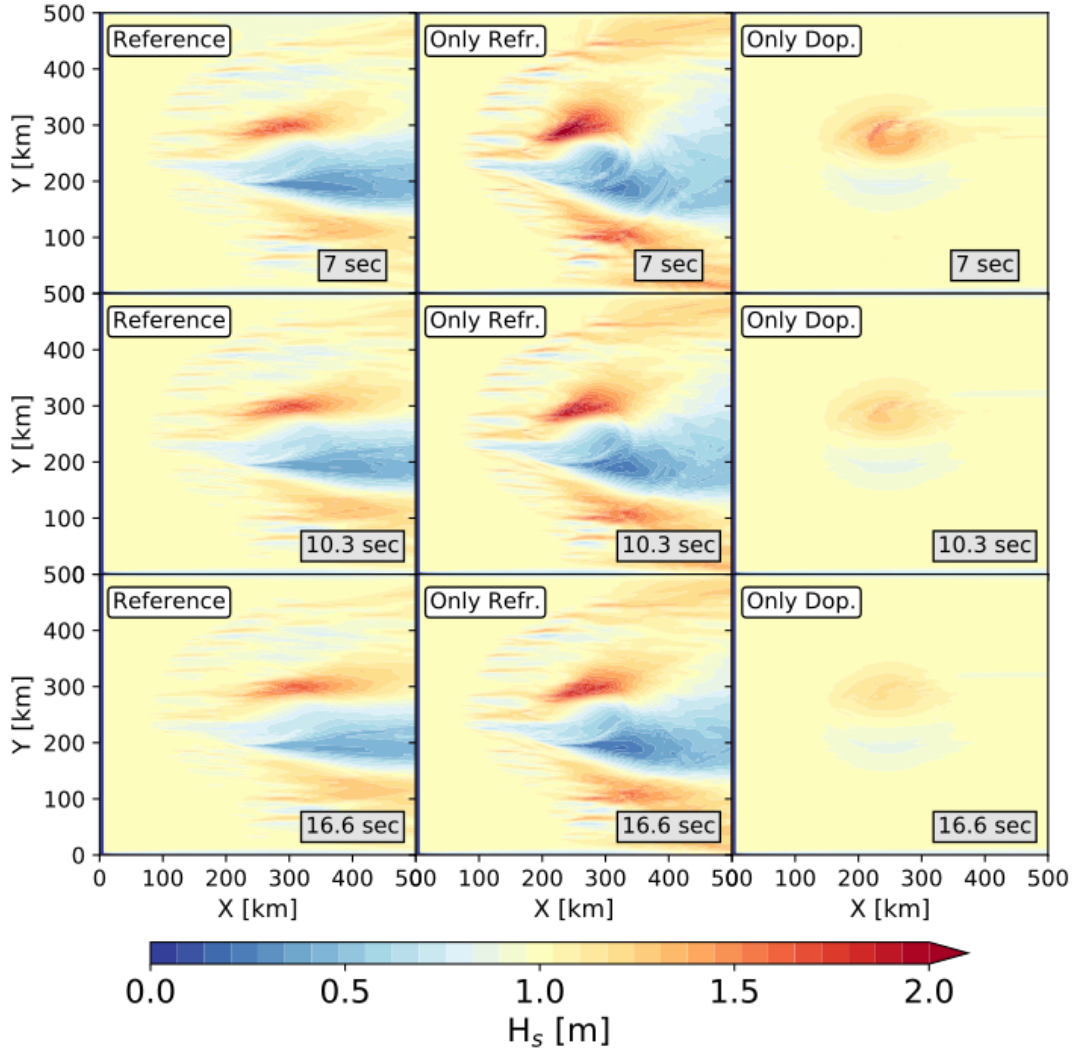

Figure 3.12: Same as Fig.3.10 but for current forcing from the fully developed eddy.

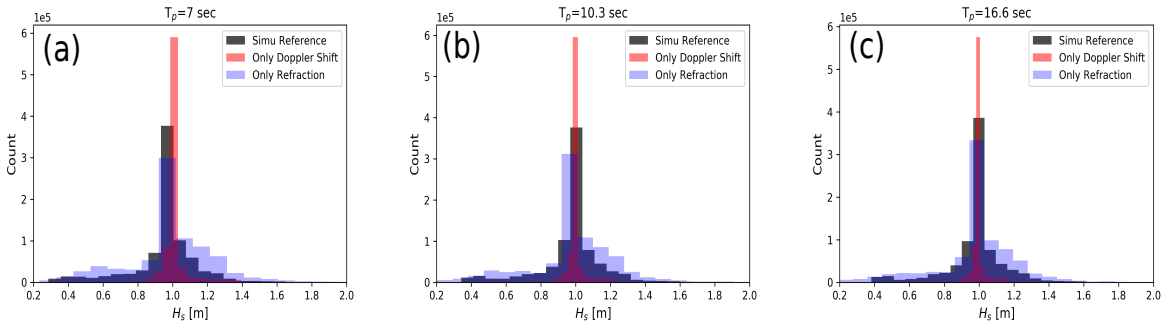

Figure 3.13: Same as fig.3.11 for simulations forced with the fully developed eddy.

3.4.3 The spatial patterns of $\Delta T_{m0,-1}$

The presence of the eddy induces a strong change of the mean period ($T_{m0,-1}$) in and outside the isolated eddy (Fig.3.6). We propose the same experiment as proposed before, i.e. separate the Doppler shift and the current-induced refraction in our simulations, to investigate their respective effects on the variability of $T_{m0,-1}$ values. Rather focusing on $T_{m0,-1}$ we are focusing on the mean period difference between a simulation with and without current, namely $\Delta T_{m0,-1}$.

Simulation outputs for the initial eddy

The initial eddy with a gaussian shape has a strong effect on $\Delta T_{m0,-1}$ both for simulations exclusively with current-induced refraction and Doppler shift (Fig.3.14). One can see that there is a strong non local effect of the current on the $\Delta T_{m0,-1}$ for simulation with only current-induced refraction. One can see a change of $+3$ sec downstream from the eddy for all initializations (see center column of Fig.3.14). The simulations with only the Doppler shift show a decrease (increase) of $\Delta T_{m0,-1}$ where waves and current are opposed (aligned), which corroborates with Eq.1.13. The shorter the incident waves, the strongest the changes of $\Delta T_{m0,-1}$ in the eddy core.

Simulation outputs for the fully developed eddy

The simulations forced with the fully resolved eddy show stronger variability in the $\Delta T_{m0,-1}$ fields (Fig.3.6). The simulations with current-induced refraction, without Doppler shift, reveal strong inhomogeneities in the $\Delta T_{m0,-1}$ field both at the meso- and the submesoscale range. The strongest inhomogeneities are noticeable both in and dowstream from the eddy core. Compared to the reference simulation, the largest patches of $\Delta T_{m0,-1}$ are less stretched in the X-direction and are sharply deviated to the top and the bottom of the domain especially at X around 250 km. In the core of the eddy, the change of $\Delta T_{m0,-1}$ is the weakest for the simulation initialized with 7 sec period (with only refraction). For simulations without refraction we observe a strong decrease of the $\Delta T_{m0,-1}$ in the upper part of the eddy core (~ -3 sec). At the bottom boundary of the eddy core, there is a moderate increase of $\Delta T_{m0,-1}$ ($\sim +1$ sec). If we refer to the velocity field of the fully developed eddy, Fig.3.1b, we see that the decrease of $\Delta T_{m0,-1}$ is associated where waves and current are opposite and at the very center of the eddy core. The increase of $\Delta T_{m0,-1}$ is associated where the current is strongly zonal and aligned with the incident waves. The submesoscale eddies induce a very weak change in the $\Delta T_{m0,-1}$ signal for the simulation without current-induce refraction.

3.5 Discussions: how the initial and the fully developed eddy induce a change in the wave field

Wave simulations over surface current induced by the presence of an isolated mesoscale eddy show strong variabilities in the wave field. We have shown the evolution of the amplitude, the wavelength and the direction of the waves through the significant wave height, the mean period and the peak direction of the waves respectively.

Wave simulations in the initial eddy with a gaussian shape show spatial gradients at the scale similar to the eddy shape with an increase (decrease) of the H_s ($T_{m0,-1}$) where waves and current are opposite. We observe the opposite (Fig.3.2, Fig.3.6 panels a,b,c) where waves and current are aligned. Simulations forced with the

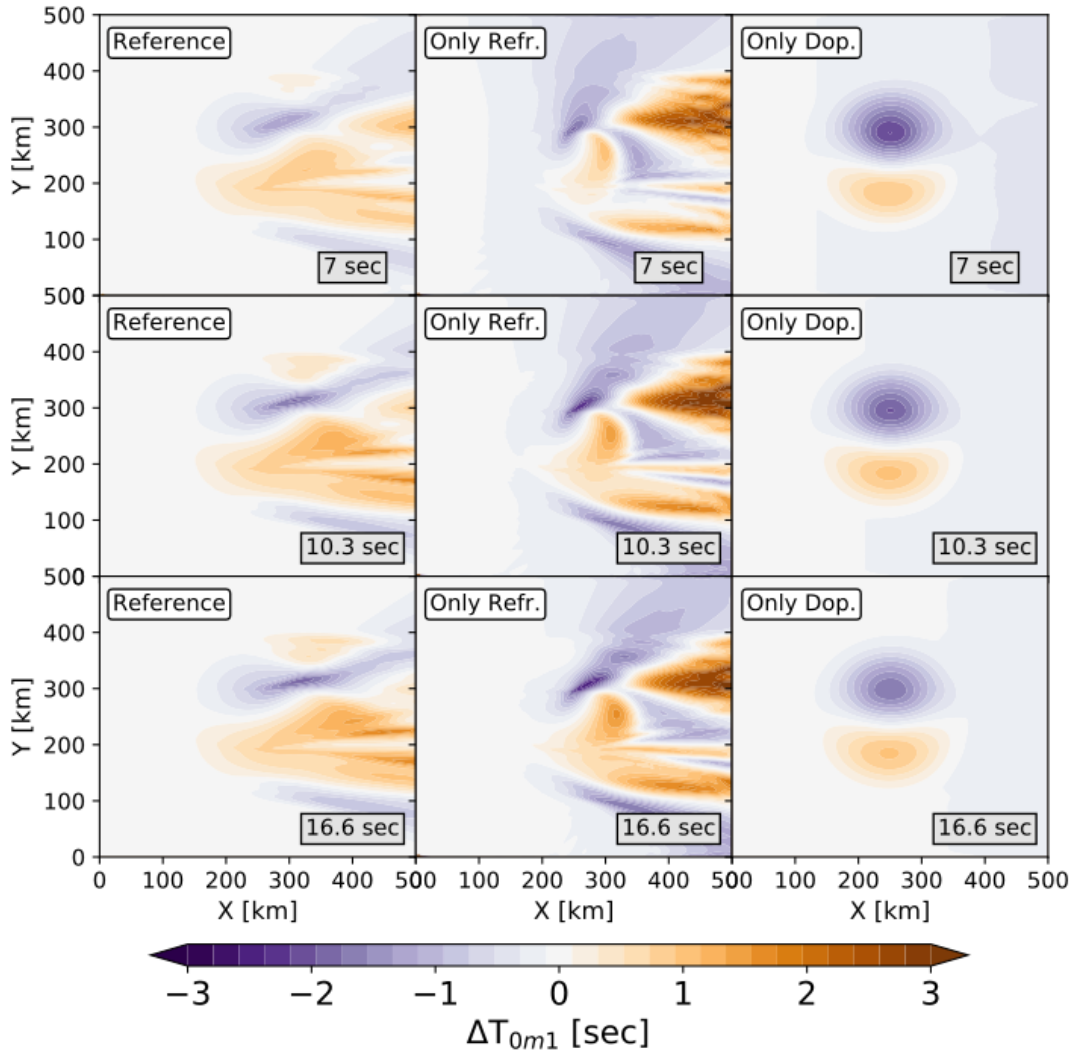

Figure 3.14: Same as Fig.3.10 but for the mean wave period difference between simulation with and without current.

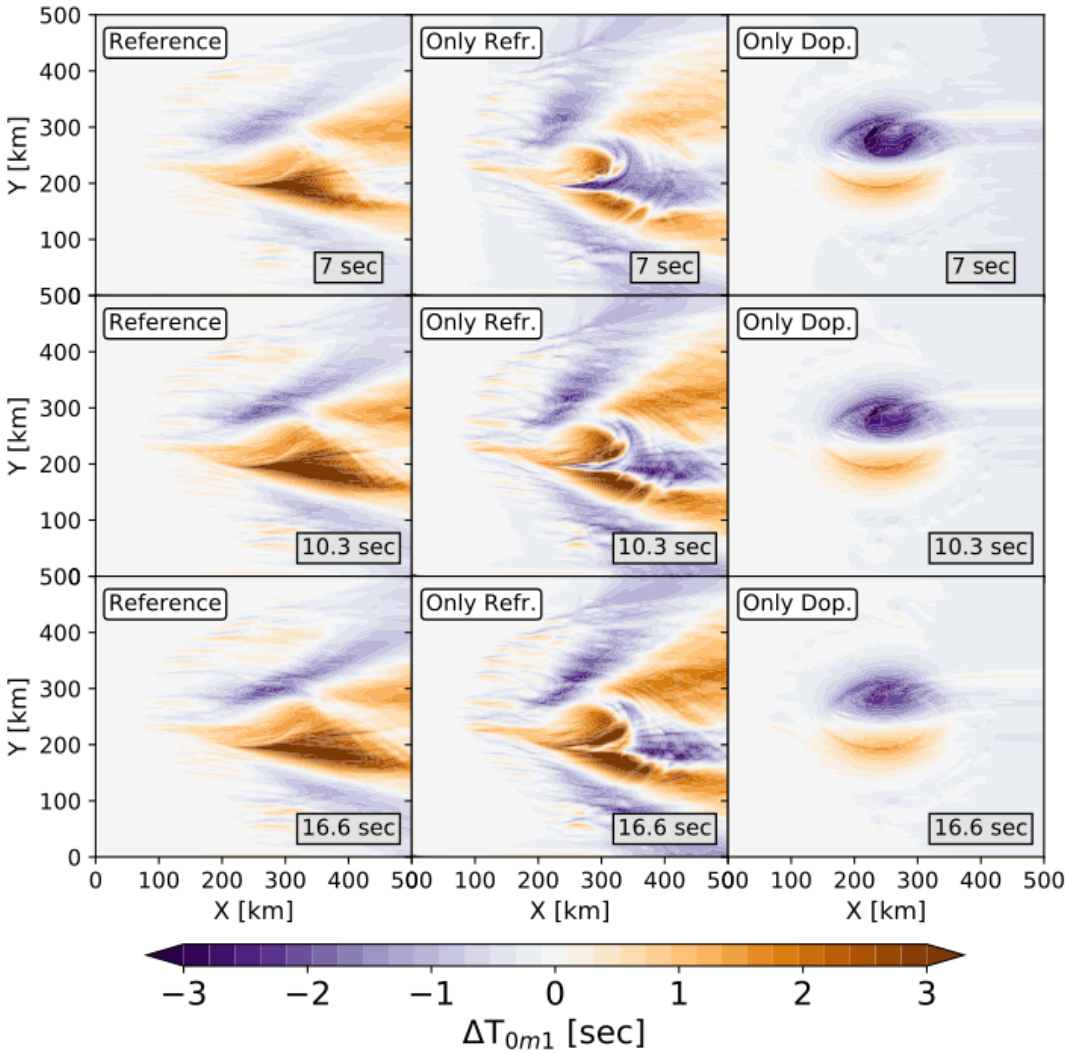

Figure 3.15: Same as Fig.3.12 but for the mean wave period difference between simulation with and without current.

fully developed eddy, with the presence of submesoscale eddies and an ellipsoid core, show one main area of enhancement (decrease) of H_s ($T_{m0,-1}$) where waves and current are opposite. We see the opposite where waves and current are aligned. The presence of the submesoscales eddies around the core of the eddy lead to secondary areas of enhancement and decrease of H_s and $\Delta T_{m0,-1}$ values(Fig.3.2, Fig.3.6 panels d,e,f). The variability of the H_s is stronger for the simulation forced with the fully developed eddy with higher extremes values in the core of the eddy (see the 99^{th} centils at X= 300 km in (Fig.3.3 and Fig.3.4). Downstream from the eddy, the extremes values of H_s are higher for the simulation forced with the initial eddy, with an increase of the H_s extreme values between 27% and 45% (depending on the frequency of the incident waves) at $X = 450$ km. For simulations forced with the fully developed eddy, the increase of the H_s extreme values do not exceed 30%. The ray tracing presented in Fig.3.9a,b, and c, shows two areas of ray focalization dowstream from the X =300 km. The shorter are the incident waves, the more distant from the left boundary are the focalization areas. Those areas of focalizations are associated to the highest extreme values of the H_s. The ray tracing over the fully developed eddy show rays much more scattered with more areas of focalization in and outside the eddy. The fact that rays focalize more dowstream from the eddy for simulations initialized with longer waves could explain why the extreme values of H_s are stronger for long waves downstream from the eddy. It could also explain why the extreme H_s values are stronger dowstream from the initial eddy than from the fully developed eddy. The wave action is more scattered by the presence of small scale current features which creating areas of focalization less intensive resulting from the current-induced refraction. It confirms, among others, the results of White and Fornberg (1998) where authors have shown that in a turbulent flow, the bigger are the eddies, the stronger are the focalization areas. The simulations with and without refraction have shown that the current-induced refraction is the main effect of the variability of the H_s and their associated extreme values, both for the initial and the fully developed eddy (Fig.3.10, 3.11, 3.12, 3.13). It confirm the results of Ardhuin et al. (2017) in the Drake Passage and Romero et al. (2020) in the Coastal California Current.

The effects current-induced Doppler shift lead to a strong local change of the mean period (or wavelength), Fig.3.14, 3.15. The refraction has also a strong local and non-local effect on the variability of the mean period which leads to a stretching of the waves in and downstream from the eddy (Fig.3.14, 3.15). Although the links between the variability of the mean period and their associated extreme values and the frequency of the incident waves are not clear (Fig.3.7, 3.8), we have shown that the variability and the extreme values of the $\Delta T_{m0,-1}$ are the strongest for the simulation forced with the fully developed eddy. Combining the results of the variability of the H_s and $\Delta T_{m0,-1}$ one can see that the presence of the eddy strongly change the "Bulk" wave steepness (proportional to the H_s and inversely proportional to the mean period) in and downstream from the eddy with maximum values for simulations forced with the fully developed eddy where the variability of the mean period is stronger. The wave steepness is a key parameter for a wide spectrum of application as characterizing the non-linear dynamic of the wave (Rocha et al., 2017), the Sea-States Bias (Gommenginger et al., 2018) and the safety at sea (Lavrenov, 1998). Explain the current-induced variability in the mean wave period fields need deeper studies to understand what are the key wave and current parameters leading to those changes.

3.6 Is it possible to reconstruct ∇U *via* the measurement of the ∇H_s?

There are surface current informations in the wave fields and more particularly in their spatial variability. The ∇H_s at scale between 200 km and $\sim$ 10 km are associated with the nature of the underlying current (structure and

intensity). The current intensity gradients ∇U ($\sqrt{\partial_x U^2 + \partial_y U^2}$) and more specifically the vorticity of the flow induces refraction leading to ∇H_s patterns correlated to vorticity patterns (Fig.3.10, Fig.3.12). Note that both ∇U and ∇H_s are scalars. Assuming that the group speeds of waves are much bigger than the intensity of the current velocity,

$$\frac{U}{C_g} << 1, \tag{3.1}$$

and that waves are stationary, the conservation of wave action simplifies to,

$$\frac{H_s}{\sigma} = Cte, \tag{3.2}$$

leading to the first order approximation in the direction of wave propagation:

$$\frac{\nabla H_s \sigma}{(H_s k)} \sim \nabla U. \tag{3.3}$$

The Eq.(3.3) shows that ∇H_s is a function of surface current gradients, wave steepness ($H_s k$) and wave incident frequency. This expression is already discussed in Villas Bôas et al. (2020) (see Eq.(15)), whereas, here, the expression is slightly different. The wave steepness is explicitly formulated. The motivation of this paragraph is to know if, from high-resolution-wave measurements from filtered altimeter data (Dodet et al., 2020), spectrometers (Hauser et al., 2020) or from optic images (Kudryavtsev et al., 2017b), the nature of the flow can be estimated from H_s measurement. Today's surface currents measurements from Sea-Level-Anomaly can capture an eddy with a shape similar to Fig.3.1a,c (if their lifetimes are sufficiently long according to the revisiting time of altimeters). However an eddy with a more realistic shape (Fig.3.1b,d) is very poorly captured (see section 5.2 of de Marez et al. (2020b)). Thanks to our numerical results, we will test the validity of Eq.3.3 in the case of the fully developed eddy. The final aim is to know if the nature of the flow can be estimated by inverting high resolution H_s knowing the wavelength-directional properties of the incident waves.

Right and left hand sides of Eq. (3.3) are shown in Fig. 3.16 in the fully developed eddy case, for incident waves at T_p=7 sec. ∇H_s and ∇U have been projected along and perpendicular to the wave peak direction respectively. Both terms of Eq. (3.3) are of the same order of magnitude with values slightly higher for the $\frac{\nabla H_s \sigma}{(k H_s)}$ field (Fig. 3.16b). ∇U shows rounded structures (Fig. 3.16a) whereas ∇H_s field shows more elongated-horizontal structures aligned with the initial wave direction (270°). From X=0 km to X=250 km, normalized ∇H_s patterns are aligned with the incident wave directions, downstream X=250 km patterns follow the rays trajectories shown in Fig.3.9d. Apart from the difference of shape, both fields are matching both at mesoscale (the central eddy) and at smaller scale (submesoscale eddies around the core of the ellipsoidal eddy) from X=0 km to X=250 km. ∇U exhibit fronts at the boundary of the central eddy also captured by the normalized ∇H_s field. Inside the central ellipsoidal eddy (between Y=200 km and 300 km), ∇U shows a smooth and homogeneous field which is captured in Fig. 3.16b only between Y=200 km and 250 km. Readers can also see discrepancies between the two fields, between the central eddy and the submesoscales eddies, where sharp ∇H_s are shown whereas ∇U are very smooth. Downstream from the eddy even if ∇U is null (Fig.3.16a), normalized ∇H_s are very sharp (Fig.3.16b).

The analysis of Fig. 3.16b shows that the wave simulations capture surface current gradient in the first half of the domain, without any information on surface currents. The inversion of the ∇H_s to infer the underlying surface currents seems to be promising. However the nonlocal effects of surface currents on waves show that the phase of current gradient is hardly reproduced in most of the part of the domain. It proved some limitations in the ∇H_s

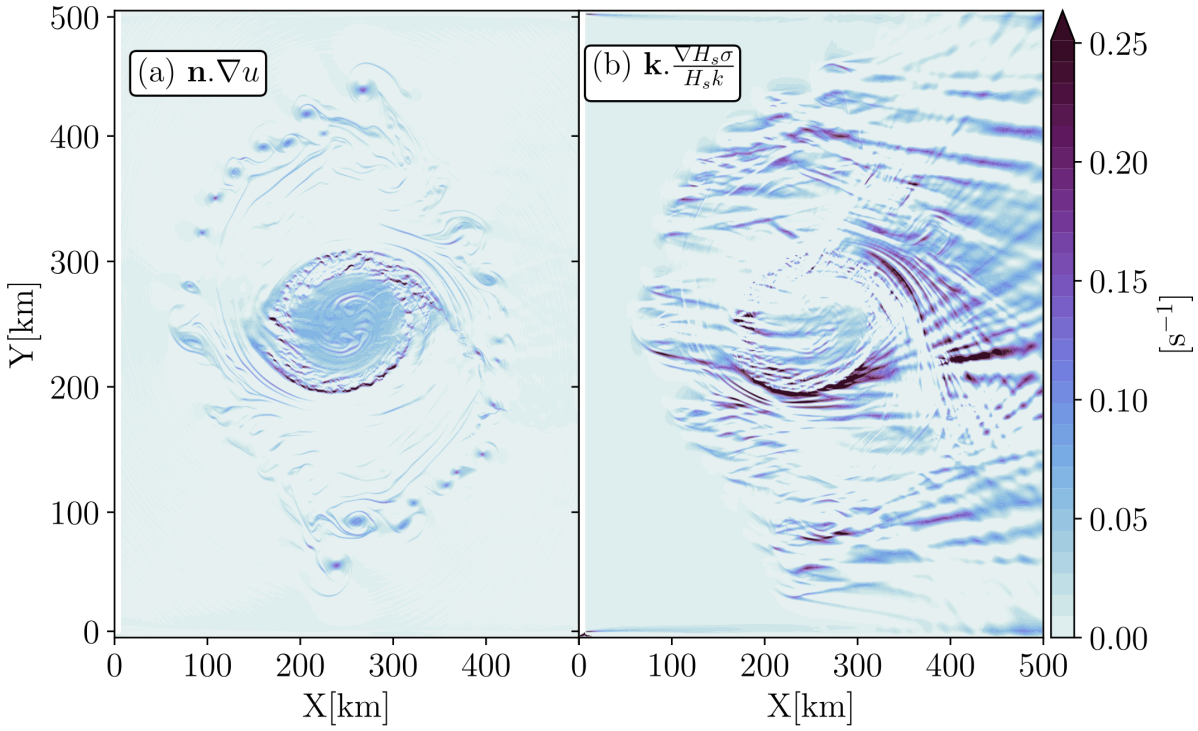

Figure 3.16: (a) Surface current gradients (∇u) projected perpendicular to the peak wave direction vector, *i.e.* the right hand side of Eq. (3.3) and (b) normalized wave height gradient ($\frac{\nabla H_s\sigma}{H_s k}$) projected in the peak wave direction vector, *i.e.* the left hand side of Eq. (3.3), both for the fully developed eddy. Panel b is for simulation initialized with T_p = 7 s.

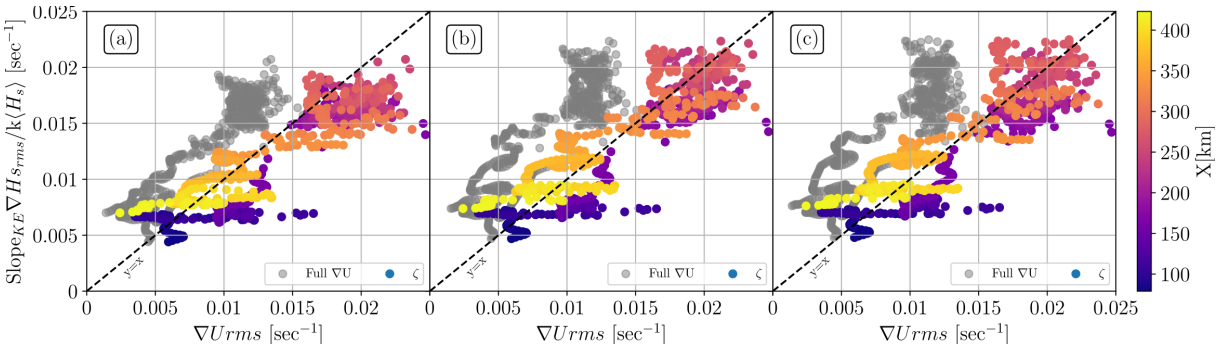

Figure 3.17: Scatter plot of the normalized root-mean-square of significant wave height gradients as a function of root-mean-square surface current gradients. Colored points are the scatter plot for the vorticity component of the surface current gradients and gray points for the full surface current gradient (diverging components + rotational components). One point corresponds to the root-mean-square of the two quantities for constant X, the value of X is given as color scale. $\langle H_s \rangle$ is the averaged value of the significant wave height when simulations reach the stationary state. Panel (a), (b) and (c) are for simulations forced with the fully developed eddy initialized with T_p=7 sec, T_p=10.3 sec, and T_p=16.6 sec respectively.

inversion to infer ∇U. To better describe the robustness of the formula given in Eq. 3.3 we proposed a scatter plot of the root-mean-square (rms) of the left-hand side as a function of the rms of the right-hand side of Eq.(3.3). Results are given in Fig.3.17. As shown numerically by Villas Bôas et al. (2020), we have multiplied the left-hand side of Eq.(3.3) by 3 which is the absolute value of the slope of the Kinetic Energy spectrum of the fully developed eddy. Note that performe the spectral analysis of such isolated eddy is highly questionable. A point in Fig.3.17 is the rms of the normalized ∇H_s and of the ∇U at fixed distance from the left boundary. The diagnostics have been done both for the full gradients of the surface currents (divergence and vorticity) and only for the vorticity component. Villas Bôas et al. (2020) proved that ∇H_s is strongly proportional to the vorticity component of the flow (see their Fig.12), we wanted to show here the effect of the divergence on the proportionality between ∇H_s and ∇U. The divergence component of the surface gradients is one order of magnitude smaller than the rotational one (not shown). We do not focus on the gradients for X<79 km and X>423 km because we are outside the eddy (∇U =0).

Thanks to a linear regression between points in Fig.3.17, we verified that ∇H_s and ∇U (vorticity) are strongly proportional in all the isolated eddy. The slopes of the fit are equal to 1.13 (0.72), 1.20 (0.8), and 1.17 (0.8) for simulations initialized with T_p=7 sec, T_p=10.3 sec, and T_p=16.6 sec. However the coefficient of determination (R2) is negative for the rms of the full ∇U with respect to ∇H_s meaning that the linear relation between ∇H_s and ∇U is not verified. When the rms of ∇H_s is compared to the rms of ζ we confirm the results of Villas Bôas et al. (2020) between X=79 km and X=423 km with R2 varying between 0.67 and 0.75 for all initializations. We have seen that the although the period of the incident waves does not have an effect on the intensity of the H_s, it has a strong effect on the location of their enhancement areas (more distant from the left boundary for simulations initialized with long waves), it motivates representing in color the distance from the left boundary of the gradients.

Where an oceanic eddy becomes unstable spontaneously due to horizontal sheared current structures (barotropic instabilities) or vertical buoyancy gradients (baroclinic instabilities, mixed layer instabilities), the resulting ocean surface shows organized ∇U patterns. Thanks to wave numerical experiments, we were able to observe ∇H_s structures which are similar to the structures of ∇U and more especially to the vorticity component of ∇U. The

amplitudes of the two gradients are comparable. It seems promising to invert the waves signal to infer the underlying vorticity field and, perhaps, retrieve the instabilities that created such structures (according to the shape and the size of $\nabla\ H_s$). Optical instruments have shown their robustness to retrieve both the phase and the amplitude of the wave fields at an unprecedented spatial resolution ($\sim$ 10 m) in a very wide swath (Kudryavtsev et al., 2017b). The use of such an instrument seems to be a good candidate to capture very small-scale current features by inverting wave characteristics as shown in the fully developed eddy. Nevertheless there is one drawback, and not least, the nonlocal effects of surface currents on H_s which make emerge ∇H_s where current is null.

Measuring surface currents from space has been a very challenging proposal for decades (Villas Bôas et al., 2019). Altimetry has proven its robustness to capture surface geostrophic current at global scale by measuring along track Sea-Level-Anomaly from multiple altimeter missions. The effective resolution of the current depends principally on the number of satellites. The resolution of a global map of surface currents derived from altimetry has been calculated and shows a mean effective resolution higher than 250 km at mid-latitudes and more than 600 km in the equatorial band (Rio et al., 2014; Ballarotta et al., 2019). Even if mesoscale eddies are observable from space (Chelton et al., 2011), surface dynamics at smaller scales are not captured by present altimeter products. As an example we can cite the small oceanic features in the fully developed eddy (see section 5.2 section of de Marez et al. (2020b)). This reality has highlighted the necessity to measure surface currents at higher resolution triggering the emergence of new satellite missions based on innovative measurements methods (Ardhuin et al., 2018; Morrow et al., 2019; Ardhuin et al., 2021).

3.7 What are the effects of the isolated eddy on the H_s downstream from the eddy?

We have shown that the effect of the isolated eddy induces a strong nonlocal effect on the H_s structures. Thanks to a new wave simulation we propose to quantify this nonlocal effect. We only focus on the fully developed eddy for incident waves from wave spectrum gaussian in frequency centered on T_p=7 sec.

3.7.1 New wave model set up

We develop a new model set up based on the same one described above. The domain size was increased in the X direction and remains identical in the Y direction. The new domain size is therefore 4000 km$\times$500 km. The spatial resolution of the new domain is downgraded in the X dimension. We performed a longer run to allow the wave model to reach a stationary state as described in the previous sections. The new framework with the current forcing and the simulated H_s fields are represented in Fig.3.18.

3.7.2 The exponential decay of H_s structures downstream from the isolated eddy

The H_s field is strongly modified downstream from the isolated eddy. H_s are both enhanced and decreased for X$>$ 400 km as presented in Fig.3.2. For X$>$ 500 km the H_s strongly decreases (Fig.3.18b), the eddy seems to have a "shadow effect" on the H_s. One can see that the eddy has an effect even far away downstream where smooth ∇H_s are noticeable. The small-scale ∇H_s are much less sharp for X$>$ 800 km.

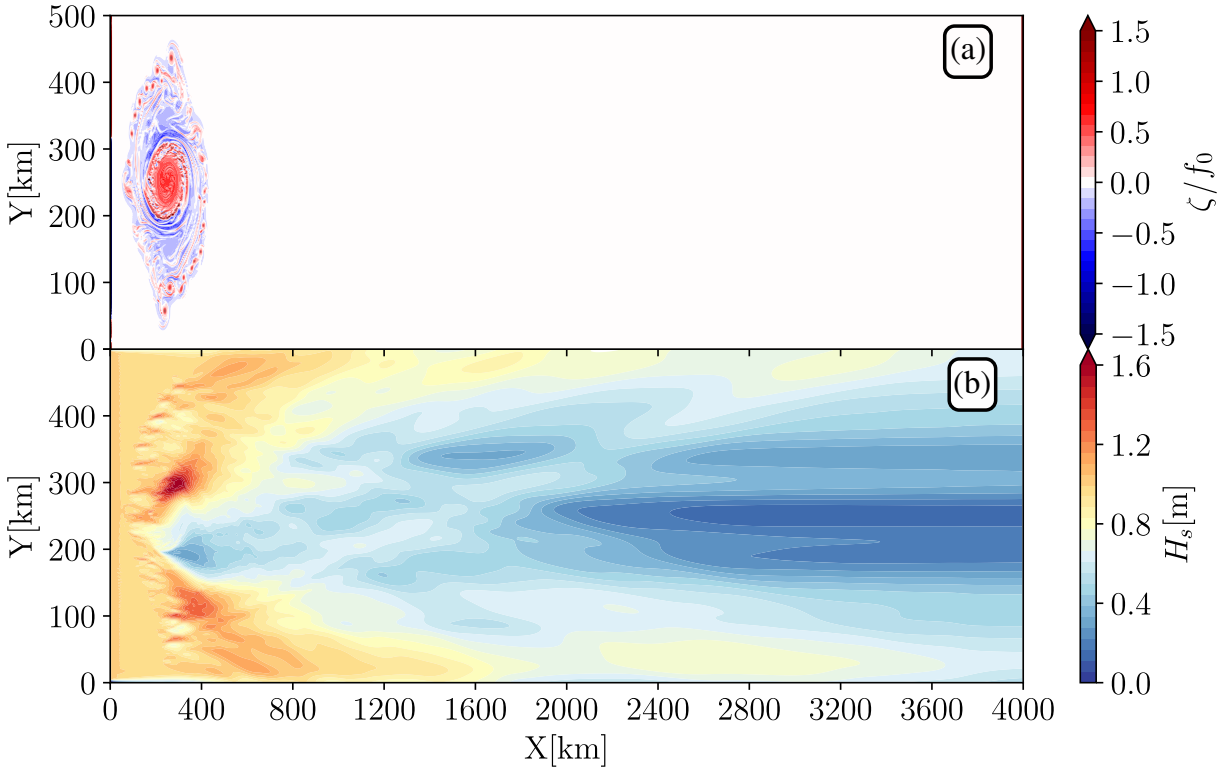

Figure 3.18: Panel (a) shows the normalized vorticity of the fully developed eddy in the new simulated domain enlarged in the X-direction. Panel (b) shows the significant wave height (H_s) for one realization of the idealized simulation when the model provides a stationary state. Without current the H_s is equal to 1 m in the entire domain.

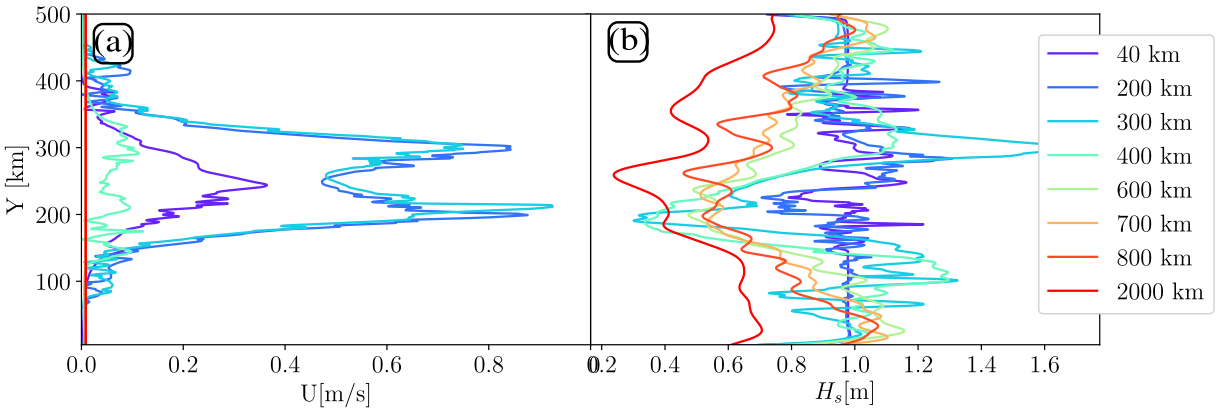

Figure 3.19: Slices of the surface current velocity module (U, panel a) and significant wave height (H_s, panel b) for eight slices along the X dimension for wave simulation in the enlarged domain. In the absence of current panel (b) gives identical values for each slice equal to 1 m.

We propose to highlight this decrease of ∇H_s by taking slices at constant X along the enlarged domain from X=40 km to X=2000 km. The associated current velocity has also been plotted along the same slices (Fig.3.19). In the eddy field (for X between 70 km and 430 km) the ∇H_s structures are proportional to the underlying ∇U with a maximum of the both gradients at X= 300 km (downstream for longer incident waves). At X$>$ 700 km non-negligible ∇H_s are noticeable whereas the current is null.

Surface current redistributes the incident wave action at a different scale depending on the scales of the current (Ardhuin et al., 2017; Villas Bôas et al., 2020). In the framework where energy input from the wind and dissipation are not taken into account, the wave action is conserved and simply reorganized along the Y-dimension (compare slices at 40 and 200 km in Fig.3.19b). The strongest values of ∇H_s coincide where wave rays are focalized, i.e around 300km (Fig.3.9d). For larger X, wave rays are less refocalized and smoother ∇H_s are noticed. One can see the diminution of the number of sharp ∇H_s along the X dimension in Fig.3.19b. We quantify this diminution by counting the number of H_s peaks higher than the H_s of the incident waves ($>$ 1 m) along the X dimension. As H_s is conserved in the domain along the wave propagation, counting the number of H_s peak higher than 1 m is equivalent to describing the distribution of the H_s pattern along the X dimension. We perform the same analysis for the current velocity field for values exceeding a threshold of 10 cm.$^{-1}$ which corresponds to the minimum velocity of the submesoscale eddies around the mesoscale eddy core. Results are given in Fig.3.20. The two distributions are roughly the same for X between 160 km and 230 km. For higher X the number of maximum decreases exponentially for both H_s and current slices. At X around 400 km one can see that the distribution of maximums for current velocity drops to zero whereas the distribution of H_s highlights a slight increase between 400 km and 450 km. We fit the distribution of H_s exceeding 1 m with an exponential function (y=x). The fit yields: log(y) =-0.0045X+4.18. One can notice that the shape of the distribution of H_s structure along X is similar to the distribution of ray caustics presented by White and Fornberg (1998) in a turbulent and random eddy field. In our case, because the current is null dowstream from the eddy, the number of H_s structures reaches zero at 1000 km.

The distribution of H_s exceeding 1 m shows two parts, the first part following the distribution of the maximum of the underlying current and the second one which drops exponentially downstream the current. The two parts of

the distribution of H_s exceeding 1 m, makes us think of the analogy of the SAR imagery technique exposed in chapter 2. The number of wave rays focalization follows first the spatial variation of the surface Kinetic Energy and then decreases exponentially downstream from the eddy in the same manner that the velocity bunching mechanism scatters the incident radar signal in the SAR transformation (Hasselmann et al., 1985a). From this analogy, the variation of the incident wave spectrum (or H_s) induced by the current depends on both the displacement of the wave rays and the correlation length scale of the eddy field in the same manner that the SAR transformation depends on the wavelength of the measured waves and the displacement of emitted radar pulses. We have seen that the number of wave rays focalization is larger for shorter incident waves (Fig.3.9) because rays are more deflected from their initial direction. It is, consistent with the SAR transformation analogy. The SAR image variance spectrum is limited by an azimuthal cut-off effect of the form of $\exp(-\delta^2 k_{waves}^2)$ with δ the displacement of the pixel induced by the velocity bunching leads by the k_{waves}, the wavenumber of the waves. In our case this δ could be the displacement of the wave rays which is proportional to the current vorticity and the incident wave wavelength (Kenyon, 1971; Dysthe, 2001). k_{waves} could be the inverse of the correlation length scale of the eddy field. Starting from this hypothesis, if we are considering two surface current fields $\mathbf{u}_{1,2}(x, y)$ with the same Kinetic omnidirectional spectrum $E_{1,2}(k)$ but with different spectral slopes $\mathcal{S}_{1,2}$. The sharper the slope is, the fewer are the small-scale patterns in the current field. For a given displacement of the wave ray induced by the current field and assuming a cut-off of the number of focalization points of the form $\exp(-\delta^2 k^2)$, the smoother is the Kinetic Energy spectrum slope, the less focalized are the wave rays. This analogy can explain why the slope of the Kinetic Energy is in Eq.(15) of Villas Bôas et al. (2020). This could have been verified by comparing the extreme values of H_s in Tab.3.1 and Tab.3.2. Because the initial eddy has larger vorticity patterns than the fully developed eddy, we should see higher extreme values for simulation forced with the initial eddy, which is not strictly the case according to the period of the incident waves. So, this short remark needs, however further investigation to link analytically the number of focalization areas of wave rays in current field with respect to the nature and the intensity of the flow.

3.8 Conclusion and perspectives of the study

In this section, we studied numerically the effect of an isolated composite cyclonic eddy on the wave properties. High resolution wave simulations have been forced by a composite eddy reconstructed from in-situ measurements in the Arabian Sea. The wave model has been forced, on the one hand, by the initial eddy field (with a gaussian shape) and, on the other hand, by the fully developed eddy resulting from the destabilization within the composite eddy. Waves have been simulated by the use of a third generation phase averaged spectral model initialized with narrow wave spectra centered at different frequencies (T_p =7 , 10.3, and 16.6 s). Although wave scattering by an oceanic vortex has already been studied in former papers (Mapp et al., 1985; White and Fornberg, 1998; Gallet and Young, 2014), this study completes studies performed in the past with *(1)* a description of the evolution of the wave bulk parameters as significant wave height and mean wave period inside and outside the isolated vortex, and *(2)* the investigation of how a fully developed eddy (that actually occur in a real ocean) modify the wave field. Both wave dynamic and kinematics are changed by the presence of an underlying current. The changes of the wave peak direction is more pronounced where the underlying current gradients are strong and when incident waves are short. This is coherent with the studies of Kenyon (1971); Dysthe (2001). As multi-scale dynamic eddies are certainly more realistic in the ocean than Gaussian eddies, former studies of interaction between wave and Gaussian eddy

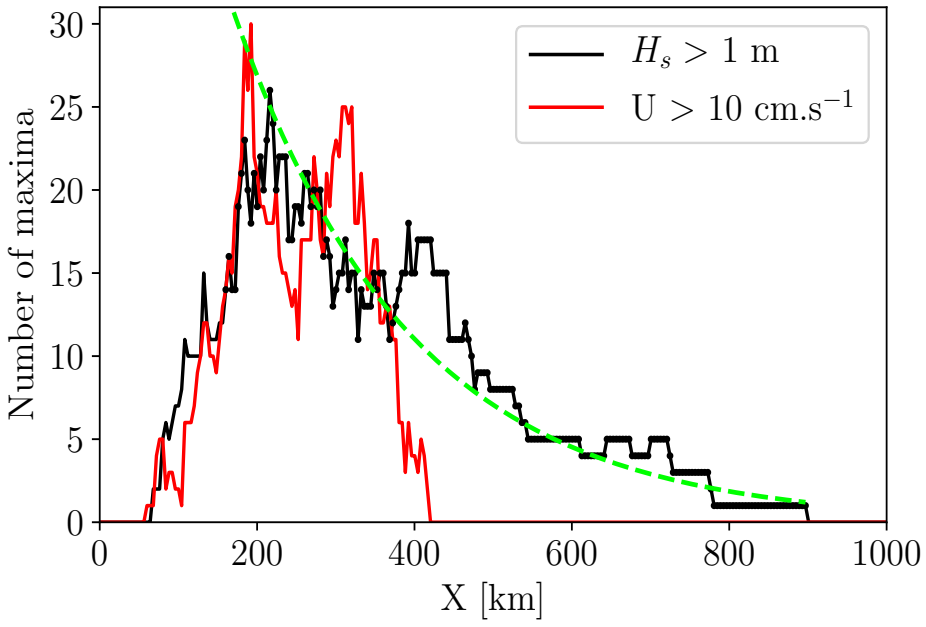

Figure 3.20: The number of times that H_s exceed 1 m with respect to the X dimension between 0 and 1000 km (solid black line). The same analysis for current velocity exceeding 10 cm.s^{-1} (solid red line). The profile of the current and the simulated H_s is given in Fig.3.18. The dashed green line is the exponential fit of the H_s distribution between 160 km and 1000 km.

underestimate wave refraction, extreme significant wave heights but also wave steepness, because surface currents lead to a non-negligible change of wave period (wavelength). Those underestimations can have a large impact on the waves forecast but also on the source of noise induced by waves in the ocean level measurements by altimeters. Tran et al. (2010) proposed to combine altimeter measurements and wave simulations in order to develop a global sea-state bias model. Thanks to the period provided by wave model (only forced by wind) the authors showed the possibility to reduce the error budget in the sea-level retrieval. However they parametrized their wave model on a too coarse grid ($1° \times 1°$) without taking into account current forcing. As we proved here, short-scale currents induce significant changes of wave period at regional scale (smaller than wind scale patterns). Indeed, even in a very idealized eddy, $\Delta T_{m0,-1}$ oscillates within 1 sec (Fig. 3.6a-c) and reaches $\sim$3 sec for a more realistic eddy pattern (Fig. 3.6a-c). Redoing the same work of Tran et al. (2010) at higher resolution with current sufficiently resolved (Marechal and Ardhuin, 2021) would be beneficial to improve their sea-states bias model at regional scale.

Under the WKB approximation and in the geometric theory framework, the significant wave height gradients normalized by the incident wave frequency has been described as a function of the surface current gradients. Besides a good coherence in terms of magnitude between the two gradients, structures of significant wave height gradient are very sensitive to the underlying surface current. We know that measurements of sea level anomaly from space are able to monitor surface currents at global scale with a wavelength resolution of several hundreds kilometers in ice-free areas (Villas Bôas et al., 2019). All the surface dynamics at smaller scales cannot be captured by altimeters, whereas a lot of oceanic processes occur at those scales (from 1-100 km). This chapter has shown the possibility to infer the vorticity of the eddy field from the inhomogeneity in the waves field, as proposed in Villas Bôas et al. (2020). Infer vorticity patterns could allow capturing the small-scale processes (vertical movements, mixing, shear flows...) without measurement of surface currents. Nevertheless, this inversion could not work in the vicinity of a strong ∇U field, as the isolated eddy presented here. Indeed, because waves keep in memory the effect of the upstream currents crossed, it leads to regional inhomogeneities in the wave field, even if the local current gradients are null. As measuring surface currents both at global scale and high resolution are a present challenge for the oceanographic community, different strategies have been imagined. Infer ∇U from ∇H_s measurement (altimeters, Quilfen and Chapron (2019) or optic imagery Kudryavtsev et al. (2017b))seemed to be a good strategy but was limited by the nonlocal aspect of current effects in the H_s field. Also, because the wave-current coupled system is too complex, much more than the one proposed here, assumption proposed in this manuscript are hardly satisfied in nature. So the best solution, to have the surface current gradients at global scale and at higher resolution than current provided by altimeters, would be a direct measurement of the current. As proposed by the SKIM mission, (Ardhuin et al., 2018).

Finally de Marez et al. (2020b) showed that the eddy used in our numerical simulations is strongly sheared along the first meters depth of the ocean (Fig.3.21). The effects of the vertical shear of the current are negligible for very deep water especially where waves are short (a few second of periods). For sufficiently long waves ($>$ 10 sec) the currents, at depth higher than 50 m, induces a change in the wave dispersion. Indeed, the depth (z) where a linear velocity profile of current contributes to the change of the phase speed of the waves, is related to the wavelength of the waves (λ) and is equal to z = 0.08 λ (see Fig.1 of Ardhuin et al. (2021) from results of Stewart and Joy (1974)). The results presented here would be certainly modified if the vertical shear of the eddy had been considered especially for simulations initialized with 10.3 sec and 16 sec waves.

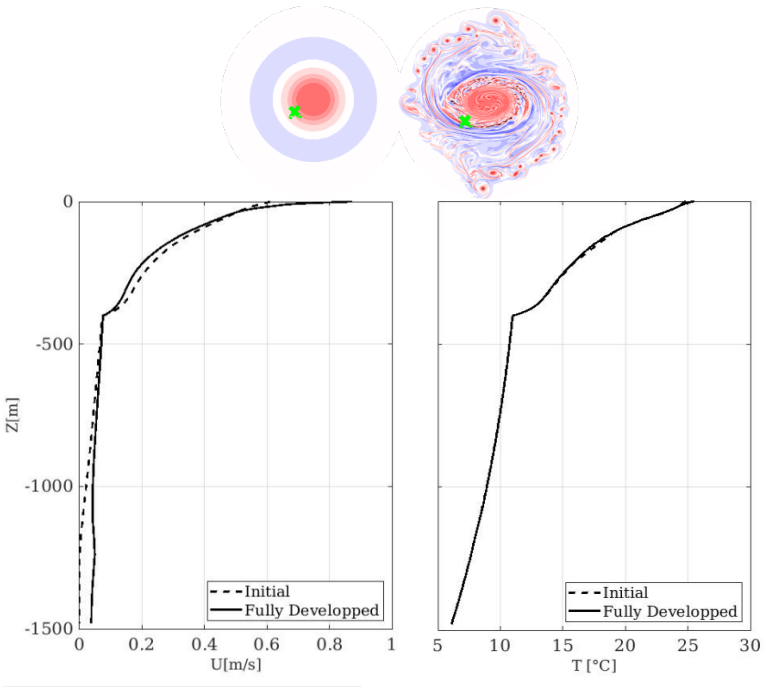

Figure 3.21: The left panel shows the current velocity along the vertical for both the initial (dashed black line) and the fully developed eddy (solid black line) in the core of the eddy (location given by the green crosses in the eddies - the vorticity of the eddies is plotted). The right panel shows the associated vertical profile of the temperature.

3.9 Summary of wave-current interactions in an idealized framework

In this chapter we have presented the effects of a realistic cyclonic eddy on wave properties. The eddy used was a composite eddy computed from Argo floats and drifters in the Arabian Sea. The eddy is highly unstable and spontaneously destabilizes due to mixed barotropic/baroclinic instabilities. After 210 days of destabilization, the core of the eddy remains quite stable, but a strong frontal dynamic emerges with filaments and submesoscale eddies. This is not the first study of how an isolated eddy modifies the wave field, however, previous studies were based on an eddy field too idealized (with a gaussian shape). We showed that contrary to unrealistic gaussian eddy, the eddy field highly dynamic at multi-scale induces strong spatial inhomogeneity and sharp gradients in significant wave height and mean period signals. Also, the influence of the frequency of the incident waves on the wave refraction has been studied and confirmed the theory of Kenyon (1971) and Dysthe (2001). Shorter waves are more refracted by the surface currents leading to gradients of H_s more or less distant from the left boundary. Those gradient are associated with regions where wave action is strongly focalized. Finally, assuming the conservation of action along wave rays and that wave kinematics are entirely described by the ray equation, surface current gradients have been estimated from the current-induced $\nabla\ H_s$. This strategy allows inferring current gradients at resolution where traditional altimeter products fail. Although the surface current gradients inferred are quantitatively consistent with the *true* current gradients inside the eddy, the non-local effects of currents on the H_s result in sharp current gradients where no current were expected.

The current-induced variability on waves generated from narrow band spectra has been studied in an idealized framework in an isolated eddy. As, in the actual ocean, eddies are rarely isolated but surrounded by other eddies

and that waves are more stochastic, the wave and current fields were not sufficiently realistic in this chapter. Also, in reality, local wind spreads the wave spectrum by creating wind sea that will be also modified by surface currents. Also the dissipation induced by wave breaking was not taken into account in this study, whereas it is important at the submesoscale range (Romero et al., 2017; Romero et al., 2020). Those remarks trigger to diagnose the effects of surface currents on waves in a more realistic framework. Also, until now, we only focus on the redistribution of the wave action by the current in numerical and theoretical framework, to diagnose how spatial wave height gradient is related to the current at the meso- and the submesoscale range it will be necessary to have a look at data. Both current and previous chapters will help to understand such data.

CHAPTER 4

SIGNIFICANT WAVE HEIGHT GRADIENTS IN GREAT BOUNDARY CURRENT: A FOCUS ON THE AGULHAS CURRENT REGION

Thanks to the recent works of Quilfen and Chapron (2019) on H_s altimeter measurements, the spatial variability of H_s at the mesoscale range ($\mathcal{O}$(100-10)km) induced by currents could be captured by altimeter measurements. Until now these variability were drowned in the measurement noise Ardhuin et al. (2017). These new altimeter data have confirmed that, in strong boundary current (Agulhas current), the sea state is highly modified by surface current gradients. Currents lead to the formation of severe crossing seas and very sharp local wave height gradients. Combining these new data with the theoretical approaches of current-induced refraction described by White and Fornberg (1998), Heller et al. (2008), or Villas Bôas and Young (2020) and the state of the art of phase averaged wave models, we tried to infer waves and current properties that are responsible for the regional wave height variability. We focus on the Agulhas current region which provides a natural laboratory to study the wave current interactions in a strong turbulent flow.

4.1 The large scale dynamic of the Agulhas current

The Agulhas current is the strongest boundary current in the southern hemisphere. It forms the western limb of the wind-driven anti-cyclonic circulation of the Indian Ocean. It is a narrow current with surface velocity that can reach 2.5 m.s^{-1}. It is a warm and salty current with temperatures that vary from 22 to 27°C and salinity within 35 and 35.5 psu. The current is composed of three main systems. The main one (Agulhas current) that flows from offshore Durban (31°E) up to offshore Cape-Town (18°E). The current runs along the coast and deviates toward the south at Agulhas Bank where the depth sharply decreases. The second system is the retroflexion of the Agulhas current where the current changes direction toward the east and creates strong meanders. Warm and salty surface mesoscale eddies and submesoscale filaments detach from the Agulhas current and drift into the cold Benguela Current. The mesoscale eddies propagate in the South-Atlantic with a lifetime of two years and more. The last system is the Agulhas return current which propagates westward toward the Indian Ocean. The return current produces a rich field of mesoscale and submesoscale eddies. During its travel, the Agulhas return current crosses several submarine ridges as the Agulhas Plateau which induces deflections of the mean westward direction (Lutjeharms, 2006). A

recap of the Agulhas dynamic is given in Fig.4.1. Waves are particularly high in the Agulhas current system due to its wide exposure to the southern ocean. In the roughest ocean on earth, storms occur perpetually and propagate waves in the Atlantic, Pacific, and the Indian ocean (Young, 1999). The coupling waves-Agulhas current creates abnormal high waves experienced by tanker crews (see chapter 1, Mallory (1974); Lavrenov (1998)).

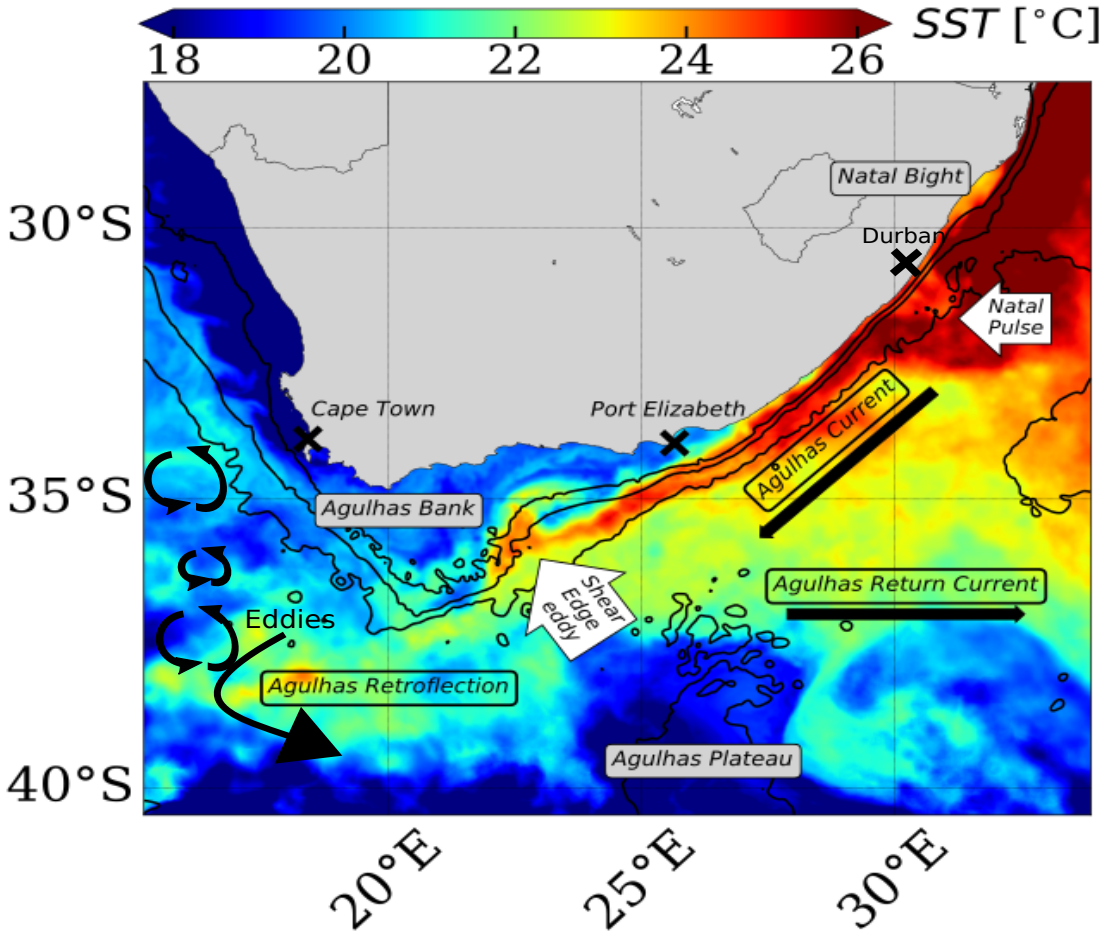

Figure 4.1: Sea surface temperature in the Agulhas current. The main topographic characteristics along the Agulhas path are displayed in gray legends. The thin black lines follow the 200, 1000, and 3000 m isobaths. Slightly adapted from Tedesco et al. (2019)

4.2 Significant wave height gradients in the Agulhas current are driven by the intensity and the nature of the underlying surface current - *published in the Journal of Geophysical Research-Ocean*

JGR Oceans

RESEARCH ARTICLE
10.1029/2020JC016564

Special Section:
Remote Sensing of Ocean Surface Currents Using Doppler Techniques from Planes and Satellites

Surface Currents and Significant Wave Height Gradients: Matching Numerical Models and High-Resolution Altimeter Wave Heights in the Agulhas Current Region

Gwendal Marechal[1] and **Fabrice Ardhuin**[1,2]

[1]University Brest, CNRS, Ifremer, IRD, Laboratoire d'Océanographie Physique et Spatiale, Brest, France, [2]Scripps Institution of Oceanography, University of California, La Jolla, CA, USA

Key Points:

- Spatial resolution of currents is key for reproducing wave height gradients
- 30 km resolution over the Agulhas current is necessary to retrieve most of the observed gradients
- Incident waves with a narrow directional spreading induce larger wave height gradients

Correspondence to:
G. Marechal,
gwendal.marechal@ifremer.fr

Citation:
Marechal, G., & Ardhuin, F. (2021). Surface currents and significant wave height gradients: Matching numerical models and high-resolution altimeter wave heights in the Agulhas current region. *Journal of Geophysical Research: Oceans*, *126*, e2020JC016564. https://doi.org/10.1029/2020JC016564

Received 1 JUL 2020
Accepted 1 FEB 2021

Abstract Advances in the understanding and modeling of surface currents have revealed the importance of internal waves, mesoscale and submesoscale features. Indeed, all these features should have a large influence on wind waves and in particular on wave heights. Still, the quantitative impact of currents on waves is not well known due to the complexity of the random wavefields and currents that are found in the ocean and the lack of observations of both currents and waves at scales shorter than 150 km. Here, we compare novel satellite altimetry data and state of the art phase-averaged numerical wave models forced both by wind and currents. Currents used are taken from the oceanic model Coastal and Regional Ocean COmmunity, run at high resolution. The influence of current field resolution is investigated by applying Gaussian filters of different width to that same high-resolution current field. We find that a numerical wave model that uses currents with resolutions of ~30 km or less and a directional resolution of 7.5° can provide accurate representations of the significant wave height gradients found in the Agulhas current. Using smoother current fields such as derived from altimeters measurements alone, coarse directional spectral resolution or larger directional spread of the wave model generally underestimates gradients and extreme wave heights. Hence, satellite altimetry provides high-resolution wave height with a gradient magnitude that is highly sensitive to underlying surface current gradients, at resolutions that may not be resolved by today's altimeters measurements. This is demonstrated here for relatively steady currents averaged over 3 years.

Plain Language Summary Mariners have learned to be wary of severe sea states, especially in strong currents like the Agulhas that flows along the South African coast, where wave heights in the current can be several meters taller than in the surrounding waters. Mariners have also learned to spot currents by watching the water ahead of them. Here, we use satellite measurements of wave heights and a numerical wave model to understand the parameters that control the spatial variation of wave heights across currents. We particularly question the necessary current magnitude and gradient that are required to explain observed wave height gradients. Modeled gradients fade for smooth surface currents like surface currents estimated from satellite measurements of sea level or typical global ocean circulation models. Also, numerical experiments have shown that when incident waves have a narrow range of directions, wave height gradients are sharper. A good wave model should thus resolve both the current features, with a spatial resolution better than 30 km, and the range of wave directions, typically using 48 directions or more. Such a good model can then be used to evaluate the quality of modeled ocean currents by matching the modeled strength of wave height gradients with measurements.

1. Introduction

Surface gravity waves generated by wind (hereinafter waves) interact with surface currents at all scales due to a wide range of processes (Phillips, 1977). Except for very short fetch near the coast or for the shortest wave components, the growth of waves in the presence of winds is only significant over large scales, so that the local gradients in the dominant wave properties are generally dominated by current gradients(Phillips, 1984). In the ocean, it appears that refraction, which focuses wave energy in current jets that flow in the wave direction, is probably the dominant source of variations of wave heights at scales 50–200 km with a minimal effect of wind gradients (Ardhuin et al., 2017). For currents speeds much weaker than the waves phase speed, it is the rotational part of the current that is expected to explain the variations in wave direc-

tions (Landau & Lifshitz, 1960; Villas Bôas & Young, 2020). This refraction can lead to extreme wave heights over large mesoscale currents, such as the Agulhas current, that are dangerous for ships and offshore structures (Gutshabash & Lavrenov, 1986). Other impacts of waves on air–sea fluxes, upper ocean mixing, or remote sensing also require better knowledge on wave–current interactions (e.g., D'Asaro, 2014; Sandwell et al., 2014; Villas Bôas et al., 2019).

Recent advances in understandings and in ocean modeling of surface ocean dynamic show that the upper ocean is highly energetic not only at the mesoscale, for which the flow is in quasi-geostrophic balance, but also at smaller scales (submesoscales) (McWilliams, 2016). Further, strong ocean currents are associated with sharp and asymmetric velocity fronts, with larger positive vorticity maxima in the Northern Hemisphere (e.g., Gula et al., 2015). Also, the generation of large surface waves has been shown to occur in the presence of strong internal waves (Osborne & Burch, 1980). All these small-scale current features may contain as much surface kinetic energy (KE) as the mesoscales but it is not clear how much they influence the waves. Refraction theory tells us that changes in wave direction for a given wave frequency are the product of the current vorticity magnitude and the scale of the current feature, so that a localized high vorticity may have the same effect as a distributed but lower vorticity. But in practice, ocean waves are random and the different components of their relatively broad spectrum are affected in different ways by the surface vorticity.

The evolution of the wavefield, represented by the wave action spectral densities $N(\sigma, \theta)$, with σ the wave frequency in the frame of reference moving with the local current and θ the wave propagation direction generally follows the wave action equation (Komen et al., 1994; Tolman & Booij, 1998):

$$\partial_t N + \partial_\lambda(\dot{\lambda}N) + \partial_\phi(\dot{\phi}N) + \partial_\sigma(\dot{\sigma}N) + \partial_\theta(\dot{\theta}N) = \frac{S}{\sigma} \tag{1}$$

The contributions of surface currents in Equation 1 come into the advection speeds in longitude $\dot{\lambda}$ and latitude $\dot{\phi}$, which is the sum of the intrinsic group speed and the surface current, the refraction velocity $\dot{\theta}$, the change of frequency velocity $\dot{\sigma}$, and in the right-hand-side source term S because the effective wind velocity that generates waves is the vector difference of wind and surface current velocities (e.g., Ardhuin et al., 2017).

Because the effect of refraction $\dot{\theta}$ at position (λ, ϕ) combines with the advection in a new direction θ to produce a change in wave action N at another location (λ', ϕ'), there is no simple relationship between the current field and wavefield, in other words, surface currents have a nonlocal effect on the distribution of the wave action in the current field.

White and Fornberg (1998) have shown theoretically that the spatial distribution of refraction-induced focusing can be predicted for monochromatic waves over a random current with a narrow band spectrum. Still, that does not say much about the spatial distribution of wave heights in this case. The problem is more complex for broad band current spectrum and random waves, for which the significant wave height combines all the spectral components:

$$H_s = 4\sqrt{\int_0^\infty \int_0^{2\pi} \sigma N(\sigma,\theta) \mathrm{d}\theta \mathrm{d}\sigma}. \tag{2}$$

Guided by these theoretical insights and the solid foundation of the wave action equation (e.g., White, 1999), our understanding of the effects of surface currents on wave height in the real ocean has relied on numerical simulations using Equation 1. These simulations are fairly successful for well-known tidal currents (e.g., Ardhuin et al., 2012), but there are very little data to validate modeled currents and waves in other regions. For example, wave simulations in the Gulf Stream and Drake Passage suggest that the patterns of H_s field induced by surface currents are dominated by the refraction (Ardhuin et al., 2017), with a significant impact of small-scale currents. These modeling results could not be validated using standard satellite altimeter data that is dominated by noise for along-track wavelengths shorter than 100 km (Dibarboure et al., 2014). The development of new denoising techniques has revealed a systematic relation between wave height gradients and current vorticity (Quilfen & Chapron, 2019; Quilfen et al., 2018). These filtered data have been compared to preliminary simulations in the Agulhas current using Equation 1 solved by either finite-difference techniques or ray tracing. These comparisons have highlighted the importance of the directional width of

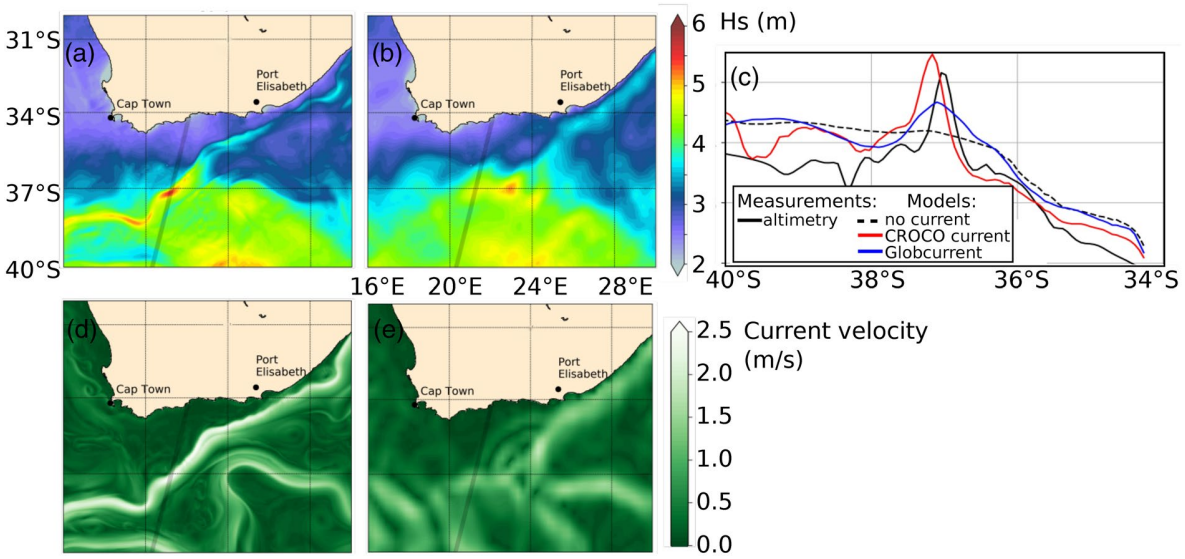

Figure 1. Snapshots of modeled H_s and surface current forcing in the Agulhas system for May 1, 2016 at 15:00 UTC. Significant wave height (H_s) field computed with (a) the WAVEWATCH III model and (b) Globcurrent surface current. (c) Along-track significant wave height measured by altimeter. The solid black line is the measurement, the red and blue solid lines are H_s along the altimeter track computed with WW3 using different current forcing, CROCO or Globcurrent, respectively. The dotted black line is the H_s simulated by the model without surface currents forcing. The position of the altimeter track and the H_s measurement is also shown on panels (a, b, d, and e). Surface current fields used in the model simulations are shown in (d and e). CROCO, Coastal and Regional Ocean Community.

the wave spectrum, with stronger H_s gradients obtained for narrower incident wave spectra even when only large-scale currents, as derived from gridded altimetry data were used (Quilfen et al., 2018).

These two previous studies by Ardhuin et al. (2017) and Quilfen et al. (2018) have suggested two possible reasons for sharp H_s gradient: namely the presence of sharp current gradients or the strong local focalization of waves on a smooth current field. Figure 1 illustrates the first possibility over the Agulhas current, using either large-scale currents of gridded altimetry or a high-resolution modeled current, both described in detail in Section 2.

The present work aims at consolidating these previous analyses and contribute to answering the following questions. What are the parameters controlling the spatial variability of wave heights in a realistic current field? How can these be best reproduced by numerical models? In particular, we focus on the effect of the spatial resolution of the current field and angular discretization of the wave model in relation with the directional spread of wave spectra. Here, we focus on the Agulhas current because of the strong H_s signature that is easily captured by satellite altimeters. Further work will be needed for other wave and current regimes.

The numerical model setup and data are presented in Section 2. Results follow in Section 3, with a discussion of the influence of the surface currents resolution in Section 4. Finally, we will conclude this wave–current interactions study in Section 5.

2. Satellite and Modeling Data for Waves in the Agulhas Current

The Agulhas current system is one of the most intense western boundary currents, with velocities exceeding 2.5 m s^{-1} along the East coast of South Africa, before retroflecting back into the Indian Ocean with large ring eddies shed in the South Atlantic Ocean (Beal et al., 2011; Tedesco et al., 2019). The Agulhas current system is also exposed to very large waves from the Southern Ocean (Young, 1999).

2.1. High-Resolution Altimetry H_s Data

Satellite altimeters have been measuring H_s continuously for 27 years, providing measurements along sparsely spaced tracks, typically every 10–30 days (Ardhuin et al., 2019). In many regions of the ocean, these

are the only available measurement of wave heights. This is particularly the case in strong current regions where moored buoys are more difficult to install. Further, H_s measurements along the satellite ground track provide a unique view of the spatial variations of H_s, although along one dimension only. Until recently, the analysis of H_s variations was limited to wavelengths larger than 100 km, due to the noise associated with the tracking methods used to interpret altimeter waveforms (Ardhuin et al., 2017; Sandwell et al., 2014). The successful application of Empirical Mode Decomposition (EMD) (Huang et al., 1998) to the denoising of H_s along-track series now makes it possible to investigate much smaller scales, possibly down to 15 km wavelength or less (Quilfen & Chapron, 2019). Here, we use denoised wave heights from the European Space Agency (ESA) Sea State Climate Change Initiative (SeaState-CCI) version 1 database (Dodet et al., 2020), that uses this denoising technique applied to calibrated Geophysical Data Records from CNES and ESA for the Jason-2, CryoSat-2, and SARAL/AltiKa missions. The analysis of 3 years from 2014 to 2016 in our region of interest gives a total of 4,746 satellite tracks, with one example shown in Figure 1. In the ESA CCI-Sea-States product, Dodet et al. (2020) give a root mean square error (RMSE) on Hs data equal to 0.21, 0.2, and 0.21 m for Jason-2, CryoSat-2, and SARAL/AltiKa missions respectively. The uncertainty of Hs is computed from in situ waves buoys located beyond 200 km offshore. The RMSEs are similar for the three missions both for calibrated and denoised (EMD method) altimeter data (Figure 10 of Dodet et al. [2020]).

2.2. Numerical Wave Model

Our numerical wave model is based on the WAVEWATCH III modeling framework (The WAVEWATCH III® Development Group, 2016) that integrates the action balance Equation 1, discretized on a regular latitude–longitude grid with a resolution of 1/30°. Our baseline configuration uses a spectral discretization into 32 frequencies from 0.037 to 0.7 Hz and 48 directions ($\Delta\theta = 7.5°$). This model is forced by surface currents, as detailed below, together with operational hourly wind forecasts from the European Centre for Medium-Range Weather Forecasts, at 1/8° resolution. The overall time step used to solve Equation 1 is 390 s, and the solution is obtained with a splitting technique (Tolman, 1992), with a spatial advection step of 130 s, a refraction step of 18 s, and an automatically adjusted source term integration step that can be as short as 10 s. We define the boundaries with three hourly wave spectra from a global model configuration that uses the same wind fields but no current, a spatial resolution of 0.5° and the same spectral discretization as our Agulhas wave model. The wave model grid covers the domain shown in Figure 1, from 40° to 30°S and 16° to 30°W.

The signature of the Agulhas systems is clearly visible in the modeled H_s field with a band of larger wave heights. On the example in Figure 1a, one can observe the effect of the main Agulhas current along the coast, including a meander known as a "Natal pulse," located at 29°E, upstream of Port Elisabeth. Large current structures typically have multiple parallel branches caused by the straining of the large-scale field and very sharp boundaries (Figure 1d). In contrast, the H_s field computed with the model using surface currents estimated from altimetry measurements (Globcurrent) has blurred patterns (Figure 1b), caused by surface currents with broader features and less intense maxima values (Figure 1e). The large-scale circulation estimated from altimeter data although less energetic is coherent with the Coastal and Regional Ocean COmmunity (CROCO) output snapshot: Agulhas current along the coast, retroflexion, and Agulhas return current. For smaller-scale features, all the 10–100 km structures are missing in the Globcurrent product, including meanders of the Agulhas current along the coast, from 28° to 23°E which play an important role in the current stability (Tedesco et al., 2019). Also, the Agulhas current has a similar transport in both current fields but much sharper gradients and higher maxima, up to 3 m/s in the CROCO model result compared to 2 m/s in Globcurrent.

Altimeter measurements show a narrow H_s maximum around 37° in the Agulhas current upstream of the retroflexion (Figure 1c). This narrow peak in H_s is closer to the one obtained with the CROCO currents, while the Globcurrent current fields lead to a broad H_s maximum.

2.3. Currents Fields Used for Forcing the Wave Model

Given the large influence of surface current details, we have designed a series of simulations with currents at different resolutions. These current fields are based on surface current estimates from the CROCO model

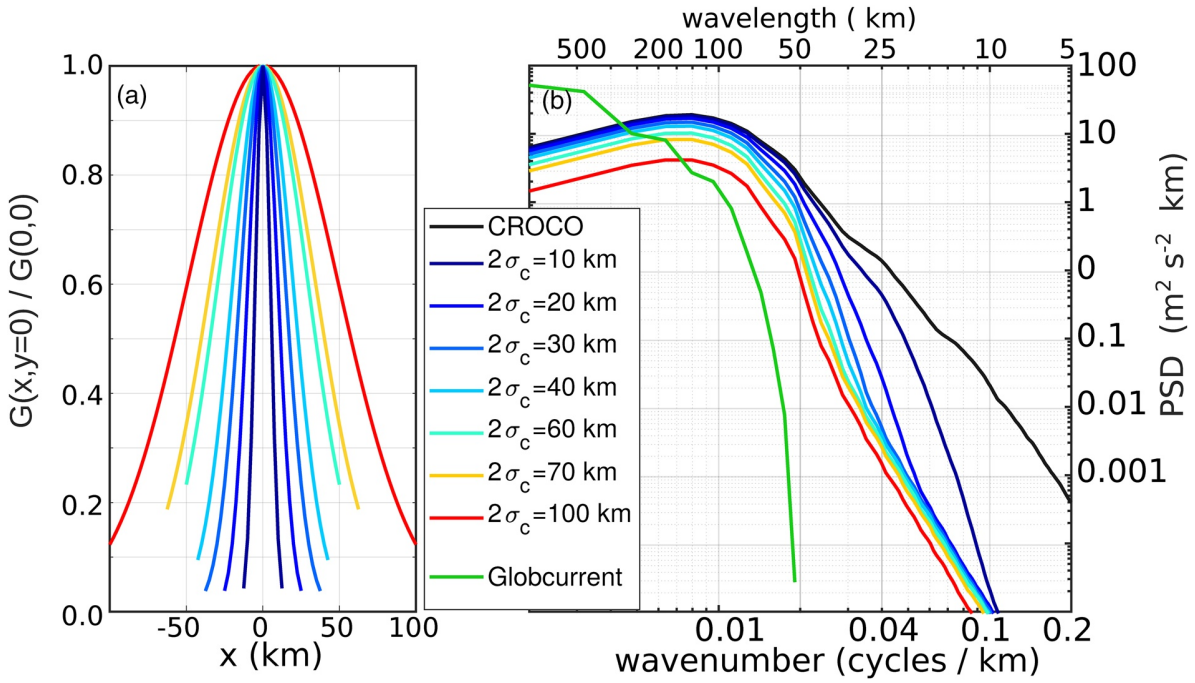

Figure 2. (a) Size and shape of the Gaussian filters G defined by their extent and the parameter σ_c. These are used to smooth the CROCO current fields. (b) Spectra of surface currents in the region 25.2°–33.7°E and 40.4°–35.3°S, from the original and smoothed CROCO currents, and from Globcurrent. CROCO, Coastal and Regional Ocean COmmunity.

(Debreu et al., 2012) without data assimilation nor tidal forcing with a resolution of 1/36° both in latitude and longitude. The CROCO model domain is larger than the WW3 model domain that is shown in Figure 1 and covers 15.1°–33.7°E and 40.4°–27.2°S. This CROCO model configuration is expected to produce surface currents that are statistically consistent with the real ocean and has been used for several process studies (Tedesco et al., 2019). However, for any particular time and location, the variable current structure is not expected to reproduce the stochastic behavior of the ocean as no data assimilation is used within the model domain. The CROCO model has been forced at the surface by the ERA-interim reanalysis and boundaries have been forced by a global reanalysis GLORYS. We have also used low-pass-filtered CROCO currents as an input forcing for the wave model. These are obtained by applying an isotropic two-dimensional Gaussian filter on both zonal and meridional components of the current velocity vector. This filter is defined by its standard deviation σ_c (Figure 2a). We emphasize that the alternative approach of rerunning CROCO at different resolutions may produce very different results and would require some tuning of each model configuration that is beyond the scope of the present work.

The filtered current fields effective resolution is the result of the convolution of the Gaussian filter and the original current field. Theoretically, the spectrum of the filtered current is the product of the original current spectrum and the spectrum of the Gaussian filter. In practice, it means that the current spectrum rolls of sharply for wavelengths shorter than $L_c = 4\sigma_c$ or an effective resolution of $2\sigma_c$. An example of omnidirectional KE (KE = $<U>^2 + <V>^2$, $<.>^2$ denotes the variable's variance) spectra are given in Figure 2b. These spectra are from an azimuthal integration of a two-dimensional spectral analysis applied on surface current fields at a specific time. Details of the spectral method are available in Section 2.2 of Ardhuin et al. (2017). These 1-D spectra represent the distribution of variance across spatial scales. The clear drop of variance for filtered surface currents at high wavenumbers shows that the Gaussian filtering process has removed small spatial scales in the Agulhas region.

Seven surface current fields have thereby been created, with effective resolutions ranging from 10 to 100 km. Figure 3 illustrates four patterns of currents with the vorticity $\zeta = \partial V/\partial x - \partial U/\partial y$ and H_s corresponding to different current resolutions.

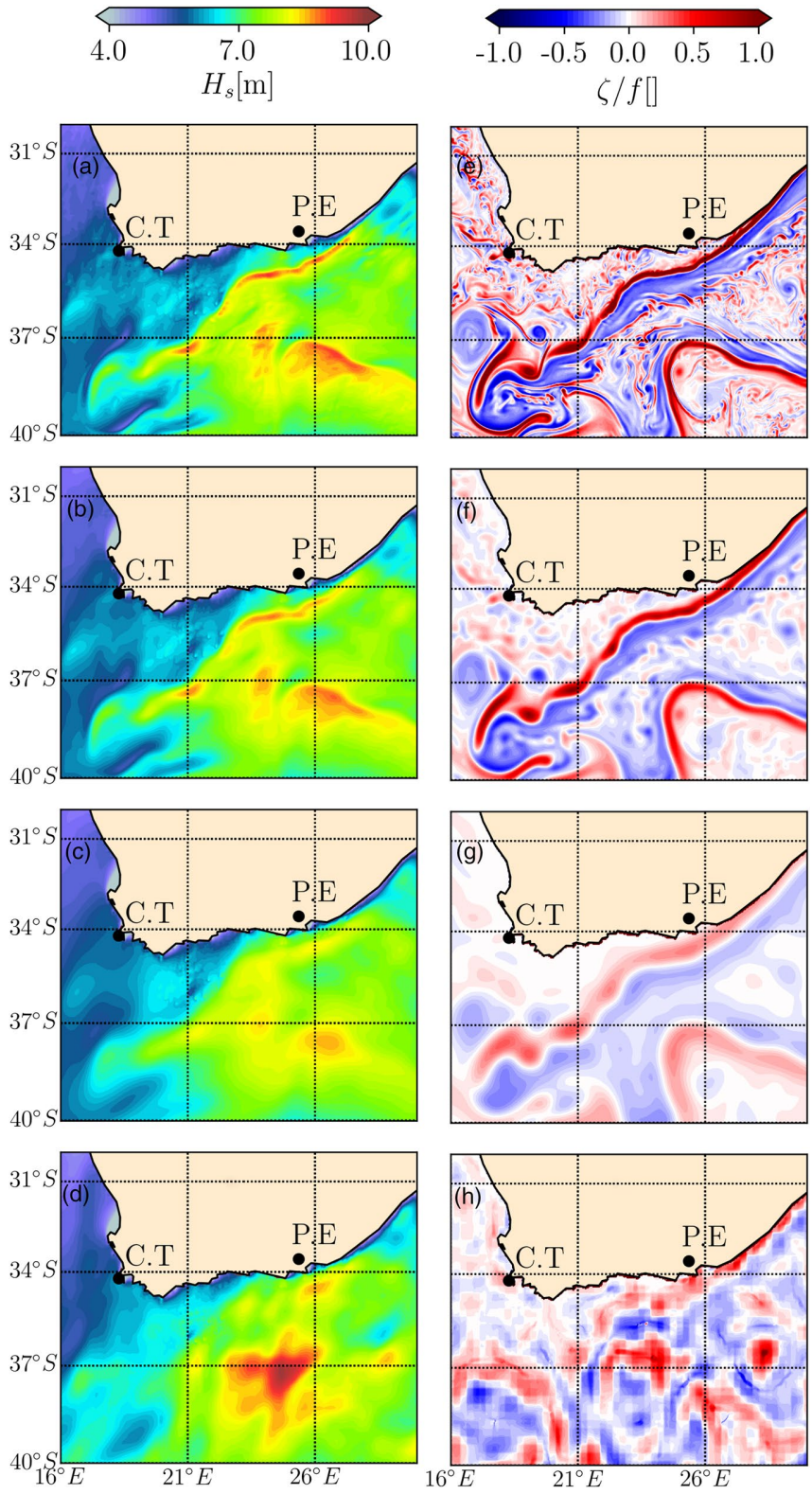

Figure 3. (a–d) Snapshots of significant wave heights (H_s) in the Agulhas region simulated on August 30, 2015 at 00:00 UTC with a current forcing resolved at 2.5, 20, 60, and 150 km (Globcurrent surface currents). (e–h) vertical normalized surface vorticity $\zeta = \partial_x V - \partial_y U/f$, in the same area for currents resolved at 2.5, 20, 60 km, and for Globcurrent product (150 km). We have used $f = 10^{-4}$ s^{-1} for the Coriolis parameter.

The filtering of the current field results in the removal of small-scale structures, including small mesoscale eddies and filaments, as well as the smoothing of the large-scale structures. Alternatively, we also used a surface current forcing taken from the Globcurrent product (Rio et al., 2014). This Globcurrent product has a spatial resolution of 1/4° both in latitude and longitude and is temporally resolved at 1 day. It provides the geostrophic component of the total surface currents estimated from the sea surface height (SSH) measured by altimeters, and a mean dynamic topography that combines other data sources (Rio et al., 2014). A similar spectral analysis described above has been applied on Globcurrent product and revealed its effective resolution 150 km. The 60 km resolution-filtered CROCO current has scales similar to those in the Globcurrent field, with a lower surface currents intensity for filtered surface current (due to filtering process). We note that the surface relative vorticity ζ of the filtered current (Figure 3) is similar to the ones presented in Figure 17c of Chelton et al. (2019) in the Coastal California current for similar resolution (few kilometers, 20 and 80 km).

Snapshots of simulated H_s in Figures 3a–3d illustrate how the wave height patterns follow the surface vorticity patterns as already shown in Figure 13 of Quilfen et al. (2018). Figure 3 (left) shows a H_s maximum where the normalized vorticity is positive in the main stream of the Agulhas (southwestward) and also show that the H_s gradient is sharp for WW3 results forced with high-resolution currents and become blurred for poorly resolved surface current. We have run our wave model during 3 years, from 2014 to 2016, with the appropriate surface currents (fully resolved from CROCO model, filtered and estimated by altimetry), wind and boundary conditions forcings.

3. Results

3.1. Spatial Variability of H_s in Realistic Surface Currents Field

Wave–current interactions have been simulated in the Agulhas current from 2014 to 2016. Filtered altimetry data have been studied for the same time frame and all model outputs have been interpolated in time and space on those altimeters tracks. One example of model-satellite comparison is displayed in Figure 1c. Except for the topographically trapped flow patterns, the high-resolution CROCO model is not expected to have current features in the same place as the real features, but it may still have realistic eddy sizes and meander shapes. We will thus compare the statistical properties of modeled and measured H_s.

In particular, we consider the statistical properties of the along-track H_s gradient defined as

$$\nabla H_s = \mid \Delta H_s \; / \; dr \mid, \tag{3}$$

with dr the along-track distance between successive 1 Hz measurements (dr is typically 7 km), and ΔH_s the difference between successive H_s measurements taken 1 s apart. Statistics of ∇H_s have been interpolated on a regular grid with a resolution of 1/8° by 1/8° in longitude and latitude. The mean values are shown in Figure 4, ranging from 0 to 3 cm per km.

A few high values of the H_s gradient right at the coast are clearly visible for the simulation without current. These high values can be explained by partial sheltering caused by headlands, all the large gradients appear in regions of strong current gradients, and specifically in the main Agulhas current, from 29°E 33°S to 17.5°E 39°S. The values of the mean ∇H_s measured in the main Agulhas branch are in the range of 1.5–3 cm/km (Figure 4i) which is remarkably high, and corresponds to the maximum values shown in Figure 1. These persistent maximum gradients are located exactly where the model has the strongest current, and where the largest H_s gradients are also predicted in Figure 4a. This is the well-known region of strong focalization of waves caused by wave refraction over the current (Gutshabash & Lavrenov, 1986; Kudryavtsev et al., 2017; Quilfen & Chapron, 2019). Indeed when propagating against a current that is uniform in the flow direction, waves of a given period and direction can be trapped: when coming from the center of the current toward its edge they turn back toward the center at the location where the current reaches a certain value (Kenyon, 1971). The waves behavior is similar to the propagation of light waves along an optical fiber where light waves are trapped and propagate within a range of specific refraction's index values that depends on their initial incidence angle. Quilfen and Chapron (2019) have demonstrated with ray tracing and assuming the wave action is conserved along the ray, that where waves are trapped, strong ∇H_s are measured.

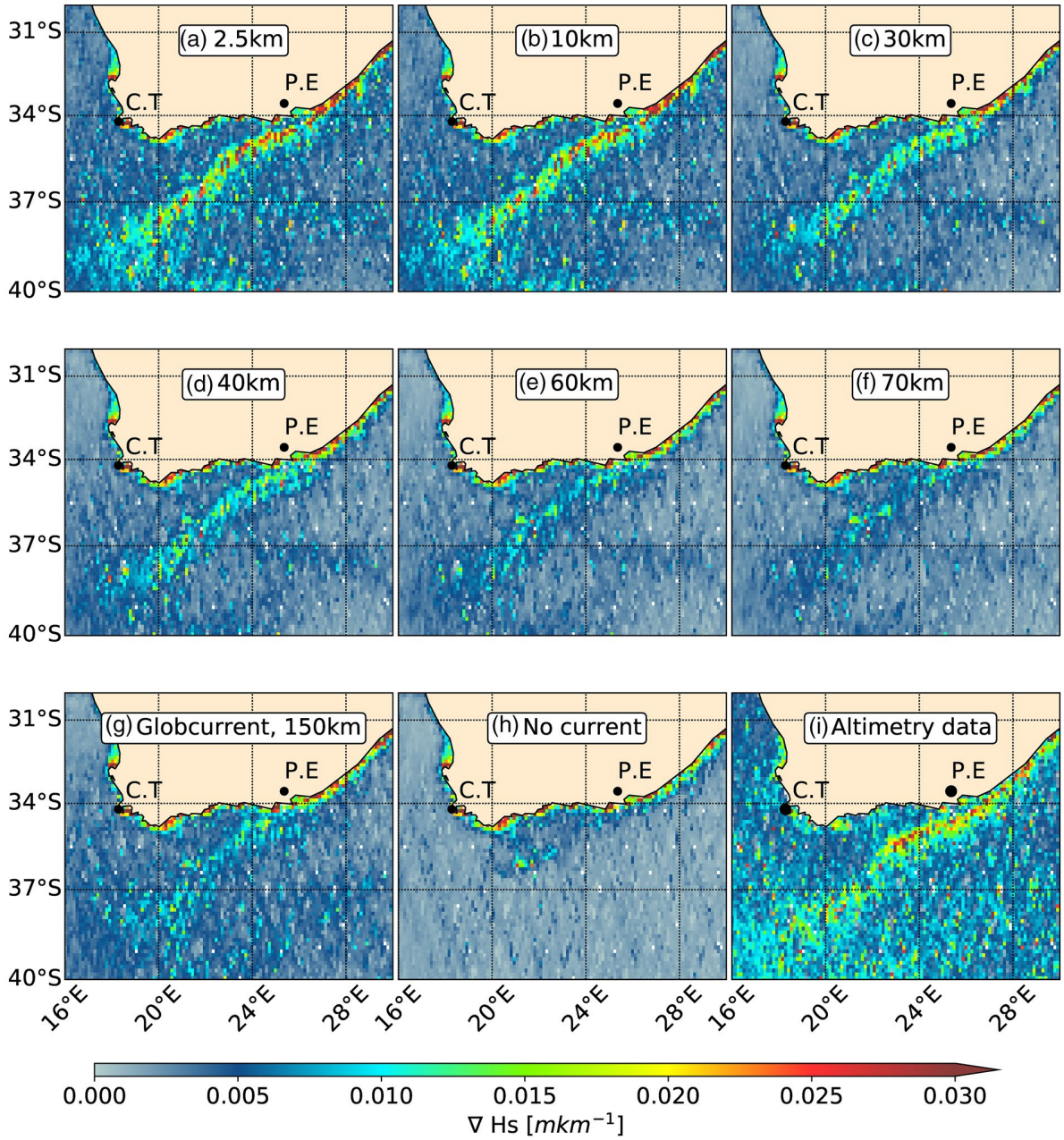

Figure 4. Significant wave height gradient (∇H_s) averaged over the years 2014–2016, from (a–h) model simulations and (i) altimeters data. ∇H_s estimated along satellite tracks are gridded on a regular 1/8° × 1/8° grid. Simulation with the original CROCO surface currents is represented in (a). Simulations forced with filtered surface currents at effective resolutions of 10, 30, 40, 60, and 70 km are displayed in panels (b), (c), (d), (e), and (f), respectively. The simulation with Globcurrent data is shown in (g) and the model result without any surface current forcing is shown in (h). CROCO, Coastal and Regional Ocean COmmunity.

Figure 4 shows that the maximum ∇H_s signal is upstream 26°E, where the main Agulhas current is known to be stable. Downstream of 26°E, the current is bimodal with occasional disturbances known as Natal pulses (Lutjeharms & Roberts, 1998; Paldor & Lutjeharms, 2009).

Around 22°E, the Agulhas current comes off the Agulhas Bank and the current direction veers to the south, which probably explains the lower values of ∇H_s as the current direction is less favorable for trapping the dominant south-westerly waves, resulting in this lower gradient of wave heights. Beyond that point, ∇H_s increases again but it is more spread out in the north-south direction.

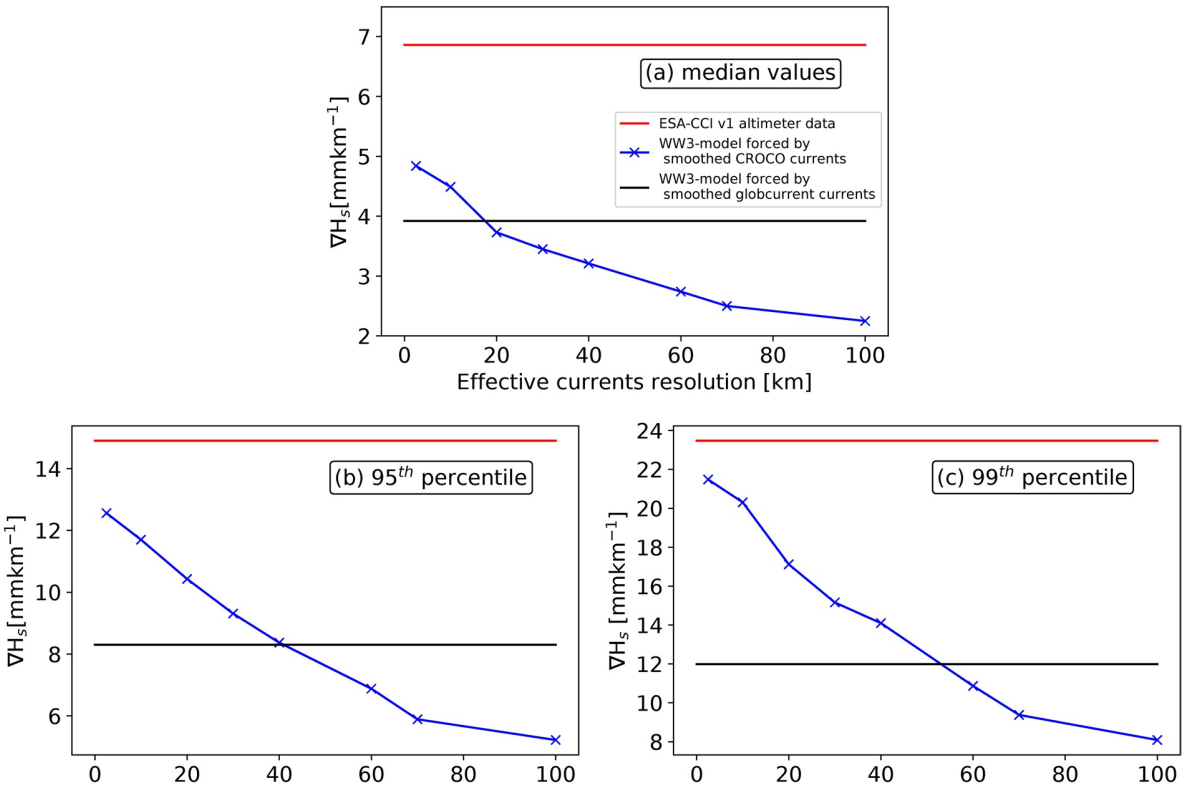

Figure 5. Statistics of the along-track gradients of H_s (∇H_s) averaged over 1/8° grid for different model runs (blue and red lines) and for the satellite altimeter data (black line). (a) Median, (b) 95th percentile, and (c) 99th percentile.

Nowhere does the much coarser and weaker current in the Globcurrent product produces H_s gradients larger than 2 cm/km (Figure 4g). Yet, the Globcurrent product leads to modeled gradients in the retroflexion region, around 38° S, 25 °E, that are similar to those given by the CROCO model, both weaker than observed. ∇H_s in the main Agulhas current are similar for CROCO filtered at 60 km and Globcurrent, as shown in Figure 3 through the H_s field. As the effective current resolution is degraded from 10 to 60 km, the mean H_s gradient progressively vanishes with a particularly clear drop from 60 km (Figure 4e) to 70 km (Figure 4f). The magnitude of the gradients can be quantified by different percentiles, as shown in Figure 5. For the 95th percentile and above, we find that 60% of the H_s gradient is obtained for effective current resolutions of 30 km or less. The uncertainty of the ∇H_s has been estimated from the known uncertainty of the altimeters Hs measurements (see Section 2.1). Assuming that the error over the ∇H_s is uncorrelated (only contaminated by a random noise), we have perturbed the Hs measurements independently with a white noise characterized by an amplitude equal to the RMSE of each satellite missions. The computed standard deviation (not shown here) is very large and disagrees with our numerical model estimations. Hence, the RMSE (estimated only from in situ wave buoy) of the denoised data from the ESA CCI-Sea-States product seems to be overestimated.

3.2. Spectral Analysis

In order to obtain a more quantitative analysis, we perform the same spectral analysis on the model and satellite data. We use overlapping windows following Welch (1967), with the Fourier transform computed after detrending and applying a Hanning window. Results are presented in Figure 6. In order to help with the interpretation, the surface current velocity ($\sqrt{U^2 + V^2}$) was also analyzed along the same tracks. One spectrum is computed for each track. All spectra have been averaged to obtain one averaged spectrum for each numerical simulation for each surface currents forcing field.

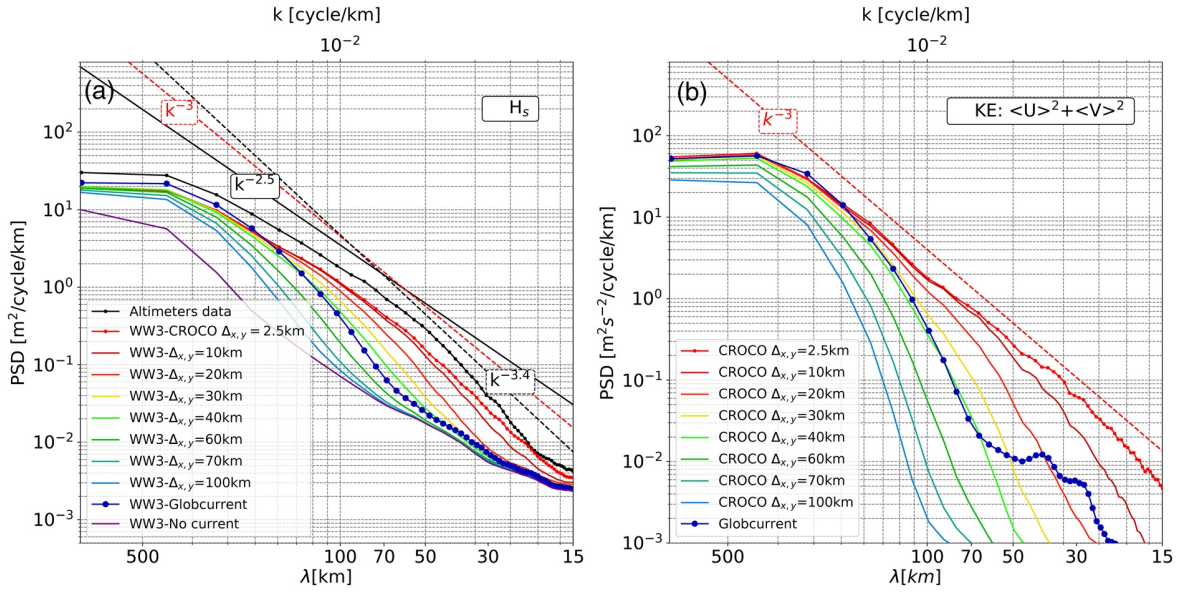

Figure 6. Left panel (a), averaged significant wave height spectra from model and altimetry data. Right panel (b), averaged surface kinetic energy spectra. All spectra have been obtained by averaging all along-track spectra (4,746 tracks) from altimeters measurements (black solid line) and interpolated simulated data (in colors). The associated surface currents resolution are given in the legend. λ is the wavelength.

The H_s spectra (Figure 6a) show that between resolutions of 200 and 30 km, and even down to the smaller resolved scale, the resolution of the surface currents drive the H_s variability. For wavelengths between 50 and 100 km, simulations forced by the Globcurrent surface currents show a H_s variability higher than simulations forced with surface currents filtered at 60, 70, and 100 km, whereas surface currents from Globcurrent have an effective along-track resolution around 150 km. This along-track resolution is consistent with the 150–250 km resolution of SSH gridded altimeter data in the Agulhas region (Ballarotta et al., 2019).

Using a wave model forced by different surface current fields, Figure 6b reveals what was already reported by Ardhuin et al. (2017), that is, the lower the surface currents KE ($<U>^2 + <V>^2$, $<.>^2$ denotes the variable's variance), the lower the H_s spectrum. Surface KE spectrum computed from surface current taken from Globcurrent fields shows a level of variability for wavelengths in the range 50–200 km that is similar to the 40-km filtered current.

For all simulations, the shape of the spectrum of the modeled H_s is very similar to the KE spectrum, and slightly steeper, around $k^{-3.4}$ for H_s compared to $k^{-3.0}$ for the KE spectrum (exponents have been computed through a linear regression) for scales smaller than 100 km. The same behavior was found for realistic simulations in Gulf Stream and Drake Passage (Ardhuin et al., 2017). As the spectral level in the current forcing is reduced, the H_s spectrum is reduced in the same proportion until it reaches a background level. For a wavelength of 100 km, this background level is around 0.08 m^2/cycle/km, which is very close to the variability associated with the wind field in the analysis by Ardhuin et al. (2017). This parallel behavior of the H_s and KE spectra may be due to the dominant balance between propagation and refraction terms in the action balance Equation 1.

4. Discussions and Perspectives

4.1. Surface Current Resolution and Gradients of H_s

In the ocean, surface currents are energetic at mesoscales and submesoscales, with features such as fronts, eddies, and filaments. Waves interact with those features, and refraction explains the spatial redistribution of the wave action density that results in a change of H_s. In the Agulhas system, numerical wave simulations forced with highly resolved surface currents, rich in mesoscale structures, show that the small features and sharp gradients are important for simulating realistic ∇H_s, statistically consistent with filtered altimeter

data (Figure 5). We find that an effective resolution of 30 km, which resolves features with wavelengths larger than 60 km is necessary to reproduce most of the wave height gradients, which can be quantified by its median value or higher percentiles shown in Figure 5. Given that the high-resolution CROCO model that provides our forcing current does not assimilate observations, its features other than the largest scales of the Agulhas current are not expected to be in the right places at the right time, it is difficult to define a wave-gradient based metric that could be used to further validate the CROCO model for different regions or scales.

Quilfen et al. (2018) argued that using a finite-difference numerical wave model to solve the action balance Equation 1 generally underestimate the ∇H_s, showing marked differences between finite differences and ray-tracing solutions. Here, we find that it is the choice of a large-scale current from Globcurrent that explains the relatively weak modeled H_s gradient.

4.2. Directional Resolution in Wave Models

In the limit of a large number of directions and a fine spatial resolution, the solution to the wave action equation obtained here with third-order finite-difference refraction and advection schemes (Leonard, 1991; Tolman, 2002) should be identical to the one obtained with backward ray tracing (Ardhuin & Herbers, 2005; Booij et al., 1999; Longuet-Higgins, 1957; O'Reilly & Guza, 1993). In practice, the number of discrete model directions is limited by the cost in memory storage and computation time, and most wave model implementations use 24–36 directions. Given the importance of refraction in the presence of current gradients (Ardhuin et al., 2012; Holthuijsen & Tolman, 1991), we used 48 directions in the analysis presented above. We examine here the importance of the directional resolution and how the numerical solution is smoothed by the use of a small number of directions. We have thus repeated our simulations (same forcing files and same boundary conditions) different directional resolutions ($\Delta\theta$), using 24 ($\Delta\theta = 15°$), and 180 ($\Delta\theta = 2°$) directions instead of 48 ($\Delta\theta = 7.5°$). The refraction time step Δt_r has been changed in proportion to keep a constant ratio $\Delta t_r/\Delta\theta$. We have further checked than reducing the other time steps had minimal effects on the solution. The spectral analysis described in Section 3.2 has been repeating for those new simulations and presented in Figure 7a. Because the $\Delta\theta = 2°$ simulation is extremely costly, the wave model has been run for 4 months only, from the January 1 to the April 30, 2015. The altimeters track have been extracted for the same time frame and the model outputs have been interpolated on those tracks.

Spectral analysis shows that the model setup with a finer directional resolution ($N_\theta = 48$ instead of 24) has a larger variability of H_s at all scales, with an increase of the Power Spectral density (PSD) by about a factor of 2, similar to what was found for Drake Passage by Ardhuin et al. (2017). In addition, for scales smaller than 100 km, H_s variability is stronger for simulations forced with higher resolution currents. Further refining the directional resolution to 180 directions gives a further increase in H_s variability. When the narrow directional discretization is combined with high-resolution currents, the modeled H_s spectrum is within 30% of the satellite measurements for all scales shorter than 100 km.

A typical example of spatial variability along a transect is shown in Figures 7b and 7c, with a much sharper peak of H_s in the model runs using 180 or 48 directions.

4.3. Influence of Incident Waves Directional Spreading (σ_θ)

We generally expect that a fine directional resolution is most important when the directional wave spectrum is very narrow. In these conditions, wave energy can be focused in a small area, as predicted by the analysis of monochromatic waves with rays traced with parallel directions outside the current region (White & Fornberg, 1998). In contrast, broad wave spectra have focal points in different locations for the different spectral components, which effectively smears the regions of maximum H_s.

In order to quantify that effect in realistic conditions, we have rerun the model with modified boundary conditions. Instead of taking the directional wave spectra $E(f, \theta)$ straight from a global hindcast, we now make these spectra broader or narrower in directions, without changing the spreading along the frequency nor the mean direction at each frequency. The details of the method are given in Appendix A. The conservation of the total variance and mean direction between all original spectra and new spectra has been verified. At each frequency, the original directional spreading has been changed by ±30%. Examples of the resulting

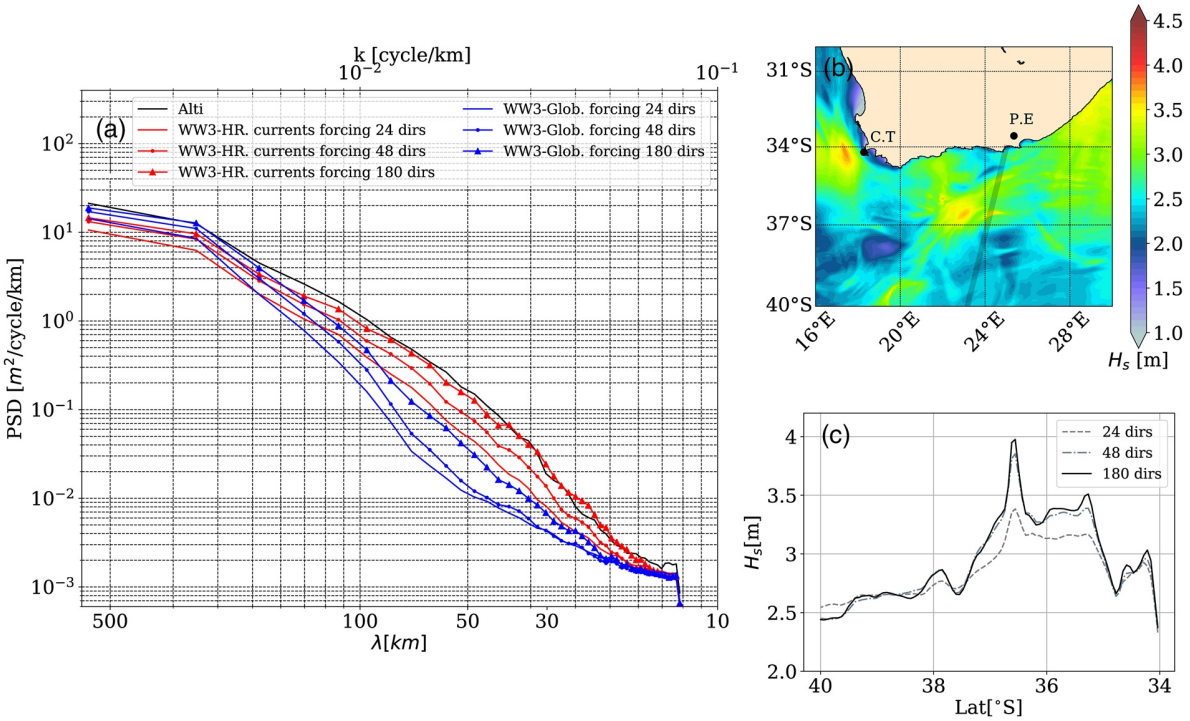

Figure 7. a) Averaged significant wave height spectra for altimeters measurements (in black) and for modeled data (colors). Blue spectra are for modeled wave height forced with surface current from Globcurrent (Glob.) and red spectra for high resolved (HR) CROCO forcing. (b) Instantaneous simulated significant wave height field highly resolved in directions (180 dirs). (c) An example of modeled wave heights interpolated along an altimeter track for different directional resolution, the location of the track is in black line on panel (b). λ is the wavelength. CROCO, Coastal and Regional Ocean COmmunity.

H_s fields are displayed in Figures 8a–8c. Figure 8 illustrates how a decrease of σ_θ induces an increase in the number of small H_s structures and an amplification of structures already existing and vice versa. This is better quantified along a track that is close to the upwave (western) boundary. The left peak at 39.5°S in Figure 8d has a variation of H_s from 3.45 m with a broader spectrum to 3.85 m with a narrower spectrum. This 25% change in wave energy is a typical order of magnitude. Besides the peak, some fluctuations of H_s between 37° and 39°S are much reduced for the broader spectra.

Following the method used previously, we now look at the averaged H_s spectra for each 1-year long simulation, with different boundary conditions. The result shows higher variability, by about 50%, at all scales for incident waves with lower values of the directional spread σ_θ. The shape of the H_s spectra is very similar for all simulations with a steeper slope for wavelengths shorter than 125 km.

Our simulations have confirmed that over a real current system like the Agulhas, the spatial variability is sensitive to the spectral width of the wavefield, and to the numerical resolution used in models with narrower spectra and finer resolution producing stronger gradients. Unfortunately, the directional spread is one of the worst modeled parameters (Stopa et al., 2016). More directional data, such as provided by the SWIM instrument on the China France Ocean Satellite (Hauser et al., 2017), may help design better model parameterizations and can be used for data assimilation with important impact in strong current regions. The performance of data assimilation for directional SWIM data has already been proved in the Southern Ocean, particularly for wave age and H_s (Aouf et al., 2021).

5. Conclusion

Surface currents modify the wavefield in a complex way that is not just local (Ardhuin et al., 2017; Kudryavtsev et al., 2017; White & Fornberg, 1998), creating a spatial pattern of wave properties that can be important for applications and that may reveal properties of the ocean currents that are otherwise difficult to obtain.

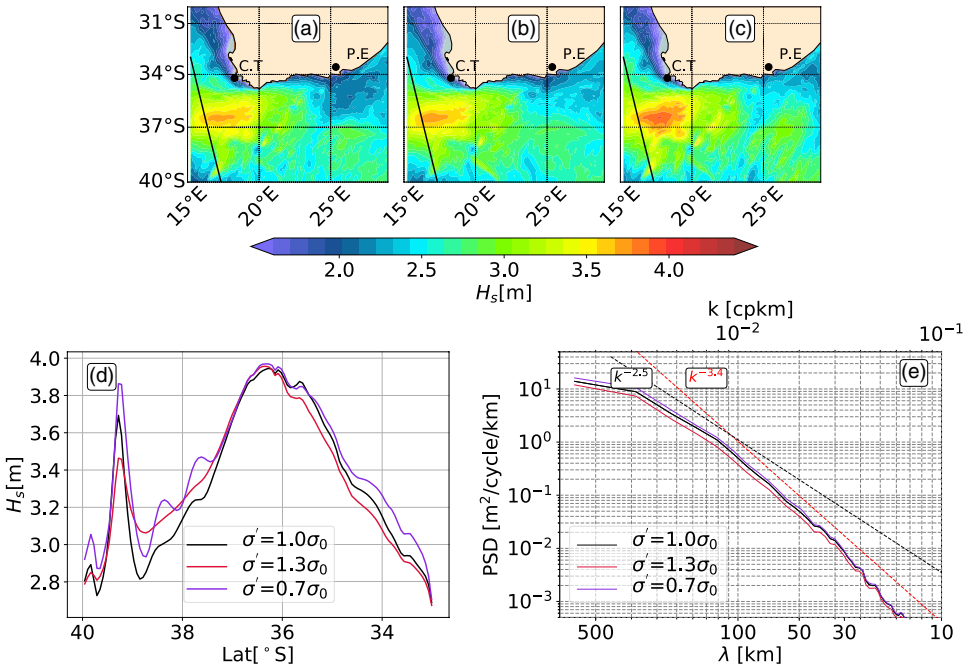

Figure 8. Up figures, two-dimensional significant wave height field snapshot (November 4 00:00 UTC) for (a) the unchanged directional spreading (σ_θ) boundary spectra, (b) the extended σ_θ boundary spectra (+30%), and (c) the reduced σ_θ boundary spectra (−30%). The solid line is the footprint of one altimeter track for the same date, the significant waves height simulated are displayed in (d) for unmodified (black line), extended (red line) and reduced (purple line) σ_θ. (e) The averaged simulated H_s spectra over 1 year for the three simulations.

Large mesoscale current systems such as the Agulhas current are places where particularly strong H_s gradients are found (Lavrenov, 1998; Quilfen & Chapron, 2019). Combining state of the art of wave modeling and novel-filtered altimetry data, we have investigated the factors that lead to these large gradients, and under which conditions they can be reproduced by numerical models. The present work shows that model forced with realistic and high resolved surface currents, statistically consistent with the real upper ocean dynamics and sufficiently discretized in direction, is able to capture sharp significant wave height gradient measured by satellite altimeters. These sharp gradients are much reduced in the results of wave models that are forced by surface currents derived from a combination of mean dynamic topography (Rio et al., 2014) and sea level anomalies derived from these same altimeters that measure the wave heights. This low resolution of satellite-derived currents (Ballarotta et al., 2019; Chelton et al., 2019) is related to the sparse tracks of existing and planned nadir altimeters, but it is also due to the along-track noise level in the processing used today for altimeter data.

Besides the structures of the forcing current, the numerical implementations of wave models will typically miss part of the true gradients of the wavefield due to numerical diffusion. Here, we find that high spectral resolutions, using 48 or more directions systematically produces finer details, in a way that is statistically consistent with altimeter data. Thanks to wave simulations, we have shown that this effect is most pronounced for waves coming from the Southern Ocean with a small directional spreading. Indeed, simulated waves in the Agulhas region show sharper wave height spatial structures when waves spectra forcing at the boundaries are narrow, for identical surface currents in the model parameterization.

Reproducing realistic wave height gradients is important not only for marine safety but also for studying upper ocean processes driven by wave breaking. It is also a necessity to capture sea states biases in ocean remote sensing of wide range of variables, from sea level (Minster et al., 1991) to sea surface salinity (Reul & Chapron, 2003) or surface currents (Ardhuin et al., 2018; Marié et al., 2020).

We found that the gradients of significant wave heights can be quantified in satellite altimeter data in a way that is useful to make a statement on the quality of the ocean currents, in the context of numerical wave

modeling. We can imagine that many future developments will further constrain the currents by using (1) more information about the wavefield than just the wave height, (2) measurements over a broader area than the narrow pencil beam of nadir altimeters, and (3) different analyses and techniques. For the first type of future developments, we can mention the use of directional measurements provided by the China France Ocean Satellite (Hauser et al., 2017), launched in October 2018 and the understanding of directional spectral evolution in currents provided by Villas Bôas and Young (2020). For the second aspect, we are expecting a wealth of data, including wave measurements, from the soon-to-be-launched Surface Water Ocean Topography mission (Morrow et al., 2019). As for the third aspect, it can involve the use of different metrics. For example, Villas Bôas et al. (2020) showed that the magnitude of the wave height gradient was also related to the slope of the current KE spectrum, which is an interesting quantity for diagnosing the upper ocean dynamics (Le Traon et al., 2008).

Appendix A: Defining New Waves Spectrum With a Modified Directional Spreading

We force the wave model at its boundaries with bi-dimensional wave spectra from a global hindcast forced without current, $E(f, \theta)$ with f the wave intrinsic frequency and θ the direction where energy is propagating. Two-dimensional wave spectrum can be divided in an omnidirectional spectrum $E(f)$ and a directional shape function $D(f, \theta)$ defined as

$$D(f,\theta) = \frac{E(f,\theta)}{E(f)} \tag{A1}$$

such that

$$\int_0^{2\pi} D(f,\theta)\mathrm{d}\theta = 1. \tag{A2}$$

Our modification of the boundary conditions is done by a modification of $D(f, \theta)$, without changing $E(f)$.

There can be an infinite number of ways to modify $D(f, \theta)$. Here, first compute the directional moments $a_1(f)$, $b_1(f)$, $a_2(f)$, and $b_2(f)$ are computed from $D(f, \theta)$ following O'Reilly et al. (1996). These are the discrete Fourier coefficients of the directional distribution $D(f, \theta)$.

From these moments, the following directional parameters have been computed.

$$\begin{cases} \theta_1 = \arctan(b_1 \,/\, a_1) & \text{(A3a)} \\ \theta_2 = \frac{1}{2}\arctan(b_2 \,/\, a_2) & \text{(A3b)} \\ \sigma_1 = 2\left(1 - \sqrt{a_1^2 + b_1^2}\right) & \text{(A3c)} \\ \sigma_2 = \frac{1}{2}\left(1 - \sqrt{a_2^2 + b_2^2}\right) & \text{(A3d)} \end{cases}$$

Both directional spreads $\sigma_1(f)$ and $\sigma_2(f)$ are multiplied by a parameter α, giving $\sigma_1'(f)$ and $\sigma_2'(f)$.

From the modified parameters, a new directional distribution $D'(f, \theta)$ is estimated using the Maximized Entropy Method (Lygre & Krogstad, 1986).

Data Availability Statement

Filtered altimeter data are from the European Space Agency Climate Change Initiative Sea State v1 data set and are freely available on the ESA CCI website (http://cci.esa.int/data) at ftp://anon-ftp.ceda.ac.uk/neodc/esacci/sea_state/data/v1.1_release. Surface currents derived from altimeters (Globcurrent product) are available in NetCDF format at ftp://ftp.ifremer.fr/ifremer/ww3/FORCING/GLOBCURGEO/NC4/. Both fully resolved currents and filtered currents are available at ftp://ftp.ifremer.fr/ifremer/ww3/FORCING/CROCO/CROCO_AGULHAS/NC4/in NetCDF format.

Acknowledgments
G. M. is supported by Centre National de l'Etude Spatiale (CNES) and by the Region Bretagne through l'Allocations de recherche doctorale (ARED). The surface currents simulation from CROCO fully resolved were kindly provided by P. Penven (WOES, Western Indian Ocean Energy Sink) and performed as part of the GENCI/IDRIS grant A0040107630. Authors also thanks M. Accensi for his contribution to the development and maintenance of the WAVEWATCH III model.

References

Aouf, L., Hauser, D., Chapron, B., Toffoli, A., Tourrain, C., & Peureux, C. (2021). New directional wave satellite observations: Towards improved wave forecasts and climate description in Southern Ocean. *Geophysical Research Letters*, *48*. https://doi.org/10.1029/2020GL091187

Ardhuin, F., Aksenov, Y., Benetazzo, A., Bertino, L., Brandt, P., Caubet, E., & Xie, J. (2018). Measuring currents, ice drift, and waves from space: The sea surface kinematics multiscale monitoring (SKIM) concept. *Ocean Science*, *14*, 337–354. https://doi.org/10.5194/os-2017-65

Ardhuin, F., Dumas, F., Bennis, A.-C., Roland, A., Sentchev, A., Forget, P., & Benoit, M. (2012). Numerical wave modeling in conditions with strong currents: Dissipation, refraction and relative wind. *Journal of Physical Oceanography*, *42*, 2101–2120.

Ardhuin, F., & Herbers, T. H. C. (2005). Numerical and physical diffusion: Can wave prediction models resolve directional spread?*Journal of Atmospheric and Oceanic Technology*, *22*(7), 886–895. https://doi.org/10.1175/JTECH1723.1

Ardhuin, F., Rascle, N., Chapron, B., Gula, J., Molemaker, J., Gille, S. T., & Rocha, C. (2017). Small scale currents have large effects on wind wave heights. *Journal of Geophysical Research*, *122*, 4500–4517. https://doi.org/10.1002/2016JC012413

Ardhuin, F., Stopa, J. E., Chapron, B., Collard, F., Husson, R., Jensen, R. E., & Young, I. (2019). Observing sea states. *Frontiers in Marine Science*, *6*, 124. https://doi.org/10.3389/fmars.2019.00124

Ballarotta, M., Ubelmann, C., Pujol, M.-I., Taburet, G., Fournier, F., Legeais, J.-F., & Picot, N. (2019). On the resolutions of ocean altimetry maps. *Ocean Science Discussions*, *15*, 1091–1109. https://doi.org/10.5194/os-2018-156

Beal, L. M., De Ruijter, W. P. M., Biastoch, A., Zahn, R., Cronin, M., Hermes, J. et al. (2011). On the role of the Agulhas system in ocean circulation and climate. *Nature*, *472*, 429–436. https://doi.org/10.1038/nature09983

Booij, N., Ris, R. C., & Holthuijsen, L. H. (1999). A third-generation wave model for coastal regions. 1. Model description and validation. *Journal of Geophysical Research*, *104*(C4), 7649–7666.

Chelton, D. B., Schlax, M. G., Samelson, R. M., Farrar, J. T., Molemaker, M. J., McWilliams, J. C., & Gula, J. (2019). Prospects for future satellite estimation of small-scale variability of ocean surface velocity and vorticity. *Progress in Oceanography*, *173*, 256–350. https://doi.org/10.1016/j.pocean.2018.10.012

D'Asaro, E. A. (2014). Turbulence in the upper-ocean mixed layer. *Annual Review of Marine Science*, *6*, 101–115. https://doi.org/10.1146/annurev-marine-010213-135138

Debreu, L., Marchesiello, P., Penven, P., & Cambon, G. (2012). Two-way nesting in split-explicit ocean models: Algorithms, implementation and validation. *Ocean Modelling*, *49*, 1–21. https://doi.org/10.1016/j.ocemod.2012.03.003

Dibarboure, G., Boy, F., Desjonqueres, J. D., Labroue, S., Lasne, Y., Picot, N., & Thibaut, P. (2014). Investigating short-wavelength correlated errors on low-resolution mode altimetry. *Journal of Atmospheric and Oceanic Technology*, *31*, 1337–1362. https://doi.org/10.1175/JTECH-D-13-00081.1

Dodet, G., Piolle, J.-F., Quilfen, Y., Abdalla, S., Accensi, M., Ardhuin, F., & Donlon, C. (2020). The sea state CCI dataset v1: Towards a sea state climate data record based on satellite observations. *Earth System Science Data*, *12*, 1929–1951. https://doi.org/10.5194/essd-12-1929-2020

Gula, J., Molemaker, M. J., & Mcwilliams, J. C. (2015). Gulf Stream dynamics along the southeastern U.S. seaboard. *Journal of Physical Oceanography*, *45*, 690–715.

Gutshabash, Y. S., & Lavrenov, I. V. (1986). Swell transformation in the cape Agulhas current. *Izvestiya, Atmospheric and Oceanic Physics*, *22*(6), 494–497.

Hauser, D., Tison, C., Amiot, T., Delaye, L., Corcoral, N., & Castillan, P. (2017). SWIM: The first spaceborne wave scatterometer. *IEEE Transactions on Geoscience and Remote Sensing*, *55*(5), 3000–3014.

Holthuijsen, L. H., & Tolman, H. L. (1991). Effects of the Gulf Stream on ocean waves. *Journal of Geophysical Research*, *96*(C7), 12755–12771.

Huang, N. E., Shen, Z., Long, S. R., Wu, M. C., Shih, H. H., Zheng, Q., & Liu, H. H. (1998). The empirical mode decomposition and the Hilbert spectrum for nonlinear and non-stationary time series analysis. *Proceedings of the Royal Society of London*, *454*, 903–995.

Kenyon, K. E. (1971). Wave refraction in ocean current. *Deep Sea Research and Oceanographic Abstracts*, *18*, 1023–1034.

Komen, G. J., Cavaleri, L., Donelan, M., Hasselmann, K., Hasselmann, S., & Janssen, P. A. E. M. (1994). *Dynamics and modeling of ocean waves*. Cambridge: Cambridge University Press.

Kudryavtsev, V., Yurovskaya, M., Chapron, B., Collard, F., & Donlon, C. (2017). Sun glitter imagery of surface waves. Part 2: Waves transformation on ocean currents. *Journal of Geophysical Research*, *122*, 1384–1399. https://doi.org/10.1002/2016JC012426

Landau, L. D., & Lifshitz, E. M. (1960). *Mechanics*. Reading, MA: Pergamon Press Addison-Wesley.

Lavrenov, I. V. (1998). The wave energy concentration at the Agulhas Current off South Africa. *Natural Hazards*, *17*, 117–127.

Leonard, B. P. (1991). The ULTIMATE conservative difference scheme applied to unsteady one-dimensional advection. *Computational Methods in Applied Mechanical Engineering*, *88*, 17–74.

Le Traon, P.-Y., Klein, P., Hua, B. L., & Dibarboure, G. (2008). Do altimeter wavenumber spectra agree with the interior or surface quasigeostrophic theory?*Journal of Physical Oceanography*, *38*, 1137–1142.

Longuet-Higgins, M. S. (1957). On the transformation of a continuous spectrum by refraction. *Proceedings of the Cambridge Philosophical Society*, *53*(1), 226–229.

Lutjeharms, J. R. E., & Roberts, H. (1998). The Natal pulse: An extreme transient on the Agulhas current. *Journal of Geophysical Research*, *93*(C1), 631–645.

Lygre, A., & Krogstad, H. E. (1986). Maximum entropy estimation of the directional distribution in ocean wave spectra. *Journal of Physical Oceanography*, *16*, 2052–2060.

Marié, L., Collard, F., Nouguier, F., Pineau-Guillou, L., Hauser, D., Boy, F., & Ardhuin, F. (2020). Measuring ocean surface velocities with the KuROS airborne near-nadir Doppler radar: A multi-scale analysis in preparation of the skim mission. *Ocean Science*, *16*, 1399–1429. https://doi.org/10.5194/os-16-1399-2020

McWilliams, J. C. (2016). Submesoscale currents in the ocean. *Proceedings of the Royal Society of London. Series A, Mathematical and Physical Sciences*, *427*, 20160117. https://doi.org/10.1098/rspa.2016.0117

Minster, J. F., Jourdan, D., Boissier, C., & Midol-Monnet, P. (1991). Estimation of the sea-state bias in radar altimeter Geosat data from examination of frontal systems. *Journal of Atmospheric and Oceanic Technology*, *9*, 174–187.

Morrow, R., Fu, L.-L., Ardhuin, F., Benkiran, M., Chapron, B., Cosme, E., & Zaron, E. D. (2019). Global observations of fine-scale ocean surface topography with the Surface Water and Ocean Topography (SWOT) mission. *Frontiers in Marine Science*, *6*, 232. https://doi.org/10.3389/fmars.2019.00232

O'Reilly, W. C., & Guza, R. T. (1993). A comparison of two spectral wave models in the Southern California Bight. *Coastal Engineering*, *19*, 263–282.

O'Reilly, W. C., Herbers, T. H. C., Seymour, R. J., & Guza, R. T. (1996). A comparison of directional buoy and fixed platform measurements of Pacific swell. *Journal of Atmospheric and Oceanic Technology*, *13*, 231–238.
Osborne, A. R., & Burch, T. L. (1980). Internal solitons in the Andaman Sea. *Science*, *208*(4443), 451–460.
Paldor, N., & Lutjeharms, J. R. E. (2009). Why is the stability of the Agulhas current geographically bi-modal. *Geophysical Research Letters*, *36*, L14604. https://doi.org/10.1029/2009GL038445
Phillips, O. M. (1977). *The dynamics of the upper ocean* (336 pp.). London: Cambridge University Press.
Phillips, O. M. (1984). On the response of short ocean wave components at a fixed wavenumber to ocean current variations. *Journal of Physical Oceanography*, *14*, 1425–1433. https://doi.org/10.1175/1520-0485(1984)014%3C1425:OTROSO%3E2.0.CO;2
Quilfen, Y., & Chapron, B. (2019). Ocean surface wave–current signatures from satellite altimeter measurements. *Geophysical Research Letters*, *216*, 253–261. https://doi.org/10.1029/2018GL081029
Quilfen, Y., Yurovskaya, M., Chapron, B., & Ardhuin, F. (2018). Storm waves sharpening in the Agulhas current: Satellite observations and modeling. *Remote Sensing of Environment*, *216*, 561–571. https://doi.org/10.1016/j.rse.2018.07.020
Reul, N., & Chapron, B. (2003). A model of sea-foam thickness distribution for passive microwave remote sensing applications. *Journal of Geophysical Research*, *108*(C10), 3321. https://doi.org/10.1029/2003JC001887
Rio, M.-H., Mulet, S., & Picot, N. (2014). Beyond GOCE for the ocean circulation estimate: Synergetic use of altimetry, gravimetry, and in situ data provides new insight into geostrophic and Ekman currents. *Geophysical Research Letters*, *41*, 8918–8925. https://doi.org/10.1002/2014GL061773
Sandwell, D. T., Müller, R. D., Smith, W. H. F., Garcia, E., & Francis, R. (2014). New global marine gravity model from CryoSat-2 and Jason-1 reveals buried tectonic structure. *Science*, *346*, 65–67. https://doi.org/10.1126/science.1258213
Stopa, J. E., Ardhuin, F., Bababin, A., & Zieger, S. (2016). Comparison and validation of physical wave parameterizations in spectral wave models. *Ocean Modelling*, *103*, 2–17. https://doi.org/10.1016/j.ocemod.2015.09.003
Tedesco, P., Gula, J., Mnesguen, C., Penven, P., & Krug, M. (2019). Generation of submesoscale frontal eddies in the Agulhas current. *Journal of Geophysical Research*, *124*, 7606–7625. https://doi.org/10.1029/2019JC015229
The WAVEWATCH III® Development Group. (2016). *User manual and system documentation of WAVEWATCH III® version 5.16* (Tech. Note No. 329) (326 pp. + Appendices). College Park, MD: NOAA/NWS/NCEP/MMAB.
Tolman, H. L. (1992). Effects of numerics on the physics in a third-generation wind-wave model. *Journal of Physical Oceanography*, *22*, 1095–1111. https://doi.org/10.1175/1520-0485(1992)022<1095:EONOTP>2.0.CO;2
Tolman, H. L. (2002). Limiters in third-generation wind wave models. *Global Atmosphere and Ocean System*, *8*, 67–83.
Tolman, H. L., & Booij, N. (1998). Modeling wind waves using wavenumber-direction spectra and a variable wavenumber grid. *Global Atmosphere and Ocean System*, *6*, 295–309.
Villas Bôas, A. B., Ardhuin, F., Gommenginger, C., Rodriguez, E., Gille, S. T., Cornuelle, B. D., & Tsamados, M. (2019). Integrated observations and modeling of winds, currents, and waves: Requirements and challenges for the next decade. *Frontiers in Marine Science*, *6*, 425. https://doi.org/10.3389/fmars.2019.00425
Villas Bôas, A. B., Cornuelle, B. D., Mazloff, M. R., Gille, S. T., & Ardhuin, F. (2020). Wave–current interactions at meso- and submesoscales: Insights from idealized numerical simulations. *Journal of Physical Oceanography*, *50*(12), 3483–3500. https://doi.org/10.1002/2016JC012413
Villas Bôas, A. B., & Young, W. R. (2020). Integrated observations and modeling of winds, currents, and waves: Requirements and challenges for the next decade. *Journal of Fluid Mechanics*, *890*, R3. https://doi.org/10.1017/jfm.2020.116
Welch, P. D. (1967). The use of fast Fourier transform for the estimation of power spectra: A method based on time averaging over short, modified periodograms. *IEEE Transactions on Audio and Electroacoustics*, *15*(2), 70–73.
White, B. S. (1999). Wave action on currents with vorticity. *Journal of Fluid Mechanics*, *386*, 329–344.
White, B. S., & Fornberg, B. (1998). On the chance of freak waves at sea. *Journal of Fluid Mechanics*, *355*, 113–138.
Young, I. R. (1999). *Wind generated ocean waves*. Oxford: Elsevier Science.

4.3 Further discussions

∇H_s are closely correlated to the nature and the intensity of the underlying current at the mesoscale range ($\mathcal{O}$(100-10) km) (Ardhuin et al., 2017; Romero et al., 2020; Villas Bôas et al., 2020), it has been confirmed by the paper of Marechal and Ardhuin (2021) with both data and numerical results.

4.3.1 Validation of current models from ∇H_s measurements

Marechal and Ardhuin (2021) have shown that realistic ∇H_s can be simulated if surface currents are sufficiently resolved in space and wave models are sufficiently resolved in direction. We propose to apply this result to validate (or not) surface currents from realistic current simulations through the simulations of ∇H_s. Based on the same numerical framework described in Marechal and Ardhuin (2021), we simulate waves in the Agulhas current regions with surface currents from Mercator model resolved at 10 km (available at: `https://marine.copernicus.eu`), MITgcm llc4320 simulation (Rocha et al., 2016a) resolved at 1.5 km and the fully resolved current from CROCO simulation resolved at 2.5 km (studied in Marechal and Ardhuin (2021)). We are basing our validation by comparing the average ∇H_s field obtained from 3-years of wave simulations with the same three years of altimeter data. One can notice that only the averaged phase and intensity of the current can be validated.

The ∇H_s field highlights the presence of the main Agulhas current system flowing southeastward (Fig.4.2). This branch emerges the most from the background signal because of its intensity and its stability over time. Simulation forced with the CROCO currents shows ∇H_s similar to the one measured by the altimeters (results showed in Marechal and Ardhuin (2021)). Simulation forced by MERCATOR model shows ∇H_s much weaker than ∇H_s provided by altimeters. Between 20°E and 22°E, the tail of the Agulhas current is almost drowned in the background signal. Simulation forced with currents from MITgcm model, albeit highly spatially resolved ($\sim$ 1 km), does not reproduce the sharp ∇H_s as well as simulations forced with current from CROCO model. Also the elbow of the main Agulhas branch at 23°E, 36.5°S is better reproduced by simulations forced with CROCO current. Indeed, simulations forced with MERCATOR and MITgcm model reveal a signal downstream from the Agulhas elbow with a sharper slope toward the south than altimeter data.

Altimeter data represent the amplest part of satellite records in number, space coverage and in duration of measurements (Ardhuin et al., 2019b). Thanks to the new filtered altimeter data, short scale H_s spatial variability ($<$150 km) can be captured. This section is one proposition to validate the averaged statistics of the current at the mesoscale range and therefore their associated flux which impacts the regulation of the world's climate and the ecosystem dynamic. It is important to note that because the refraction is the main process that induces sharp ∇H_s, the direction between waves and current is also a key parameter. So, the ∇H_s computed from wave model would depend both on the effective resolution of the current and the direction of the simulated flow. This remark can explain why MITgcm and MERCATOR oceanic models yielded similar ∇H_s, although the resolution of the current is strongly coarser for MERCATOR oceanic model.

4.3.2 Writing ∇H_s as a function of ∇U

Villas Bôas et al. (2020) (hereinafter VB20) have shown numerically, in an idealized and numerical framework that in both synthetic and realistic current fields (in the Coastal California Current), that the vorticity component of the flow is the main component that induces the formation of regional ∇H_s in opposition to the divergent component.

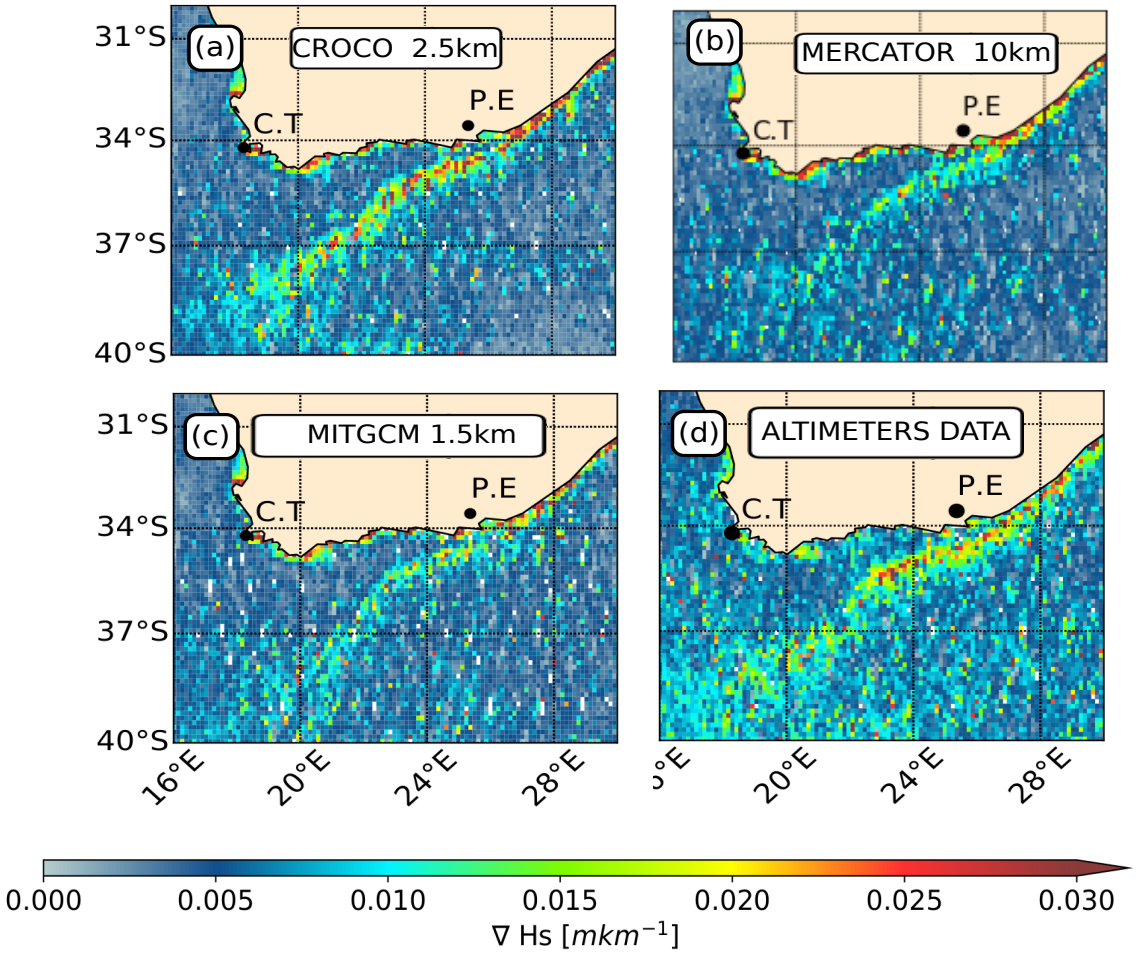

Figure 4.2: Panel (a) shows the simulated average significant wave height gradients in the Agulhas current region with current forcing from CROCO oceanic model. Idem for panel (b) but for current forcing from MERCATOR oceanic model. Idem for panel (c) but for MITgcm oceanic model. Panel (d) shows the significant wave height gradients measured by the filtered altimeters data from the CCI-SeaStates product (Dodet et al., 2020).

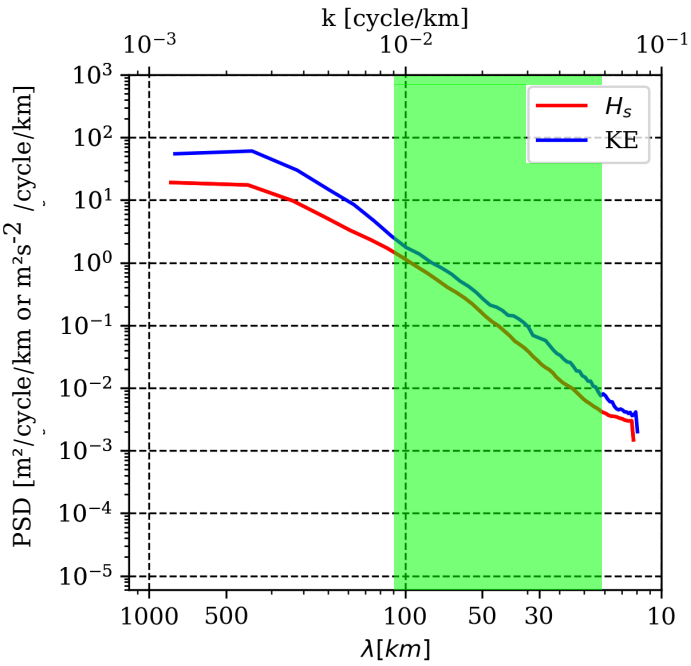

Figure 4.3: Average significant wave height spectrum (in red) and Kinetic Energy spectrum (in blue) from wave simulations in the Agulhas current region. The green area delimit the 116 km and 15 km intervals where variances have been integrated for Eq.4.2

We wanted to know if this result can be extended in other current regime as great boundary current (here the Agulhas current).

We rewrite the Eq. (3.3) of chapter 3 to have the same equation of Eq.15 of (VB20).

$$\nabla Hs_{rms} \sim \frac{2\nabla U_{rms}\langle H_s\rangle}{C_g}. \tag{4.1}$$

The Eq. (3.3) is rewritten in the Fourier space which yields,

$$\sqrt{\int_{k1}^{k2} k^{*2} PSD_{Hs}(k^*)dk^*} \sim \frac{2}{C_g}\sqrt{\int_{k1}^{k2} k^{*2} PSD_{KE}(k^*)dk^*}\langle H_s\rangle \tag{4.2}$$

$\mathrm{PSD}_{Hs}(k^*)$ and $\mathrm{PSD}_{KE}(k^*)$ are the one-dimensional power spectral density of H_s and the surface current kinetic energy. k1 and k2 are the spatial scale where surface currents have strong effects on the H_s, they are given below. $\langle H_s\rangle$ is the spatially averaged significant wave height where the PSD_{KE} and PSD_{Hs} have been computed. k^* is the spatial frequency (wavenumber) yielded by the spectral analysis. Here one can see a clear proportionality of the two spectra at the mesoscale range already discussed in Ardhuin et al. (2017); Villas Bôas et al. (2020); Marechal and Ardhuin (2021). An example of averaged spectra is given in Fig.4.3, the spectra have been obtained following the same method of Marechal and Ardhuin (2021).

4.3.3 Application in the Agulhas current region: is the vorticity of the flow the main contributor of sharp ∇H_s formation?

Here we propose the same study performed by VB20 but in the Agulhas current. The present framework is considered as more realistic than VB20 because:

- incident waves are from realistic spectra from global simulation (not narrow wave spectra Gaussian in frequency, different than chapter 1 and 2.),
- waves shorter than 7 s period are taken into account (wind sea contribution in the wave spectrum),
- source and sink of wave energy are activated (wind input, dissipation, nonlinear wave-wave interactions),
- currents are from realistic regional oceanic simulations.

Let us note that the Eq.(4.1) is based on the assumption that source terms are not activated, it is possible that the right hand side of the equation solved by the WAVEWATCH-III framework, (Eq.(1.21)) has a contribution of local ∇H_s. As well as in VB20, we applied a Helmholtz's decomposition on the current field to separate rotational and divergent components of the surface current. Thus, flow is decomposed into a purely divergent/strain (U_ϕ) and a purely rotational/shear component (U_ψ),

$$\mathbf{U}_{tot} = \mathbf{u}_\phi + \mathbf{u}_\psi. \tag{4.3}$$

The Helmotz's decomposition has been applied on the fully resolved CROCO surface currents (see section 2.3 of Marechal and Ardhuin (2021)). This decomposition is possible because the surface current velocity field is considered as sufficiently smooth. Please note that each term on the right-hand side of Eq. (4.3) has a zonal and a meridional component (u, v). We have rerun our wave model with the same model set-up of Marechal and Ardhuin (2021), the difference is, the surface current forcing has been edited to force the wave model by purely divergent surface currents, on the one hand, and by purely rotational current on the other hand. A snapshot of instantaneous surface current velocity fields is given in Fig.(4.4). The main difference between VB20 is that the mean kinetic energy of the flow in the Agulhas current is not the same for the divergent and the rotational component. One can see that the current velocity for the divergent component does not exceed 0.5m.s^{-1} whereas the rotational component reaches 2.5m.s^{-1} in the most energetic area of the Agulhas current. In terms of H_s, simulation forced with purely divergent do not captured the regional ∇H_s presented in (Marechal and Ardhuin, 2021). The simulation forced with purely divergent flow shows H_s field similar to a simulation forced without current. As current is considered as statistically realistic, in the Agulhas current the contribution of the divergent component on H_s variability is negligible, it confirms the results of VB20.

As done in VB20, we verified the equality between the rms of the normalized ∇U and the rms of the ∇H_s, in the Agulhas current region (Eq.(4.1). Fig.4.4 shows that Agulhas current is principally rotational in the mesoscale range . To obtain the two PSD in Eq.4.1 we performed a two-dimensional analysis through a 2D discrete Fast Fourier Transform of H_s and surface current fields. VB20 and chapter 3 showed, in an idealized framework, that the regional ∇H_s induced by surface currents have patterns oriented in the same direction as the initial direction of the waves. Contrary to VB20, where the incident wave directions were controlled, waves are propagating in the Agulhas from all the boundaries with many incidence directions. To be the most consistent with VB20's works we re-project the H_s field such that the mean wave direction is aligned with the x-axis (toward the east). 2D H_s and KE spectra have been integrated along their respective first dimension which yields one dimensional spectrum for

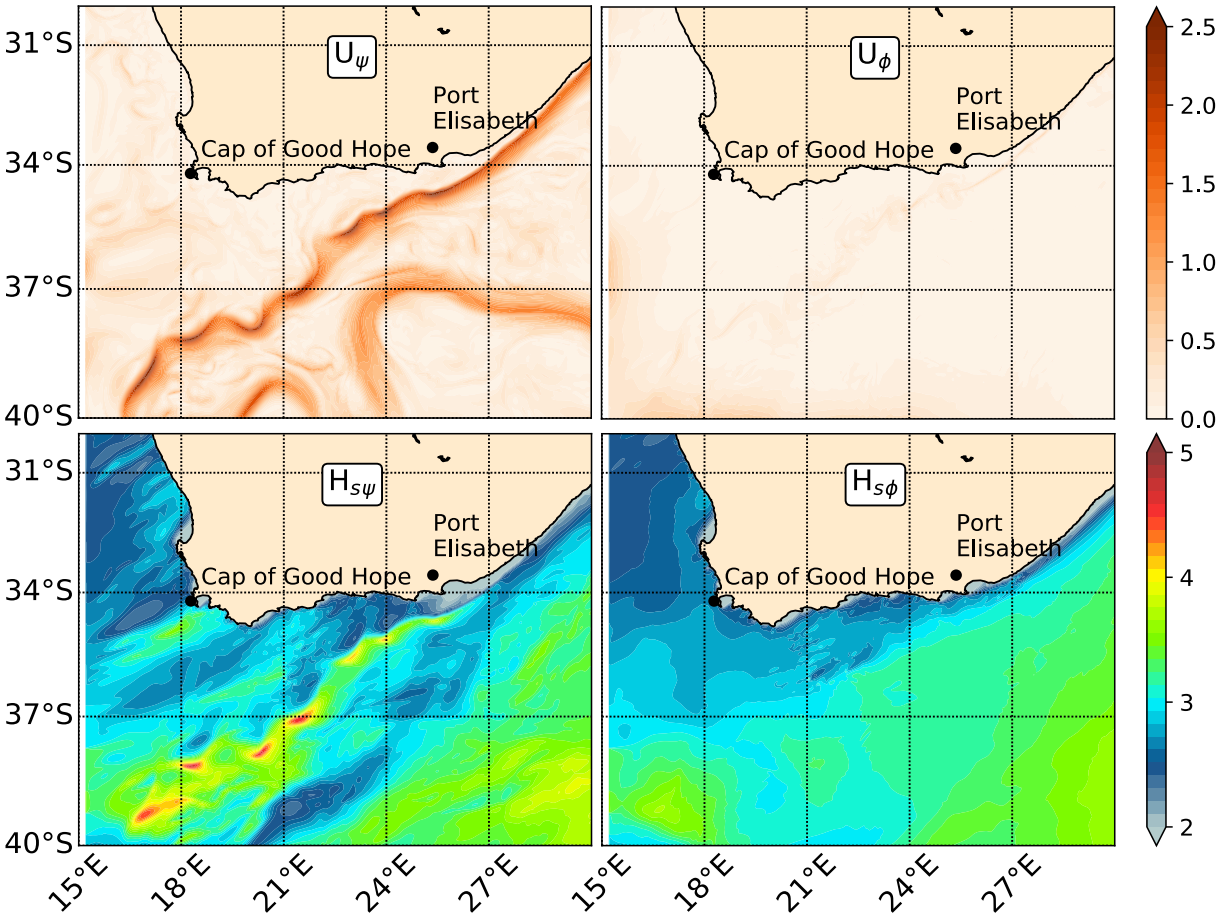

Figure 4.4: Top panels: instantaneous surface currents velocity fields for the purely rotational component (U_ψ) and divergent component (U_ϕ). Bottom panels: instantaneous significant wave height simulated fields with current forcing purely rotational ($H_{s\psi}$) and purely divergent (($H_{s\phi}$).

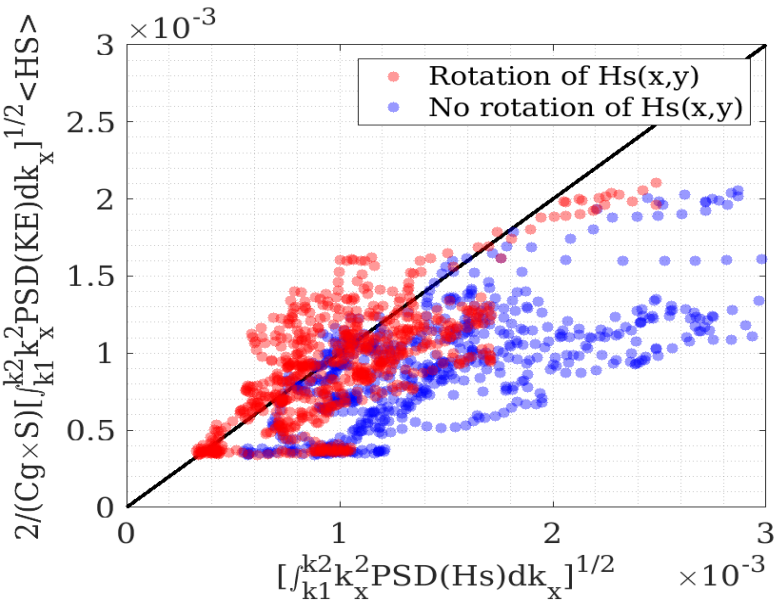

Figure 4.5: Scatter plot of the right-hand side and the left-hand side of Eq.4.2. Red dots are for 2D-H_s field rotated such that waves and x-axis are aligned. Blue dots are for unrotated fields. One dot represents one numerical output throughout September 2015.

each variable. The two PSD (for one instantaneous output) have been integrated between 2π/160 km and 2π/15 km (mesoscale range, with a slight part in the submesoscale range highlighted in green in Fig.4.3) and the resulting values have been stored. The spectral analysis has been performed on numerical results throughout September 2015. The right-hand side and the left-hand side of Eq.(4.2) have been plotted in Fig.4.5 both for rotated and unrotated H_s fields. One can see that under the same framework of VB20, ∇H_s and normalized ∇U are proportional for purely solenoidal flow (Fig.4.5). The rotation of $\mathrm{H}_s(x, y)$ significantly improves the proportionality between the two gradients.

Thanks to a Helmotz decomposition of the surface current, we have shown that the results proposed in VB20 are verified in the Agulhas current region. The main difference between the present and VB20's studies is that we do not have control on the surface KE. In the Agulhas current, the divergent component of the surface currents is strongly weaker than the rotational component. Snapshot of H_s field forced with purely divergent flow does not show ∇H_s in the mesoscale range (Fig.4.4). Let us note that the spreading around the one-to-one line of the red scatter dots in Fig.4.5a is much larger than the spreading shown in VB20. Which differences with respect to VB20's studies (enunciated in the beginning of the section) could explain this spreading? Is it due to the contribution of the source's terms, the wind seas ? Thanks to the results given in Appendix 2, it would seem that non-linear wave-wave interactions have an effect on the intensity of the ∇H_s for incident waves generated from a sufficiently wide frequency spectrum. It could be interesting to verify this in the Agulhas current.

4.3.4 Current effects on higher moments of the wave spectrum

Until now we have only focused on wave parameters computed from the 0^{th} moment of wave spectrum (H_s) or its first negative moment ($\mathrm{T}_{m0,-1}$), i.e., parameters computed from the integral of the wave spectrum $\mathrm{E}(f, \theta)$

multiplied by f^n with n the wave spectrum moments. What about higher moments? Ardhuin et al. (2017) studied the spectra of the first 5 wave moments in the Drake Passage and have shown a similar tendency for each of them between 100 km and 10 km. Nevertheless, the higher the moments were, the higher was the variability at small scales (high wavenumber). From this former results and all the studies performed up to now, we propose to study the modulation of the mean square slope (mss, proportional to the 4^{th} moment of the wave spectrum, Eq.(4.5)) in the Agulhas current for simulation forced with purely rotational current, on the one hand, and purely divergent current, on the other hand. The mss is a vector quantity, for weak wind around 5 ms^{-1} the mss can be reduced to a scalar (Munk, 2009), such that,

$$\mathrm{mss} = \mathrm{mss}_{upwind} + \mathrm{mss}_{crosswind}, \tag{4.4}$$

with the mss,

$$\mathrm{mss} = \int_{f=0}^{\infty}\int_{\theta=0}^{2\pi} \frac{(2\pi f)^4}{g^2} E(f,\theta) df d\theta. \tag{4.5}$$

We plot in the Agulhas current region an instantaneous mss field (Fig.4.6a,b) for a moderate wind event (6 $\mathrm{m.s}^{-1}$ in main Agulhas systems, wind reaches 12.s^{-1} at the east boundary of the domain and offshore the Cape of Good Hope). One can see that mss is very sensitive to the wind speed which is consistent with the works of Cox and Munk (1954), the higher is the wind speed, the higher is the mss value. Agulhas current strongly modulates the mss signal both for purely rotational (ψ) and divergent (ϕ) flows (Fig.4.6) even if the MSS_ψ values are strongly higher for the purely rotational flow, certainly because the simulated surface currents in the Agulhas current are principally rotational (Fig.4.4). However small structures are visible in MSS_ϕ field as shown in the California Bay by Romero et al. (2020). To quantify the small-scale current effects on the mss, omnidirectional mss wavenumber spectra have been computed. Spectra are computed from a 2D discrete Fourier Transform averaged in all directions. Results are displayed in Fig. 4.6c. Spectra show variability strongly higher for simulation forced with purely rotational flow between 600 km and 20 km. At smaller scales, between 15 km and 7.5 km, the variability of the mss is equal for both simulations with rotational and divergent surface currents. The mss variability induced by the current (for rotational and divergent component) is significant from 50 km to 7.5 km.

Ardhuin et al. (2017); Villas Bôas et al. (2020); Marechal and Ardhuin (2021) have shown that the 0^{th} moment of the wave spectrum, through H_s, θ_m, and σ_θ, are strongly modified by the vorticity of the flow. In Fig.7 of Ardhuin et al. (2017), authors showed that the higher the moments are, the smaller the variability is at large scale ($\mathcal{O}$(100 km)) but the higher the variability is at small scale. In Fig. 4.6, we show that the mss is strongly modulated by the current both at the meso- and at the submesoscale range ($\mathcal{O}$(<30km)) by the vortical and divergent component of the current. The key message in this experiment is that small-scale surface current patterns induce a change of mss even if the flow is purely divergent. It confirms some observations through images of the sea surface roughness (Rascle et al., 2014).

Romero et al. (2020) showed that other high moments of the wave spectrum are also modulated by the small-scale current patterns as whitecap coverage and air-entrainment rate.

Up to now we have shown that the H_s variability is proportional to the current gradients induced by the rotational component of the flow. The inversion of H_s signal to estimate the velocity and the phase of surface current features is limited due to the nonlocal effect of the current on the H_s. The changes of the mss led by the current gradients are much more local (Rascle et al., 2018). As mss is modulated locally by small-scales

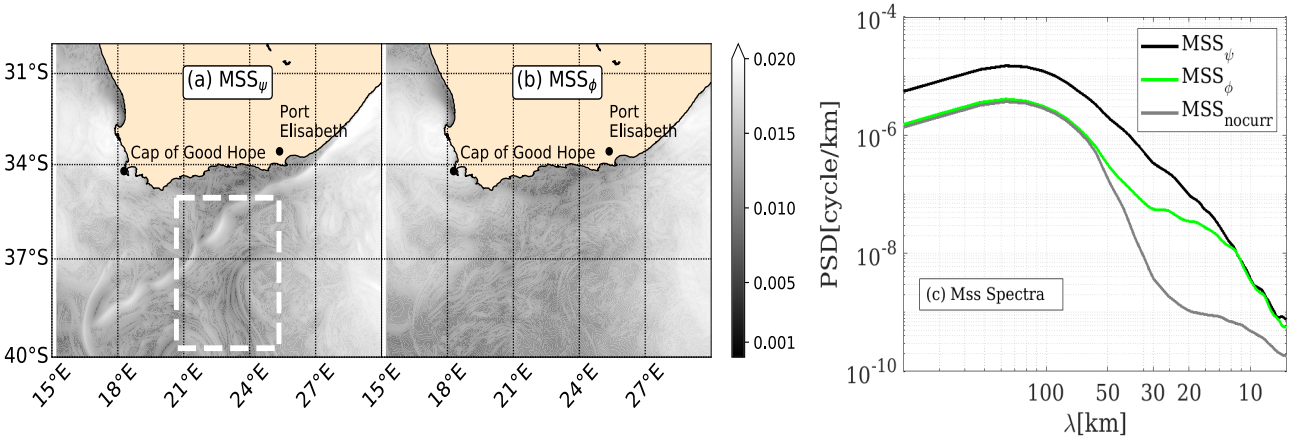

Figure 4.6: Panels (a): instantaneous mean square slope (MSS) field in the Agulhas current for purely rotational current (MSS$_\psi$). Panel (b) instantaneous MSS field for purely divergent current (MSS$_\phi$). Panel (c) omnidirectional mean square slope spectra associated to the field in panel (a) and (b) and for simulation without current forcing. The area where the spectral analysis has been performed is displayed on panel (a).

surface current, the measurements of the mss provide an estimation of the underlying current even if the flow is not geostrophically balanced ($U_\phi \neq 0$). For instance, Rascle et al. (2018) discussed the performance of Sentinel-2 sunglint images (Drusch et al., 2012) to retrieve the intensity and the position of small-scale current gradients from mss measurements under low-wind condition.

4.4 Seasonality of wave height gradients from high resolution altimetry

Villas Bôas et al. (2020) showed, with semi-realistic numerical simulations in the Coastal California Current, a clear seasonal variation of ∇H_s due to the change of the nature of the flow throughout the year (see Fig.1.14). In Quilfen et al. (2018), **Quilfen&Chapron20 19**, and Marechal and Ardhuin (2021), authors highlighted that altimeters measure very sharp ∇H_s in the Agulhas current. Combining the fact that the nature of the flow and the wavelength of the waves are determinant for the ∇H_s intensity and position and that the new CCI-Sea-States dataset (Dodet et al., 2020) provides altimeter data that can capture the small-scale ∇H_s, we investigate the seasonal variability of the ∇H_s with altimeters data on a global scale. We did the work at global scale. We assume the good quality of H_s altimeters data with respect to in-situ measurements at >200 km of the coast even if in-situ data are lacking in some parts of the world (as in the Southern Ocean). As operational surface current (at global scale) cannot reproduce realistic ∇H_s (Marechal and Ardhuin, 2021), we will not compare the altimeters data with the model. The aim of this section is to know if we can infer some flow properties from the variability of H_s throughout seasons until spatial resolution of several altimeter footprints (30 km)?

4.4.1 Altimeter data used

As altimeters provide measurements of H_s at global scale, sparsely spaced in space and time (Ardhuin et al., 2019b), global climatology both for H_s and ∇H_s can be estimated. We used the H_s data provided by the Saral-AltiKa altimeter which operates in Ka-Band (between 26.5 GHz and 40 GHz) with a range resolution of 30 cm. Data used

were filtered with the Empirical-Method-Decomposition (Quilfen and Chapron, 2019; Dodet et al., 2020) which provides a much thinner spatial resolution than the unfiltered level-2 data. The number of altimeter tracks used for the climatology are 12037 for winter (December-January-February, DJF), 10419 for spring (March-April-May, MAM), 15797 for summer (June-July-August, JJA) and 13728 for fall (September-October-November, SON). The study covers the period between 2013 and 2018. The averaged H_s and ∇H_s field have been projected and averaged on a 1/3° × 1/3° regular grid from 80°S to 80°N. This is the thinnest resolution to map the entirety of the global ocean by using solely SAral-AltiKa altimeter. The relative differences between global map of ∇H_s derived by others' altimeter missions are significant (not shown), that is why we do not merge altimeter missions. This difference can be explained by the difference in the orbit of the different altimeter missions.

4.4.2 Surface vorticity and H_s climatologies

Surface vorticity climatology

We give the seasonal climatology of the absolute value of the surface vorticity (ζ=∂_xv- ∂_yu). Surface geostrophic and Ekman currents are from the Globcurrent product (Rio et al., 2014) estimated from Sea-Level-Anomaly measurements provided by altimeters and in-situ buoys. The spatial resolution of the current is 1/4° × 1/4°, the effective resolution of such currents is meridionally dependent (Ballarotta et al., 2019) and vary between 100km at mid-latitudes and 600km at the equator.

The large-scales boundary currents (Gulf-Stream, Kuroshio, Brazil current, Australian boundary current, Equatorial current, and Circumpolar Current) are well highlighted throughout the year with a mean vorticity of $\sim 2.5\times 10^{-4}$ (Fig.4.7). Although such currents are strongly seasonal, with submesoscales current productions among other (Callies et al., 2015; Rocha et al., 2016b; Tedesco et al., 2019), those small-scale variabilities cannot be represented by altimeters-derived currents because of the lack of resolution of the retrieved currents. The intensity of the current vorticity is roughly identical in all the boundary currents. Regional vorticity patches appear seasonally in some parts of the ocean as in the Arabian Sea in Fall (perhaps due to Monsoon), along the west coast of Mexico in Winter. Let us note that the mouth of the Amazon and Congo River have strong vorticity signatures up to several kilometers offshore. Globally the mean surface vertical vorticity is constant throughout the year and confirms the well known global distribution of mesoscale eddies of Chelton et al. (2011).

H_s climatology

Before focusing on the climatology of ∇H_s we computed the climatology of H_s from CCI-Sea-States dataset (Fig.4.8). Mean H_s maps show a clear meridional dependency with the lowest values around the equator band and highest values in the Southern Ocean and in the North Atlantic during winter. This is consistent with the high wind speed seasonal climatology (Ribal and Young, 2019). Storms that occur continuously in the Southern Ocean are well captured by the Saral-AltiKa altimeter where the mean values of H_s do not fall below 4 m throughout the year. The maximum values of H_s in the Southern Ocean are measured in JJA below 35°S and between 60°E and 120°E where the mean H_s reaches ∼6.5 m. Both in the North Atlantic and in the North Pacific (above 35°), the strongest value of H_s are measured during winter (H_s ∼7 m in the Atlantic and H_s ∼6 m in the Pacific) whereas in summer those mean values decrease significantly between 2 m and 3 m. Along the equatorial band, mean H_s is relatively constant along the year (H_s oscillates around 2 m). However a clear 4 m spot emerges in the Arabian

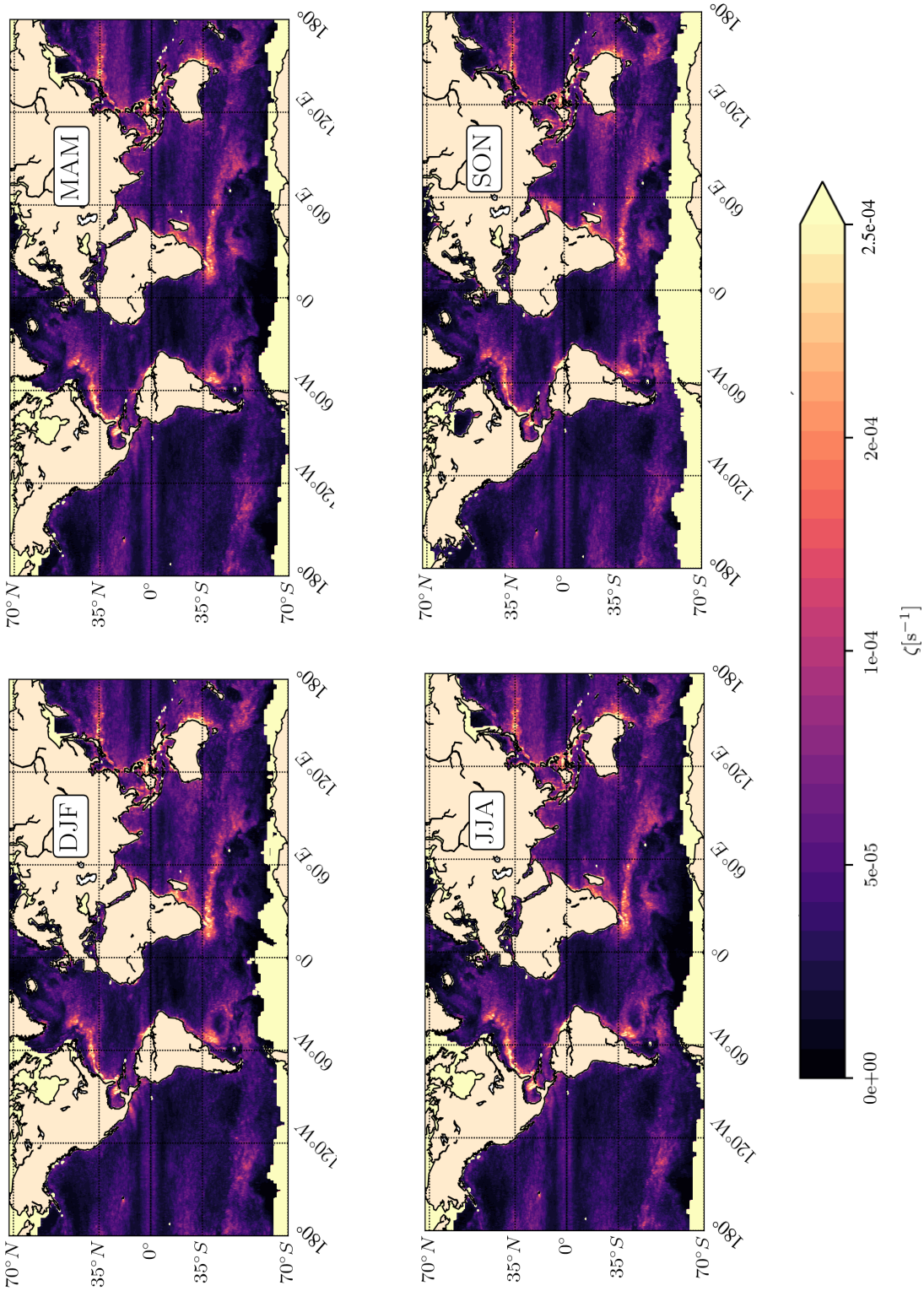

Figure 4.7: Mean absolute value of vertical surface vorticity (ζ). DJF refers to December-January-February, MAM refers to March-April-May, JJA refers to June-July-August and SON refers to September-October-November.

Sea in summer (JJA). For the reader, a global H_s climatology from CCI-Sea-States without seasonal distinction is given in Dodet et al. (2020) and compared with ERA-5 climatology and the Ribal and Young (2019) climatology.

4.4.3 Seasonal climatology of ∇H_s

We wanted to present a ∇H_s climatology to approach the surface current climatology at global scale at a resolution where tradition currents derived from Sea-Level-Anomaly measurement fail. Also we wanted to know the parameters that can drive the evolution of ∇H_s in the global ocean during the year. The climatology of ∇H_s has been computed in two different ways. The first one is similar to the one showed in Marechal and Ardhuin (2021),

$$\nabla H_s = \frac{\Delta H_s}{dr}, \tag{4.6}$$

with dr fixed and equal to 30km and ΔH_s the along-track difference between two H_s measurements spaced 30 km apart. Results are given in Fig.4.9.

The global spatial variability of ∇H_s is more regional than the H_s climatology. One can notice that, ∇H_s values match pretty well with the global ζ distribution (Fig.4.7). ∇H_s are the strongest at mid-latitude in boundary western currents and in the Southern Ocean. The seasonal variability of ∇H_s is following the seasonality of H_s. In winter, strong ∇H_s are measured in the North Atlantic in and around the Gulf Stream ($\sim$ 0.01 m/30km). At the same location ∇H_s strongly decreases in summer revealing only the Gulf-Stream fronts in all the North Atlantic. During spring and fall, the Gulf Stream is more highlighted than in summer with a wider spread of the ∇H_s signal. Still in the north hemisphere, one can see that the Kuroshio current is well visible in the ∇H_s signal especially during winter where ∇H_s values reach $\sim$ 0.01m/30km. The Kuroshio is slightly less captured during spring and almost invisible during summer and fall. In the southern hemisphere, the strongest ∇H_s values are measured during summer (JJA). Strong signal is captured in the Southern Ocean between 60°W and 60°E where vorticity is significant (Fig.4.7), i.e., in the Drake passage and in the Agulhas current, in the Agulhas return current and in the south Indian current up to 60°E. The spread of the ∇H_s follows the H_s climatology (Fig.4.8), the higher the mean value of H_s, the wider the ∇H_s patches. Finally, we highlighted a H_s anomaly in the Arabian sea during summer in the H_s climatology (Fig.4.8), the ∇H_s climatology also reveals an anomaly at the same spot during summer. It is known that the mesoscale and submesoscale activity at this location is very strong throughout the year (l'Hegaret et al., 2015) with a specificity in summer where the Eddy Kinetic Energy increases. Is this patch due to an intensification of the mesoscale activity or due to the local enhancement of the H_s? This remark can be extended to other parts of the global ocean. We try to answer this question by creating a new climatology of ∇H_s.

To remove the potential contribution of the storms which lead to a clear change of the average ∇H_s as in the North Atlantic Ocean (Gulev and Grigorieva, 2006)), we normalized ∇H_s measured by the altimeter by the H_s averaged over 170 km (Eq.(4.7)). This distance is sufficiently short not to take into account the effects of local storms on the intensity of the ∇H_s and sufficiently long not to remove the current-induced variability of H_s at the mesoscale range (<200 km, Ardhuin et al. (2017)). The new ∇H_s values are computed as,

$$\nabla H_s = \frac{1}{\langle H_s \rangle} \frac{\Delta H_s}{dr}. \tag{4.7}$$

We can notice a certain similarity with the Eq.(3.3). Results are given in Fig.4.10. We see that ∇H_s ar still enhanced in areas where surface current vorticity is strong, i.e., in the western boundary currents and in regions

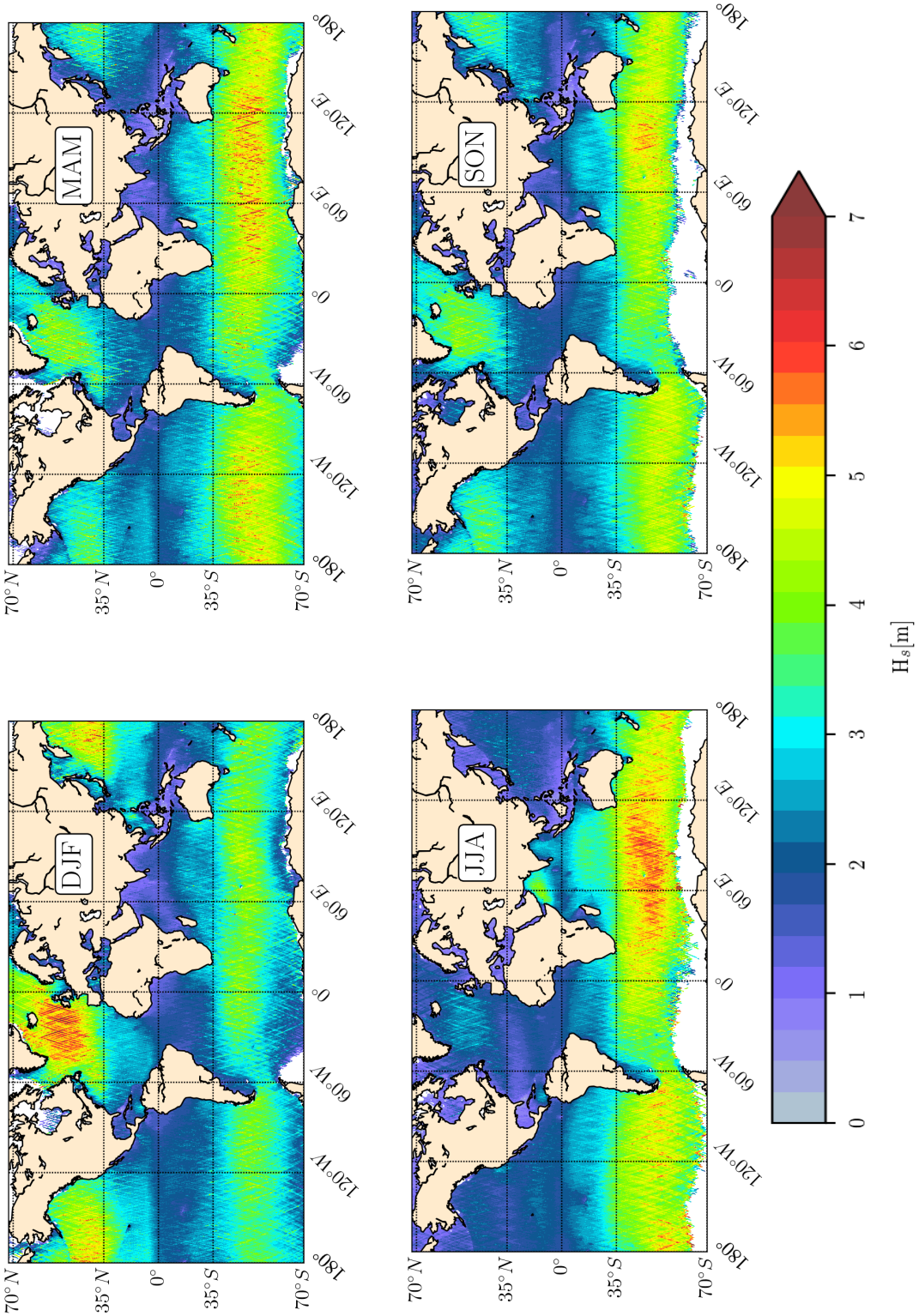

Figure 4.8: Mean significant wave height (H_s) from altimeter carried by Saral-AltiKa from 2013 to 2018. The grid resolution is 1/3° x 1/3°.

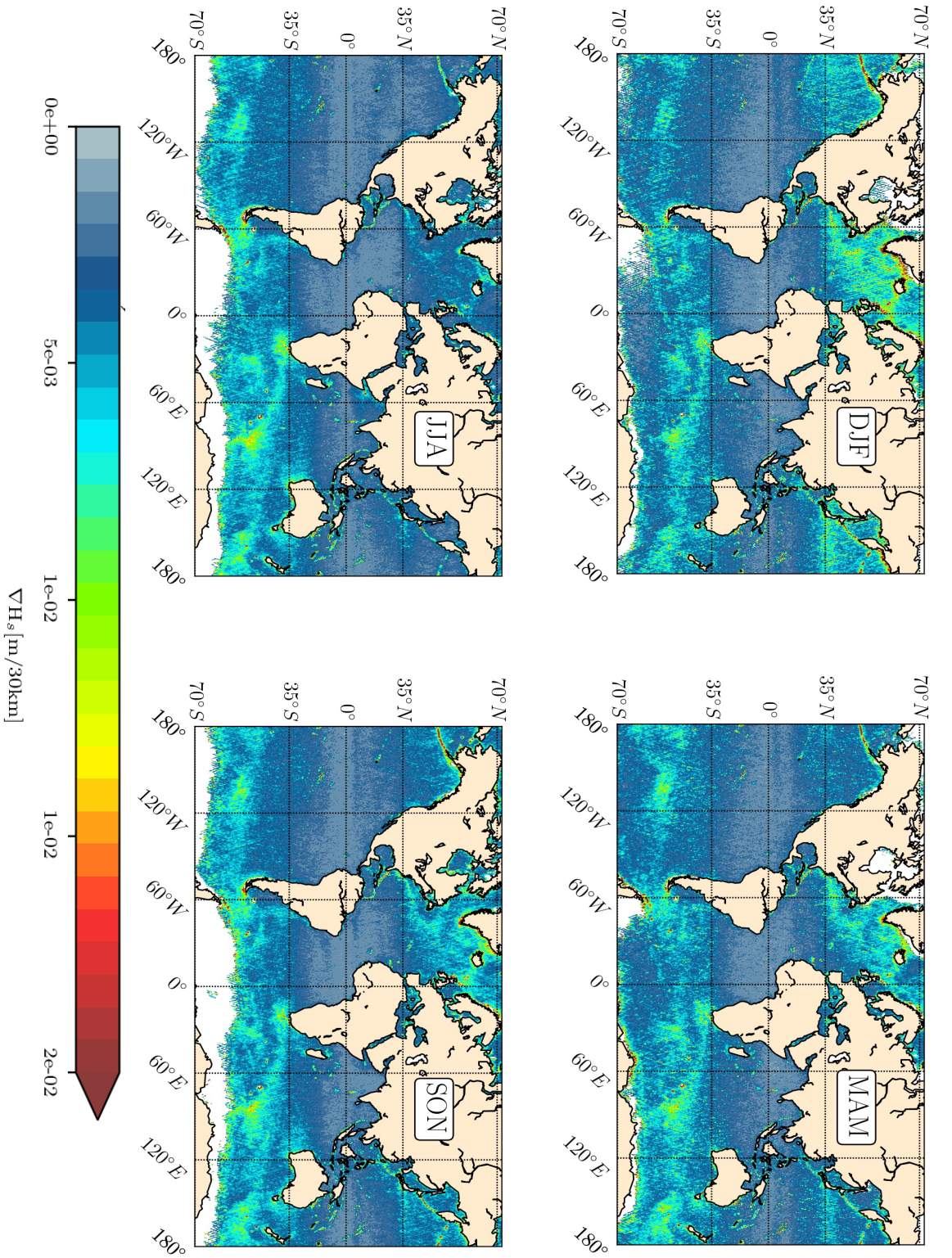

Figure 4.9: Same figure as Fig4.8 for mean significant wave height gradient (∇H_s).

with energetic mesoscale and submesoscale current features as in the Drake Passage, (Fig.4.10). One can see very sharp ∇H_s in close seas and more generally at the land boundaries. We do not discuss those areas. The effects of storms is less visible in this new seasonal climatology. Many differences between seasons in the ∇H_s signal are noticeable at global scale. We focus on six areas highlighted in Fig.4.10 with letters.

(a) In the northernmost branch of the Gulf Stream, the ∇H_s are the strongest during summer (JJA). Also, on both side of the main branch of the Gulf Stream, high signal around 3.10^{-3} km^{-1} are noticeable. This signal spreads almost all in the north-Atlantic basin.

(b) During spring, meridional ∇H_s stripes are visible in the north-east Pacific.

(c) At the North of the equator, in the East-Pacific, a thin band of $1.5.10^{-3}$km^{-1} is apparent during winter and spring. In summer and fall the signal is much less visible.

(d) At the mouth of the Amazon, strong ∇H_s values at $2.5.10^{-3}$ km^{-1} are measured only during summer and fall.

(e) In the Agulhas return current that flows eastward and join the South Indian current up to 90°E, we observe the sharpest ∇H_s during winter. This band of ∇H_s is split at 60°E in summer.

(f) At the west of Australia, one can notice that the signal is visible much further offshore in the Indian Ocean during fall where measured ∇H_s are around 2.10^{-3} km^{-1}. During spring we do not notice these patterns in the ∇H_s signal.

In the absence of wind forcing and wave dissipation, at the meso- and submesoscale range, the current-induced ∇H_s is dependent on the intensity and the nature of the underlying flow and of the incident wave group speed (Eq.15 of Villas Bôas et al. (2020)). Young (1999) combined model outputs and satellite data set spanning a period of 10 years to construct a global climatology of wave properties (significant wave height, period and mean direction) and wind (intensity and direction). Please note that in deep water, wave group velocity is proportional to the wave period ($C_g=\frac{gT}{4\pi}$). Combining the works of Young (1999), the numerical outputs of Ardhuin et al. (2017); Villas Bôas et al. (2020) and results in chapter 3, we try to explain the difference of ∇H_s measured by altimeter throughout the seasons. We refer to the Fig.4.10.

In (a), during winter, the mean wave period is the highest ($\sim$ 10 s), in summer this value drops to 6 s. These seasonal changes can be explained, as well, by the decrease of the wave period in summer leading to the fact that waves are more refracted with the apparition of trapped wave systems, or by the enhancement of the rotational flow at the mesoscale range in summer. Mensa et al. (2013) highlighted numerically that the production of submesoscale patterns in the Gulf Stream is much stronger in winter than in summer, nevertheless the currents at the mesoscale range stay constant most of the year. Thus this change of ∇H_s seems to be induced by shorter incident waves rather than an intensification of the flow. In (e), from works of Young (1999), the seasonality changes of ∇H_s can be also driven by either the fact that wave periods are globally shorter in winter than in summer (9 s in winter and 12 s in summer) or by the surface dynamic of the currents. The results shown in Fig.4.7 do not highlight a seasonal variability of the soleinodal flow. Higher resolved current data are necessary to remove this ambiguity. In area (b), the regional ∇H_s enhancement during spring is less intuitive. We try to explain these stripes from Qiu (1999) works with Topex-Poseidon altimeter data. The author highlighted a maximum of eddy kinetic energy during April-May due to the intensification of baroclinic instabilities. At these latitudes, the typical size of emerging eddies from

baroclinic instabilities is $\sim$ 60 km (see. Fig.1.5). The emergence of such eddy field current at the surface could explain the observed ∇H_s at the mesoscale range. We do not have another assumption for the appearance of such striped structures. In (c), the large-scale mesoscale eddies are stable during the years (Fig.4.7). However such currents are far from the true current (Yu et al., 2019). As Coriolis force goes to zero at the equator we cannot use altimeter measurements to estimate geostrophic currents. The buoy measurements and satellite radiometers are the only data that can be used to infer surface currents. Nevertheless we give some notes to try to explain those seasonal variations of ∇H_s. In the equatorial band, the wave period oscillates between 8 s and 11 s throughout the year. The dominant mean wave direction also changes throughout the season (Fig. 3e of Young (1999)) from northward in winter and eastward in summer. As the relative direction between waves and current is key in the refraction intensity (see equations of geometrical approximation in the introduction) it could explain why gradients are much less visible in summer. In (d), the mean period is constant most of the year ($\sim$ 7s). Richardson and Reverdin (1987) showed from lagrangian drifter trajectories that the North Brazil Current strongly retroflects and creates eddies strongly energetic in the period from July to December. During the rest of the year, the current remains stationary and propagates northward against the American coastline. This seasonality of mesoscale current could explain the seasonality of ∇H_s in this area. In (f) the wave direction is almost stationary throughout seasons, as well as the mean wave period equal to 11 s throughout the year with a slight drop in winter where 9 s wave period is measured. Thus the appearance of ∇H_s in fall is not explained by the wave climatology proposed by Young (1999). Nevertheless, Fig.4.7 shows a slightly higher value of surface vorticity during fall which is in agreement with the enhancement of ∇H_s during the same season.

Through those six areas, it has been shown that the new CCI-SeaStates dataset captures regional scale ∇H_s patterns changes throughout seasons. Through different hypotheses we tried to explain those changes. Combining the state of the art of current effects on waves and the works of Young (1999), the measured ∇H_s intensity evolution during the year could be explained. It could also be a first estimation of the intensity and the nature of the flow at the mesoscale range from wave measurements (as proposed in Fig.4.2). A better description than the one proposed above would be possible by creating clusters in terms of wave group velocity, wave direction and current vorticity intensity to infer which variables drive the enhancement of ∇H_s in different areas of the global ocean. One can note that the potential contribution of the σ_θ on the intensity of ∇H_s has not been discussed. Another application of this kind of seasonality description in terms of waves and current properties could be fruitful for the forecast of severe sea states, crossing seas and abnormal high waves in currents with applications for marine safety (Mallory, 1974; Lavrenov, 1998).

The ∇H_s are computed along altimeter tracks. The intensity of ∇H_s is dependant to the orbit of Saral-AltiKa altimeter which is strongly meridional. Thus, from equator to mid-latitudes ($< 60°N$ and $> -60°N$), most of the ∇H_s discussed are more meridional than zonal. We also took the absolute value of the ∇H_s. New works could be done by splitting the descending and ascending tracks without the absolute value and dealing with other altimeter missions.

4.5 Summary of the chapter

In this chapter we have extended the works proposed in the chapter 3 in a realistic framework in the Agulhas current region. The current-induced change of the H_s at the meso- and at the submesoscale range is captured by altimeter data. In the literature, some study stipulates that the measured sharp ∇H_s are underestimated by wave

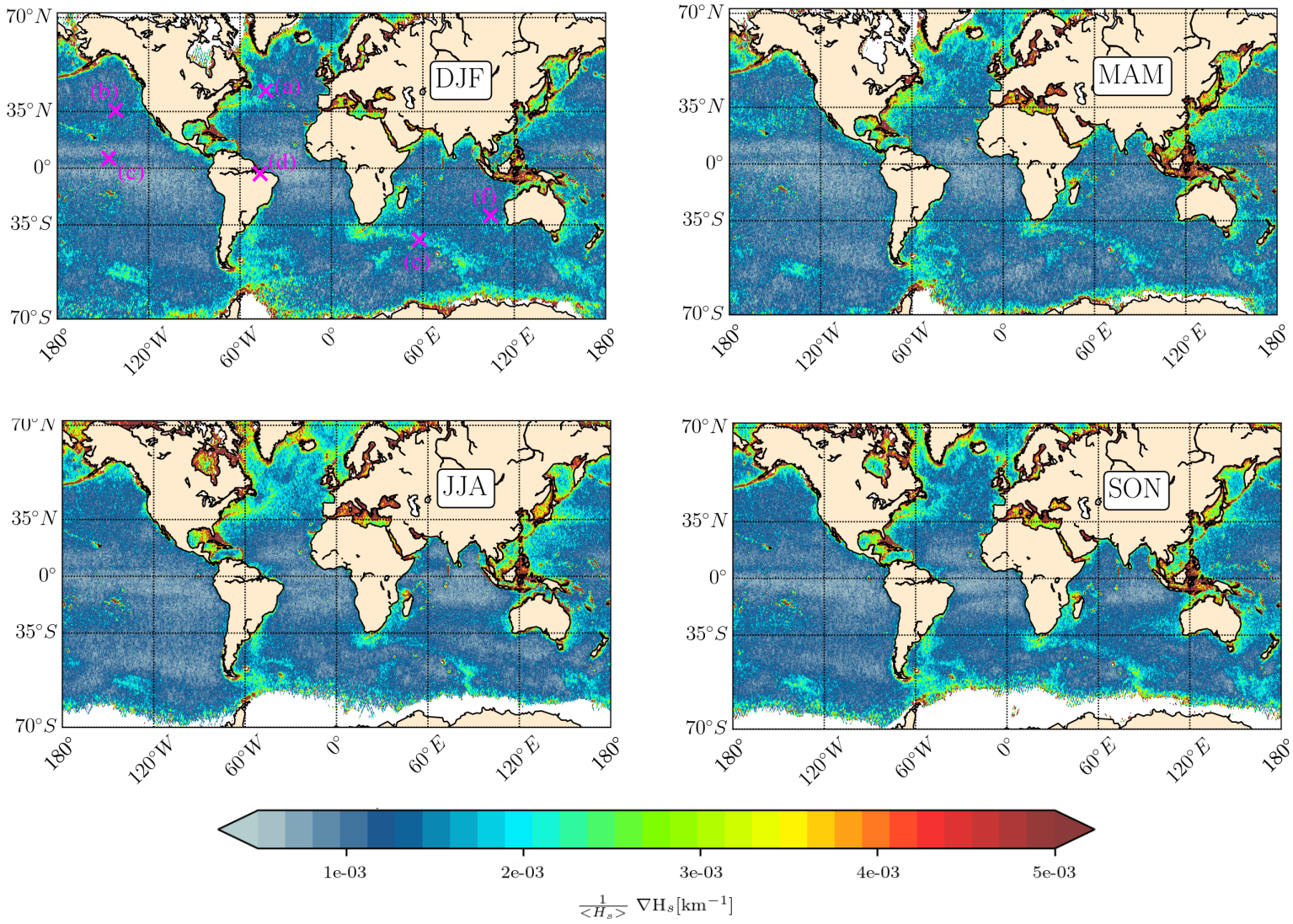

Figure 4.10: Same figure as Fig4.8 for mean significant wave height gradients (∇H_s) over 170km. Highlighted areas mentioned in the manuscript, assigned with letters (from a to g), in the winter map (DJF).

models. In the case where models are forced with sufficiently resolved surface currents and sufficiently discretized in direction, the redistribution of the wave action in the current is better represented and the resulting ∇H_s are closer to the altimeter data. This result shows, in a realistic current, that the small and intense currents structures are crucial in the focalization of the wave action in the Agulhas current. Up to now the best numerical approach of the regional current-induced H_s variability was based on wave models forced by operational currents derived from altimeter measurements. Such current has the advantage to map currents on global scale and retrieve mesoscale eddies with a radius of $\sim$100 km, but underestimate strongly the intensity of ∇U and therefore the ∇H_s.

Additional works based on the same numerical framework, proposed to verify the findings of Villas Bôas et al. (2020) which stipulates that rotational component of the surface current is the main contributor of ∇H_s formation at the mesoscale range. Thanks to a Helmotz decomposition that split the rotational and the divergent component of the current, and with numerical experiments based on the same numerical set-up of Marechal and Ardhuin (2021), we verified the findings of Villas Bôas et al. (2020) at the meso- and the submesoscale range (from 116 km to 15 km). Results show more variability in our cases than in the idealized and semi-idealized numerical experiments of Villas Bôas et al. (2020).

The new numerical outputs from simulations forced with purely rotational and divergent flows show that the mean square slope (4^{th} moment of E(f, θ)) is strongly modulated both at the meso- and submesoscale range by the rotational component of the surface current. The divergent component of the current does not modify the mss as much as the rotational component at the mesoscale range, however, at submesoscale, the mss values are modulated by the divergent flow as much as the rotational flow. It confirms that, because of this mss modulation, the current gradients can be inferred from mss contrast measured from space (Rascle et al., 2014; Rascle et al., 2018). Thanks to those measurements, one might ask whether the vertical exchanges processes driven by divergent submesoscale dynamics could be estimated.

Strong ∇H_s are related to the nature and the intensity of the underlying current. Very sharp ∇H_s have been measured and simulated in the Agulhas current. Other parts of the open ocean also reveal very strong regional ∇H_s specifically in Western-Boundary currents. A new ∇H_s seasonal climatology on global scale has been created from filtered altimeter data. The ∇H_s are based on the along track ∇H_s normalized by the mean H_s over 170 km. This normalization has been considered to avoid the contribution of the storms on the intensity of ∇H_s. This climatology highlights strong variability in the ∇H_s field throughout the year at the regional scale. At such locations it is not very clear if the intensity of ∇H_s are more driven by the properties of the incident waves or by the underlying flow. Direct measurements of waves and currents at such locations will allow knowing which waves or/and current properties are responsible for the sharpness of the ∇H_s. Where ∇H_s are mainly driven by the current, measuring ∇H_s at high resolution will allow retrieval of the statistics of the flow but not necessarily the phase because of the nonlocal effects of the flow on the H_s.

Finally, it has been proved that the intensity and the scales of ∇H_s are dependent on the directional spreading of the incident waves. More waves are directional (small σ_θ) more small-scale ∇H_s patterns appear, it confirms the freak wave index presented in Heller (2005). Abnormal high waves are a source of safety issues at sea for every type of vessel. The σ_θ, the wavelength of the incident wave and the intensity of the current are the main parameters that can increase the probability of abnormal high waves at sea. It is known that surface current is a key parameter for wave current interactions processes but they are still poorly measured (Villas Bôas et al., 2019). Wave directional-wavelength measurements (wave directional spectrum) are not left behind. Although remote sensing imagery satellites (SAR and optical) can retrieve the wave spectrum at very high resolution (spatial and

spectral, Chapron et al. (2001); Kudryavtsev et al. (2017a)) their processing are heavy, their coverages are not continuous in the global ocean and images can be inverted in specific wther condition. In addition to this, phase average wave models do not simulate accurately σ_θ (Stopa et al., 2016). Thanks to the new spectrometers SWIM onboard CFOSAT satellite (Hauser et al., 2020), direct directional measurements are possible on global scale, which allow following the wave spectrum transformation in wavenumber and direction in surface current. Those measurements could also be used to improve the quality of σ_θ estimated by wave models.

In this chapter we have shown that the small-scale changes of the H_s highlighted in previous chapters occur in realistic current. These changes are captured both by high resolution wave numerical simulations and filtered altimetry data. Numerically, it has been shown that the spatial gradients of the H_s is proportional to the spatial gradients of surface current Kinetic Energy, and it has been confirmed by altimeter data. Although the H_s variability has been well captured, the focalization processes of the wave action in the current field have not been highlighted because altimeters provide only a one directional measurement of H_s. Collocalized H_s variability and wave directional measurements could provide how surface current vorticity reorganizes the wave action in the current field. This kind of measurement is provided by the SWIM antenna on CFOSAT platform.

CHAPTER 5

SURFACE CURRENT EFFECTS ON WAVES MEASURED BY CFOSAT-SWIM

CFOSAT (Chinese-French Oceanic SATellite) is a new satellite launched at the end of 2018, resulting from a collaboration between the French and Chinese space agencies (CNES and CNSA). It carries two payloads: SCAT, a wind scatterometer and SWIM, a wave spectrometer delivered by CNSA and CNES respectively (Dong et al., 2012; Hauser et al., 2020). Both instruments will contribute to improving our knowledge about waves and wind physical processes. Here I focus on the SWIM instrument.

5.1 Wave measurements provided by the SWIM rotating antenna

5.1.1 Presentation of nadir and off-nadir measurements

The SWIM (Surface Waves Investigation and Monitoring instrument) instrument is a wave spectrometer operating in Ku Band (13,575 GHz). SWIM used 5 beams at small incidence, called off-nadir beams hereinafter, at 2°, 4°, 6°, 8°, and 10°. The footprint size of the beams is ∼18 km × 18 km wide. One altimeter is also onboard, scanning the ocean surface at the nadir. The instrument is dedicated to estimating the directional wave spectrum and its derived parameters (height, direction and wave wavelength). The illumination of the surface is modulated by long gravity waves (wavelength greater than a few decimeters). The radar measures the backscattered signal with a range resolution of around 1.5 m for each incidence. The antenna rotates and illuminates sequentially the ocean at a speed rate of 5.6 r p.m.. A cycle of measurement is composed of one scan of the 2°, 4°, 6°, 8°, and 10° beam. We call macro-cycle when the 5 off-nadir beams have scanned the ocean over a rotation of 2π rad. The five antenna translation and platform rotation imply that some area of the ocean surface is sampled multiple times for each pass: this reduces the uncertainty of the wave spectrum estimation. A sketch of the SWIM beams rotations and incidences angle is given in Fig. 5.1.

The microwave backscatter (σ_0) occurs through quasi-specular reflections from wave facets oriented normal to the radar's line of sight. The altimeter onboard SWIM (0° incidence) allows an estimation of H_s. In this chapter, we only use data from the 6°, 8° and 10° incidences: the respective footprints and azimuths (θ) are given in Fig. 5.2. Notice that the geographical north and 0° azimuth of SWIM (θ=0) is not aligned (Fig. 5.2b).

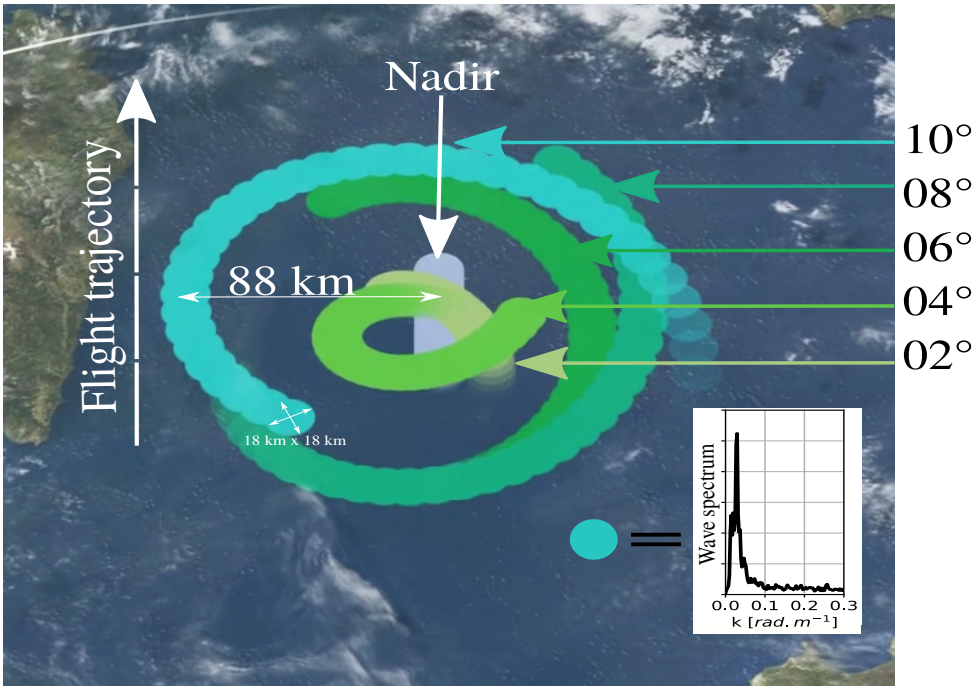

Figure 5.1: SWIM antenna footprint geometry. Each colored circle is one surface illumination which provides a one-dimensional wavenumber wave spectrum.

5.1.2 Waves parameters from SWIM measurements

What does SWIM measure?

It is important to highlight that SWIM is the first space-borne instrument working with the concept of real-aperture radar with rotating scanning beams. There, the performance of the measurement is continuously evaluated. The first signals received by SWIM are the modulation associated with the presence of waves at the ocean surface. This modulation is a function of three variables, the azimuth (θ), the wavenumber (k) and the incidence angle (ϕ), its spectrum is noted $P_m(k, \theta, \phi)$ and is linked to the wave spectrum as,

$$P_m(k, \theta, \phi) = E(k, \theta, \phi) MTF. \tag{5.1}$$

MTF is the Modulation Transfer Function that switches from the modulation to the wave spectrum and is defined as,

$$MTF(\phi) = \frac{\sqrt{2\pi} k^2}{L_y} \alpha^2(\phi). \tag{5.2}$$

The modulation spectrum is proportional to the wave slopes (Jackson, 1987) that is why the term k^2 in Eq.(5.2). L_y is the azimuth length of the footprint and α the sensitivity coefficient proportional to the normalized radar cross-section (σ_0). In Eq.(5.1), $E(k, \theta, \phi)$ is the wavenumber spectrum linked to the frequency spectrum, $E(f, \theta, \phi)$, by the Jacobian ($\mathcal{J}$),

$$\mathcal{J} = \frac{2\pi}{C_g}. \tag{5.3}$$

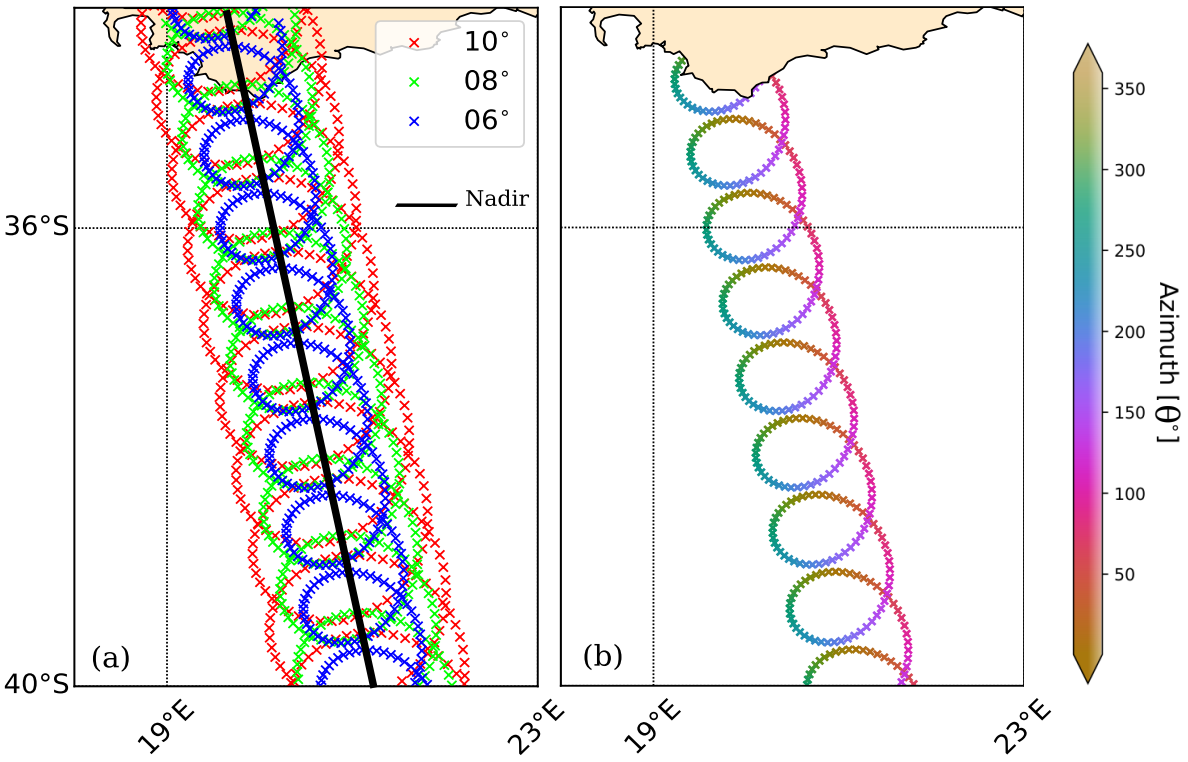

Figure 5.2: Panel (a) shows the footprint for 8 macrocycles of SWIM 6° (blue), 8° (green) and 10° beams (red). Panel (b) shows the azimuths of the 6° beam. Both panels are in the Agulhas current region. Those measurements were acquired on June 11, 2019 at 05:00-UTC p.m..

In general, computing the MTF for a radar is not straightforward because of α ; for SWIM, computing this MTF is even more challenging because of its rotating beams resulting in a large number of variables that contribute in the MTF variation (θ, ϕ, k, wind speed). This complexity is the computation of the MTF led to imagine a new strategy to estimate the wave spectrum. The nadir measurement of H_s (H_{snadir}) is information that can be used to get around this computational complexity. The idea is to assume that the H_{snadir} is identical to the H_s computed from the closest spectrum provided by off-nadir measurements. One can notice that off-nadir measurements are more or less distant from the altimeter path according to the incidence angle. This assumption is very strong, indeed it is equivalent to say that H_s is homogeneous in a distance of 180 km on both sides of the altimeter track. Rewriting Eq.(1.4) as,

$$H_{s_{nadir}} = 4\sqrt{\int_{k_0}^{k_{max}} \int_0^{2\pi} E(k,\theta) dk d\theta} = 4\sqrt{\frac{\int_{k_0}^{k_{max}} \int_0^{2\pi} P_m(k,\theta,\phi) dk d\theta}{MTF}}, \tag{5.4}$$

so for a given incidence ϕ,

$$MTF = \left(\frac{4}{Hs_{nadir}}\right)^2 \int_{k_0}^{k_{max}} \int_0^{2\pi} P_m(k,\theta) dk d\theta, \tag{5.5}$$

with k_0=$2\pi/500\ m^{-1}$ and k_{max}=$2\pi/30\ m^{-1}$.

5.1.3 Wave spectra and bulk parameters

SWIM measures the modulation induced by the presence of waves at the ocean surface. Thanks to the MTF (Eq. (5.5)) one can have access to the wave spectrum E(k,θ). As SWIM carries five beams at different incidences, the resulting footprints are not at the same position on the ocean (Fig. 5.2a) and are more or less distant to the nadir measurements (H_{snadir}). Before applying the MTF, the footprints have been grouped in 70 km length $\times$ 90 km wide boxes to obtain a means modulation spectrum in wavenumber and direction per box. The size of the boxes is defined by the distance between the nadir and the furthest measurements (performed by the 10° beam) which is equal to 90 km and the half distance between two identical azimuths measurement for the 10° which is equal to 70 km. Boxes on both sides of the altimeter track are slightly shifted according to the SWIM-flight axis. Then the MTF is applied to retrieve the wave slope spectrum. Five successive macrocycles, for the 6°, 8° and 10°, are highlighted in Fig. 5.3. The value used for H_{snadir} in Eq. (5.5) is the closest to each footprint, thus H_{snadir} is not the same for one azimuth and different incidence angles (and vice versa). One can obtain E(k,θ) for each incidence angle or one averaged spectrum by combining all incidences. In the following sections, we chose to split spectra per incidence.

Inside each boxes a two-dimensional wave spectrum is retrieved in k and θ with k $\in 2\pi$[1/500 m^{-1},1/30 m^{-1}] and θ $\in$[0,180°]. Assuming an homogeneity between up and downwave fluctuation spectra measurements, which is an approximation (Li et al., 2021), bulk parameters have been computed for the west and the east parts of the wave spectrum (H_s, $T_{m0,-1}$,θ_m, σ_θ). The formulas are given in the first chapter (Eq.(1.4), Eq.(1.5), Eq.(1.7) and Eq.(1.9)).

The signal along the track within a cone of 16° is contaminated by a high speckle noise, measurements are unusable in this cone. This area will be called the blind angle later in this manuscript and will be removed. An example of a SWIM slope spectrum with this blind angle is given in Fig. 5.3f. The spectra have been rotated to match θ=0° with the geographical north (Fig.5.4).

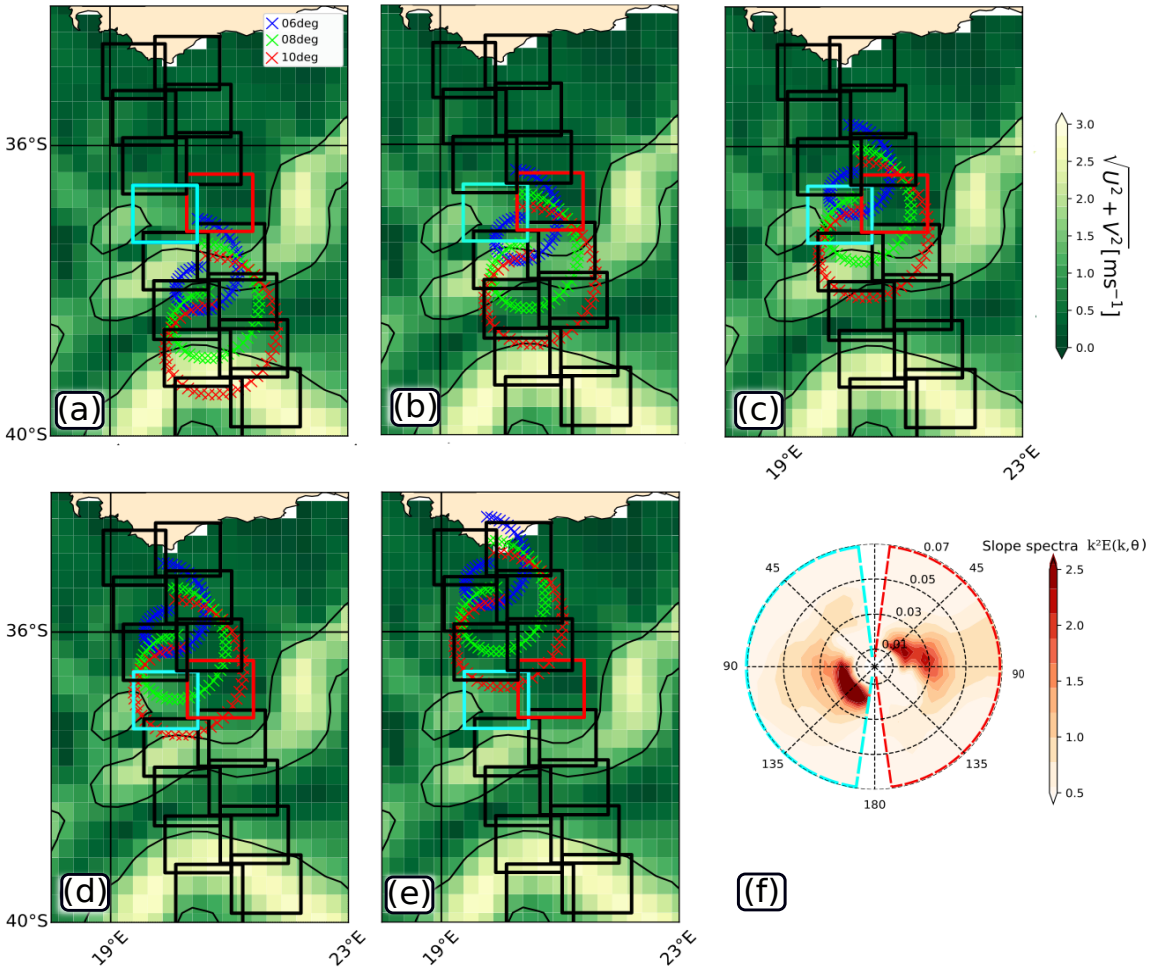

Figure 5.3: Panels a-e show the Agulhas current velocity (background, and black lines: the 1m^{-1} contours). Colored crosses are SWIM footprints for 6° (blue), 8° (green), 10° (red) incidence angles. Panels show 5 successive SWIM macrocycles that enter the blue and red boxes. In each box a *semi* slope spectrum is estimated (0-180°) by averaging (and combining the 3 incidences on this plot) measurements. An averaged spectrum is given in panel f. These SWIM measurements were acquired June 11, 2019 at 05:00-UTC p.m..

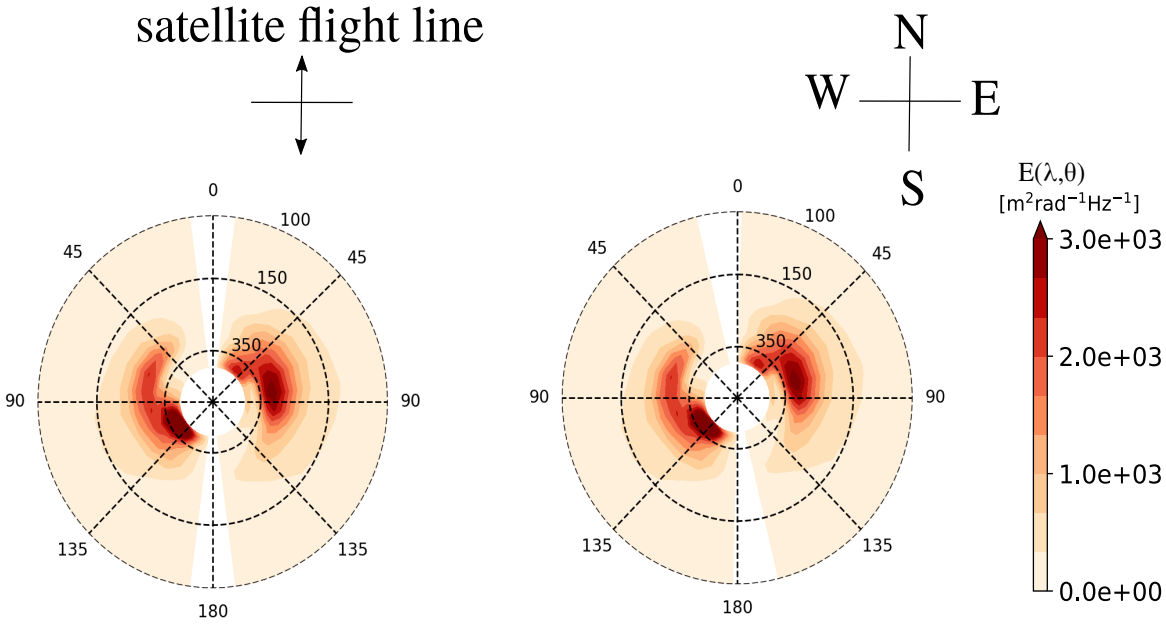

Figure 5.4: Left panel, example of a two-dimensional wave spectrum in the coordinate frame of the CFOSAT platform provided by the 06° incidence. Right panel is the same spectrum in the North-East-South-West frame of coordinate.

5.2 Wave spectra variability in the surface current field

We have shown in the chapter 4 that current-induced sharp ∇H_s is well capture in the Agulhas current with altimeter data. The associated change in wave frequency and direction have been studied in chapter 2 and 3. The directional wave data provided by SWIM seem to be able to validate, or not, the previous theoretical results.

5.2.1 Cases studied in the Agulhas region.

Six different SWIM tracks have been studied in the Agulhas current region (same dimensions of previous chapter, Marechal and Ardhuin (2021)). All of the measurements are performed in different waves, wind, and current conditions. Wind velocity and direction are from the ECMWF reanalysis (Dee et al., 2011), surface current intensity and direction are from Globcurrent product (**rio&al.2014**), i.e. currents are estimated by altimeters, wave height and direction are obtained from wave simulations using WAVEWATCH-III forced by winds and currents from products cited above. Wave height is also measured by the altimeter carried by SWIM platform (SWH in the figures below). Note that the surface current intensity is certainly underestimated. The description focuses mostly on the areas where effects of surface currents on waves are noticeable.

1. (2019-05-07 at 07:00 a.m.-UTC) SWIM track is outside the main Agulhas system. It crosses current fronts, between 37°S and 39°S which resemble the famous warm and salty Agulhas rings. The velocity of these rings is about 1 m.s^{-1}. Waves are coming from the south boundary of the Agulhas domain and U_{10} is southeastward with a velocity of 15 m.s^{-1}. Simulated H_s is the highest where the wind velocity is the strongest. Waves mean direction is not homogeneous in the Agulhas domain. The 1 Hz altimeter onboard

SWIM is measuring a maximum of H_s ∼5.5 m at the edge of the Agulhas ring. Associated fields and altimeter measurements are available in Fig. 5.5.

2. (2019-05-16 at 05:00 a.m.-UTC) SWIM track is crossing the main Agulhas system (flowing southwestward) at 35°S 27°E and the Agulhas return current (flowing eastward) at [38°S 26.5°E]. The intensity of the current is more than 2 m.s^{-1} and around 1 m.s^{-1} respectively. Waves enter the Agulhas domain by the west boundary, they are refracted by the current northward and waves exit the domain by the east boundary with a direction of around 0° (parallel to the North). Two wind regimes occur in the domain, to the west ([15°E, 22.5°E]) the wind is homogeneous and flowing northwestward around U_{10m}=5 m.s^{-1}, to the east ([22.5°E, 30°E]) the wind is homogeneous and flowing north/northeastward around U_{10m}=15 m.s^{-1}. The altimeter monitors a sharp ∇H_s in the main structure of the Agulhas current with a maximum of $H_s \sim 5.5$ m and a minimum of 3.5 m in the return current. Throughout altimeter track less sharp ∇H_s are measured (between 39°S and 35°S). Associated fields and altimeter measurements are available in Fig. 5.6.

3. (2019-05-30 at 06:00 p.m.-UTC) SWIM track is crossing the main Agulhas system (flowing southwestward) at [36°S 24°E] and is aligned to one branch of the Agulhas return current (flowing northward) between 37°S and 40°S. Waves enter in the Agulhas domain from the west, the south and the east boundaries. Waves are refracted by the current and are trapped inside the southwestward branch of the Agulhas where they propagated in the opposite direction of the current. In the south of the main Agulhas system and in the Agulhas return current, waves are traveling west, southwestward. Two wind regimes occur in the domain, to the west ([15°E, 27°E]) the wind speed is moderate ($U_{10m} \sim 7$ m.s^{-1}), to the east ([27°E, 30°E]) wind is southward and stronger ($U_{10m} \sim 13$ m.s^{-1}). H_s measured by altimeters oscillated between 4 m and 3 m within 40°S and 36.5°S. To the north of 36.5°S H_s decreases and reaches 1.5 m to the coast. Associated fields and altimeter measurements are available in Fig. 5.7

4. (2019-06-11 at 06:00 p.m.-UTC) SWIM track is crossing the southernmost part of the main Agulhas branch at 38°S 20.5°E (flowing southwestward) and the Agulhas retroflexion (flowing eastward) at 39.5°S 21°E. The intensity of the current fronts crossed are 2 m.s^{-1} and 2.5 m.s^{-1} respectively. A storm is entering the domain from the west boundary with winds reaching 20 m.s^{-1}. Waves are coming from the southwest boundary and are propagating toward the north-east. H_s measured by the altimeter shows two main gradients along its track, one negative (with respect to the mean H_s measured throughout altimeter track) in the Agulhas retroflexion and a strong positive one at 37.25°S where H_s increases by more 3 m in less than 100 km (from 10 m to 6.25 m). Associated fields and altimeter measurements are available in Fig. 5.8

5. (2019-06-13 at 06:00 p.m.-UTC) SWIM track is crossing the main branch of Agulhas current during a Natal pulse event (Lutjeharms and Roberts, 1988) at 35°S 27°E. The SWIM track also crosses the Agulhas retroflexion (flowing eastward) at 38°S 28°E. The velocity of the crossed currents are respectively 2 m.s^{-1} and 1.5 m.s^{-1}. Waves are coming from the southern boundary and are refracted by the Agulhas current. Waves exit the domain northeastward. A clear signature of the Natal Pulse is visible in the H_s field. Albeit winds are globally weak in the entire Agulhas region (U_{10m} <10m.s^{-1}), a storm partially enters the domain with southeastward winds blowing at U_{10m} >12 m.s^{-1}. The altimeter monitors two main H_s gradients along its track, one negative in the Agulhas retroflexion at 38°S where H_s drops from 4 m to 3 m, and a positive one at 37.25°S where H_s increases from 3 m to 5 m. Associated fields and altimeter measurements

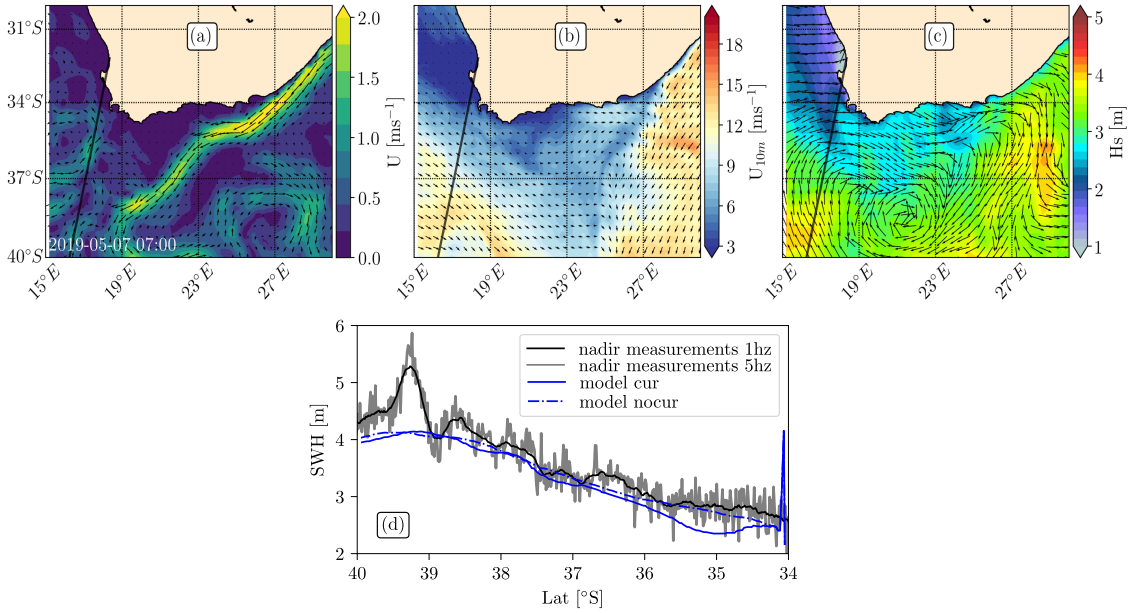

Figure 5.5: SWIM-altimeter track over instantaneous current, wind, and wave field on May 07, 2019 at 07:00a.m.-UTC. Panel (a) shows the current intensity from Globcurrent product (estimated from altimeter sea surface height anomaly measurement), panel (b) shows the wind intensity from ECMWF reanalysis and panel (c) shows the significant wave height (H_s) field simulated with the wave model. Arrows show the direction where current, wind and waves are propagating. Panel (d) shows the significant wave height along the altimeter track for altimeter measurements and for wave simulation interpolated along the same track. The solid black line is for the H_s measurements at 1-Hz and the solid gray line for measurements at 5-Hz. Simulations forced both by winds and currents are given by the solid blue line and simulations forced exclusively by wind are in dashed blue line.

are available in Fig. 5.9

6. (2019-07-08 at 06:00p.m.-UTC) SWIM track is crossing the Agulhas where its main branch is detached from the coast due to the presence of the Agulhas bank offshore Port-Elisabeth (at 36°S 24°E ; current is flowing westward). The satellite is crossing the current front in the Agulhas return current between 40°S and 37.5°S flowing northward. Both currents are ∼2 m.s^{-1} speed. Wind is homogeneous and blowing westward at 15 m.s^{-1} over the two main branches of Agulhas current. H_s measured at the nadir is quite constant along the track with a sharp peak centered at 36.5°S where H_s varies from 7.5 m to 5.5 m south of the Agulhas current and from 7.5 m to 6 m to its north. Associated fields and altimeter measurements are available in Fig. 5.10.

5.2.2 Results of altimeters measurements and the wave model

Wave height gradients (∇H_s) induced by surface currents are captured by traditional altimeters measurements (Ardhuin et al., 2017; Quilfen et al., 2018; Quilfen and Chapron, 2019; Marechal and Ardhuin, 2021). We expect that the SWIM nadir beam also captures those gradients.

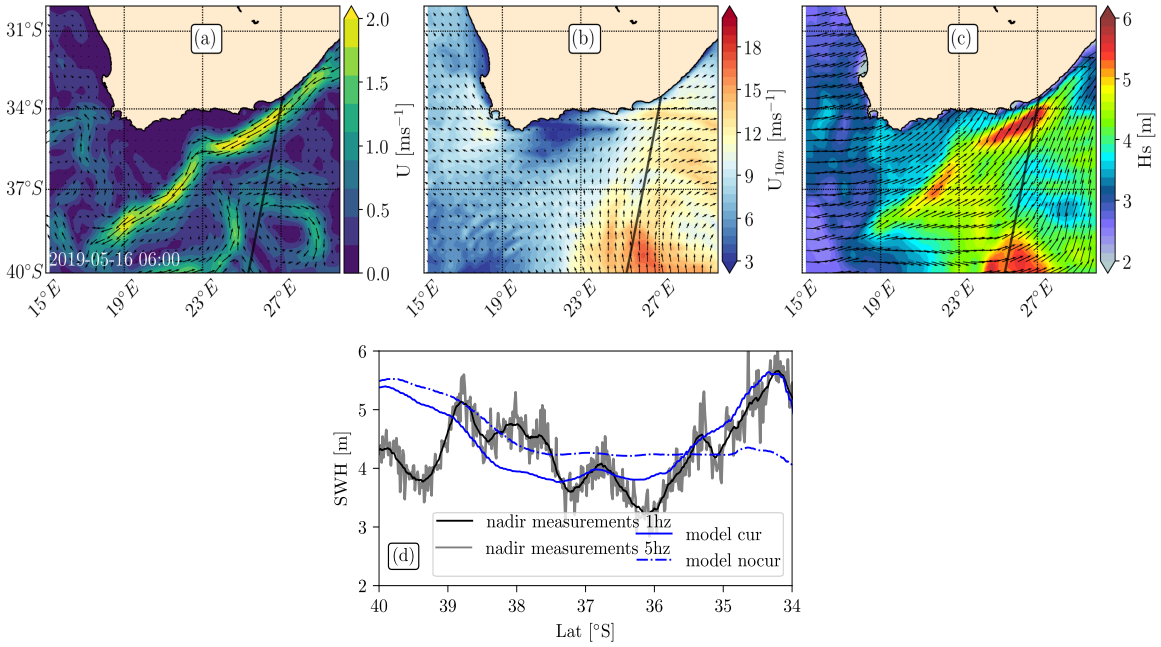

Figure 5.6: Same as Fig.5.5 for on May 16, 2019 at 05:00 am-UTC.

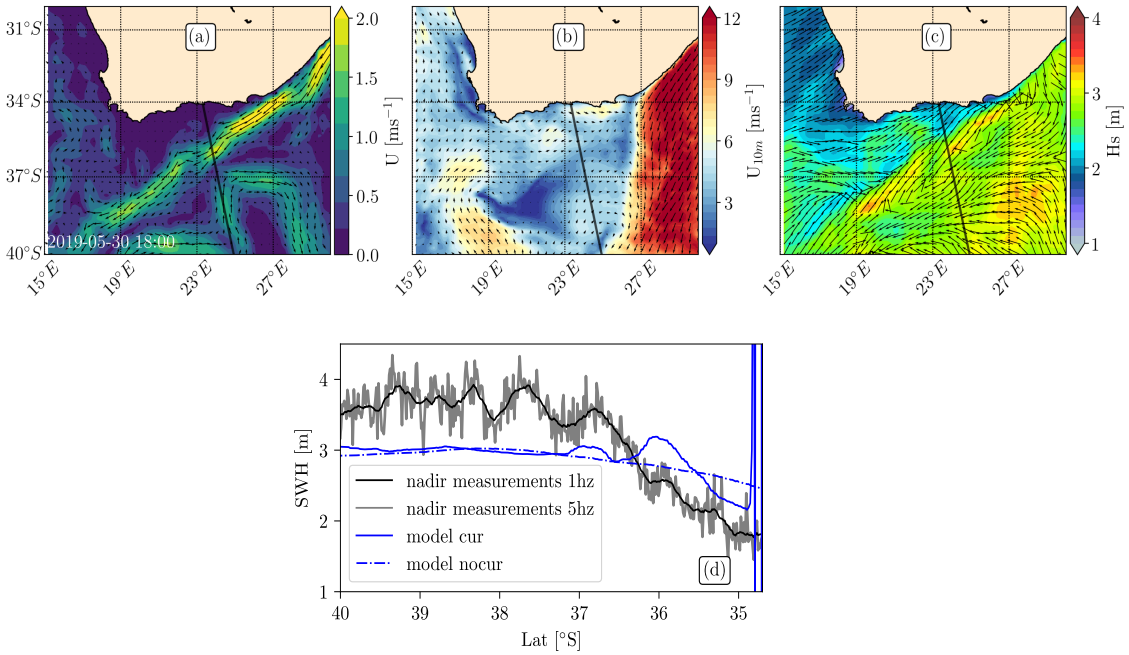

Figure 5.7: Same as Fig.5.5 for on May 30, 2019 at 06:00 p.m.-UTC. The blue peak at the right of panel (d) is spurious.

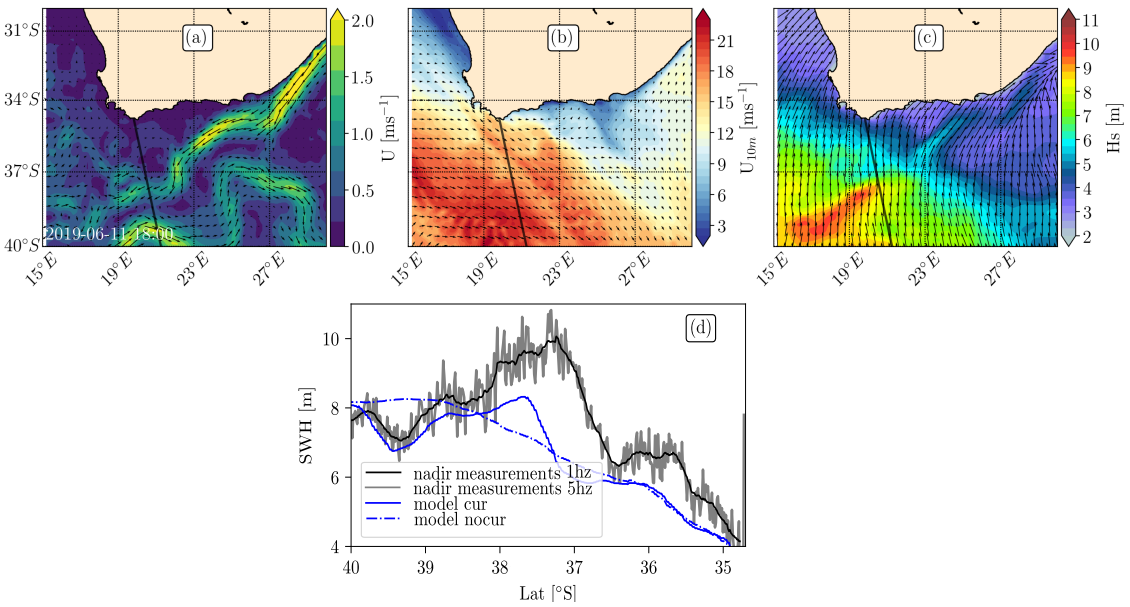

Figure 5.8: Same as Fig.5.5 for on June 11, 2019 at 06:00 p.m.-UTC.

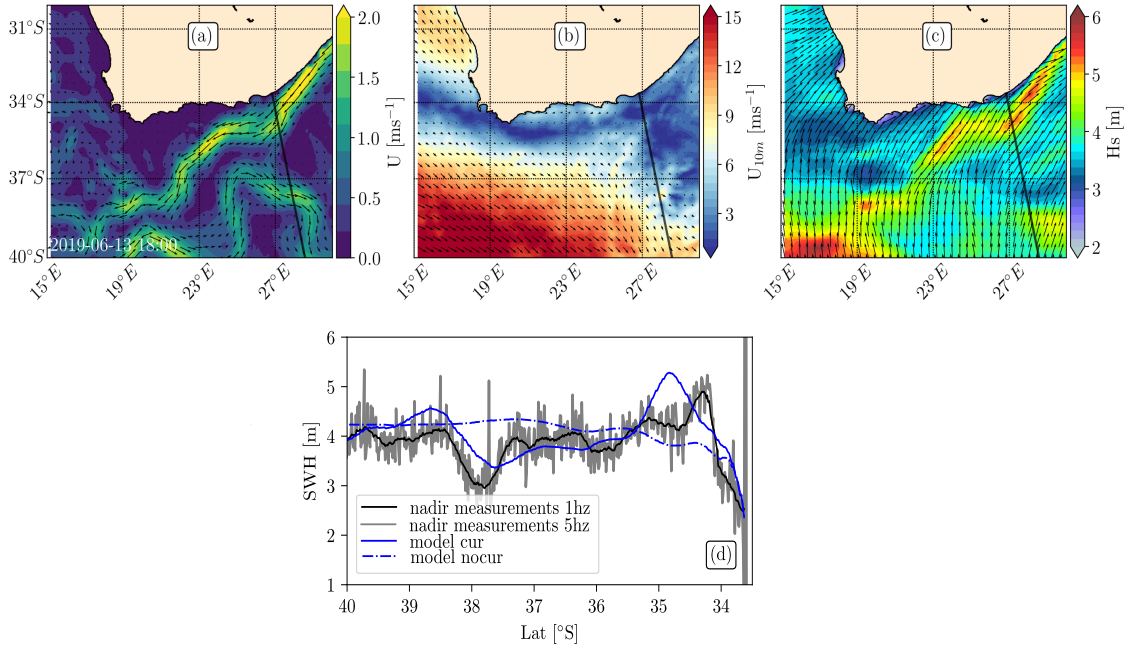

Figure 5.9: Same as Fig.5.5 for on June 13, 2019 at 06:00 p.m.-UTC. The gray peak at the right of panel (d) is spurious.

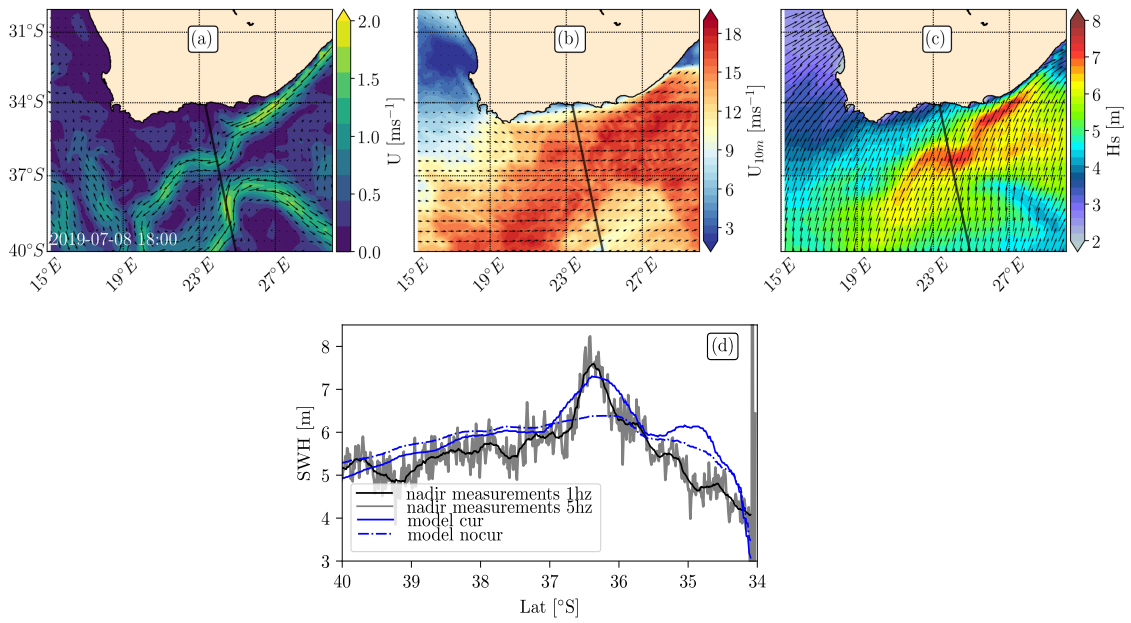

Figure 5.10: Same as Fig.5.5 for on July 08, 2019 at 06:00 p.m.-UTC.

Wave model setup

Waves have been simulated in the Agulhas region using the of WAVEWATCH-III framework with the same parametrisation presented in the previous chapter. Current forcing used is from the Globcurrent product (**rio&al.2014**) spatially resolved at 1/4° × 1/4° but with a very low effective resolution (**ballarotta&al.2019**; Marechal and Ardhuin, 2021). Winds are from the ECMWF model reanalysis. The simulations have been performed for all 2019 long with wave field parameters output every hour over a grid resolved at 3.3 km both in latitude and longitude. Simulated wave spectra are discretized into 32 frequencies and 48 directions. Simulated H_s model outputs have been interpolated over SWIM altimeter footprint.

Wave model do not reproduce realistic wave height gradient

As demonstrated in the previous chapter (chapter 4), high resolution currents are crucial to reproduce realistic ∇H_s. This is once again shown with SWIM altimeter measurements and the wave model outputs forced with current derived from altimetry ; panel (d) of Fig 5.5 5.6, 5.7, 5.8, 5.9,and 5.10. Indeed small-scale H_s variations measured by SWIM altimeter (1 Hz and 5 Hz data) are not captured by the wave model. Moreover extreme values of H_s are completely underestimated (one can refer to the example given in Fig. 5.8) and/or shifted in latitude as shown in Fig. 5.9. Albeit 5 Hz data seems to be contaminated by noise and shows outliers (Fig. 5.9 at 37.7°S), they provide small-scale geophysical signatures as well as the wave modulation by small mesoscale currents or submesoscale. Models forced only by wind do not reproduce H_s variability at the mesoscale range ($\mathcal{O}(100-10)$) km which confirms results of Ardhuin et al. (2017) and Marechal and Ardhuin (2021).

Wave systems entering the Agulhas current region show a relationship between ∇H_s intensity and the rela-

tive direction between mean wave direction and mean current direction. For all cases studied, altimeter measures positive ∇H_s where waves and current are propagating in an opposite direction (Fig. 5.6, 5.7, 5.9, 5.10). Either waves are entering the Agulhas current already with a direction opposite to the current direction or they can also be refracted by the current structure upstream and then be deviated from their original direction to a direction against the current. In those cases waves are expected to become shorter. This case can be considered as a realistic illustration of the case studied in the first chapter (Fig.1.7,1.9). In reality, in boundary currents (Agulhas current, Gulf Stream or Coastal California Current), the wave height enhancement resulting from currents is mainly driven by refraction (Ardhuin et al., 2017; Kudryavtsev et al., 2017b; Romero et al., 2020) which redistributes spatially the wave energy explaining why H_s are decreased or enhanced. The reader can refer to the second chapter where the redistribution of the wave action is discussed. Studying the evolution of the period (wavelength) and the direction at the same time could be a solution to decompose the effect of refraction and Doppler shift on the wave height variability.

5.2.3 Evolution of the wave spectrum in the Agulhas current region from SWIM measurements

Until now, only wave height properties have been investigated in the Agulhas current region, what about other wave parameters? As inhomogeneities in the H_s field induced by surface currents are due to a superposition of dynamical processes, can the effects of currents on wave parameters be investigated to explain the change of H_s at the mesoscale range ($\mathcal{O}(100-10)$km)? Thanks to the SWIM spectrometer and its rotating 6°, 8°, 10° beams, the evolution of wave properties with a novel resolution in the direction-range might be captured in surface current field studying simultaneously the different incidences (Fig 5.2a). Please note that the data from 2°, 4° beams are not studied in this manuscript. Indeed, without going into too much detail, at low incidence angles the relation between the one-dimensional modulation spectrum and the wave spectrum is non-linear. This non linearity is not taken into account in the inversion leading to a deformation of the wave spectrum: peak direction shifted, spectral width issue, and bias in the spectral energy.

Wave spectrum is modified along latitudes, we propose to highlight the variability of the wave spectrum for two cases introduced above for the 06°, 08°, and 10° incidences.

- May 30, 2019 at 05:00 p.m.
- June 11, 2019 at 05:00 p.m.

The goal of this part is to introduce briefly and superficially the change of wave properties in a strong current regime before performing a more accurate description. To justify the current effects on the wave spectrum, we use the Globcurrent product. Albeit these currents do not represent current features below 150km and are in general too weak with respect to the reality (due to the space time interpolation of altimeter data), the phase of large-scale currents is well resolved. The spectra are organized as follows, panel (a-i) show nine E(f, θ) from 0° to 180°, the left semi-spectra are estimated from spectral measurements in the boxes at the West of the altimeter track and the right semi-spectra from measurements on the East of altimeter track. The first spectrum (panel a) is for the southernmost boxes and the last spectrum (panel i) is for the boxes close to the coast of South-Africa.

May 30, 2019 at 05:00 p.m.

For a wave, wind and current hindcast please refer to Fig.5.7 and the associated paragraph in the previous section. The evolution of wave spectra with respect to latitude is given in Fig. 5.11, 5.12 and 5.13 for 06°, 08° and 10° incident beam respectively. For each incidence one can see a strong evolution of the wave spectrum. At 06° incidence, the southernmost measurements (top left spectrum, 5.11a) reveal that a wave system is propagating southeastward (agree with Fig.5.7c) with a frequency around 0.1 Hz and 0.06 Hz. A secondary wave system shows shorter waves (f ∼0.08Hz) propagating northwestward or southeastward (180° ambiguity ; following the studies performed by Li et al. (2021) it seems that we can remove this ambiguity by focusing on the antisymmetry in the wave spectrum, hence, here waves are certainly propagating northwestward). The longest wave system is cut by the blind angle. Fig.5.12a, 5.13a are showing the same waves systems with an exception for the longest wave system, which is not captured by the 10° incidence. One can see that nor the 08° incidence nor the 10° incidence capture the longest wave system in (Fig.5.12b, Fig.5.13b) whereas it is well visible in the spectrum measured by the 06° (Fig.5.11b)). In the fourth boxes, all incidences reveal that one wave system emerges above all the other ones at ∼ 0.1 Hz propagating northeastward (Fig.5.11d,5.12d,5.13d). In the fifth boxes, the system becomes much more spread on both sides of altimeters track for all incidences (Fig.5.11e,5.12e,5.13e). A very interesting wave system is visible in the sixth boxes for the 06° incidence in its left portion (Fig.5.11f). Waves are very long (f=0.06 Hz) and propagating around the azimuth θ=90°. The wave system is not as visible in the 08° incidence but records two energetic wave systems at f=0.08 Hz and at 0.1 Hz (Fig.5.12f). For the same box, the 10° incidence only reveals a unique wide variance patch between the azimuth 90° and 180° at f between 0.08 Hz and 0.1 Hz (Fig.5.13f). In the seventh boxes, one can see in the left part of the wave spectrum that a wave system at θ=135° is unique for the 06° incidence and strongly bimodal in frequency for the 08° incidence. The same system is slightly shifted toward the azimuth θ=90° for the 10° incidence (Fig.5.11g,5.12g,5.13g). The last spectra, acquired close to the coast, shows a clear decrease of variance for each incidence (Fig.5.11i,5.12i,5.13i).

June 11, 2019 at 05:00

For a wave, wind and current hindcast please refer to Fig.5.8 and the associated paragraph in the previous section. In comparison to the previous case, one can see that all SWIM incidences reveal a much stronger variance which is in agreement with the simulation exposed above (higher H_s). The strongest variance patches are measured on panels e to g at the tail of the main Agulhas current. Please note that the first boxes are cut in Fig.5.14,5.15,5.16j but the associated spectra are given in Fig. 5.14a,5.15a,5.16a. In the Agulhas return current one can see that wave spectra are strongly anti-symmetric (panel a-b of Fig.5.14,5.15,5.16). Focusing on the 08° incidence (5.15a), the left spectrum shows strong bimodal wave systems at f in the vicinity of 0.08 Hz whereas right spectrum reveals very directional and a highly energetic wave system at $\theta \sim 60°$. The same antisymmetry is visible in Fig.5.15e where a very directional and bimodal wave system is captured by the 08° antenna. In the same boxes, the two other incidences also reveal wave systems highly directional and aligned with the underlying current (Fig.5.14e, 5.16e). In the same boxes the wave variance of the short-wave systems ($f > 0.08$ Hz) is weaker for the 10° incidence. In the sixth boxes, all incidences capture crossing seas (signal drawn for the 06^{beam}). Finally, one can see that waves are much more northwestward (ambiguity is removed thanks to the position of the coast) at the north to the Agulhas current than at the south where waves propagating along the θ ∼90°. In this case the wind intensity was much stronger than the previous case. It has certainly an effect on the high frequency part of the wave spectrum.

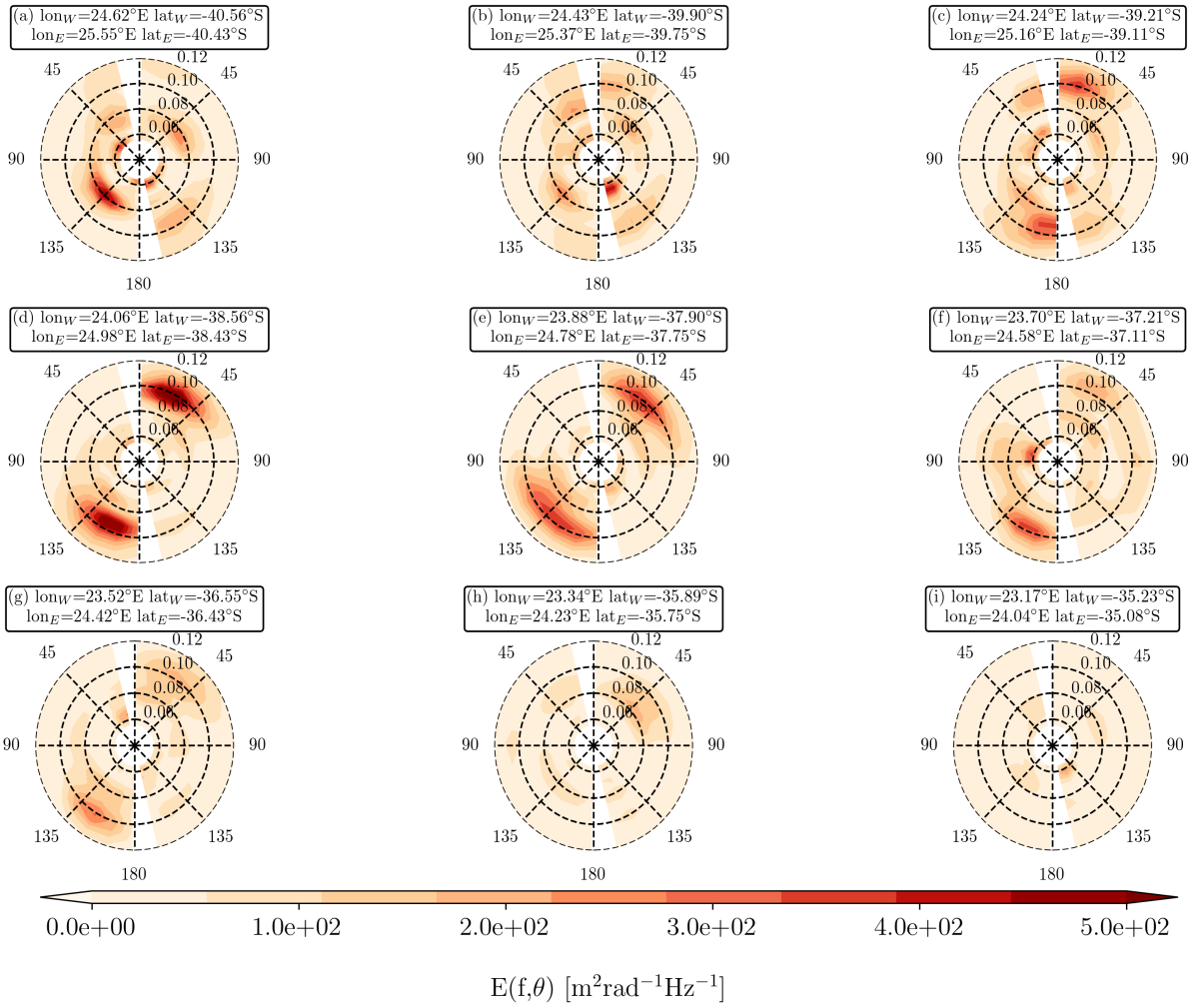

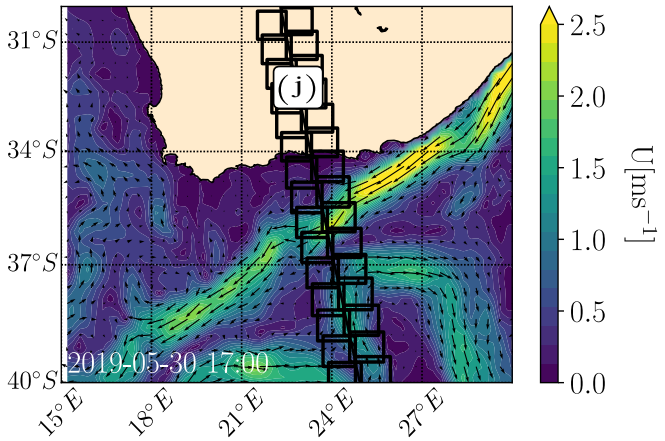

Figure 5.11: Panel (a-i): Wave frequency-direction spectra along SWIM altimeter track measured by 06° beam on May 30, 2019 at 05:00 p.m. The blind cone on both sides of flight direction has been removed. The 0° and 180° are aligned to the geographical north. The center box coordinates (70km x 90km) are given above each spectrum. The southernmost boxes are plotted in the top left panel (a) and so on until the northernmost boxes which are plotted on the bottom right panel (i). Panel j shows instantaneous current velocity (Globcurrent product).

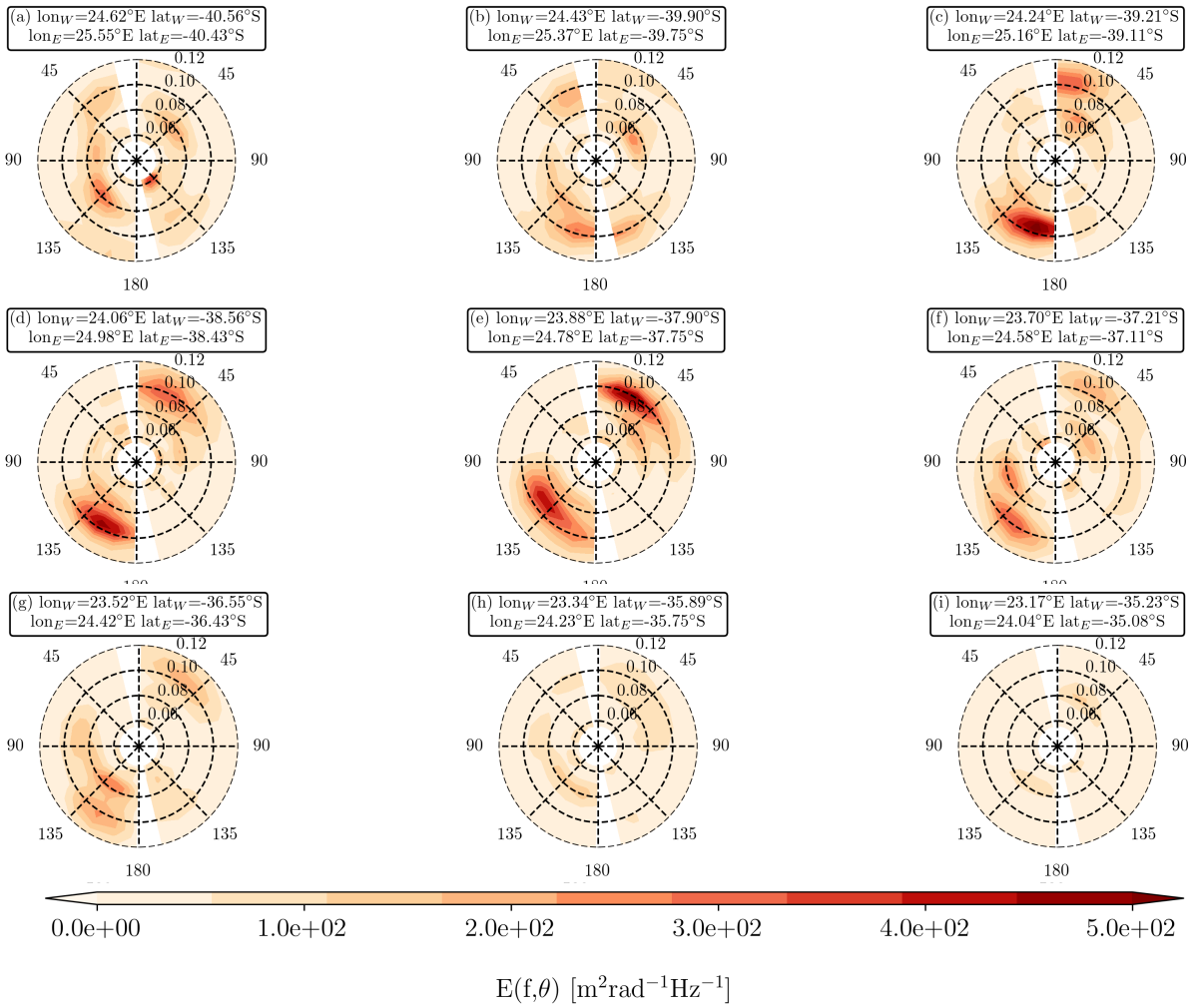

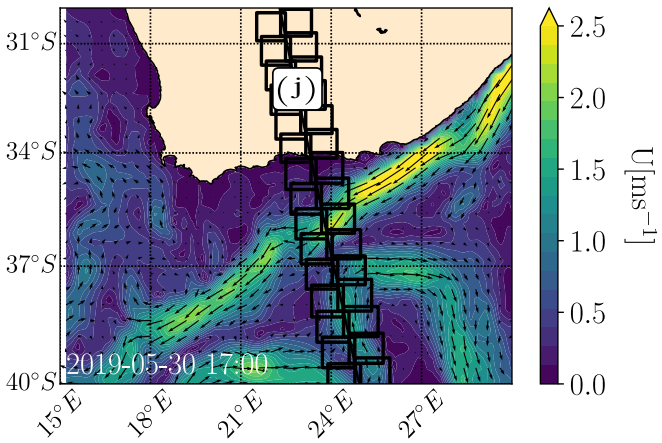

Figure 5.12: Same as Fig. 5.11 for 08° incidence.

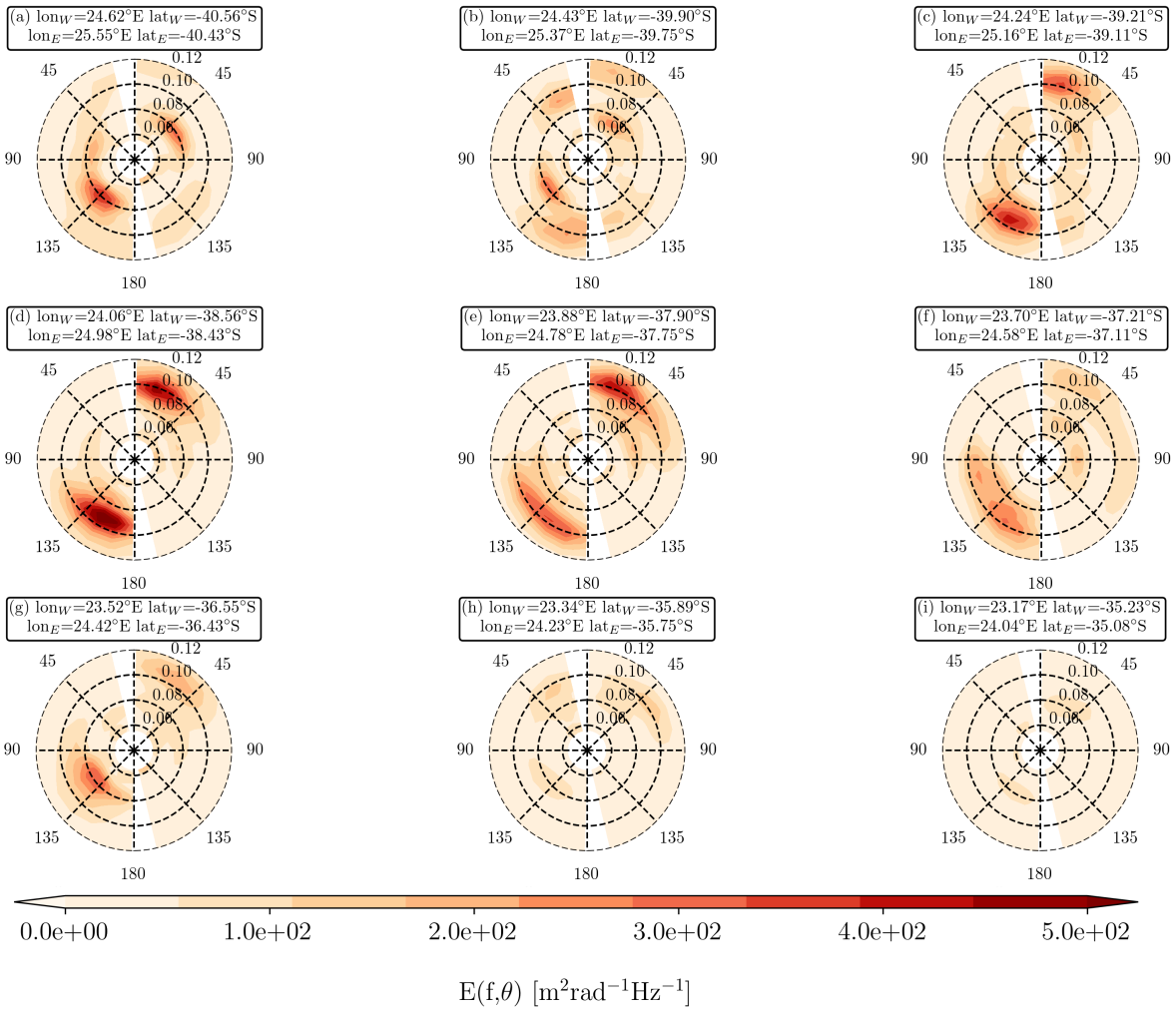

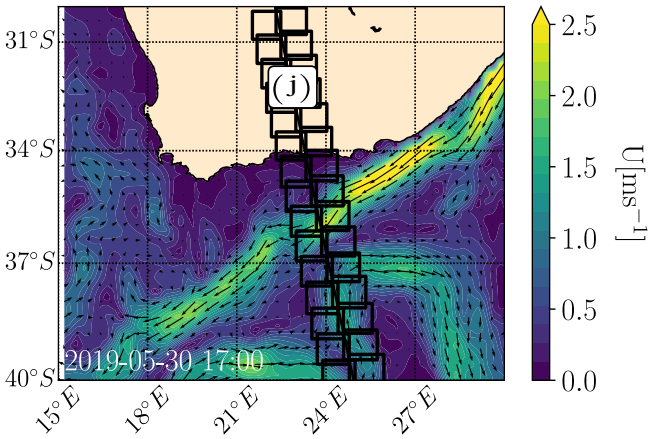

Figure 5.13: Same as Fig. 5.11 for 10° incidence.

However the separation between swell and wind sea is not trivial in this example, indeed both systems can be hidden in the frequency band of the other. Also we have only displayed waves longer than 100 m, modifying the upper frequency band to 0.14 Hz (shorter waves) in the sixth boxes it reveals wind sea partition spread both in direction and frequency but much less energetic than the swell partitions (not shown).

For both cases, please note that we have not shown all the changes in azimuth, frequency, or the emergence of bimodal sea states. However one can say that via the three studied SWIM-incidences and the wave frequency-direction measurements, the wave spectrum is strongly modified in the Agulhas current region. We propose to summarize those perturbations by looking at the evolution of the associated bulk parameters (H_s, $T_{m0,-1}$, θ_m, σ_θ) for the six cases introduced above.

5.2.4 Bulk parameters from SWIM spectra

We now focus on integrated wave parameters H_s, $T_{m0,-1}$, θ_m, and σ_θ calculated from SWIM directional spectra and their evolution across currents fronts. The mean wave direction, θ_m, computed for the east and the west boxes (on both sides of SWIM altimeter) have been projected on the same frame of coordinate between 0° and 180°. We will see that the H_s computed from off-nadir measurements match with the H_{snadir} (see Eq.5.5).

May 07, 2019 at 05:00 a.m.

A warm and salty Agulhas ring that detaches from the Agulhas tail at $\sim$ 40°S induces a strong gradient in the wave height signal (Fig. 5.17b). At 39.3°S, ∇ H_{snadir} is very sharp but hardly reproduced by off-nadir measurements. Indeed ∇H_s are spread out over 70 km (height of the boxes). As SWIM altimeter is not the unique satellite that provides H_s nadir measurements in the Agulhas current region, we compare its results with other altimeters missions for on May 07, 2019[1]. In particular we use one Cryosat-2 track which crosses the 70x90km east boxes (Fig. 5.18left), altimeter data are from Dodet et al. (2020). Cryosat-2 altimeter does not capture the strong ∇H_s around 39.5° (Fig.5.18) meaning that ∇H_s is very localized spatially. This highlights one of the limits of the simplified MTF, although spectra are estimated on both sides of the altimeter track the integrated H_s are identical. It means that H_s is assumed to be homogeneous over a distance of 180 km which is not consistent with Ardhuin et al. (2017); Quilfen et al. (2018); Marechal and Ardhuin (2021) findings. Further note that 1 Hz SWH data provided by nadir measurement of SWIM instrument is less noisy than Cryosat-2 *adjusted* measurements.

$T_{m0,-1}$ estimated in boxes reveals a longitudinal $T_{m0,-1}$ gradient (triangles versus crosses, Fig.5.17c) around 38.5°S meaning that waves are globally shorter at the west of the altimeter track typically where the localized ∇H$_s$ has been measured (Fig.5.18). At smaller latitudes $T_{m0,-1}$ are more coherent for each incidence and are increasing by 2s. One can see a sharp period gradient at 06° incidence between 37°S and 36°S where $T_{m0,-1}$=4 s is measured in the west box. It is located where a smooth ∇H_{snadir} is measured.

θ_m seem to capture the surface current-induced refraction (Villas Bôas et al., 2020). θ_m oscillate around θ=100° (Fig.5.17d). Measurements performed by 06° antenna show several quick changes of θ_m particularly where the surface current is strong (Fig.5.17a,f). We focus on the measurements in west boxes acquired by the 06° incidence. From 40°S and 38°S wave direction changes from 80° to 120°, then changes from 120° to 90° between 38°S and 36.5°S and finally changes from 90° to 120° between 36.5°S and 35°S. θ_m in east boxes are quite consistent with those measurements. For the 08° and 10° incidences between 40°S and 38°S, the θ_m oscillations are weaker, mean

1. in 2019 we count 9 operational altimeters monitoring wave height at global scale – Ardhuin et al. (2019b))

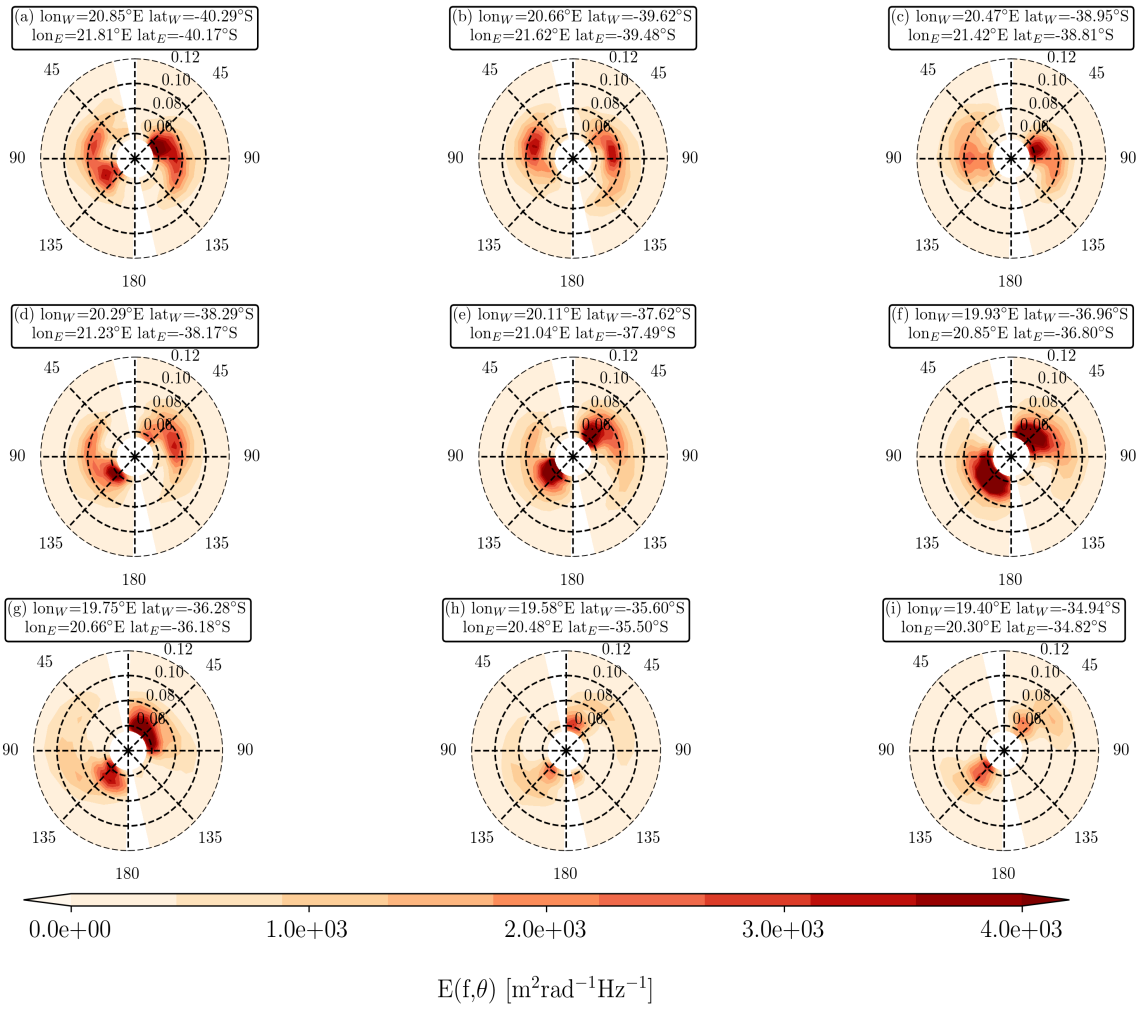

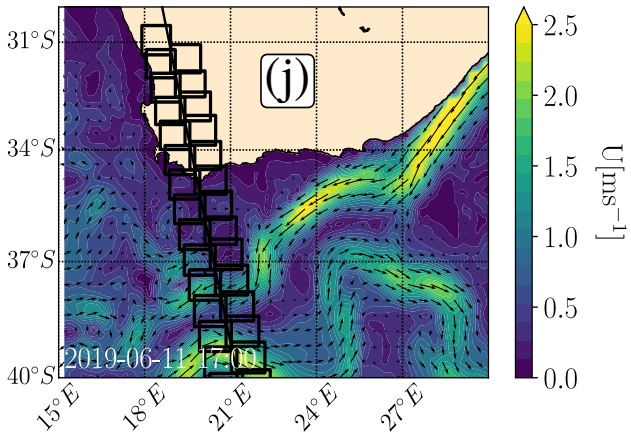

Figure 5.14: Same as Fig. 5.14 for measurements on June 11, 2019 at 05:00 p.m.

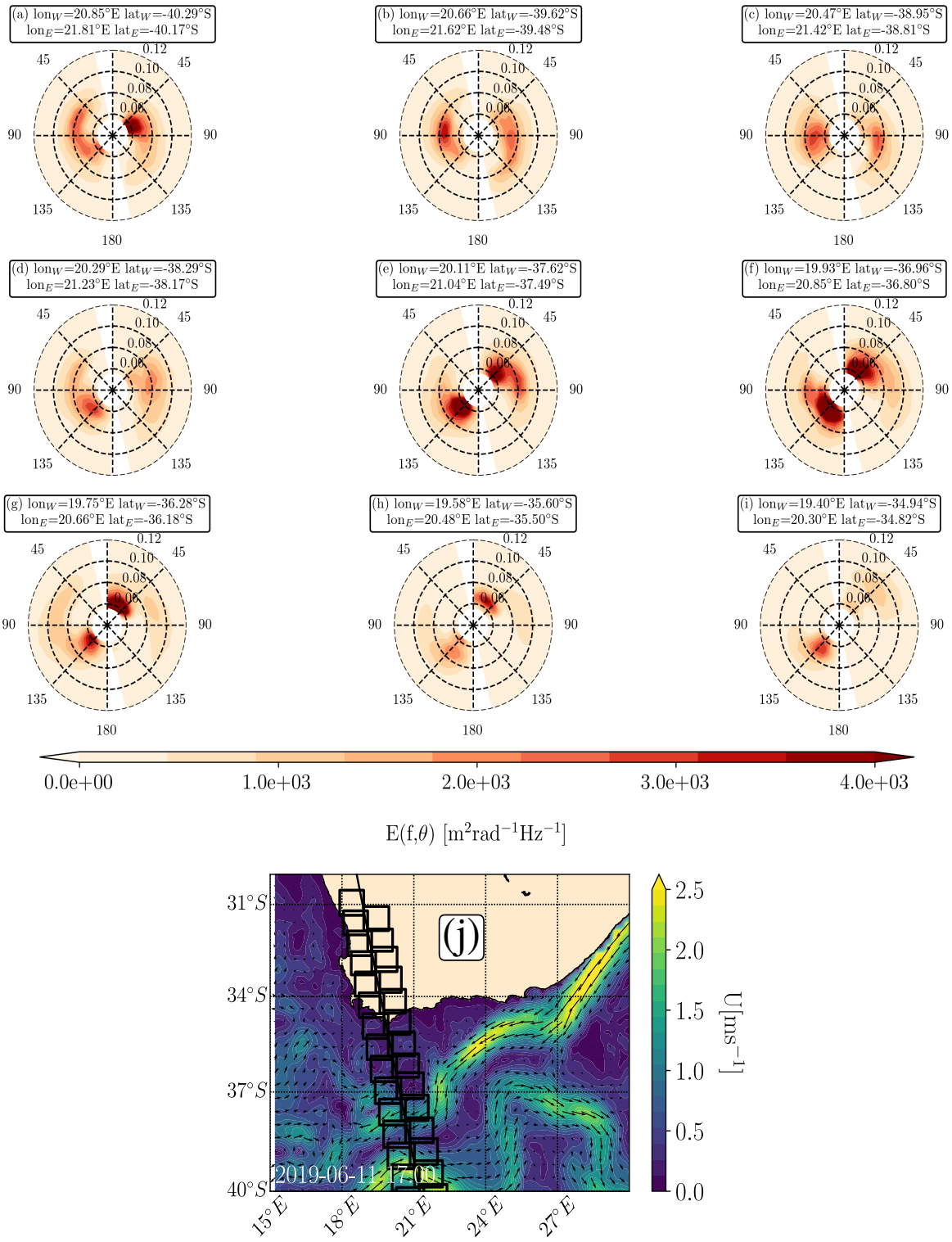

Figure 5.15: Same as Fig. 5.14 for 08° incidence.

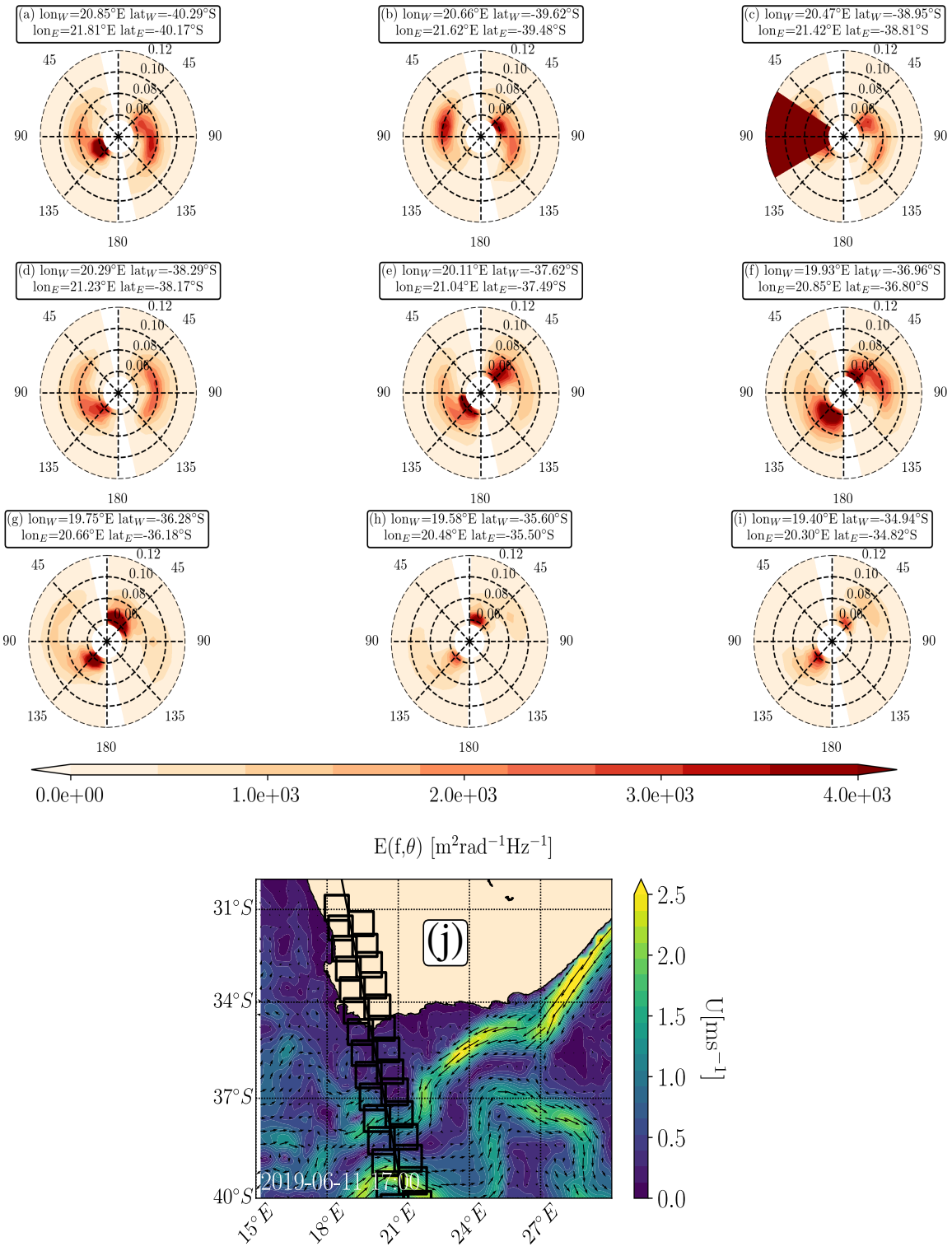

Figure 5.16: Same as Fig. 5.14 for 10° incidence.

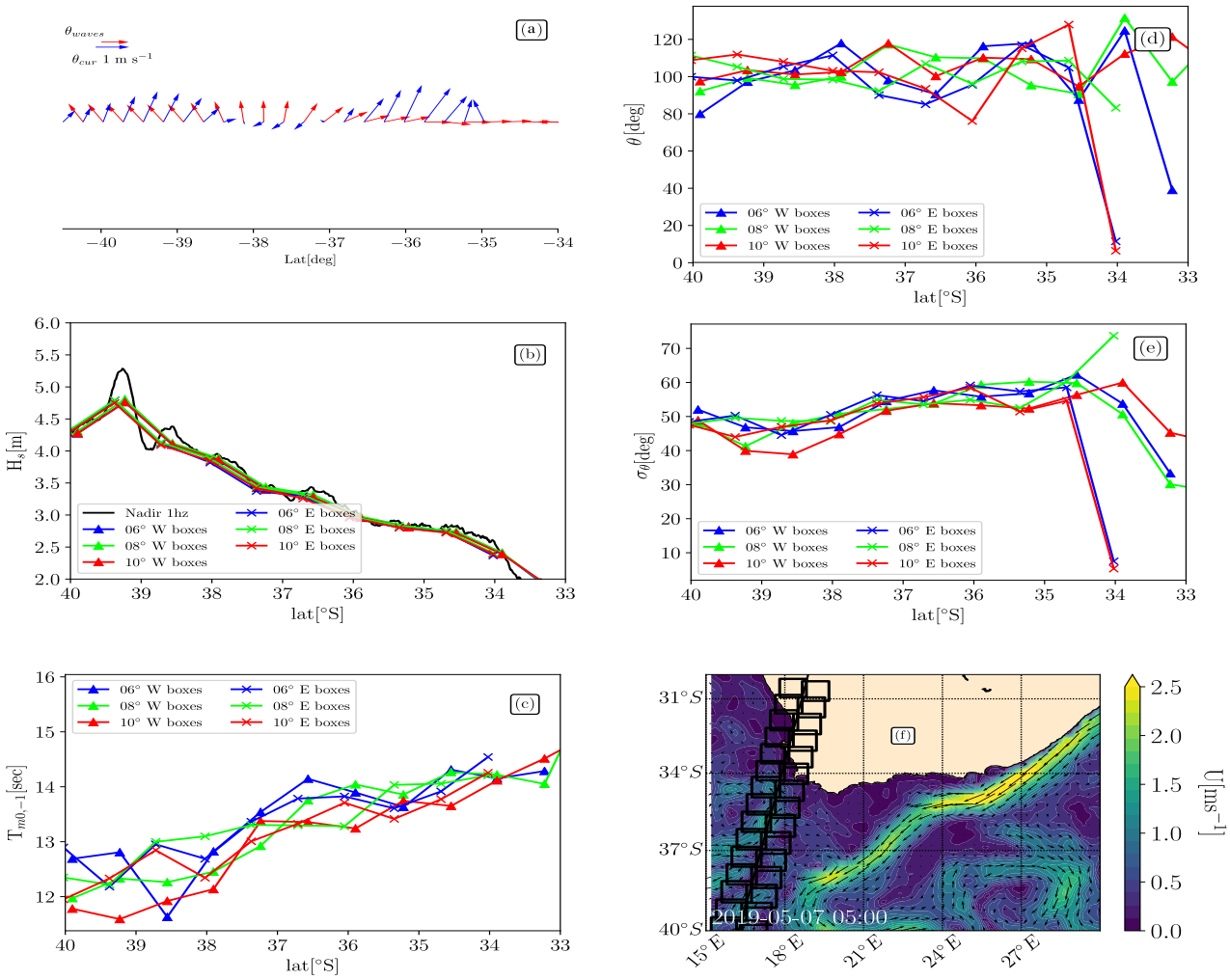

Figure 5.17: The left column: (a) waves and current direction from wave simulations (current direction is given by the blue arrows and waves direction by the red arrows) interpolated along SWIM-altimeter track, (b) significant wave height (H_s) measured by SWIM-altimeter and calculated from SWIM off-nadir beams, (c) mean wave period ($T_{m0,-1}$). Right column: (d) mean wave direction (θ_m), (e) directional spreading (σ_θ, (f) snapshot of the surface current from the Globcurrent project during SWIM flight over the Agulhas current. Altimeter track and boxes where wave spectra are averaged are given over the current field. Blue lines, green lines and red lines on panels (b), (c), (d), (e) are SWIM measurements performed by the 06°, 08° and 10° SWIM beams respectively.

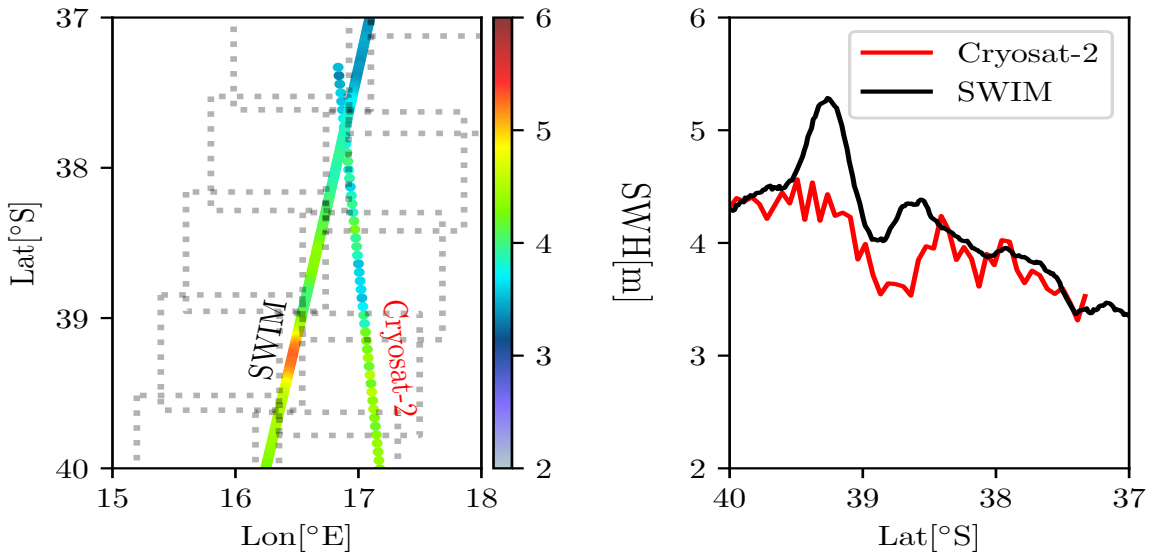

Figure 5.18: (left) Significant wave height measurements provided by SWIM and Cryosat-2 altimeters in the Agulhas current region. (right) Along track significant wave height for both altimeters.

gradient directions are, however, noticeable at smaller latitudes specially for measurements in east boxes performed by the 10° incidence. We notice a mean direction change from 75° to 125° between 36°S and 34.5°S. At smaller latitudes, when measurements approach the South African coast, θ_m show outliers (06° and 10° incidence).

The directional spreading, σ_θ, follows the tendency of $T_{m0,-1}$ (Fig.5.17e). The directional spreading is the thinnest where the sharpest $\nabla \mathrm{H}_{snadir}$ is measured (Fig.5.17b) especially for 10° measurements in the West boxes. At latitudes smaller than 38°S, σ_θ remains constant and oscillates around 55° for each incidence and both sides of altimeter tracks.

May 16, 2019 at 05:00 a.m.

Sharp $\nabla \mathrm{H}_{snadir}$ are measured at 39°S (in the Agulhas return current's elbow), ∼37.5°S (in the Agulhas return current) and between 36°S and 34°S (in the main Agulhas system) (Fig.5.19b). At these latitudes surface currents are weak and perpendicular to the mean wave direction, strong and aligned with the waves (then at 45° at 37°S) and finally very strong and opposed with waves (Fig.5.19a). Every off-nadir beam measurement is consistent with each other, nevertheless quick changes of H_{snadir} measured by 1 Hz altimeter data are not at all captured by SWIM spectrometer due to the size of boxes as noticed above.

The mean wave period (Fig.5.19c) oscillates around 12 s. A clear decrease of $T_{m0,-1}$ is captured by all incidences on both sides of the altimeter track where waves and currents start to be in opposite direction as between 36°S and 34°S (except for the 06° incidence, we will not consider this beam for this case). These gradients are consistent with the dispersion relationship in a current field ($\omega = \sigma + \mathbf{k.u}$), waves become shorter if waves and current are opposite Between 38°S and 37°S,the 08° beam measure a strong gradient of $T_{m0,-1}$ on both sides of the altimeter track ($\Delta T_{m0,-1} \sim 1$ s). One can see a convergence of $T_{m0,-1}$ around 12s for each incidence between 39°S and 38°S which seems to be associated to the Agulhas return current.

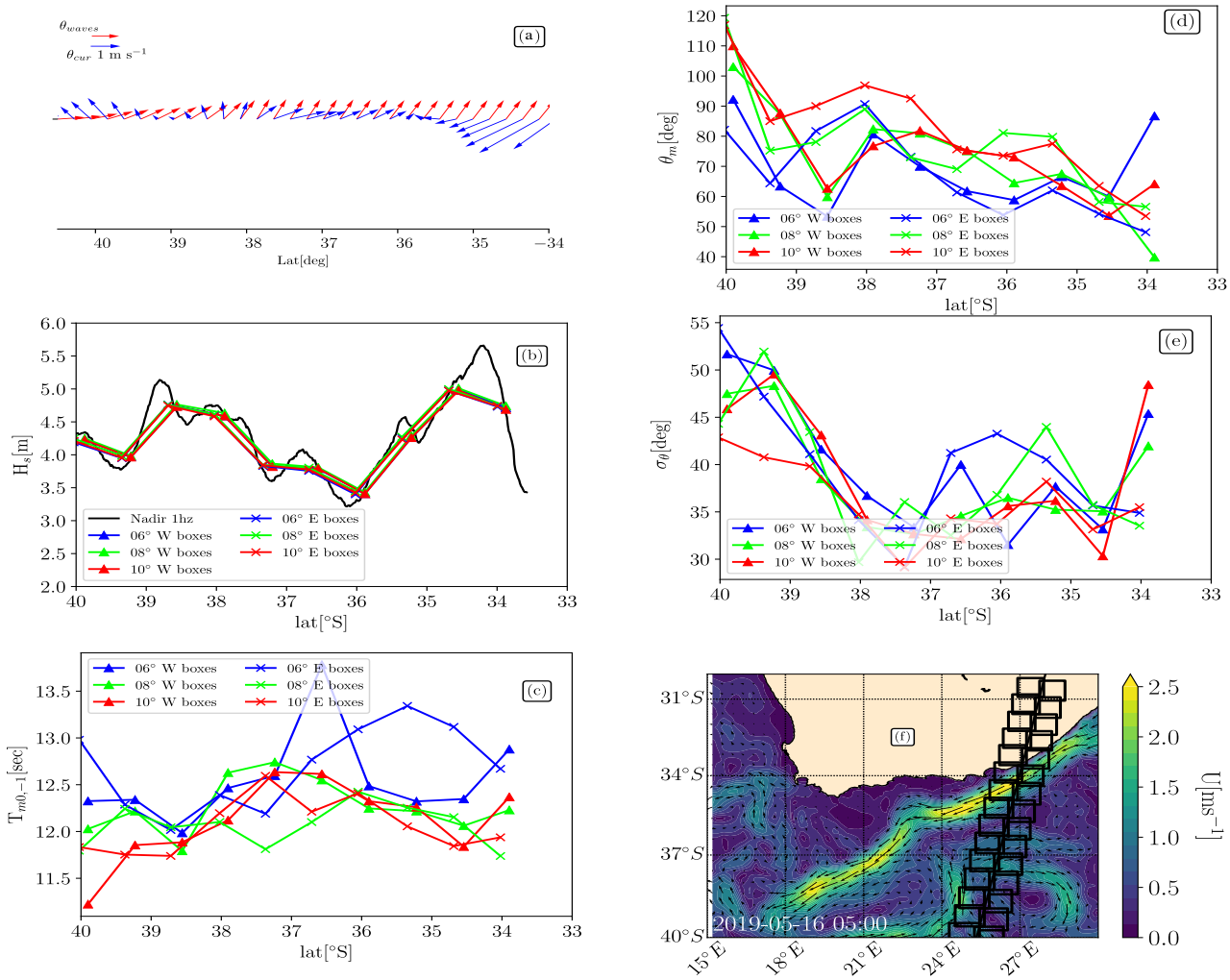

Figure 5.19: Same figure as Fig.5.17 for SWIM measurements acquired on May 16, 2019 at 05:00 a.m

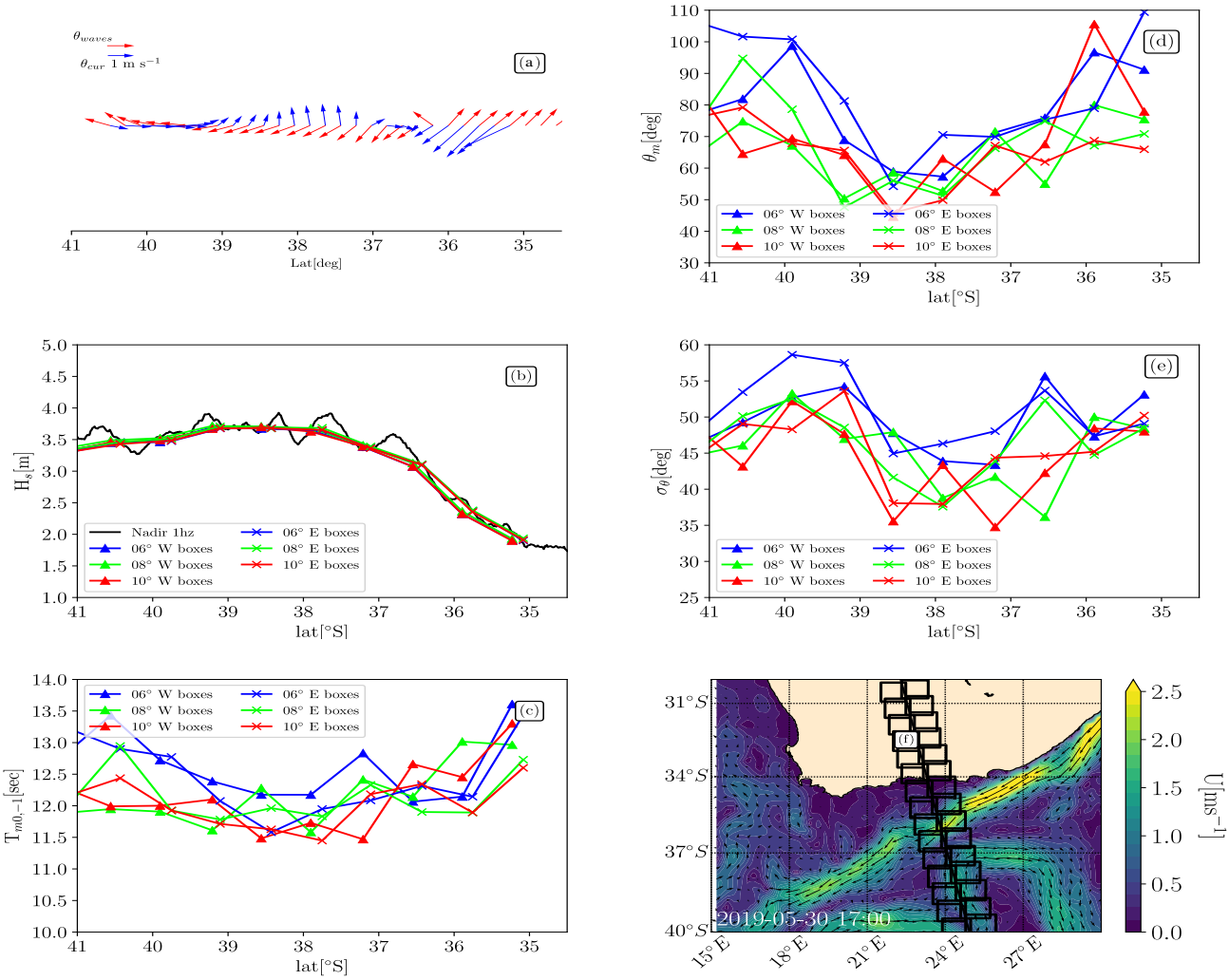

Figure 5.20: Same figure as Fig.5.17 for SWIM measurements acquired on May 30, 2019 at 05:00 p.m.

One can see a gradient of mean direction according to the incidence angle at 40°S. Then, along latitudes, wave mean direction (Fig.5.19d) shows four waves regimes. A first regime is noticeable between 40°S and $\sim$ 38.5°S, a second one between 38.5° and 36.5°S, a third one between 36.5°S and 35.5°S and a last one between 35.5°S and 34.5°S. The four regimes are located where the four main ∇H_s are measured (Fig.5.19b). The computed θ_m show a large variability according to the incidence especially in the Agulhas return current between 40° and 37°.

The directional spreading decreases strongly for each SWIM incidences from 40°S to 37°S (from σ_θ=50° to σ_θ=30°). At smaller latitudes the directional spreading oscillates around 35°. We recall that we are not interested in the 06° incidence for the east boxes. Finally, σ_θ strongly increase in the west boxes at the location of the coastal Agulhas current at 34°S.

May 30, 2019 at 05:00 p.m

H_{snadir} measurements show two H_s regimes, one oscillating between 3 m and 4 m within 40°S and 36.5°S and a clear decrease from 36.5°S to South Africa's coast where $H_s = 2$ m. Let us note that the H_s variability between 37° and 36.5° is due to the main Agulhas branch (flowing southwestward, Fig5.20a,f) and the other ones due to the Agulhas return current (flowing northward,Fig5.20a,f). One can see that H_s from off-nadir measurements does not capture the effects of the current. $T_{m0,-1}$ reveal longer waves where H_s decreases (from 36.5°S to South Africa's coast at 35°S, Fig.5.20c), period changes by an average of 1.5s in a half a degree. From 41°S to 36.5°S $T_{m0,-1}$ oscillates around a mean value of 12s with the highest value for the spectra measured by 06° in west boxes. In the main Agulhas branch (36.5°S), $T_{m0,-1}$ converges to $\sim$ 12s for all incidences. θ_m captures two wave regimes (Fig.5.20d) which corroborate the position of the Agulhas current fronts. One between 41°S and 37.5°S where mean directions change abruptly and a second one between 37.5°S and 35.5°S where waves cross the main Agulhas current branch. One can see a clear mean wave direction gradient according to the incidence angle of the beams especially in the Agulhas return current (between 41°S and 38°S). The evolution of σ_θ follows qualitatively the evolution of $T_{m0,-1}$ and θ_m. Where waves becomes shorter (smaller $T_{m0,-1}$) σ_θ becomes smaller and the mean direction changes sharply (between 41°S and 38.5°S). Between 38.5°S and 37°S, σ_θ oscillates around 35° and 45°, and finally converge between 45° and 50° for all incidences north of the main Agulhas front.

June 11, 2019 at 05:00 p.m.

The most striking point in the case studied here is the strong ∇H_{snadir} measured within 37.3°S and 36.5°S (Fig 5.21b). At those latitudes, the simulated mean wave direction is perpendicular to the large-scale current (Fig.5.21a). There is globally a good coherence between nadir and off-nadir measurements along latitudes, however, this huge gradient is hardly reproduced by off-nadir beams. It is likely that with an analytical MTF between $P_m(f,\theta)$ and $E(f,\theta)$ (i.e., based on Jackson (1987) works among others), we might see a difference in the measurements performed on both sides of altimeter tracks. Fig 5.21c shows very different $T_{m0,-1}$ acquired in west boxes and east boxes between 39°S and 36°S. Fig.5.21d shows that θ_m changes from θ_m $\sim$90° at 40°S to 65° at 37.5°S. These changes are not captured by the numerical model (Fig.5.21a). It is likely that these changes are current-induced. Thus waves might be refracted by the Agulhas retroflexion just before inducing the strong ∇H_s at latitude equal to 37°S. Between 37°S and 35°S θ_m strongly oscillates with a convergence of the θ_m at 35.5°S where waves are propagating at 50° (northeastward) which is consistent with simulated wave direction (Fig.5.21a).

Contrary to the previous cases, σ_θ is relatively constant for all incidences between 41°S and 37°S. Also waves are much more directional than the previous cases, σ_θ $\sim$35°. In the Agulhas retroflexion one can see a symmetry in the σ_θ measurements. In the east box σ_θ is stronger than in the west box. Where the strong ∇H_s is measured one can see an increase of σ_θ for each incidence. A little further north the 06° incident beam measures wave systems less directional. Those quick changes seem to be contaminated by the measurement noise.

June 13, 2019 at 05:00 p.m.

H_{snadir} shows high frequency variability both in the large-scale Agulhas current (return current and main system) and outside. The negative gradient at 38° (Fig.5.22b) coincides with the Agulhas return current flowing toward the east (Fig.5.22f) whereas waves and currents are not aligned (Fig.5.22a). One can see that the extremes are strongly

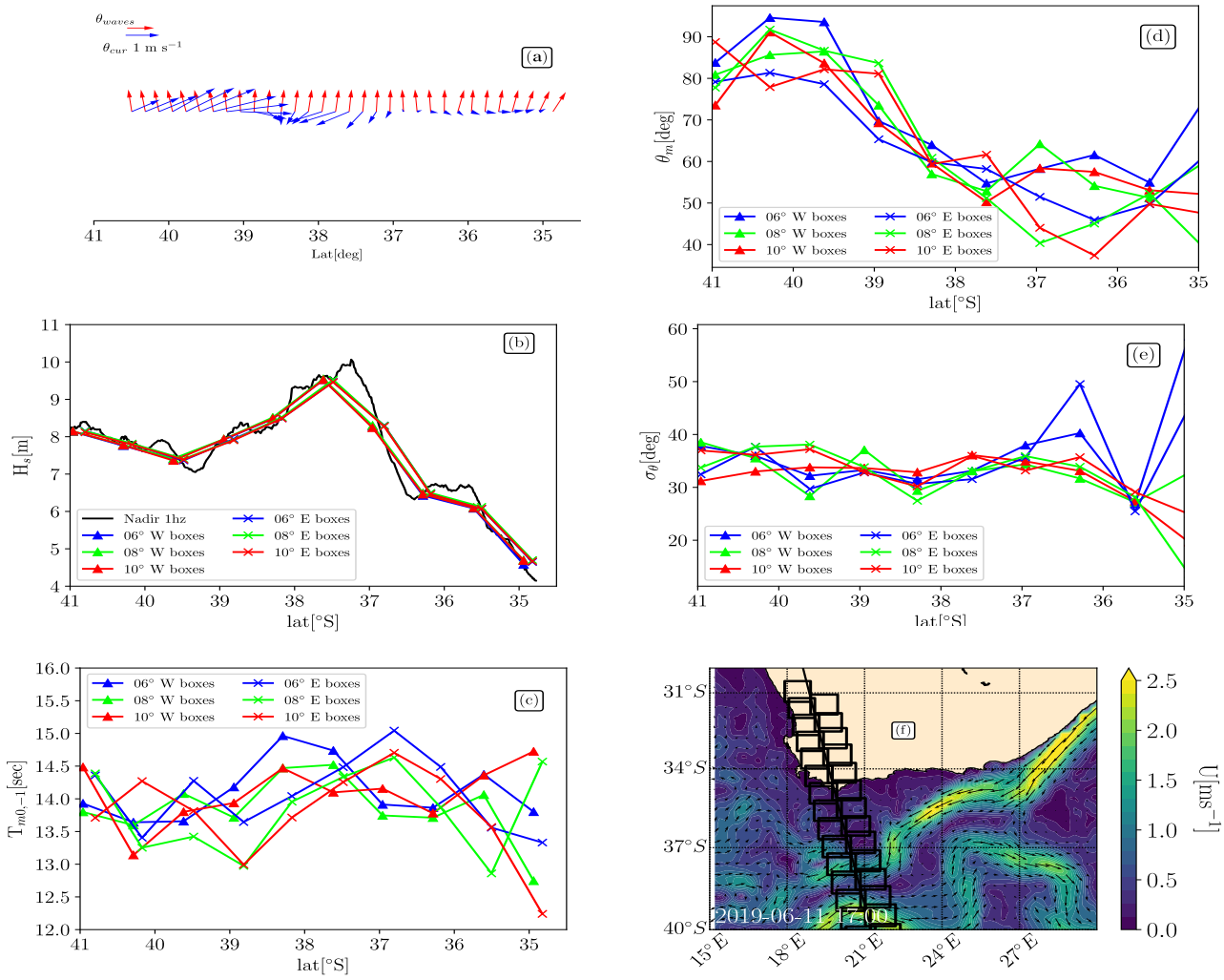

Figure 5.21: Same figure as Fig.5.17 for SWIM measurements acquired on June 11, 2019 at 05:00 p.m.

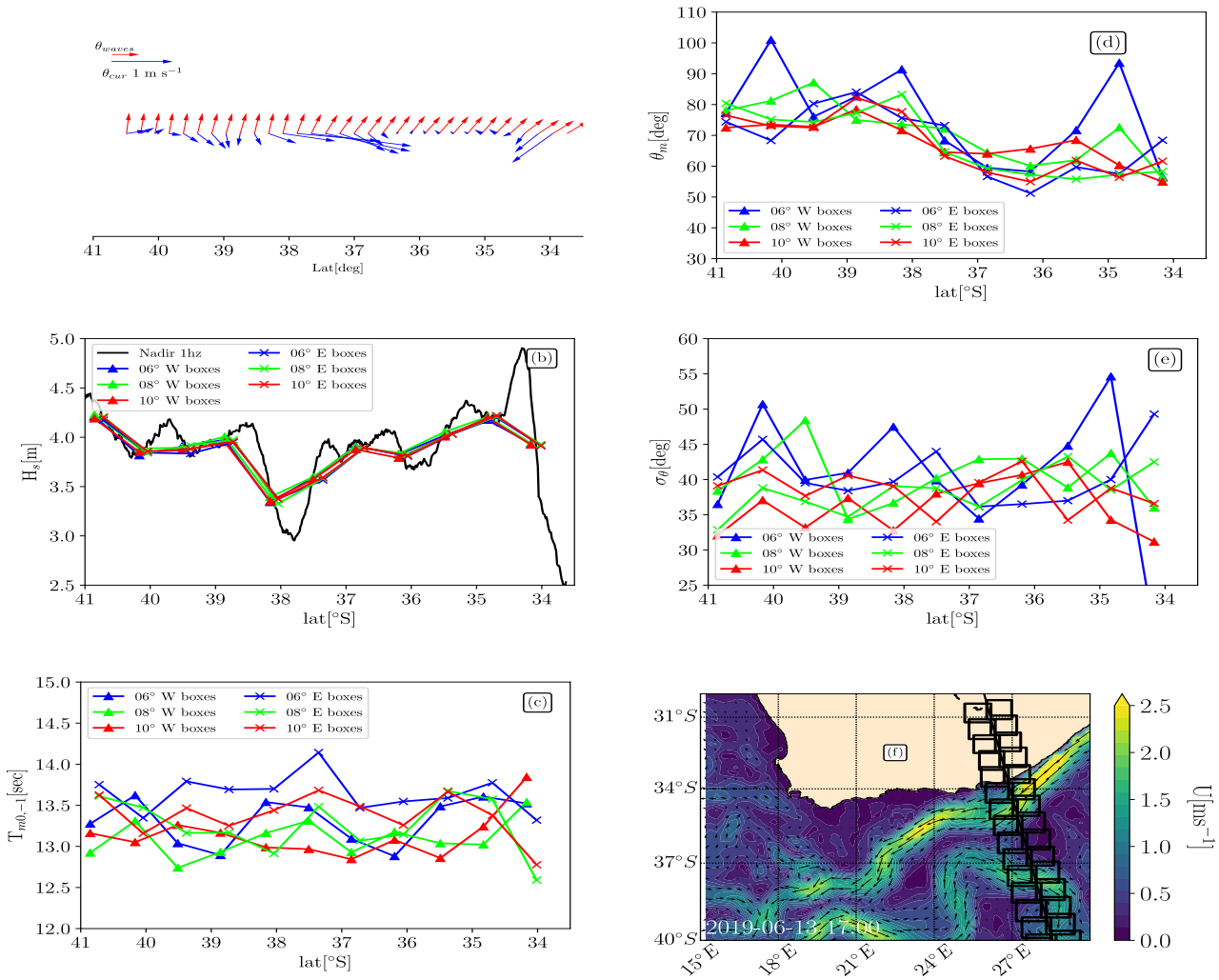

Figure 5.22: Same figure as Fig.5.21 for SWIM measurements acquired on June 13, 2019 at 05:00 p.m.

underestimated by the off-nadir H_s or even completely missed as for the very sharp $\nabla \mathrm{H}_{snadir}$ along the coast at the south of South Africa, at 34°S.

SWIM measurements do not show strong variability of the $T_{m0,-1}$ in the Agulhas current region except around 38°S where all the incidence angles on both sides of altimeter track measure a slight increase of $T_{m0,-1}$ (Fig.5.22c), an exception at least for measurements in west boxes performed by the 10° incidence. According to the current-induced Doppler shift theory, the quick changes of H_s at the same latitude could be associated with the change of wavelength. Similarly it is expected that the strong H_{snadir} enhancement at 34° and the fact that waves and currents are in opposite direction is associated with a decrease of $T_{m0,-1}$. This is only the case for measurements in the last east boxes for all incidences. In terms of θ_m we can see two wave regimes (Fig.5.22), we do not consider the measurements performed in the west boxes by the 06° beam. One between 41°S and 38°S where θ_m oscillates around 70° and 80°, and a second one between 38°S and 34°S where $\theta_m \sim 60°$ (deflected toward the northwest). This transition occurs where waves start to leave the Agulhas return current and where the altimeter measures a strong negative ∇H_s. Finally, σ_θ is strongly modified on both sides of the altimeter, for each incidence and all along the SWIM flight over the Agulhas current region. We observe that σ_θ globally increase for each incidence between 41° and 40° and between 35.5° and 34° where almost all incidences present an increase in between the two parallels.

July 08, 2019 at 05:00p.m.

A very high and localized $\nabla \mathrm{H}_{snadir}$ is measured in the vicinity of 36°S. This $\nabla \mathrm{H}_{snadir}$ is hardly reproduced by off-nadir measurements. Nevertheless the secondary $\nabla \mathrm{H}_{snnadir}$ within 40°S and 39°S is well captured by off-nadir observations because the gradient is not too sharp. Waves and current are globally aligned in the same direction between 40°S and 37°S, whereas around the main $\nabla \mathrm{H}_{snadir}$, simulated waves and large-scale currents are totally opposed (Fig.5.23a). Simulated mean wave direction is homogeneous all along SWIM flight which is not the case for measurements by off-nadir measurements (Fig.5.23d). Waves turn from $\theta \sim 100°$ in the southernmost part of the Agulhas to 40° close to the South coast of South Africa. 06° beam measurements provide the same trend in the directional measurements with some variations especially for measurements in the west boxes. One can notice a clear gradient between 41°S and 40°S between the three incidences.

$T_{m0,-1}$ oscillates around 12s for the three incidences on both sides of the altimeter measurements (Fig.5.23). There is a slight trend from shorter wave systems to longer wave systems between 41°S and the South coast of South Africa.

The directional spreading shows three wave regimes along the SWIM track. Waves become more and more directional between 41°S and 39°S, then their spreading oscillate around 40° between 39°S and 37°S. Finally waves become much more directional downstream the sharpest $\nabla \mathrm{H}_{snadir}$.

Summary of six cases measured by SWIM in the Agulhas current region

H_s is measured by altimeter carried by the SWIM antenna. Strong $\nabla\ H_s$ are captured along the SWIM track. Those $\nabla\ H_s$ monitored can be negative or positive (with respect to the mean H_s measured along the track.) Positive $\nabla\ H_s$ are mainly measured in the main Agulhas branch in agreement with Quilfen et al. (2018),Quilfen and Chapron (2019), Marechal and Ardhuin (2021) results, and negative ones are seen at the edge of the Agulhas return current (flowing eastward). SWIM is a new spectrometer at rotating beams measuring at 5 different incidences

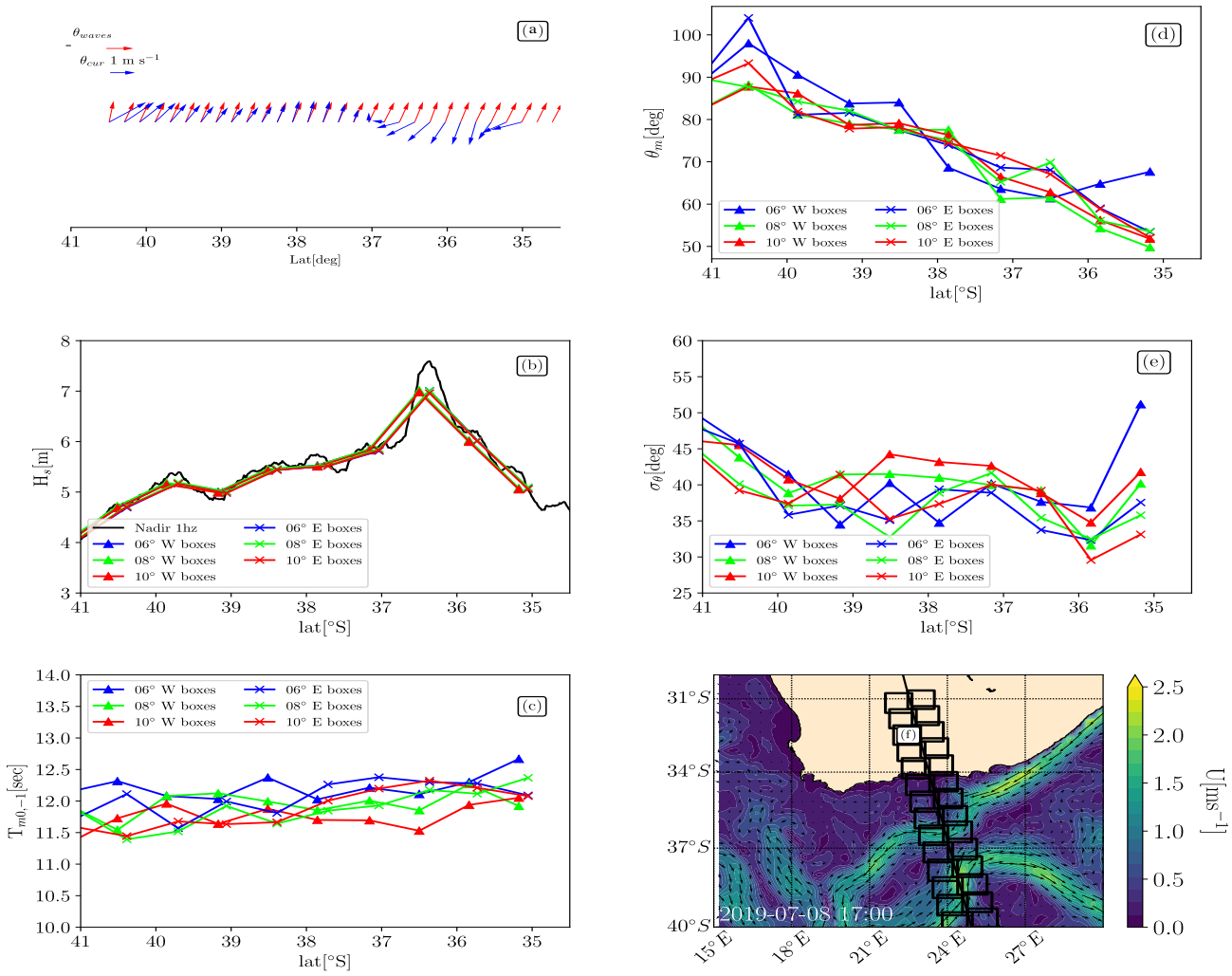

Figure 5.23: Same figure as Fig.5.17 for SWIM measurements acquired on June 13, 2019 at 05:00 p.m

the modulations induced by a wavy surface. A transfer function between modulation and wave spectrum has been developed combining modulation spectra and H_{snadir}. Thanks to this wave spectrum, wave parameters (significant wave height, mean direction, mean wave period and directional spreading) are estimated every ∼70 km in 70 km × 90 km boxes. H_s from off-nadir measurements coincide with the altimeter because of the considered MTF. Nevertheless very localized ∇ H_s are not reproduced by off-nadir measurements (06°, 08° and 10°) due to the under-sampling of wave spectra induced by box size (too coarse). Mean wave period ($T_{m0,-1}$) is sampled along the satellite flight at each incidence. Current-induced Doppler shift on the wave frequency is well captured by SWIM wave spectrometers. Some cases (panel (c) of Fig.5.17,5.19) have shown that $T_{m0,-1}$ decreases where H_s increases, typically in the main Agulhas current. This H_s enhancement was expected by the linear theory described in the introduction chapter. However all data do not provide an easy link between current-induced H_s changes and $T_{m0,-1}$ variability. It has been shown as well that the 06° beam provides, statistically, more variability with respect to 08° and 10° which are more stable. One could combine those measurements with other remote sensing of in-situ observation to conclude if those differences are geophysical or driven by the antenna itself.

Finally mean wave direction and directional spreading have been estimated in each box. As refraction is the main source of H_s variability (Ardhuin et al., 2017; Romero et al., 2020; Marechal and Ardhuin, 2021) there was a lot of reliance on wave measurements provided by SWIM. The six previous cases have shown some changes of the directional variables along SWIM flight, particularly where the satellite crosses current fronts. However we couldn't be more conclusive than former studies also dealing with a wave spectrum retrieved from space (Kudryavtsev et al., 2017b; Quilfen et al., 20180). Nevertheless one can note that the strongest ∇ H_{snadir} were, most of the time, associated with wide directional wave system as described in Heller (2005) and in chapter 1. The current refraction redistributes the wave action and creates some areas where wave action are focalized. It leads to a large directional spreading (see Fig.2.3d). Also in the study of Marechal and Ardhuin (2021), authors find that the more incident waves are directional, the more wave action is focalized and the sharper are the ∇H_s. In the case on June 11, 2019, around the strong ∇H_s the incident waves have an incident σ_θ of around 30° then this σ_θ increases at 37° where the maximum value of H_s is measured by the altimeter. Downstream σ_θ . This case agrees with the theoretical results presented in chapter 1 (Fig.2.3).

Limitations of this study include the fact that boxes in which wave parameters are estimated are too wide to assume a homogeneous wave and wind field. Also, the ocean surface is very dynamic at the mesoscale and submesoscale range $\mathcal{O}(100km - 1km)$, thus all the wave variability induced by such small oceanic features are averaged in the wave spectrum in the boxes. A proof why the box size is an issue for studying current effects on waves is given in Fig.5.24 for a current front. One can see that two wave regimes are measured inside one box, a rough and a smooth sea. If the three incidences overlap the two systems, we are not able to have access to wave parameters gradients induced by such current patterns. Those gradients will certainly be drowned in the averaged signal. We face to the same issue that was discussed on Marechal and Ardhuin (2021). As small currents have large effects on the wave parameters, the resolution of the currents is crucial to reproduce those effects well in numerical models. In a similar manner, the devices used to capture the surface current effects on waves must be sufficiently efficient to measure waves at small scale. It was one of the motivations of the filtering of the altimeter data with the EMD method.

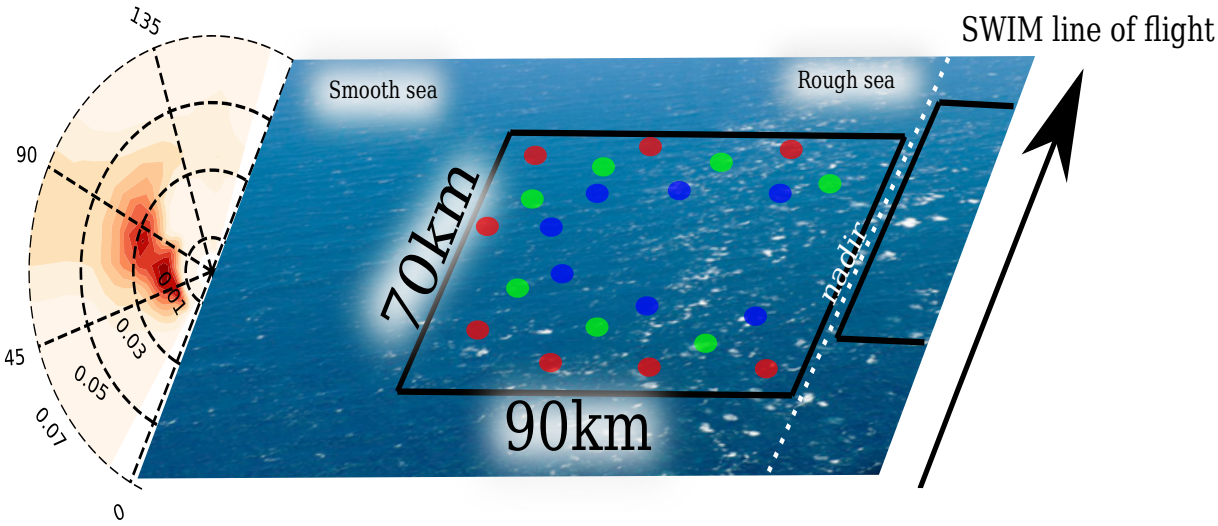

Figure 5.24: (Right) Sketch of SWIM spectral measurements on a non-homogeneous field due to the presence of current front (sea surface from Romero et al. (2017)). Red, green and blue spots are footprints of 10°, 08°, 06° incidences. (Left) an example of averaged spectrum in the 90 km x 70 km box.

5.3 Why not working on raw level1 data?

Due to this lack of spatial resolution described in the previous section, we have focused on the same SWIM tracks, but without any averaging.

5.3.1 Presentation of the data

Here we do not present again the instrument and how it measures the ocean wave spectrum (see section above) In this section we are working on one-dimensional wavenumber spectra (P(k)) located at each footprint position (Fig.5.2a). Spectra are represented in the form of ribbons describing the fluctuation induced by the presence of surface gravity waves in function of wavenumber. We did not try to retrieve the wave spectrum. An example is given below for May 30, 2019 and June 11, 2019 (studied in the previous section). The main difference with this study is that we do not consider coarse positions of measurements (center of the boxes), but each discrete position of each footprint.

Peak parameters have been computed along SWIM measurements (θ_p,λ_p) rather than Bulk parameters (H_s, $T_{m0,-1}$, θ_m, σ_θ) for 06°, 08°, 10°. Each macrocycle (2π azimuth) has been cut according to the nadir measurements to provide semi spectra (E(f,θ) with $\theta \in$ [0,180°]) on both sides of the altimeter track . For each semi-macrocycle, the azimuth (ribbon) exhibiting the biggest fluctuation has been picked and the wavenumber as well. Considering that peak parameters are "true" (verified by the model outside current area by Li et al. (2021)), refraction and Doppler shift current induced might be followed.

5.3.2 Results of spectral SWIM ribbons

We considered two cases, already studied in the section above:

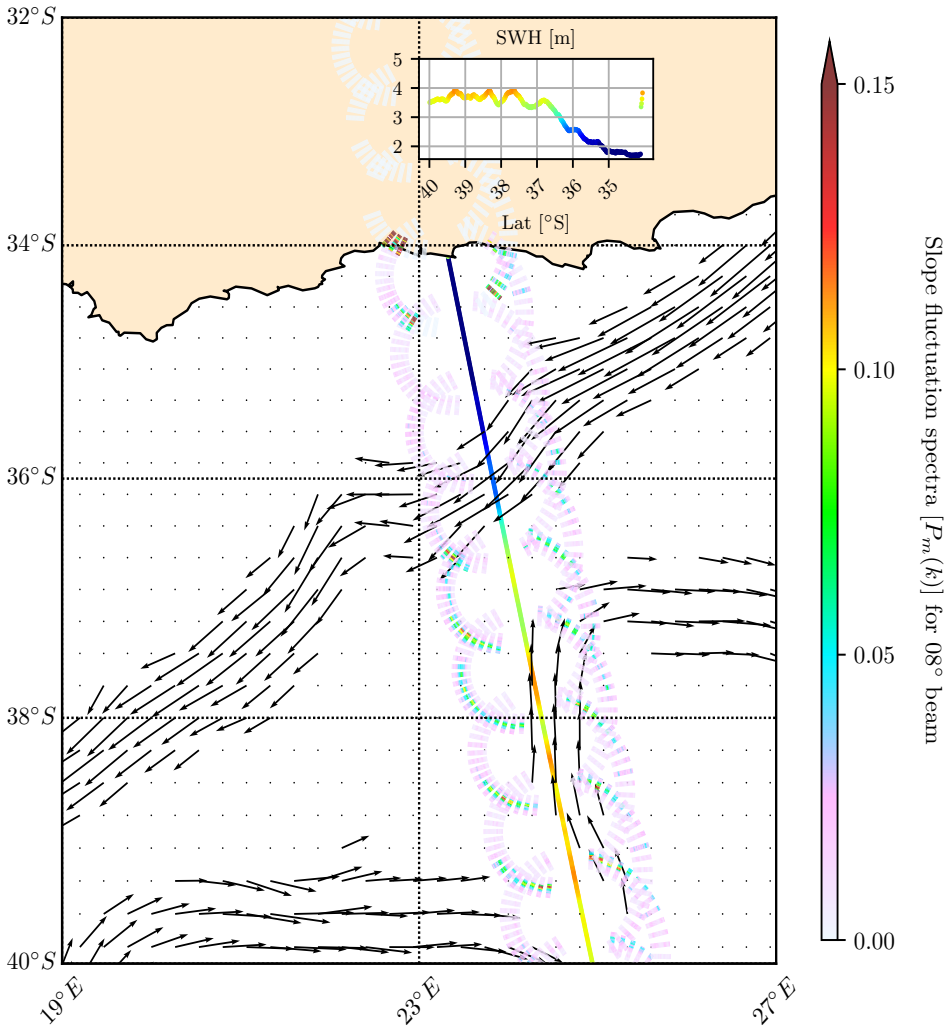

Figure 5.25: SWIM measurements over Agulhas current on May 30, 2019 at 05:00 p.m. (large-scale Agulhas current is plotted with arrows ; Globcurrent product). The altimeter measurements are given in the sub-panel and one dimensional fluctuation spectra (for 08° incidence measurements) are represented as colored ribbons.

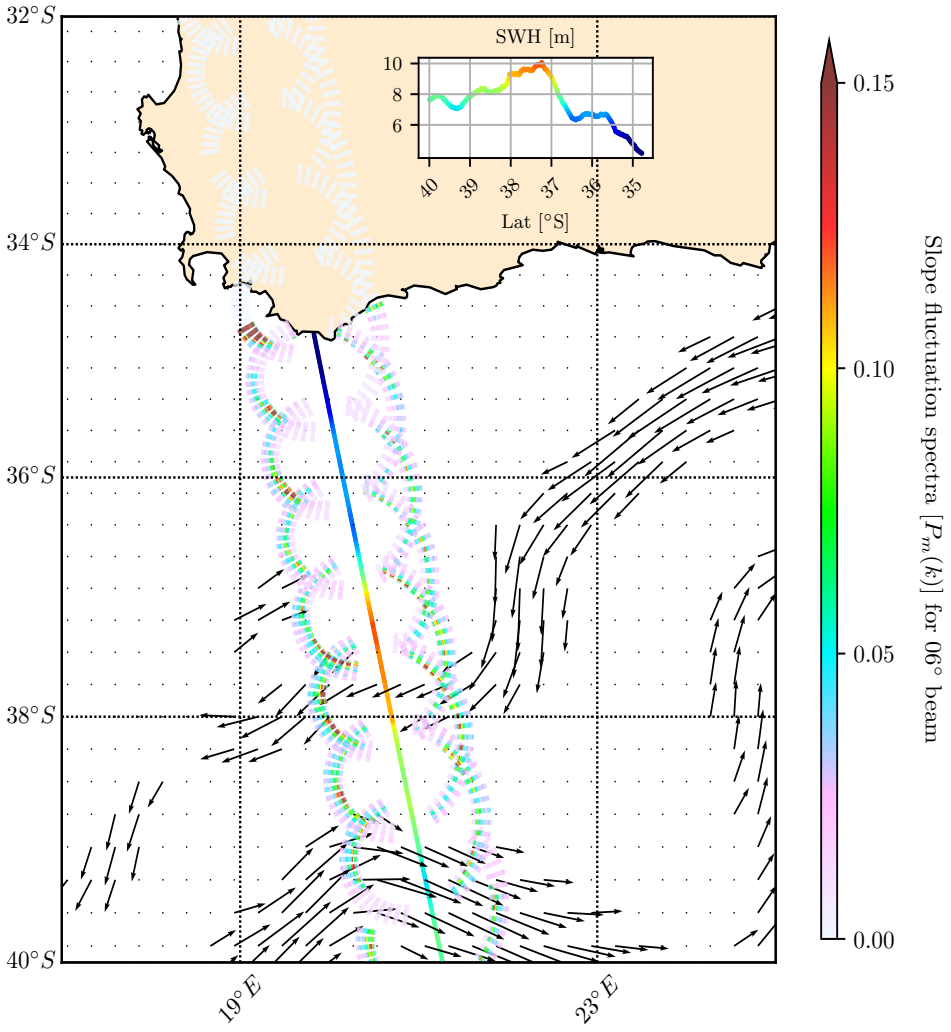

Figure 5.26: Same as 5.26 but for on June 11, 2019 at 05:00 p.m.

- May 30, 2019 at 05:00 p.m. -UTC
- June 11, 2019 at 05:00 p.m.-UTC

The two cases show a homogeneous wind field beneath SWIM measurements (Fig.5.7b and Fig.5.8b). Surface currents are not stationary between the two flights (see the Natal Pulse flowing southward, Fig.5.7a and Fig.5.8a). More accurate descriptions of those measurements and underlying geophysical fields are given earlier in this chapter.

May 30, 2019 at 05:00 p.m.-UTC

Here we focus on the peak parameters provided by each SWIM semi-macrocycles (west part and east part, both around the blind angle and altimeter track, Fig.5.26). Measurements all along a branch of the Agulhas return current, between 40° and 37.5° show homogeneous peak directions with a slight shift measured by the 06° beam at 37.5° (Fig.5.27). Between 36.5°S and 35°S all incidence beams, both for west and east measurements, are measuring a deviation toward the east ($\theta_p \sim 90°$). Only the 06° incidence does not capture this deviation and remains constant. The last measurements, close to the coast, highlight a new deviation southward with an exception for the 10° beam at the west of the nadir which shows a much stronger deviation of the peak energy.

Peak wavelengths are constant in the Agulhas return current as well. Waves become slightly longer to the north of the beginning of the deviation shown in Fig.5.27a with a very high value measured by the 10° beam around 35°S. Note that as wind is homogeneous beneath SWIM trajectory, this change of λ_p might not be from a switch from a swell partition to a wind sea partition along the latitudes. Looking at Fig.5.27d we see once again that current effects on wave properties are not local, i.e., having a strong and localized surface current does not necessarily induce a localized variability of wave properties.

June 11, 2019 at 05:00 p.m.-UTC

θ_p and λ_p exhibit strong and localized variability both in latitude and in incidences. Wind is particularly strong during the measurement but is homogeneous along SWIM track. Within 39.5°S and 38.5°S, θ_p show a strong θ_p gradient on both sides of SWIM measurements for 06° and 08° whereas the 10° remains constant. At smaller latitudes θ_p slightly turn to 40° (for all incidences) and then oscillate around 50° until 35°S. We do not consider measurements to the north of 35° because it is certainly contaminated by land.

The evolution of λ_p provide strong variability along latitudes with a clear tendency of the waves to be elongated within 39° and 37° and shortened within 37°S and 36°S, except for the west 10° beam where the λ_p remains constant. This discrepancy might be due to the fact that the areas measured by the off-nadir beams are not at the same location, i.e., west measurements performed by the 10° beams are outside a current pattern (Fig.5.1) which is not the case for the other incidences. If the surface currents are the reason for this change of λ_p, studying at the same time all SWIM incidences will allow inferring the current intensity from this change of wave wavelength. Finally, from 36°S to 35°S waves are elongated for west measurements performed at 06° and 08° incidence and are shortened for the other measurements (waves λ_p oscillated around 200m). Measurements on the north of 35°S are also not taken into account. The fully two-dimensional spectra around latitudes where the strong ∇H_s is measured (Fig.5.15e) shows crossing seas, one trapped in the Agulhas current and one free propagating obliquely to the large-scale Agulhas current. These crossing seas are not captured by the peak metric.

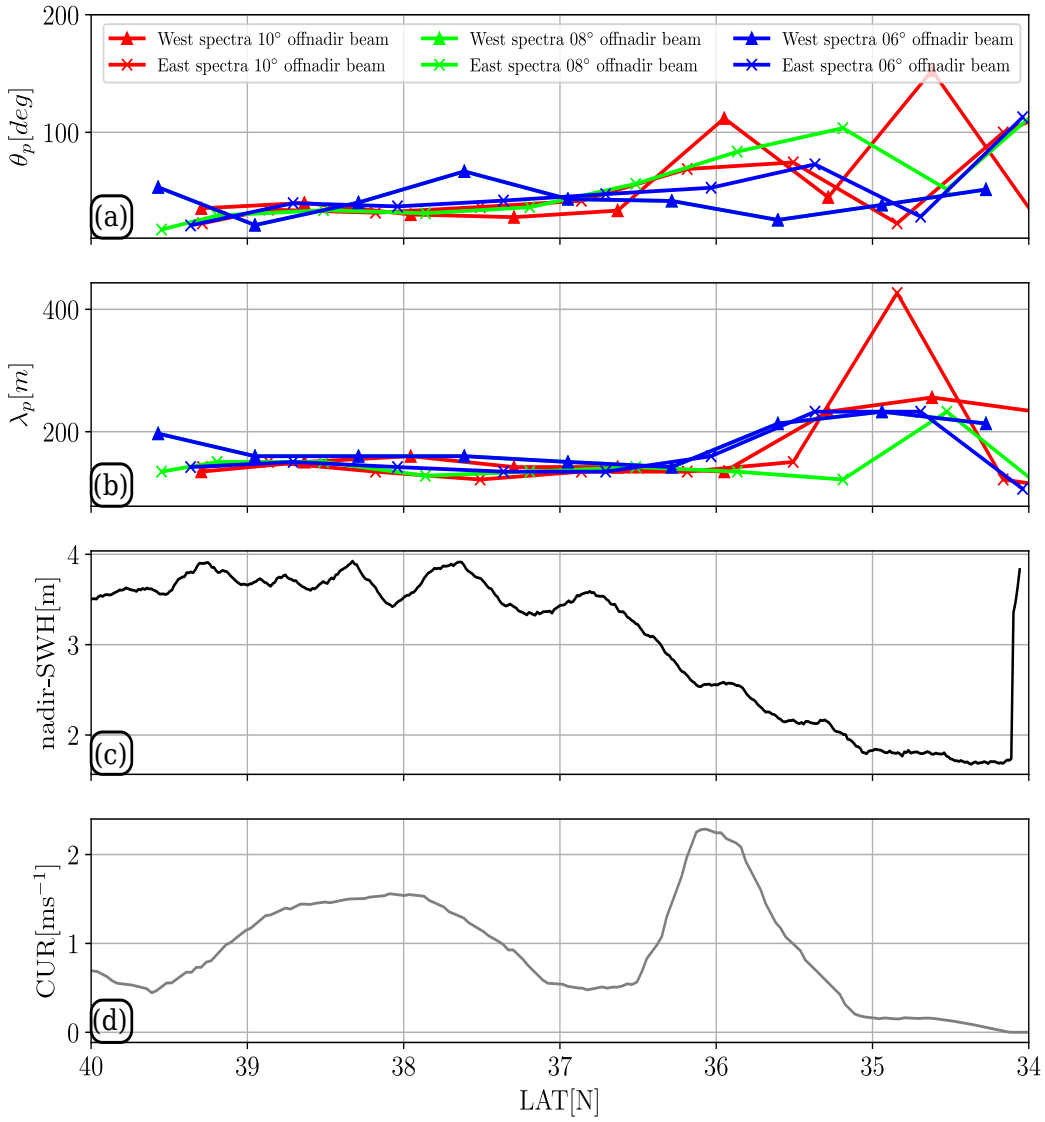

Figure 5.27: From top to the bottom. The panels (a) and (b) show the peak direction and wavelength (θ_p,λ_p) along SWIM measurements respectively. The panels (c) and (d) exhibit the SWIM nadir SWH measurements and the surface current intensity (from Globcurrent product) interpolated on the nadir track respectively.

Thanks to these two short examples, we see that working with the spectra and their associated locations allows increasing the resolution of the wave measurements. For three incidences and one macrocycle, we have three measurements at different places where the data averaged in boxes provided only one data. Throughout the manuscript we described the current-induced refraction in the framework of the optical geometry. For future work, we have sufficient information to invert the change of wave peak directions through the three incidences to infer current intensity and direction at a resolution of $\sim$ 30 km (as done numerically in Fig.13 of Villas Bôas et al. (2020)). Here the inversion is possible because the refraction has a local effect on the wave field. If a future algorithm is able to follow each partition of waves along incidences and macrocycles, it will certainly be able to map the current at global scale at an unprecedented resolution.

5.4 Conclusion and perspectives

In this chapter we propose a new method to study the different effects of the current on wave parameters in the realistic field of the Agulhas current during 2019. We used the new French-Chinese spectrometer SWIM onboard the CFOSAT satellite which estimates the 2-D frequency-direction wave spectrum. First we proposed to follow the evolution of mean wave parameters (H_s, $T_{m0,-1}$, θ_m, σ_θ) provided by off-nadir measurements along SWIM flight over Agulhas current fronts. The estimation of mean wave parameters has been possible by assuming the equality between the H_s computed from off-nadir beams and the closest H_s measured by the nadir. Wave spectra have been estimated on both sides of the altimeter track in 90 km $\times$ 70 km boxes. The size of such boxes led to an underestimation of ∇H_s with respect to the nadir measurements and even more to the omission of very sharp ∇H_s in certain cases. Nevertheless, the off-nadir measurements provided new data of $T_{m0,-1}$, θ_m, σ_θ which were, until now, only available by radar or optical images which needed very technical processes to retrieve the wave spectrum and favorable conditions (azimuth cut-off, cloud-free area). SWIM provides a more direct wave spectrum measurement. Although we confirmed some results of wave-current interactions with SWIM data in the Agulhas current region, we were strongly limited by the fact that mean wave parameters were computed from the entire wave spectrum. The resulting wave parameters may have been strongly contaminated by the presence of several wave systems in the large boxes. One solution could have been to split the spectrum in partitions to individually follow wave systems and their associated parameters across current fronts. As currents have an effect on waves at small scale, keeping the position of the measurements and the antenna geometry rather than averaging all measurements in large boxes, would increase the capability to capture current-induced wave modulations. Through two short examples, we proposed some first results of peak parameters variation in strong rotational current. The results highlighted were in line with the expected effects. A next step could be to develop an algorithm that detailed in the spectral ribbons (as represented in Fig.5.27 and 5.28), the effects of the currents on waves (change in direction and wavelength) at every incidence (2°, 4°, 6°,8°, 10°). The algorithm could exploit those current effects on waves to invert the currents. SWIM is a new remote-sensing device that measures waves in an innovative way. It has not been designed to capture the wave modulations induced by currents but results displayed here present promising results to survey those modulations.

In the previous chapter, we have seen that altimeters are able to capture sharp H_s variations in current fronts, which was also the case for the altimeter carried by SWIM platform. The off nadir measurements allow for the first time to measure the wave spectrum at global scale from 70 m to 500 m wavelength. As currents induce strong modifications of the wave spectrum, use data from SWIM allow us to improve our knowledge on the current

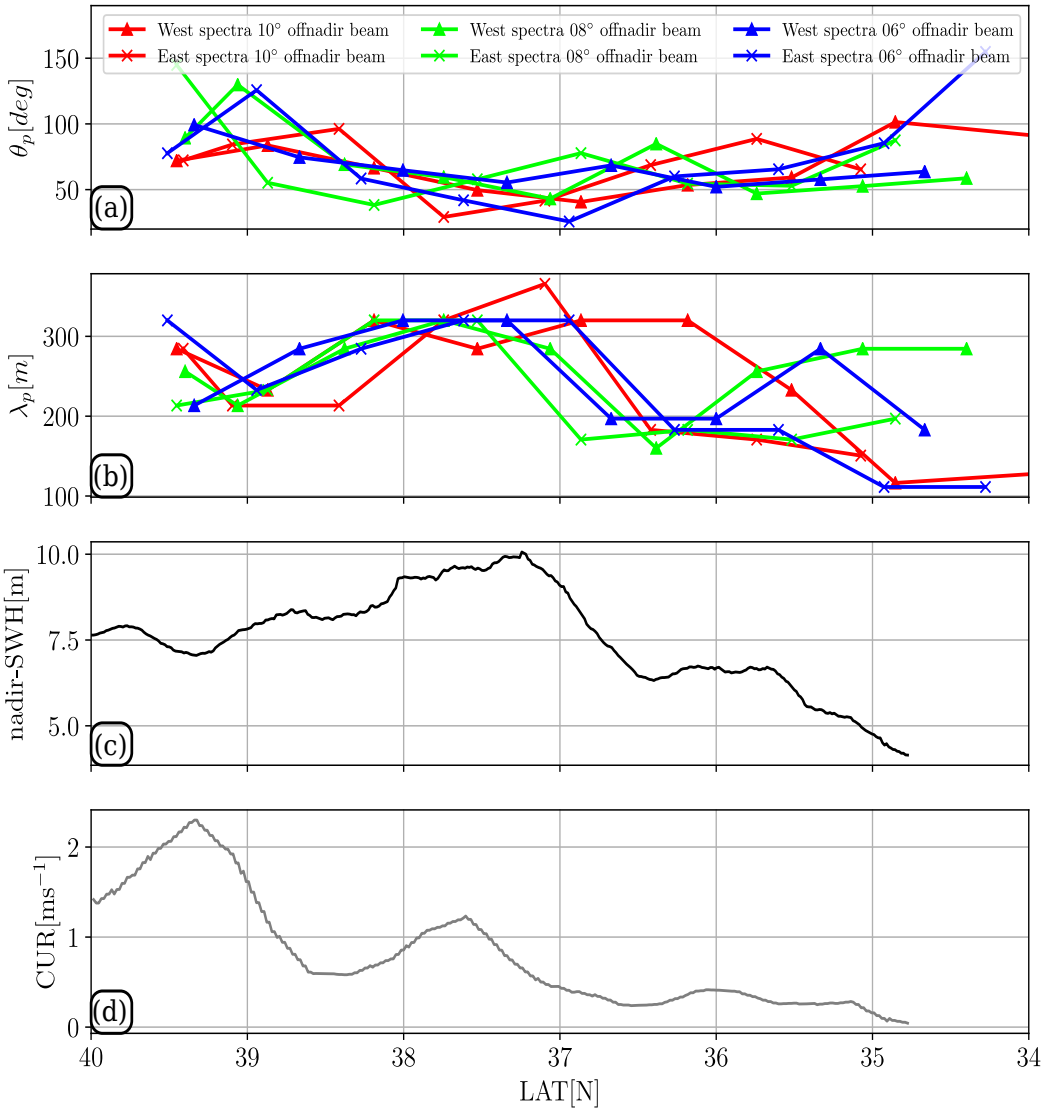

Figure 5.28: Same as 5.27 for on June 11, 2019 at 05:00 p.m.-UTC

effects on the waves, in the same manner that localized remote sensing measurements LIDAR, SAR, optical images were able to quantify those effects in a strong rotational current (Romero et al., 2017; Irvine and Tilley, 1988; Kudryavtsev et al., 2017b). In the context of this thesis, we wanted to know how H_s variability at meso- and submesoscale are related to the underlying current. We have seen that the redistribution of the wave actions induced by the refraction is the main contributor of sharp ∇H_s formation with ∇H_s is a function of the intensity and the nature of the underlying flow. However the refraction process is not the only one as recalled in the introduction. Clustering the different changes of wave properties captured by SWIM will help to capture which surface current effects change the wave field and quantify these effects in the open ocean. We are certain that SWIM will be able to improve our knowledge on current effects on the waves and particularly at global scale. The antenna will be able to capture very localized wave dynamics specific to certain regions. As the current effects on the waves are crucial for air-sea fluxes and remote sensing issues, SWIM will certainly help for both large-scale atmospheric and oceanic model parametrization and contributes to the removal of wave signal contamination in certain remote sensing measurements. As a perspective of this work, more in a context of SWIM instrumentation and measurement, one could compare the SWIM measurements with other directional wave measurements as provided by Synthetic Aperture Radar (SAR) in strong current fronts. It could also improve the wave measurements yielded by SAR measurements.

Now that we have shown that how significant waves height variability is related to the underlying surface current in strong rotational current, from numerical simulations both idealized and realistic, altimeters data and directional spectral data, we propose to extending those works to other current regimes that can be found in the ocean.

CHAPTER 6

PERSPECTIVES: CURRENT-INDUCED WAVE PROPERTY VARIABILITY IN INTERNAL WAVES AND INERTIAL CURRENTS

6.1 Waves modulation in Internal Waves

6.1.1 A few notes on Internal Waves

Oceans that are stratified by density into distinct layers support internal waves LeBlond and Mysak (1981). Internal waves are mainly generated from external tides impinging on the continental shelf radiating away from the ocean-interior internal waves at semi-diurnal (M2) frequency (Wunsch, 1975). Other sources of non-tidal internal waves generation exist but are not described here (see McPhee and Kantha (1989); Clément et al. (2016); Marez et al. (2020); Mendes et al. (2021)). The phase speed of internal waves depends on the stratification of the ocean and is of the order of a few dozen centimeters per second. Their typical spatial and temporal scales are $\mathcal{O}$(0.1-20 km) and $\mathcal{O}$(1-24 hours). According to the Rossby deformation radius (see chapter 1), internal wave spatial scales are associated with submesoscale ocean processes.

Up to this chapter, wave-current interactions and their effect on the H_s have been studied in current fields highly rotational (currents-induced of a realistic cyclonic vortex, western boundary currents with a focus in the Agulhas current region). However, a very large portion of the total ocean surface Kinetic Energy is within divergent ocean motions such as in internal wave fields. For instance, in the Coastal California current, Chereskin et al. (2019) showed that, thanks to a wave-vortex decomposition, the entire contribution of the diverging component of surface currents is from internal waves. Those divergent/convergent flows have a significant impact on the enrichment of biomass and nutrients at the surface (Shea and Broenkow, 1982). Understanding the interactions between internal and surface gravity wave fields is, therefore, crucial for biological applications.

6.1.2 Observation of surface signatures of Internal Waves

The surface manifestation of internal waves can be captured by in situ or remote sensing measurement of the sea-level height (Curtin and Mooers, 1975; Ray and Zaron, 2011) or skin temperature measurements using infrared cameras (Farrar et al., 2007; Marmorino et al., 2004). As well as altimeters, remote sensing imagery techniques

can capture surface signature of internal waves. Through surface roughness measurements, synthetic Aperture Radar (SAR) provides clear observations of a wide range of small-scale oceanic phenomena such as internal waves (Alpers, 1985; Jackson et al., 2013). Recently, Lenain and Pizzo (2021), using a combination of remote sensing devices onboard an aircraft (Lidar, IR camera, and hyperspectral camera), showed the robustness of such deployment to retrieve one internal wave field and its effect at the ocean surface.

From the theoretical works of Kudryavtsev (1994), it has been shown that waves and internal waves are a coupled system. As refraction is a very important source of wave parameter change at submesoscale (Smit and Janssen, 2019; Romero et al., 2020), the presence of internal waves in the ocean should lead to modifications of the wave field. However, as the surface current induced by an internal wave train is purely divergent, the resulting current-induced refraction would be negligible (Dysthe, 2001; Villas Bôas and Young, 2020) and therefore the changes in the H_s as well (Villas Bôas et al., 2020). However, the pictures taken by Osborne and Burch (1980) show strong modifications of the sea states and an enhancement of wave breaking during the passage of an internal soliton during a 17-minute interval. Also, in an internal wave field, Lenain and Pizzo (2021) revealed a short scale variability of wave properties both in direction and wavenumber. To conclude, although idealized numerical studies stipulate that internal waves would not have an impact on low moments of the wave spectrum, the wave field is, nevertheless, disturbed by the presence of an internal tide. The aim of this section is to capture the wave properties in internal wave field from optical-data acquired by the Copernicus Sentinel-2 Multispectral Instrument (S2, Drusch et al. (2012)). The seco

6.1.3 Data: S2 images

S2 image properties

Optical images provided by S2 are well described in Kudryavtsev et al. (2017a) ; we will just recall their main characteristics. S2 satellite was successfully launched by the European Space Agency in 2017 to acquire high-resolution multi-spectral images. S2 satellite acquires data over 13 spectral bands both in the visible and in the infra-red bands (443–2190 nm). The spatial resolution of these bands varies from 10 m to 60 m. Surface roughness can be retrieved inside and in the vicinity of the sun glitter. This roughness (or sun glitter spatial gradients) provides a snapshot of oceanic feature gradients at scale from a few dozen of meters to several dozen of kilometers. Those features are associated with regional current patterns as fronts, filaments, meso- and submesoscale eddies and internal waves. Because the sun glitter intensity depends on the mean square slope (mss) of the waves (Cox and Munk, 1954), the current effects on waves can be inverted to infer the underlying current. Contrary to H_s, the effects of current on the mss is more local, allowing for the inversion of sea surface brightness into current gradient under favorable wind conditions (Rascle et al., 2018). Beyond surface current gradients retrieval, the two dimensional wave spectrum, $\mathrm{E}(f,\theta)$, can also be deduced from the sun glitter image assuming the wave field as homogeneous and stationary (Kudryavtsev et al., 2017a). As the smallest pixel size of S2 image is 10m, S2 provides an instantaneous description of the sea-states at wavenumber much larger than traditional buoy (see Fig.12c of Kudryavtsev et al. (2017a)). Combining all bands of S2, the obtained optical image allows to cover the ocean (and land) in a swath width of 290 km. The time shift between sensors can be taken as an opportunity to measure current velocity and direction from the doppler shift of the waves at a very high resolution in cloud free area during the day (Yurovskaya et al., 2019; Ardhuin et al., 2021).

S2 image offshore San Francisco Bay

The probability to observe internal waves is higher in summer than in winter because of the ocean stratification in the first hundred meters. A well organized internal wave train was observed offshore San Francisco Bay on June 27, 2019 at 07:00pm-UTC (Fig.6.1). The internal wave field is propagating toward the coast (eastward). We noticed that the internal wave is over the continental shelf followed by other internal wave trains (not shown). Swell is visible perpendicular to the internal wave train, there is a 180° ambiguity in the wave direction. This ambiguity has been removed through a phase spectrum obtained from cross-spectral analysis between two not-synchronised-S2 bands (not shown, reader can refer to Fig.8 of Kudryavtsev et al. (2017a) for an example). Other internal waves have been identified in the Gibraltar strait and offshore Virginia Beach (east coast of the United States) but we have focused on the one presented in Fig.6.1(c) because the internal wave train is isolated from other oceanic features and a wave buoy was available very close to the acquired image (Fig.6.1b). The wave buoy provides wave Fourier parameters to estimate the E(f, θ) via MEM method (Lygre and Krogstad, 1986) and the associated parameters every 30 mins. All of these values are plotted in Fig.6.2. During the S2 acquisition (from 07:00 pm-UTC to 09:15 pm-UTC, purple lines in Fig.6.2) three wave partitions are measured by the buoy. One swell partition at T_p=13,5 sec propagating at 180° (towards the south, the convention is the meteorological convention, i.e where the waves are propagating) and one wind sea partition propagating toward the north-west at $T_p \sim 8$ sec. A very narrow partition is also noticeable at T_p larger than 20 sec. The associated H_s, computed from Eq.(1.4) is 1.1 m. Here the buoy is outside the internal wave train (Fig.6.1b), even assuming that internal wave have traveled over the wave buoy, the coarse time resolution of the buoy measurement cannot capture the potential internal wave-induced variability on the wave field (sampling issues). Also, as the buoy is assimilated to a point, the spatial variability of the wave field cannot be captured by buoy measurements. Here the buoy can be used as a reference if we want to invert the S2 image into a wave field as performed by Kudryavtsev et al. (2017a) offshore San-Diego. Thus, S2 image seems to be, at a very first look, a good candidate to capture the spatial modulation of the wave field by the internal wave at a very high spatial resolution ($\sim$ 10 m).

Sensor-sun angles from S2 metadata

The surface brightness captured by S2 is a function of the slopes Probability Density Function (PDF). In other words each pixel of S2 image is characterized by its slope (s_x,s_y) that gives a specular reflection. The intensity of the brightness is thus intrinsic of the sea surface slopes (Eq. 6.1),

$$B = \frac{\rho E_s}{4 cos\theta_v cos^4\beta} PDF(s_x, s_y, \text{mss}). \tag{6.1}$$

The sun glitter brightness (B) can therefore be computed from the angles of the sun (θ_v is the zenith sensor) and of the sensors, the pdf of the slopes and the mss. In Eq.(6.1) E_s is the solar irradiance and ρ the Fresnel coefficient which is dependent on the atmospheric composition. So, here we have a clear relation between the intensity of the sun glitters and the wave slopes. The geometry of the measurement is given in Fig.6.3(a) with the associated sun and sensor angles. We propose to superimpose sun and sensor angles over the studied S2 image (shown in Fig6.3 c-f.) One can see that the internal wave is at the edge of two detectors (Fig.6.3b). Combining sensors and sun angles we can compute the angle of the bisectrix (angle β), drawn in Fig.6.3a) between sun and sensor. This

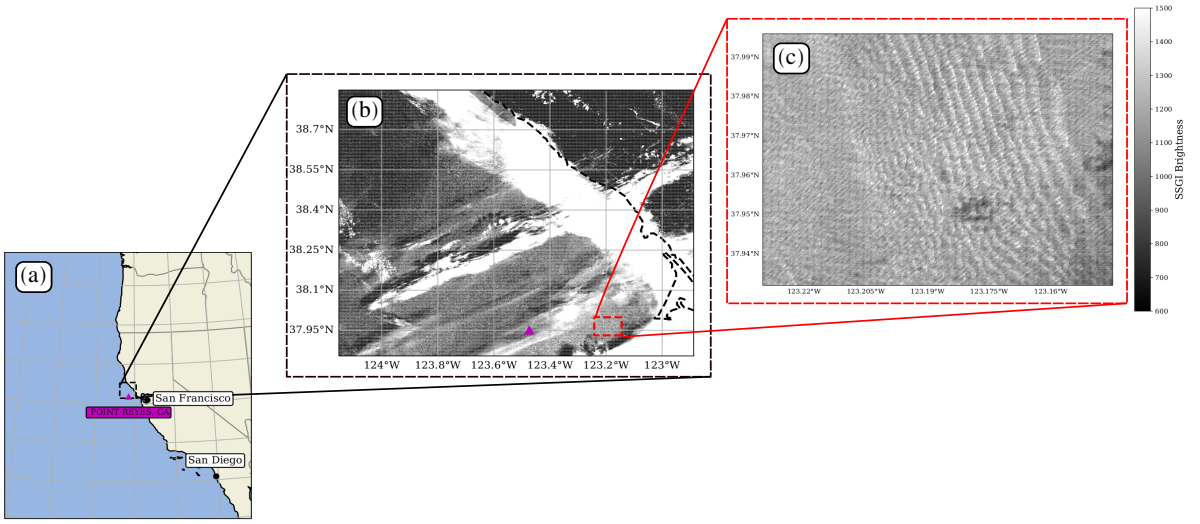

Figure 6.1: Panel (a) shows the location of the studied S2 image (dashed black square) offshore San Francisco Bay. The closest CDIP wave-buoy is represented by the purple triangle (`https://cdip.ucsd.edu/m/products/?stn=029p1`). Panel (b) shows the full-image brightness captured by S2 (resolution has been reduced to 500m both in longitude and latitude). The dashed red line square is a sub area where internal waves has been picked (panel (c)).

bisectrix gives the normal vector of the facet (Eq.(6.2)),

$$\tan(\beta) = \sqrt{s_x^2 + s_y^2}. \tag{6.2}$$

The values of s_x and s_y can be computed via a simple trigonometry from Fig.6.3a or from Eq.(2) of Kudryavtsev et al. (2017a). Note that β is not homogeneous for all detectors (Fig.6.3c-f). This is one of the reasons why shades of grey stripes are visible in Fig.6.1 (better visible in Fig.6.9).

6.1.4 Computing the mss and the wind speed from optical image

Mss and wind velocity in the vicinity of the internal wave field

Thanks to the mss contrast, the surface current gradient can be retrieved under moderate wind conditions (Kudryavtsev et al., 2012; Rascle et al., 2018). This method has the advantage to estimate the surface currents at resolutions where traditional altimeters fail. Also, current gradients can be inferred without any assumption on the balance of the flow. In other words, both the geostrophic and the ageostrophic circulation in an area of the optic image size can be estimated from sun glitters. In this chapter we do not try to retrieve the current velocity field.

Firstly let us compute the mss from Eq.6.1. The obtained value will be validated with wind measurement. Indeed Cox and Munk (1954) wrote an empirical relationship between mss and wind speed (Eq.6.3), for an isotropic mss,

$$\text{mss} = 2 \times (0.001 + 0.00316 \times U_{10}). \tag{6.3}$$

U_{10} is the wind velocity at 10m. The isotropic assumption is quite acceptable for weak winds ($U_{10m} \sim 5\text{m.s}^{-1}$,

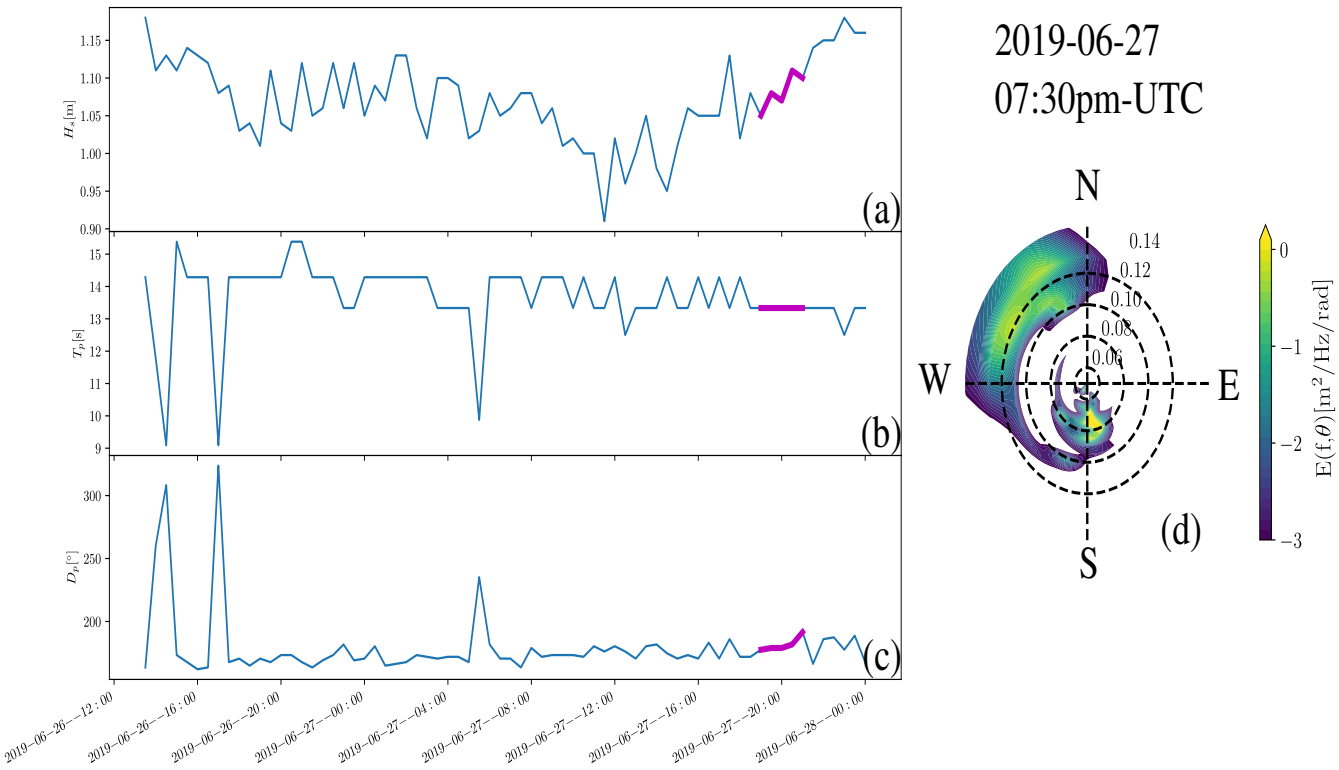

Figure 6.2: Wave parameters on June 27, 2019 measured by Point Reyes wave buoy (ID: 029). Panel (a) shows the evolution of the significant wave height, panel (b) shows the peak period, and panel (c) shows the peak direction. Panel (d) is the wave spectrum reconstructed using the Maximized Entropy Method at 07:30pm UTC. The colorscale is in log-scale.

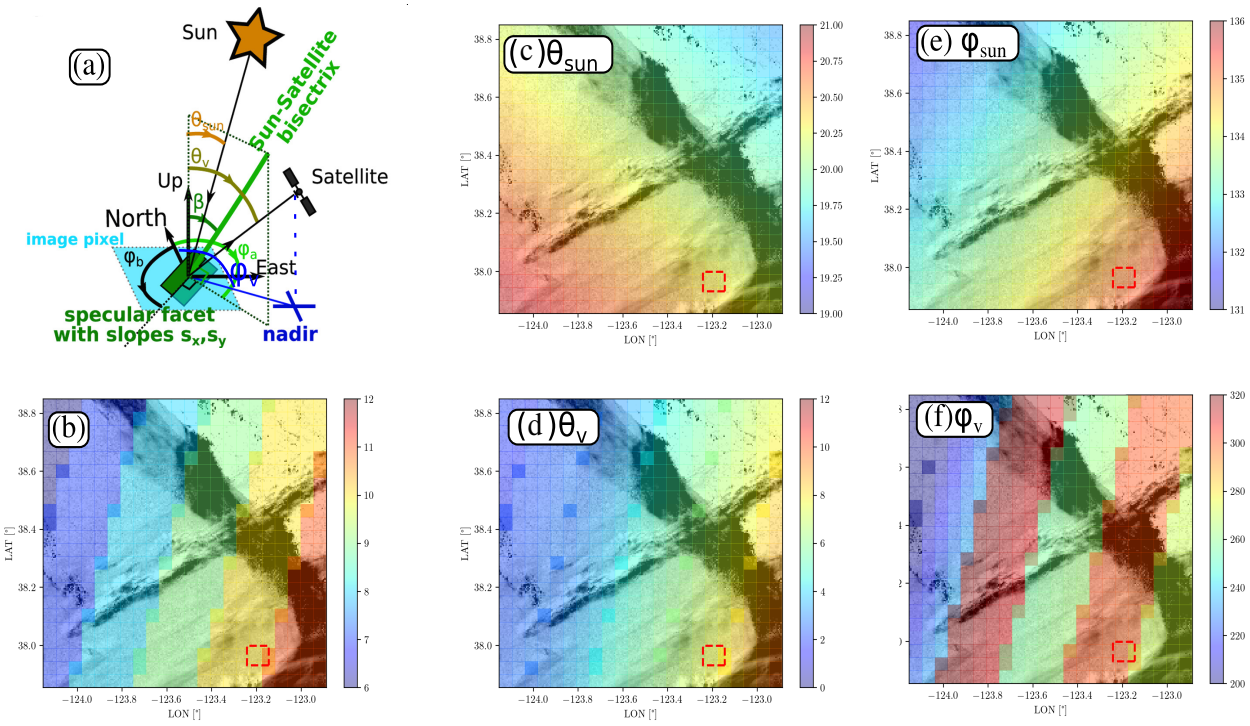

Figure 6.3: Panel (a) is a sketch of the geometry of the S2 viewing (slightly adapted from Ardhuin et al. (2021)). Panel (b) shows the footprint of the S2 bands 6 to 12 (colors are id's bands). The sun and sensor zeniths are given in panel (c) and (d) respectively. The sun and sensor azimuths are given in panel (e) and (f) respectively. In each panel the position of the sub domain where the internal wave has been picked is drawn as a dashed red square.

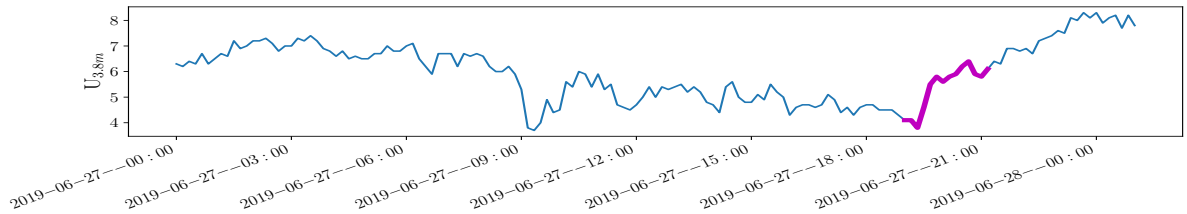

Figure 6.4: Wind velocity at 3,8 m height on June 27, 2019 measured at NDBC 46026 station (https://www.ndbc.noaa.gov/station_page.php?station=46026). Purple solid line is the wind velocity during the S2 acquisition.

Fig.4 of Munk (2009)). Wind data are from the NDBC wind buoy at station 46026 (Fig.6.4) which is around 50 km from the S2 image studied. This is the closest wind-in-situ measurement. The buoy provides wind data every 10 min. The PDF in Eq.(6.1) is entirely defined by the mss, we assume the sea surface slope PDF is Gaussian and azimuthally isotropic,

$$PDF(s_x, s_y) = \frac{1}{2\pi \mathrm{mss}} exp(\frac{-\tan(\beta)^2}{\mathrm{mss}}). \tag{6.4}$$

At the edge of two detectors (10 and 11, downstream from the internal wave) we assume the continuity of the mss (scalar). Thanks to the gradient of the brightness and the gradient of the β, combining Eq.6.1 and Eq.6.4 yields,

$$\mathrm{mss} = \frac{\tan(\beta_{11})^2 - \tan\left(\beta_{10}\right)^2}{ln(\frac{B_{11}}{B_{10}})}. \tag{6.5}$$

One can notice that the change of β at the edges of the two detectors is sufficiently small to neglect the contribution of the term $\cos^4\beta$ in Eq.6.1. In this method we removed the influence of ρ and E_s. The numerical application gives mss=0.0614 so applying Eq.(6.3), it yields to a wind velocity equal to 4.54m.s^{-1}. The result is comparable to the measurements provided by the wind buoy (Fig.6.4).

Mss modulation by the internal-wave

We propose a first guess of the mss in the internal wave field via the brightness signal provided by S2 satellite. We assume that the $\mathrm{E}_s\rho$ term in Eq.6.1 is homogeneous in the subdomain (Fig.6.1c), the mss is isotropic and the sun and the sensor angles are provided by the detector 10 even if detector 10 and 11 are overlapped. We assume that the mss controls the variations of other slope parameters of the sea surface. The mss is strongly supported by short waves of $\mathcal{O}(1)$m (Vandemark et al., 2004). Both wind sea and swell modulate the short waves which support the mss. We assume that the tilt and the hydrodynamic modulations of the short wave are principally induced by the swell propagating southeastward. If we average the total brightness in the direction of the swell (see Eq. (6) of Kudryavtsev et al. (2017a)), we obtain a direct transfer function between the brightness anomaly and the mss.

Let's do an application in our case in the internal wave field offshore the San Francisco Bay. Assuming the PDF of the slope gaussian and the mss is isotropic, we can write,

$$B = \frac{E_s\rho}{4\cos(\theta_v)\cos^4(\beta)} \frac{1}{2\pi \mathrm{mss}} \exp(-\frac{\tan(\beta)^2}{\mathrm{mss}}). \tag{6.6}$$

At the edge of two detectors (see Fig.6.3b) we consider the mss identical. This mss has been computed and validated above (mss=0.0614). At this step we know one value of the mss. We use this computed value to estimate E_s ρ with the Eq.6.6 at the same location. We consider that, in the restricted area studied, the sun irradiance and the Fresnel coefficient is homogeneous Fig.6.1c. The term E_s ρ is now known. As the PDF of the slopes varies at scale of the long wave (swell), we remove the contribution of the long waves by averaging the brightness image along the swell in a square domain of 2000m $\times$ 3000m. At this step we have a one dimensional averaged brightness perpendicular to the swell. We re-write the Eq.6.6:

$$\underbrace{\frac{\rho E_s}{4\cos(\theta_v)\cos^4(\beta)} exp(-\tan(\beta)^2/\mathrm{mss})}_{LHS} = \overbrace{2\pi \mathrm{mss} B}^{RHS}, \tag{6.7}$$

here B is one dimensional. The same method has been applied to a thumbnail image outside the internal wave field but still in the same band and showing the same wave systems (Fig.6.5). Comparing the two thumbnail images one can notice that the maximum brightness is captured at the internal wave crest. Outside the internal wave, the brightness is much more homogeneous. For each value of the averaged image we resolve numerically the Eq.6.7, (an example is given Fig.6.6). The retrieved mss for both averaged thumbnail images and their associated PDF are given in Fig.6.7. The averaged mss for the homogeneous wave field outside the internal wave shows averaged mss in the same order of magnitude than the mss retrieved in the internal wave. However the variability around the mean value, represented by the root-mean-square, is three times stronger in the internal wave packets with respect to mss outside the internal wave packets (Fig.6.7a,b). The averaged mss along the swell in the internal wave is in lines with results showed in Fig.6a of Lenain and Pizzo (2021) with mss values $\sim$ two times smaller in our case, certainly explained by the average along the swell direction.

The estimation of the mss by the use of the wide swath S2 optical instrument has a lot of applications. As recalled in Kudryavtsev et al. (2017a) and Rascle et al. (2018), it allows quantifying satellite observations of oil spills and submesoscale ocean currents from 10 m to several dozen of kilometers. Also, mss seems to be related to sea-spray generation (large droplets with radius >20 μm) (Bruch et al., 2021) which has an important role in the Earth's radiation budget. Finally the mss is directly linked to the wind speed at the wave boundary layer, optical S2 image thus provides measurement of the wind speed at very high spatial resolution as already performed in the past by Cox and Munk (1954) aboard their B-17G airplane.

6.1.5 Limits to estimate wave field in internal Wave with a *classical* method

In the present chapter we estimated the mss in and outside the internal wave train. Contrary to the previous chapters we do not focus on the wave parameters integrated from the wave spectrum as H_s, this is the main perspective of this section. Although wave spectrum can be retrieved accurately from optical images (Kudryavtsev et al., 2017a), in the studied internal wave field, the *classical* method cannot be applied.

Homogeneity of the wave field and scale separation

Kudryavtsev et al. (2017a) demonstrated the possibility to retrieve the wave spectrum from S2 image and the associated short-crested wave field (with a random phase, see Fig.5 of Kudryavtsev et al. (2017b)). This retrieval is based on the assumption that the waves are globally homogeneous and stationary during the acquisition. Kudryavtsev et

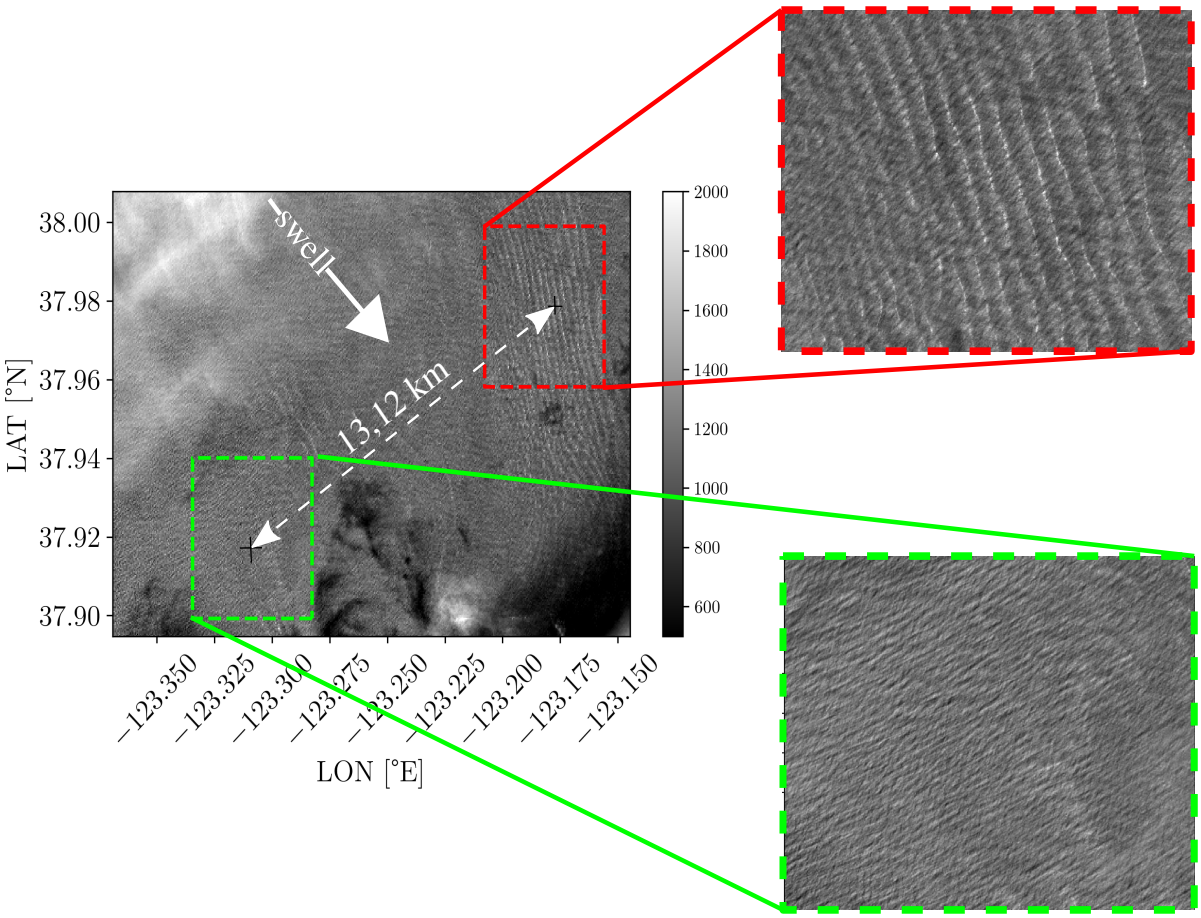

Figure 6.5: Two thumbnail images from a large Copernicus Sentinel-2 Multi-Spectral Instrument image acquired offshore San Francisco Bay, one where we can notice an internal wave train (red) and one without (green). Both thumbnail images have a dimension of 4.5km $\times$ 4.5km.

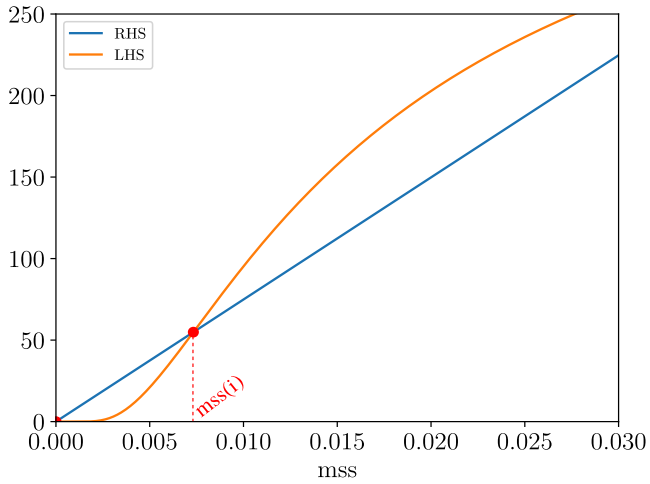

Figure 6.6: Find a value of mss where RHS and LHS of Eq.6.7 are equal. The red dots are the intersections between the two terms, the root 0 is not taken into account because not physical. The associated mss value of the intersection point ($x(i)$) corresponds to one averaged brightness.

al. (2017b) studied the evolution of the wave spectrum in the Great Agulhas current by the use of thumbnail images sufficiently small (to have a homogeneous wave field) and sufficiently large to solve the longest swells. However in smaller current patterns (typically submesoscale), the swell wavelength can be drowned in the spectral-band of submesoscale current (typically between 500 m and 100 m, Villas Bôas et al. (2022)). In the present study, the wavelength of the internal wave is around 300 m which is typically in the swell-spectral band. This wavelength can be computed through a wavenumber brightness spectrum, as presented in Fig.6.8. Power spectral densities were computed from the two-dimensional Fast Fourier Transforms for a 300 $\times$ 300 pixels box taken in the middle of Fig.6.1c in a cloud-shadow-free area. The subdomain is windowed with a Hanning window. The resulting 2D spectrum has been integrated in azimuth providing an omnidirectional brightness spectrum shown in Fig.6.8. One can see that in the image spectrum 2 peaks are centered at λ=250m and λ=100m. Those peaks coincide with the wave spectral peaks measured by the wave buoy (Fig.6.2d). In Fig.6.1c, the image brightness is mainly modulated by the presence of the internal wave train which explains why the spectral peak at λ=250m is the most energetic, making it evident that the swell is drowned in the internal wave spectral band. Applying the classical method in this internal wave field will overestimate the variance of the slope spectrum because it will confuse the contribution of the internal wave with the surface gravity waves.

Isotropy of the mss

Although the retrieval of the full wave spectrum in the internal wave field was not possible, a first guess of the mss in the internal wave signal has been proposed. We based this guess on several assumptions, and in particular on the fact that mss could have been considered as isotropic. Remote sensing field measurements, under the same wind condition, showed that the mss is not isotopic at all in intrnal wave field (Fig. 6 of Lenain and Pizzo (2021)). Authors show a discrepancy between the along-wind and crosswind by more than a factor of two. Although the proposed method to infer the mss from the sun-sensor angles and the image brightness is quite simple, it has to be

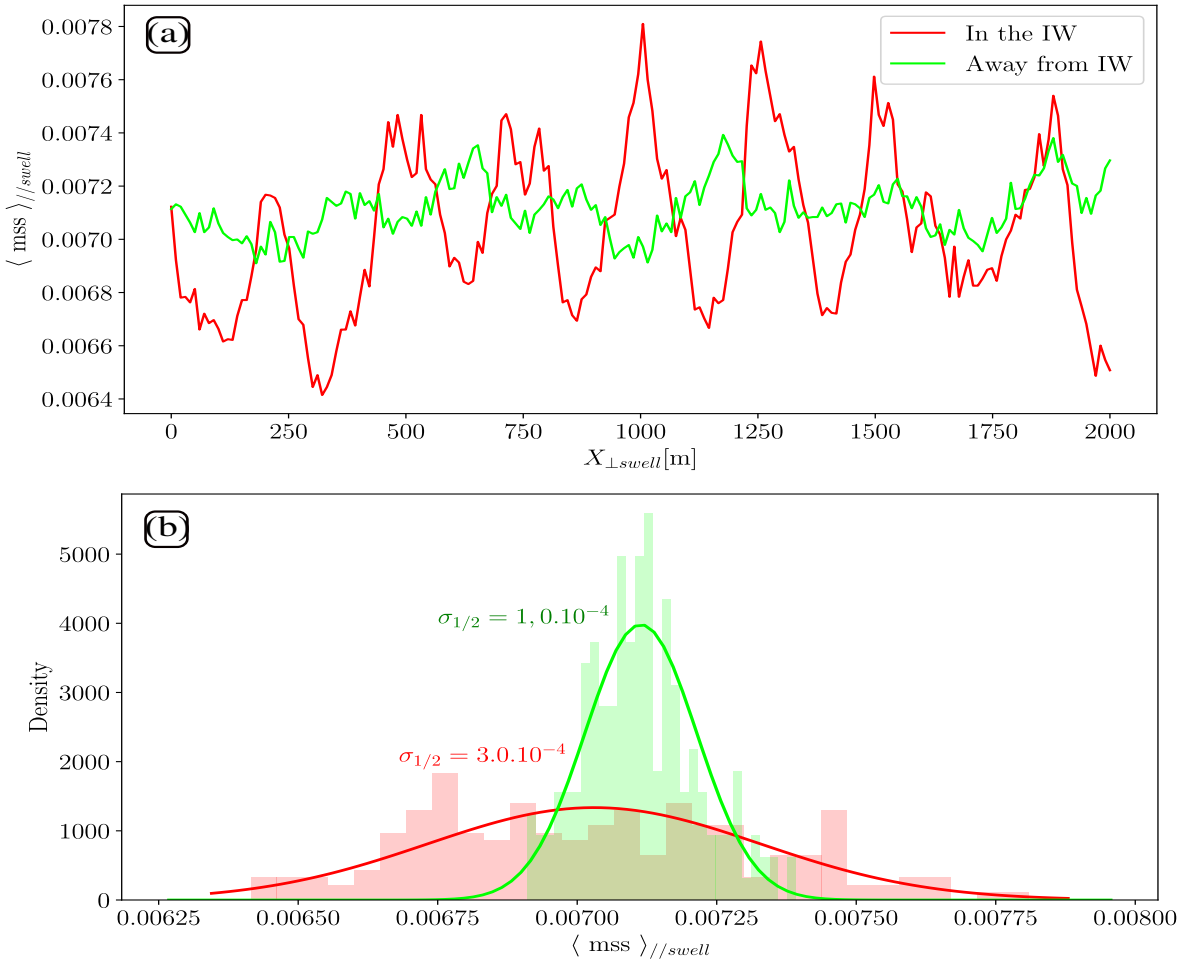

Figure 6.7: Panel (a) shows the averaged mss along the swell direction. Panel (b) shows the normalized Probability Density function of the signals given in panel (a) panel with their associated gaussian fit. Green plots are for wave field away from the internal wave packet and red plots for wave field in the internal wave packet. Both fields are given in Fig.6.5.

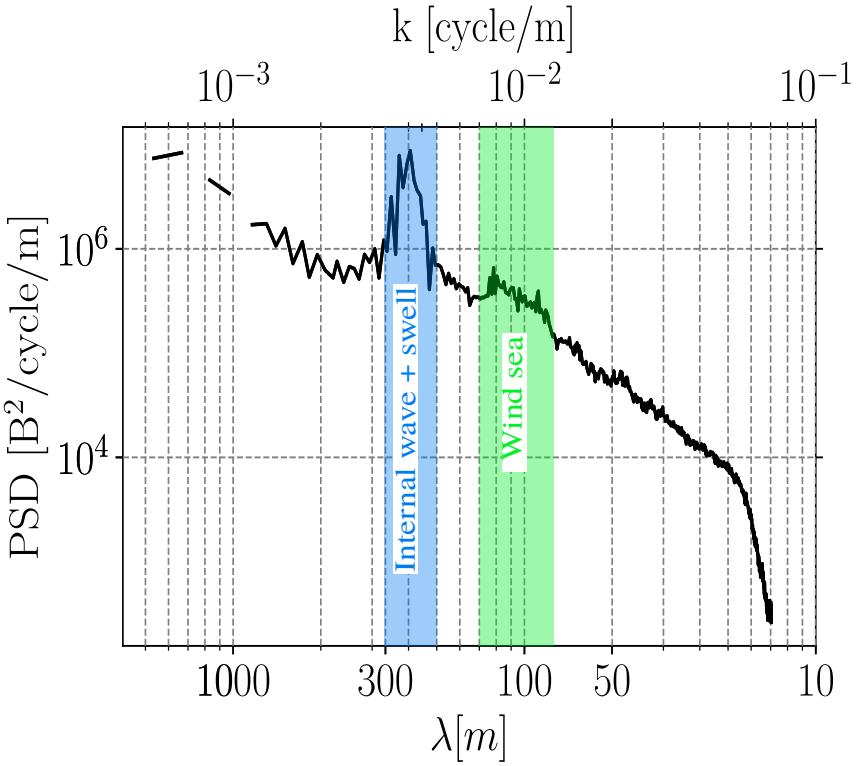

Figure 6.8: Omnidirectional S2-image brightness spectrum from a subdomain of Fig.6.1c. The domain is given explicitly in Fig.6.5

.

completed to better match with existing studies especially by assuming that the mss cannot be isotropic. Once the mss is validated, we would be able to apply our method to other internal wave regimes without expensive aircraft deployment, and approach the modulation of surface gravity waves and surface roughness induced by internal waves on global scale.

The whitecap coverage in S2 image

The steepness of the wave field is strongly modulated by the internal wave (Lenain and Pizzo, 2021). This modulation is a function of the phase of the underlying internal wave signal in the similar manner that short waves are modulated by longer waves (Peureux et al., 2021). Based on this modulation, surface current can be normally retrieved (Rascle et al., 2018), but where steepness becomes too sharp, the breaking probability of the waves strongly increases. Fig.6.1c shows very bright pixels due to whitecaps close to the internal wave crests. According to the Eq.(6.1), high brightness results in a sharp surface slope, whereas where whitecaps are measured we expect that slope becoming smoother. The retrieved wave slope at the location of the whitecap pixels is thus erroneous. This remark can be extended in other submesoscale current patterns thanks to the numerical works of Romero et al. (2020).

Summary and perspectives

It has been shown that the S2 Instrument captures surface oceanic processes through the sun-glitter imagery at very high spatial resolution. Wave slope modulations induced by surface current allow us to describe the wave field until wavelength of a few dozen of meters following the method proposed by Kudryavtsev et al. (2017a). Here we focus on internal wave surface signatures offshore the San Francisco Bay with a $\sim$ 300m wavelength. As internal wave wavelength is in the swell spectral-band, capturing the wave modulation induced by internal waves is challenging. Kudryavtsev et al. (2017b) well identified the current effect of the Great Agulhas current on wave field through wave spectrum variability. Here, this method cannot be applied because a large portion of the wave spectrum variance will be from the internal wave signal contribution. One possibility to remove the internal waves contribution in the brightness spectrum could be to perform a spectral analysis outside the internal wave signal and use the resulting spectrum as a filter for the spectrum presented in Fig.6.8. Another possibility is to study other internal wave regimes as in the Gibraltar strait where internal wave-wavelengths are often much larger than wave wavelengths (Fig.6.9). Also, the contribution of whitecaps in the image brightness is a source of error in the wave spectrum retrieval. A more direct measurement as proposed in Lenain and Pizzo (2021) would be a better manner to approach the modulation of the wave field in the internal waves, but such deployment is very expensive.

Otherwise, idealized numerical wave experiments forced with idealized internal wave train (Ponte and Klein, 2015) could be an appropriate approach to verify the present results. Also it will gives the Bulk parameters and will verify, among others, Villas Bôas and Young (2020) findings that stipulate divergent surface dynamics do not affect the waves kinematic. It would be beneficial to extend such numerical experiments with realistic wave train forcing and finally coupled wave and current models to verify the theory proposed by Kudryavtsev (1994).

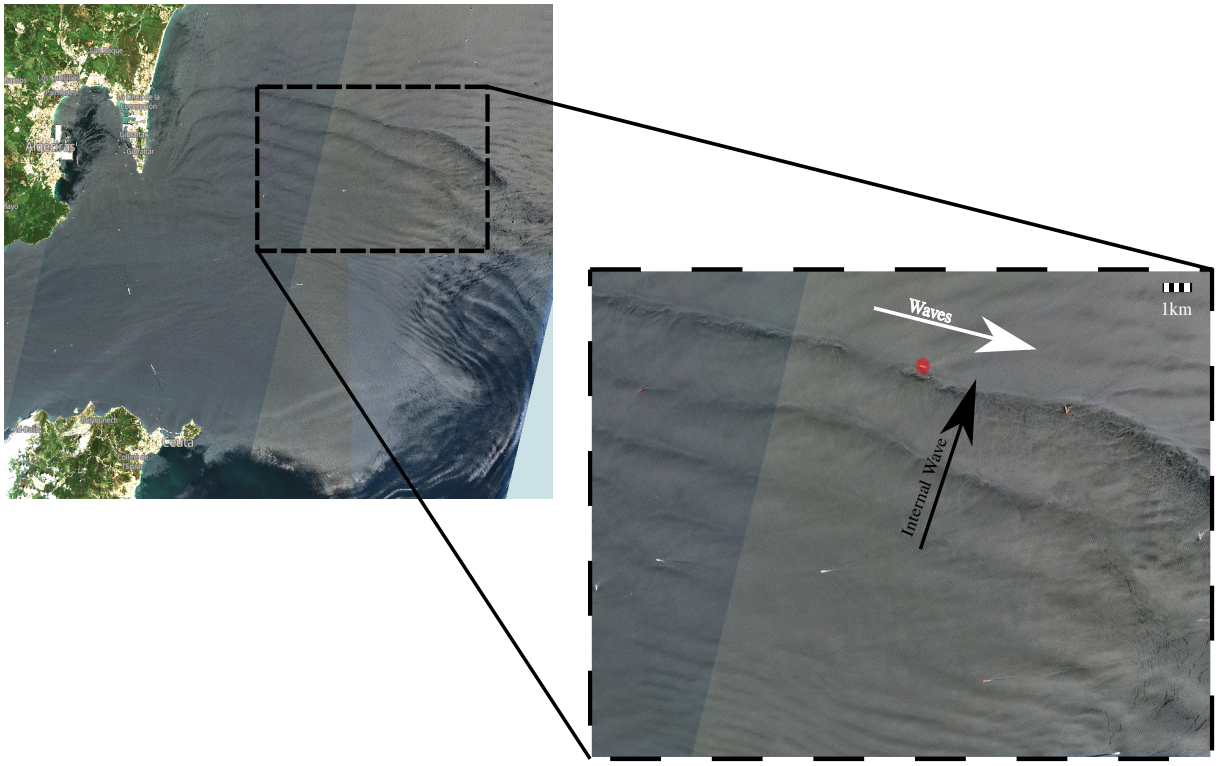

Figure 6.9: S2-image in the Gibraltar strait on April 27, 2018. Short wave trains and long internal waves trains are highlighted with white and black arrows respectively. A container-ship is given by the red spot in the figure on the right which provides an idea of the internal wave wavelength.

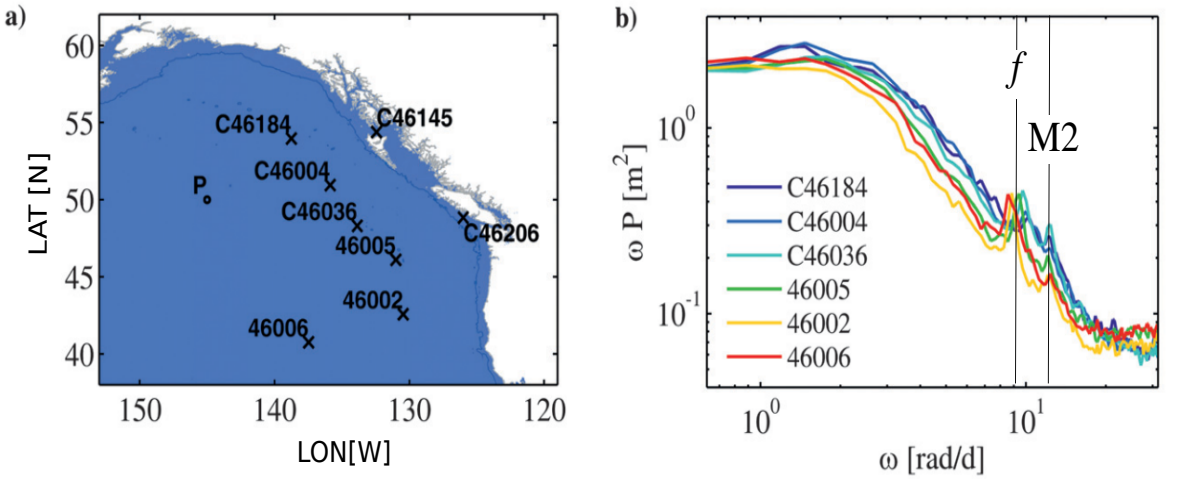

Figure 6.10: (a) Location of wave buoys measurements. (b) Frequency spectra of significant wave height at location of wave buoys. The frequency (ω) is the near inertial frequency defined by the sum of the local inertial frequency f, the first vertical mode phase speed (Chelton et al., 1998) and the local vorticity. M2 is the semi-diurnal tidal frequency. From Gemmrich and Garrett (2012).

6.2 Waves modulation in Inertial Oscillations

We have explored wave properties in great boundary currents, in an isolated eddy, and in internal wave field. Those current regimes have a large contribution of the downscale/upscale kinetic energy transfers in the (turbulent) ocean budget (Chelton et al., 2007; Ferrari and Wunsch, 2009). However we did not explore the effects of inertial and near inertial currents on waves, which are typically the most energetic currents in the open ocean (Park et al., 2005; Ferrari and Wunsch, 2009). In a lagrangian framework, inertial currents are rotating currents with a scale dependant on the local Coriolis parameters $f = 2\Omega \sin(\text{lat})$ and the current velocity. Inertial currents have a very short lifespan $\mathcal{O}$(1-5 days) and a length scale around $\mathcal{O}$(10-200 km). One can expect that surface gravity waves will interact with such oceanic processes, according to previous chapters and the state of the art of wave-current interactions. In the bibliography, a unique study of Gemmrich and Garrett (2012) shows the signature of the inertial currents on wave height measurements through long term wave buoy measurements offshore North American west coast (Fig.6.10). H_s spectra show strong variability at the semi-diurnal frequency (M2), confirmed by Ardhuin et al. (2012), and at frequency in the vicinity of the local inertial frequency (f). For future work, the author proposes to extend the Gemmrich and Garrett (2012) results to highlight the wave-current interaction processes that induce this temporal variability. Is refraction still the main source of variability? Also, Gemmrich and Garrett (2012) only proposed a one-dimensional view of inertial current effects on wave height. One can wonder, what is the spatial signature of such modulation. As inertial currents have a very short lifespan $\mathcal{O}$(1-5 days) and a length scale around $\mathcal{O}$(10-200 km), a numerical study similar to Marechal and Ardhuin (2021) applied on inertial currents will require very high resolved surface current especially in time. We could take the benefit of the recent works on coupled ocean-atmosphere simulations (`https://data.nas.nasa.gov/viz/vizdata/DYAMOND_c1440_llc2160/MITgcm/index.html`) and/or data provided by High Frequency (HF) coastal radar (Kim and Kosro, 2013) to force our wave model. Although (near)inertial currents are well captured thanks to HR radar up to 100 km offshore the coast,

their spatio-temporal properties in the open ocean are still misunderstood due to the lack of direct measurement. Eventually, the best solution would be to have a direct measurement of the surface displacement from space based on the HF technology as proposed by Ardhuin et al. (2019a). Understanding how wave parameters are modified due to such currents could be beneficial for remote sensing applications and also to understand the roles of the interactions of the waves and inertial currents in the global ocean-atmosphere system.

CONCLUSION & PERSPECTIVES

In this thesis we focus on the effects of meso- and submesoscale surface currents on the variability of surface gravity waves (waves) with a focus on their significant wave height (H_s).

Firstly, after an introduction of how currents affect waves, we proposed an analytical and idealized framework to study how the wave action is spatially redistributed due to the presence of currents. In this short chapter, we were able to explain in a simplified way how H_s is modified by the current-induced refraction which seems to be the main effect on the spatial variability of H_s in strong rotational current fields. Our main focus was the study of monochromatic waves without wind and wave dissipation. The current-induced wave action redistribution is nonlocal which leads to a non-local significant wave height variability. From a Monte Carlo ray-tracing method, we show that current gradients bend wave rays and create convergence and divergence ray areas. The wave-ray convergence-divergence areas can only occur for current profiles which provide at least one inflection point with a second derivative different to 0. In our idealized framework and assuming that the action flux is conserved along the rays, we show that the H_s spatial distribution follows the distribution of the rays. We verify our analytical findings with idealized wave simulations based on phase-averaged wave model. Numerical results corroborate theoretical results up to caustics (i.e. where waves rays create intersection points). At those points, the theory stipulate the wave amplitude is infinitely enhanced. The numerical model show that the H_s stays finite and with patterns similar to the focalization of the rays. It has been shown that patches of H_s enhancement are located where rays converge and form cusp shapes. In the opposite way, wave ray divergence coincides with H_s decrease. Although the theoretical framework does not reproduce quantitatively the numerical results of H_s, it shows with great accuracy the position of the first caustic position according to the intensity of the current and the incident wave wavelength.

Starting from this simplified view of how current induced inhomogeneity in the wave field, we have extended the very idealized framework to a realistic and isolated eddy. We quantify the variability induced by an isolated eddy on the H_s, the mean period and the peak direction of the wave field. The approach is based on idealized numerical simulations and a ray-tracing method. The wave model is forced both by eddy with idealized and realistic shape, i.e., Gaussian, on the one hand, and multi-scale dynamic with strong meso- and submesoscale current patterns, on the other hand. The eddy is from a composite eddy reconstructed from in-situ data (Argo floats and drifters) in the Arabian Sea. The realistic shape of the eddy is obtained thanks to the high resolution simulations of de Marez et al. (2020b). The sensitivity of the incident wave wavelength on the intensity of the wave field characteristics is also studied. Waves are generated continuously from one boundary of the domain such that a stationary state is reached. We observe that the characteristics of the wave field are strongly modified by the presence of the eddy and in particular for the a simulation forced by short waves and realistic eddy. The submesoscale patterns in the realistic eddy induce stronger refraction and stronger spatial gradients of H_s and period. The H_s gradients (∇H_s) are proportional to the current gradients (vorticity) but the nonlocal effects of the current on the H_s induced strong H_s patterns downstream of the eddy. We proposed to infer the surface current from the variability of the wave field in a geometrical optic framework. The motivation of this inversion is triggered by the fact that present surface current measurements are not able to map small-scale surface currents gradients. Taking the opportunity

of the short scale variability of the wave field induced by the current we highlight the advantages and the limits of such an inversion. In the eddy field, the inferred current gradients are quantitatively close to the real current gradients. Downstream of the eddy this inversion is not applicable due to the nonlocal effect of the current on the H_s. To conclude this chapter we show that the number of H_s structures downstream of the realistic eddy decay exponentially with the distance. The intensity of the H_s increasingly decreases downstream of the eddy because of the shadow effect of the eddy.

As eddies are not isolated in the actual ocean, we have extended the idealized study of waves in an isolated eddy to realistic simulations in strong mesoscale boundary current. We focus on the Agulhas current region of the South African coast. High resolution numerical simulations combined with filtered altimetry data to characterize the intensity of the ∇H_s in such current regime. Thanks to this study, we are able to characterize the dependency of both currents and waves parameters responsible for changes of intensity of the ∇H_s. The main result is that the resolution of the currents is a key parameter in the intensity of the ∇H_s. Up to now, studies have stipulated that numerical wave simulations are not able to capture sharp ∇H_s measured by the altimetry. Most of those study use operational current forcing from operational surface currents from altimeter-sea-level-anomaly measurements. Such currents are poorly resolved both in space and time. It lead to a strong underestimation of the ∇H_s. Forcing wave models with high resolved currents with structure resolved up to few kilometers, allowing to retrieve the true sharpness of the ∇H_s. Averaged H_s spectra from both numerical simulations and altimeter data show the proportionality of the H_s and the surface Kinetic Energy from several hundred kilometers up to dozen few kilometers. This proportionality is also verified numerically on the basis of optical geometry assumptions. The sensitivity of the directional spreading of the incident waves is studied in the Agulhas current region, and indicating that the more directional the waves are, the more they are focused in the current with sharper ∇H_s values. In the Agulhas current region, altimeter data shows very sharp ∇H_s, Villas Bôas et al. (2020) show a certain seasonality of such gradient due to the seasonality of the flow in the Coastal California Current. Starting from these findings, we studied the seasonality of the ∇H_s on a global scale. Exclusively from six year of Saral-AltiKa altimeter data, we show that ∇H_s values are seasonal on a global scale due to the seasonal aspect of the storm at mid-latitudes. After normalizing the ∇H_s measured by altimeter over 170km, it seems that the seasonality of the currents and the wave wavelength is captured through the seasonal normalized ∇H_s maps. Further studies could be possible with direct and co-localized measurements of the currents, and wave spectrum both on a global scale and at high resolution. But such measurements are still a present challenge for the oceanography community.

However the new French-Chinese satellite CFOSAT (Chinese-French Oceanic SATellite) with its SWIM (Surface Waves Investigation and Monitoring instrument) platform onboard, provides measurements of the wave spectrum on a global scale at five incidences (2°, 4°, 6°, 8°, 10°). From these spectral measurements, we tried to follow the wave spectrum and its spectral parameters across the Agulhas current fronts. In this study we describe the capacity of this new device to capture the variability of the wave field induced by surface current. The altimeter carried by the SWIM platform captured sharp ∇H_s in current fronts. Measured spectra at 6°, 8°, and 10° across current fronts capture the change of wave directions and wave wavelengths. The change of the wave energy is also captured but this energy is normalized by the H_s measured at the nadir. Computed integrated parameters (mean period, mean direction and directional spreading) for each incidence shows variability of the waves field which are difficult to link with the dynamic of the surface due to the lack of accuracy of the estimated underlying current and also due to the non-partitioning of the wave spectrum. The H_s estimated by the off-nadir antenna do not bring information of how the H_s are changed by the current due to the normalization of the energy by the H_s measured

at the nadir. Because the wave spectra are averaged in an area of 70 km $\times$ 90 km, the change of wave properties at scales smaller than the boxes is not accessible, whereas numerical investigations revealed a strong dependency of the current gradients and ∇H_s at these scales. This resolution could be regained by considering individual footprints (or one-dimensional spectrum) without averaging and with a clear modulation transfer function between the wave modulation spectrum and the wave spectrum. However as SWIM is a very new kind of satellite instrumentation and that the modulation on the signal is dependent of the incidence, the wave wavenumber, and the azimuth of the antenna, the modulation transfer function is very difficult to develop and requires a better knowledge of the instrument. Nevertheless, some results from averaged spectra , corroborate with results presented in previous chapters as the directional spreading dependency on the focalization of the wave energy (where strong $\nabla H_s values$ are measured).A new strategy based on machine-learning methods is currently in process to inverse the modulation spectrum to retrieve the wave spectrum.

This thesis has allowed us to increase our knowledge of how the variability of the H_s field is related to the underlying currents. We do not yet have an accurate answer for this question because the problem is strongly linked to other aspects of oceanography that have not been taken into account in this manuscript. Indeed we have only focused on the effects of the current on the waves, but, because, the two systems are strongly coupled, the reciprocal effects should be taken into account. Also, we only considered the surface current, however, in the ocean, the currents are not strictly barotropic in the first meters. For instance in the eddy studied in chapter 3, the dynamic in the first meter are strongly baroclinic (see the three-dimensional structure of the eddies in de Marez et al. (2020b)). The depth dependency of the currents on the H_s could be a next step to this present manuscript. Finally, we have only focused on current regimes strongly rotational with a long lifetime. Our last chapter has shown that other current regimes as internal waves and (near) inertial oscillations strongly interact with the wave field which modulate wave characteristics. Also, only the effects of the current on the Hs have been studied. The effect of the currents on the other wave parameters would have a wide spectrum of application. For instance, studying the current effects on the wave period from the combination of the wavelength measurements from SWIM antenna (or from other remote sensing devices) and the state of the art of wave simulations would be fruitful for applications dealing with wave steepness. Pushing further these investigations will allow us to increase our knowledge of the joint spatial and temporal variability of waves and currents. These new studies will be profitable for remote sensing applications as well as for a better parametrization of air-sea fluxes in large scale models.

CHAPITRE 7

RÉSUMÉ DE LA THÈSE EN FRANÇAIS

7.1 Contexte et introduction

Les interactions entre les vagues et les courants de surface sont fortes à la méso- et à la sousmésoéchelle (échelles spatiales de l'ordre de $\mathcal{O}(100-10)$ et $\mathcal{O}(<10)$ km respectivement). Ces interactions sont réciproques : les vagues modifient la dynamique superficielle de l'océan (PHILLIPS, 1977 ; SUZUKI et al., 2016 ; D.HYPOLITE et al., 2021) et les courants modifient la dynamique et la cinématique des vagues. (ARDHUIN et al., 2017 ; VILLAS BÔAS et al., 2020). Les courants vont moduler la raideur des pentes (JOHNSON, 1947 ; MEI, 1989) ce qui peut conduire d'une part à une variation du "form-drag" et de la turbulence PHILLIPS (1977) ; LONGUET-HIGGINS (1969) et d'autre part à de fortes zones de déferlements à des échelles spatiales de l'ordre du kilomètre. Les modulations des vagues induites par les courants ont donc un rôle primordial dans les flux à l'interface air-mer (ROMERO et al., 2017 ; ROMERO et al., 2020). Dans ces travaux de thèse, je me suis focalisé sur les effets des courants sur les vagues et plus particulièrement sur la modulation des hauteurs significatives des vagues (H_s) induite par les courants. ARDHUIN et al. (2017) ont montré que dans des régimes de courants de bord-ouest (Gulf-Stream, Passage de Drake), la variabilité des H_s est déterminée par les gradients de courants avec un spectre des H_s proportionnel au spectre d'énergie cinétique des courants de surfaces. Cette propotionnalité serait due à la réfraction induite par les gradients de courants. En effet, ces derniers vont redistribuer spatialement l'énergie des vagues incidentes à des échelles spatiales comprises entre $\mathcal{O}(10^2$ et $10^0)$ km, similaires aux échelles de courants. La réfraction induite par les courants est principalement induite par la composante rotationnelle des courants de surface (VILLAS BÔAS et YOUNG, 2020). C'est pourquoi, dans les courants fortement rotationnel (Gulf-Stream, Passage de Drake, courant de Californie ou encore le courant des Aiguilles), on observe de fortes variabilités de H_s à des échelles comparables aux échelles des tourbillons et des fronts peuplant ces courants (ARDHUIN et al., 2017 ; ROMERO et al., 2017 ; KUDRYAVTSEV et al., 2017b ; QUILFEN et al., 2018). Bien que la réfraction soit le processus principal expliquant les variabilités spatiales des H_s, il en existe d'autres. En effet les courants modifient la longueur d'onde des vagues et modulent l'advection de leur action (PHILLIPS, 1977). La superposition de tous ces processus est responsable du caractère non-local de la variabilité des H_s induite par les courants de surfaces.

Dans cette thèse, j'ai essayé de répondre à la question suivante, en quoi les variabilités des hauteurs significatives des vagues sont-elles liées aux propriétés des courants sous-jacents ? J'ai construit mon étude comme suit : dans un premier temps, j'ai étudié au moyen d'un modèle analytique idéalisé, de simulations idéalisées et de tracer de rayons comment les courants de surface induisent une variabilité des hauteurs significatives à des échelles régionales. J'ai ensuite étendu cette étude à des simulations numériques toujours idéalisées, mais dans un cas plus réaliste où je me suis attardé sur l'impact d'un tourbillon océanique de mésoéchelle isolé sur le signal de H_s, de période moyenne et de direction des vagues. Ensuite, car un tourbillon océanique est rarement isolé dans

l'océan, j'ai étendu cette étude numerique dans un cadre réaliste dans le courant des Aiguilles au large des côtes sud-africaines. L'étude a été validée au moyen de données altimétriques filtrées issues du nouveau jeu de données CCI-SeaStates (DODET et al., 2020). Finalement, l'analyse des H_s dans le courant des Aiguilles a été étendue dans une description directionnelle et en longueur d'onde de l'effet des courants sur les vagues au moyen des données du satellite CFOSAT (Chinese-French-Oceanic-SATellite) et de son antenne rotative à 5 incidences proches nadir SWIM (Surface Waves Investigation and Monitoring instrument). En perspective de ces travaux de thèse, j'ai proposé d'étudier les effets des vagues dans des régimes de courants différents des courants fortement rotationnels étudiés jusqu'à présent, comme dans les mouvements divergent de surface induits par les champs d'ondes internes (LENAIN et PIZZO, 2021) ou dans les oscillations inertielles et proche-inertielles décrit par (GEMMRICH et GARRETT, 2012).

7.2 Chapitre 1-Étude analytique des amplifications des hauteurs significatives des vagues induites par la présence de courant et analogie avec l'imagerie SAR.

7.2.1 Modèle analytique de la variabilité des hauteurs significatives des vagues en présence de courant

La variabilité des hauteurs significatives dans les courants est expliquée par la superposition de plusieurs effets avec un effet dominant de la réfraction dans les forts courants rotationnel (ARDHUIN et al., 2017 ; VILLAS BÔAS et al., 2020). Dans un cadre idéalisé, j'ai essayé de lier la réfraction induite par les courants de surface et l'amplification des H_s en aval de cette réfraction. Ci-dessous le cadre considéré :

Les courants de surface réfractent les vagues ce qui induit une réorganisation de l'action des vagues dans les courants. Cette nouvelle réorganisation des vagues explique l'inhomogénéité des H_s dans des champs de courants aléatoires.

Dans le cadre idéalisé proposé Fig.7.1 j'ai calculé les H_s à une distance x du bord gauche. Ce calcul se base sur les hypothèses de l'optique géométrique, que le courant est stationnaire et que l'action des vagues est conservée dans le domaine. En considérant que le flux d'énergie dans les tubes de rayons de vagues (un tube de rayons de vagues est considéré comme l'espace entre deux rayons successifs Fig.7.1) est conservé,

$$\nabla.(\mathbf{C}_g \frac{E}{\sigma}) = 0, \tag{7.1}$$

σ est la fréquence intrinsec des vagues incidente et C_g la vitesse de groupe associée. Suivre l'évolution des H_s,

$$H_s = 4\sqrt{E}, \tag{7.2}$$

dans le champ de courant revient à suivre la largeur des tubes de rayons de vagues. Cette variabilité dans la largeur des tubes est due aux déplacements des rayons le long de l'axe Y, le déplacement est proportionnel à $\frac{C_g}{\zeta}$ avec ζ la vorticité du courant sous-jacent (KENYON, 1971 ; DYSTHE, 2001). Après un calcul rapide, je me suis retrouvé avec l'expression suivante pour l'énergie des vagues à une distance x,

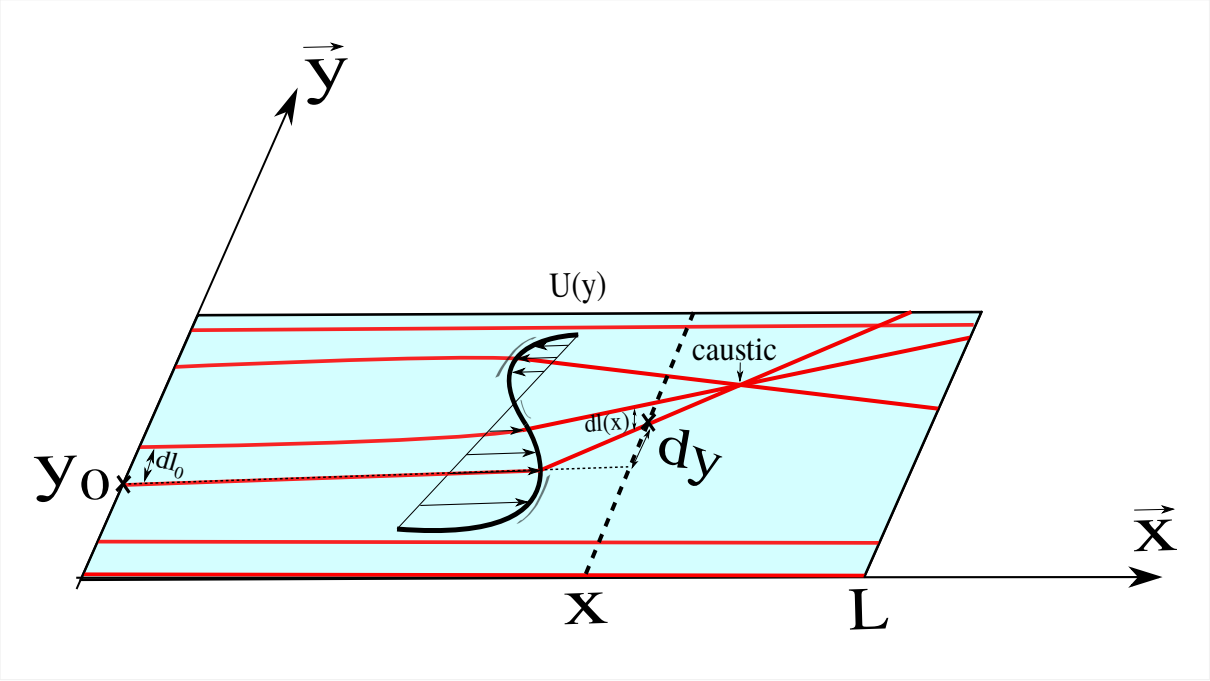

FIGURE 7.1 : Réfraction des rayons des vagues lors du passage d'un front de courant. La largeur entre 2 rayons est assimilée comme la largeur d'un tube de rayons de vagues égale à dl_0 au bord gauche et égal à dl(x) à une distance x.

$$E(x,Y) = \frac{C_g(0)E(0)}{C_g(x,Y)} \frac{1}{\partial Y/\partial dy_0} = \frac{1}{1 + \frac{1}{C_g(0)} \int\int \frac{\partial^2 U}{\partial y^2} \mathrm{d}x' \mathrm{d}x''} E(0), \tag{7.3}$$

E(0), C_0 font référence à l'énergie des vagues incidente et à leur vitesse de groupe initiale. Cette expression est valable pour des vagues se propageant dans la direction x et des courants perpendiculaires à la direction de propagation des vagues. Pour des courants de surface avec un profile de vitesse n'ayant pas de point d'inflexion (une dérivée seconde différente de 0), l'énergie des vagues n'est pas redistribuée le long de l'axe y à une distance x. Si l'énergie des vagues n'est pas refocalisée/défocalisée, les H_s ne sont pas modifiés. Des simulations numériques et des tracés de rayons ont confirmé cette remarque (Fig.7.2).

Le modèle analytique retrouve avec précision la position des premières caustiques (là où les rayons se croisent) par rapport au bord gauche du domaine. Cette distance se trouve là où le dénominateur de l'Eq.(7.3) s'annule. Cette distance est dépendante de la vitesse de groupe des vagues incidente et de l'intensité de la vorticité du courant sous-jacent. Cependant, le modèle théorique ne reproduit pas avec précision les champs de H_s simulés par le modèle de vagues lorsque la largeur des tubes de rayons devient trop petite. L'expression proposée Eq.(7.3) se doit d'être développée de sorte de ne pas prendre en compte exclusivement la largeur des tubes de rayons. En effet la forme en cupside Fig.7.2d formée par les rayons est reproduite par le champ de H_s simulés ce qui semble confirmer la nécessité de suivre la distribution de tous les rayons à des distances x plutôt que la largeur des tubes de rayons.

Des études numériques supplémentaires ont montré que des profils de courants avec un point d'inflexion parallèle à la trajectoire des vagues n'induit pas de changement d'amplitude des vagues.

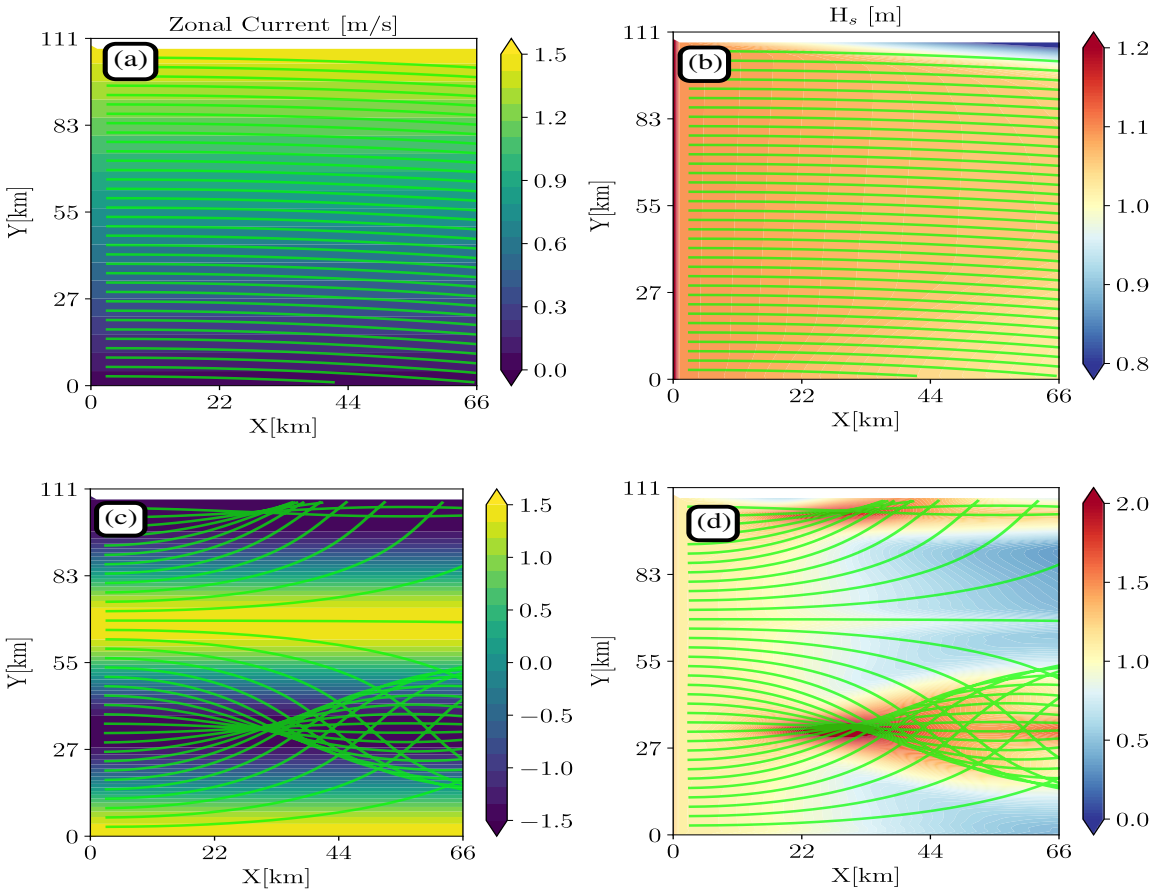

FIGURE 7.2 : Simulations numériques de vagues dans un domaine rectangulaire forcés par des courants zonaux avec un profile avec et sans point d'inflexion (u=U_0y, u=U_0cos(y) respectivement, U_0=1.5ms^{-1}). Les profiles de courants utilisés sont représenté sur les figures a et c, les hauteurs significatives des vagues associés sont données sur les figures b et d. En vert, j'ai tracé la trajectoire des rayons de vagues en considérant la conservation de l'action le long de ces derniers.

7.2.2 Analogie de la réfraction induite par les courants et la transformation SAR

Les courants de surface redistribuent spatialement l'action des vagues se concluant par une inhomogénéité dans le champ de H_s. Le résultat numérique et les résultats du tracé de rayons représenté Fig.7.2d montrent que pour des distances X différentes, la distribution des rayons n'est pas identique. La répartition des structures des H_s suit la distribution des rayons et cette distribution dépend du déplacement des rayons par rapport à leur direction initiale. Ces déplacements des rayons m'ont fait penser à la transformation SAR (HASSELMANN et al., 1985a). Dans cette transformation, les vagues focalisent et défocalisent le signal radar incident dû aux regroupement des vitesses orbitales des vagues (velocity bunching en anglais) à la surface de l'océan. Le signal renvoyé par la surface de l'océan dépend du champs de vagues. La focalisation du signal radar, où la capacité du SAR à reconstituer le champ de vagues, est limitée par une échelle de coupure proportionnelle au déplacement du signal incident par les vagues et à la longueur d'onde des vagues mesurées. Dans notre cas, le signal radar émit sont les H_s initiaux et la vitesse orbitale des vagues est notre courant de surface. On peut donc imaginer que l'échelle de corrélation des courants (la taille des tourbillons dans l'océan par exemple) et l'intensité de la réfraction, a pour effet de mener à des échelles limites de focalisation des rayons des vagues et donc de l'intensité des gradient de H_s. Cette analogie est plus flagrante pour des champs de courants plus réalistes et aléatoires comme montré dans WHITE et FORNBERG (1998) où la distribution des rayons à une distance donnée est fonction de l'échelle des tourbillons considérés.

Ce premier chapitre a permis de mettre en évidence comment les courants de surface induisent des variabilités dans le champ des H_s. Egalement il a été prouvé qualitativement que la nature du courant est primordiale dans l'intensité des variabilité des H_s. Dans le chapitre suivant, je m'attarde sur la variabilité du champ de vagues par des structures océaniques plus réaliste que les profils de vitesse analytiques étudiés jusqu'à présent.

7.3 Chapitre 2-Simulations numériques idéalisées des vagues dans un tourbillon océanique

7.3.1 Au delà de l'étude idéalisée du tourbillon océanique Gaussien

Au moyen du modèle numérique WAVEWATCH-III (THE WAVEWATCH III ® DEVELOPMENT GROUP, 2019) j'ai simulé des champs de vagues se propageant dans un champ de courant induit par la présence d'un tourbillon océanique de mésoéchelle. L'objectif de ce chapitre est de montrer que les courants ont un effet non-local sur les H_s et que les structures spatiales des courant sont déterminante dans l'intensité et les tailles caractéristiques des structures de H_s. Cette étude, idéalisée, a beaucoup été étudiée au cours des dernières décennies (MAPP et al., 1985 ; MATHIESEN, 1987 ; HOLTHUIJSEN et TOLMAN, 1991 ; GALLET et YOUNG, 2014), néanmoins les études précédentes se limitaient à des tourbillons aux motifs très idéalisés, peu réalistes (circulaire, Gaussien). L'augmentation récente des moyens de calculs et la meilleure compréhension de la fine échelle à la surface océanique ont permis de simuler la dynamique océanique à des échelles très fines de l'ordre d'un demi-kilomètre. Ainsi, j'ai pu aller au-delà des études précédentes qui décrivaient la réfraction et (pour certaines études) l'évolution des paramètres des vagues exclusivement dans des tourbillons océaniques idéalisés. Cette étude est également motivée par le fait que les tourbillons océaniques de méso- et de soumésoéchelles sont omniprésents à la surface de l'océan (CHELTON et al., 2011 ; MCWILLIAMS, 2016), l'étude isolée et idéalisée des interactions entre vagues et tourbillon réaliste

permettrait donc de mieux quantifier les flux induis par les interactions vagues-courants à l'échelle globale. Enfin dans l'approximation de l'optique géométrique en l'absence de forcage et de dissipation, les gradients de H_s et ceux des courants sont statistiquement liés. Je me suis donc demandé si les gradients de courants pouvaient être déduits à partir des gradients de H_s ce qui permettrait d'avoir accès aux informations des courants de surfaces, sans information préalable, à des échelles spatiales où les altimètres traditionnels peinent à les estimer.

7.3.2 Le tourbillon océanique utilisé pour forcer le modèle de vagues

Le tourbillon utilisé dans notre expérience numérique a été estimé à partir de mesures in-situ dans la mer d'Arabie présentées dans DE MAREZ et al. (2019). La stabilité du tourbillon a été ensuite étudiée au moyen du modèle océanique CROCO (Coastal and Regional Ocean COmmunity model, SHCHEPETKIN et MCWILLIAMS (2005)). Le tourbillon se destabilise spontanément via des instabilités mixtes barocline/barotrope faisant apparaitre des structures de sous-mésoéchelle très intenses en périphérie de la structure principale du tourbillon. Le coeur du tourbillon devient plus elliptique après destabilisation qu'il ne l'était à l'initial. Les structures du tourbillon déstabilisés sont en accord avec ce qui est observé depuis l'espace faisant du tourbillon destabilisé une structure plus réaliste que la structure Gaussienne et circulaire considérée jusqu'à présent. Des champs instantanés des courants associés sont donnés Fig.7.3a,b. Dans le modèle de vagues, j'ai considéré le courant comme stationnaire. La déstabilisation du tourbillon est détaillé dans DE MAREZ et al. (2020b).

7.3.3 Paramétrisation du modèle de vagues

J'ai donc considéré un domaine carré de 500km de côté avec des vagues se propageant de gauche à droite à partir de spectres de vagues étroits en fréquences. Les expériences ont été répétées de sorte que les vagues incidentes soient plus ou moins courtes afin d'analyser l'influence des longueurs d'ondes incidentes des vagues sur la réfraction induite par la présence du tourbillon océanique. Le modèle de vague a été forcé d'une part par un tourbillon de mésoéchelle circulaire et Gaussian et d'autre part par un tourbillons plus réaliste issu de la destabilisation spontanée du tourbillon de mésoéchelle, le champ de courant utilisé a été extrait après 210 jours de simulation. Des vagues ont été générées au bord gauche du domaine de sorte qu'un état stationnaire émerge après un certain temps d'intégration. Chaque heure, le modèle de vagues calcule en chaque point de grille (espacé de 500m) la valeur de H_s, de période moyenne ($T_{m0,-1}$) et celle de la direction dominante.

7.3.4 Inhomogeneité dans le champ de vagues et réfraction induite par un tourbillon océanique

L'intensité des gradients de hauteurs significatives (∇H_s) dépend de la nature et de l'intensité des gradients des courants sous-jacents (VILLAS BÔAS et al., 2020). Le résultat stationnaire du modèle montre de forts ∇H_s dans et en aval du tourbillon (Fig.7.3(c),(d)). Également l'émergence de tourbillons de sousmésoéchelle en périphérie de la structure principale du tourbillon (Fig.7.3f) induit la formation de ∇H_s à des échelles similaires (Fig.7.3d). On remarque que les inhomogénéités dans le signal ∇H_s sont bien plus fortes pour le modèle forcé avec le tourbillon destabilisé. La direction privilégiée des ∇H_s est allignée à la direction initiale des vagues. On note que les valeurs maximales (minimales) de H_s sont plus forte pour le tourbillons réaliste. Dans le tourbillon océanique étudié, la vorticité normalisée par le paramètre de Coriolis local (f_0=5.2.10^{-5}) présente de fortes valeurs ($\frac{\zeta}{f_0} \sim 2$). D'après

les résultats theoriques de KENYON (1971) ; DYSTHE (2001) on s'attend à une forte réfraction du champ de vagues par les courants. Pour imager cette réfraction, j'ai proposé une méthode de tracer de rayons qui suivent le système de vague en considérant l'action des vagues comme constante le long de la trajectoire. Le tracé de rayons est une approximation de la réalité, car la méthode considère des vagues monochromatiques avec une direction initiale unique et imposée. On remarque que les rayons convergent et divergent lors du passage du tourbillon (Fig.7.3(e,f)). La déflection des rayons est bien plus importante pour le tourbillon déstabilisé que pour le tourbillon Gaussien alors que les valeurs moyennes de vorticités sont similaires. Les zones de convergence de rayons coïncident avec les zones d'intensification de H_s. J'ai pu également noter que la période des vagues incidentes induit des zones de focalisations des rayons de vagues, plus ou moins éloignés du bord gauche du domaine. Plus les vagues sont longues, plus la focalisation des rayons à lieu loin du bord gauche, de même pour les zones d'augmentations des valeures de H_s.

7.3.5 ∇H_s et ∇U dans le tourbillon océanique

Comme discuté par ARDHUIN et al. (2017) et VILLAS BÔAS et al. (2020), les ∇H_s sont fonction de la nature et de l'intensité du courant. Quand on observe les sorties du modèle de vagues, on observe une certaine cohérence de phase entre la vorticité de surface et les structures de H_s. En faisant l'hypothèse que le courant est stationnaire sans forçage ni dissipation, on peut écrire que,

$$\nabla H_s \sim \frac{\nabla U}{\sigma}(\langle H_s \rangle k), \tag{7.4}$$

les étapes du calcul sont données en annexe A. En faisant l'hypothèse que la contribution de la divergence du courant n'induit pas de variabilité dans le champ de H_s (verifié dans VILLAS BÔAS et al. (2020)), on peut remplacer ∇U par ζ. σ est la fréquence intrinsèque des vagues (=$2\pi f$), k est le module du vecteur d'onde et $\langle H_s \rangle$ est la moyenne spatiale de H_s dans tout le domaine. Via cette égalité, il semblerait possible d'inverser le signal de vagues pour estimer les gradients de courants (∇U) responsables de la variabilité des propriétés des vagues. On propose de tracer les champs associés aux deux termes de Eq.7.4. Le résultat est donné Fig.7.4, les gradients de H_s ont été projetés le long de la direction des vagues et les gradients du courant ont été projeté perpendiculairement à la direction de propagation. En terme d'intensité les gradients normalisés de H_s sont légèrement plus intenses que les gradients de courant. Cette différence semble venir de la pente du spectre d'énergie cinétique du courant qui pourrait intervenir dans l'égalité Eq.7.4 (montré numériquement dans VILLAS BÔAS et al. (2020)). La remarque principale que l'on peut formuler est que l'on mesure de très forts ∇H_s même à l'extérieur du courant. Pour X>400km les ∇U sont nuls alors que ce n'est pas le cas pour les ∇H_s. On remarque bien ici l'aspect non-local des ∇U sur les H_s. Bien que ∇U et ∇H_s soient statistiquement liés, il n'est pas possible de retrouver la phase des gradients de courants via la mesure des ∇H_s. L'idée initiale était la suivante, ayant accès à de nouvelles mesures altimétriques de H_s filtrées permettent de mesurer les ∇H_s à des échelles très fines (QUILFEN et CHAPRON, 2019), ainsi qu'aux propriétés directionnelles et de longueur d'onde du champ de vagues via le nouveau satellite CFOSAT (où même via des techniques d'imagerie par télédétection), il semblait possible d'inverser le signal de vagues pour retrouver le champ de courant sous-jacent, néanmoins les courants ayant un effet non-local sur les H_s cette inversion est donc limitée du fait que les fronts de courants seraient potentiellement mal positionnés.

Dans ce chapitre, j'ai quantifié les variabilités du champ de vagues dans un tourbillon de mésoéchelle isolé avec, d'une part, un tourbillon Gaussien et d'autre part un tourbillon dynamique à la fois à méso- et sousmésoéchelle.

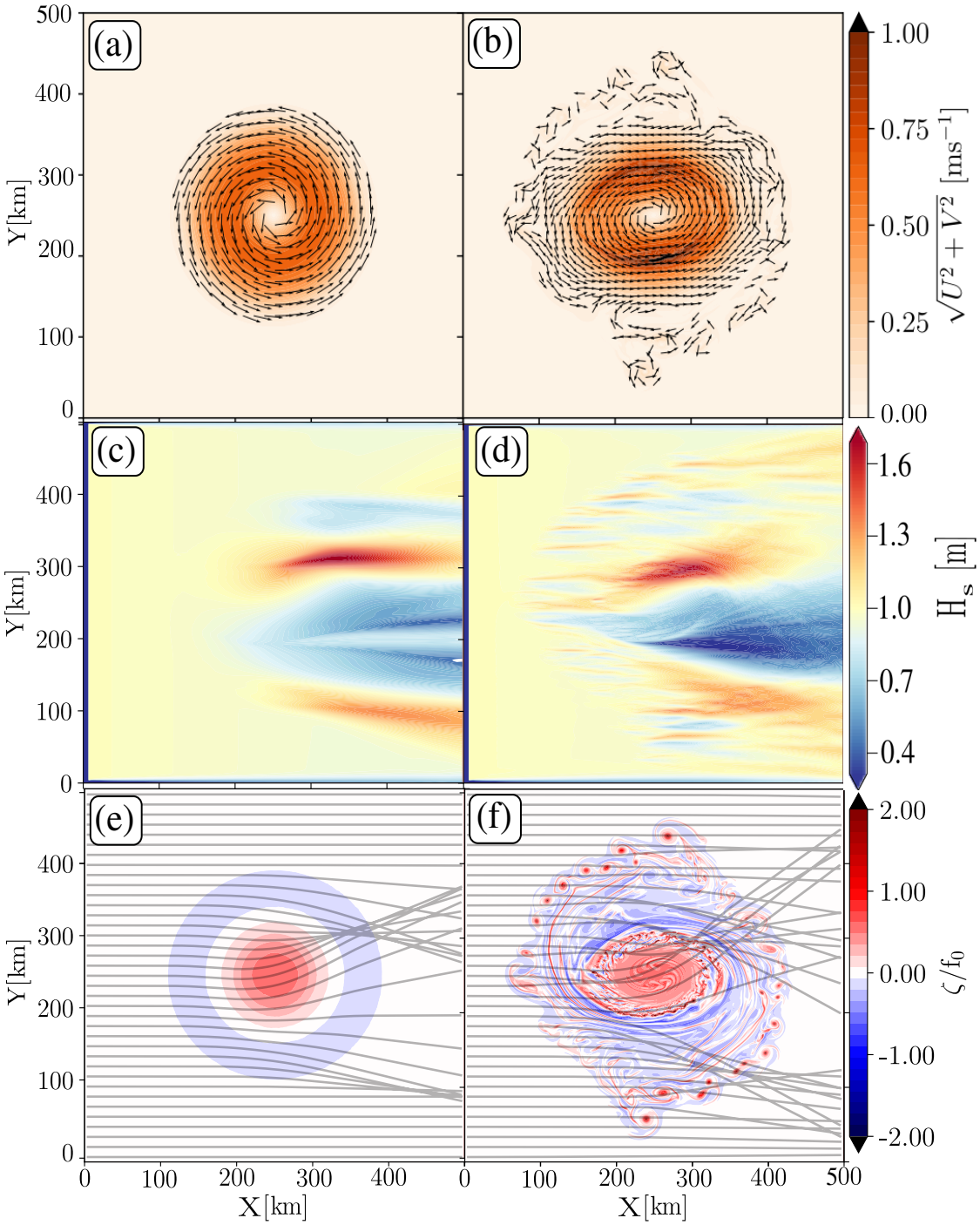

FIGURE 7.3 : Colonne de gauche, expérience numérique forcée par un tourbillon cyclonique Gaussien. Colonne de droite, expérience numérique forcée par un tourbillon plus réaliste. Les figures (a) et (b) montrent l'intensité du courant de forçage ainsi que ses directions. Les figures (c) et (d) montrent les hauteurs significatives des vagues (H_s) une fois l'état stationnaire atteint, sans courant la valeur de H_s est égale à 1 m dans tout le domaine. Les figures (e) et (f) montrent un tracé de rayons superposé à l'intensité de la vorticité normalisée par le paramètre de Coriolis du courant. Les figures de (c) à (f) sont pour des vagues incidentes de 7 s de période et une direction initiale vers le bord droit perpendiculaire à l'axe-Y. Sans courant,les rayons restent parallèles à l'axe-X. $\zeta = \partial_x V - \partial_y U$ et f_0=5.2$\times 10^{-5}$s^{-1}

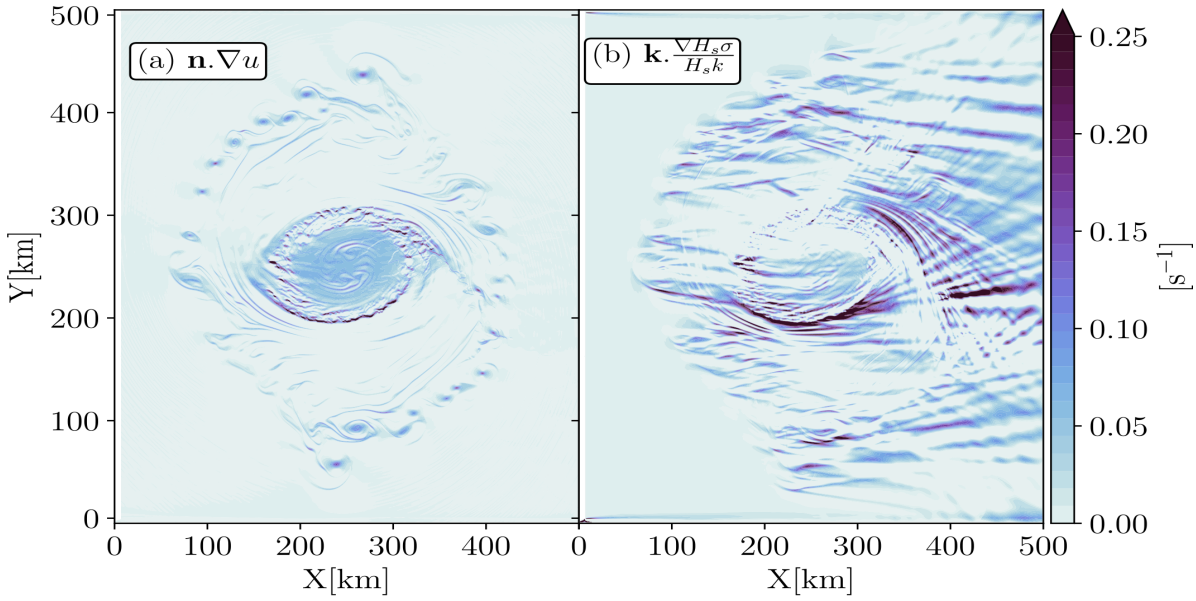

FIGURE 7.4 : Vérification graphique de l'Eq.7.4 pour le tourbillon réaliste. Figure de gauche (a) les gradients de courants projetés perpendiculairement à la direction de propagation des vagues. Figure de droite (b), les gradients de hauteurs significatives des vagues normalisés projetés le long de la direction de propagation.

Egalement il a été vu que les gradients spatiaux de H_s sont proportionnelles aux gradients spatiaux des courants de surface. Dans le chapitre suivant je propose d'effectuer une étude similaire dans un cadre réaliste où les tourbillons ne sont plus isolés mais entourés d'autres structures océaniques avec des patterns et des intensités différentes.

7.4 Chapitre 3-Variabilité des hauteurs significatives des vagues dans un régime de courant de bord ouest : un exemple dans le courant des Aiguilles

Dans le chapitre précédent, nous avons vu que les hauteurs significatives des vagues étaient grandement modulées localement de la méso- à la sousmésoéchelle. Comme dans la réalité un tourbillon est rarement isolé, j'ai proposé d'étudier ces modulations dans un cadre plus réaliste en se concentrant dans le courant des Aiguilles. La variabilité des H_s dans le courant des Aiguilles a grandement été étudiée durant le XX^{ème} et lors des deux dernières décennies (IRVINE et TILLEY, 1988 ; LAVRENOV, 1998 ; QUILFEN et al., 2018 ; QUILFEN et CHAPRON, 2019 ; LEÓN et GUEDES SOARES, 2021). Dans ce chapitre, j'ai souhaité dans un premier temps comprendre pourquoi les forts ∇H_s mesurés par l'altimétrie dans les forts courants de bord ouest ne semble pas être reproduit par les modèles numériques de vagues (ARDHUIN et al., 2017 ; QUILFEN et al., 2018). En parallèle j'ai souhaité comprendre quels sont les paramètres de vagues et de courants responsables de la formation de ∇H_s pentus dans le courant d'Aiguilles.

7.4.1 Résumé de MARECHAL et ARDHUIN (2021)

Dans ce papier, les auteurs se sont focalisés sur le courant des Aiguilles, celui-ci étant un bon laboratoire naturel pour mesurer l'effet que peuvent avoir les courants sur le signal de vagues du fait de son exposition à l'océan Austral où se forment tout au long de l'année des tempêtes générant des vagues aux H_s conséquents (YOUNG, 1999). Les auteurs se sont basés sur des simulations numériques construites sur le cadre de WAVEWATCH III THE WAVEWATCH III ® DEVELOPMENT GROUP (2019). Le modèle a été forcé en ses bords par des spectres de vagues issus d'un modèle global forcé exclusivement par le vent. Le domaine régional (défini par les bornes : $[15°E, 30°E], [40°S, 30°S]$) a été forcé avec des vents du centre européen (ECMWF, DEE et al. (2011)) et des courants à la fois issus de simulations réalistes et hautement résolues spatialement (à partir du modèle CROCO) et dérivés des mesures de la hauteur des océans effectuées par les altimètres opérationnels (**rio&al.2014**). Les courants hautement résolus ont également été dégradé en résolution jusqu'à des résolutions comparables aux courants estimés par l'altimétrie. À titre comparatif, une simulation sans forçage de courant a été effectuée. Les auteurs ont confirmé le résultat de ARDHUIN et al. (2017) qui stipule que l'intensité des ∇H_s est dépendante de la résolution en direction du modèle de vagues, plus précisément que plus la grille spectrale est discrétisée en direction mieux la réfraction est résolue. J'ai donc discrétisé la grille spectral en 32 fréquences et 48 directions. Les sorties du modèle de vagues ont été interpolées en temps et en espace sur les traces altimétriques disponibles dans le domaine du courant des Aiguilles pendant les trois ans de simulation (2014-2016). Les données altimétriques utilisées viennent du nouveau jeu de données du programme CCI-SeaStates (DODET et al., 2020). Les ∇H_s ont été calculés le long des traces altimétriques pour le modèle et les données, puis projetés sur une grille régulière à la résolution de $1/8° \times 1/8°$. Les cartes de moyenne de ∇H_s dans le courant des Aiguilles montrent que le modèle de vagues ne reproduit pas les gradients moyens mesurés par les altimètres si les courants sont trop faiblement résolus (Fig.7.5). En effet les courants dérivés des mesures altimétriques, bien qu'ils permettent de cartographier à l'échelle globale la dynamique de surface, ne sont pas suffisament résolus ni suffisament intenses (vitesse des courants souvent sous-estimée dû à l'interpolation spatiale et temporelle des données altimétriques) pour reproduire des ∇H_s réalistes. QUILFEN et al. (2018) ont relevé que les variations rapides de H_s le long des altimètres n'étaient pas reproduit par leur modèle de vagues, cependant ces derniers étaient, en effet forcés par des courants trop faiblement résolus. L'utilisation de courants statistiquement réalistes (pas forcément résolus en terme de phase, c'est à dire que les tourbillons de petites échelles ne sont pas forcément à la bonne place dans le champ de courant) permettent de reproduire la carte moyenne des ∇H_s mesurés par les altimétres. Enfin on confirme également que les ∇H_s régionaux sont générée par la présence de courants au vu des résultats simulations sans courant (Fig.7.5e). La proportionnalité des gradients spatiaux de H_s et ceux d'énergie cinétique de surface ont également été prouvé dans cette publication aux moyens d'études spectrales. Les spectres moyens des H_s simulés et observés suivent la pente des spectres d'énergie cinétique des courants (Fig.7.6a,b).

Dans ce même chapitre, les auteurs ont aussi confirmé l'importance de l'étalement directionnel des vagues incidentes σ_θ) sur l'intensité des ∇H_s (HELLER, 2005 ; QUILFEN et al., 2018) . Pour cela de nouvelles simulations numériques ont été effectuées en modifiant la largeur en direction des spectres au bord du domaine E(f, θ). Il a été montré que plus les spectres sont directionnels (σ_θ petit) plus les ∇H_s sont abruptes. Il est important de noter que ce même étalement angulaire du spectre de vague est une quantité qui nécessite des améliorations dans les modèles spectraux (STOPA et al., 2016). Les nouvelles données du satellite CFOSAT et de son antenne SWIM, qui mesure le spectre directionnel des vagues (HAUSER et al., 2020), pourront être mises à profit pour améliorer la représentation de σ_θ dans les modèles spectraux.

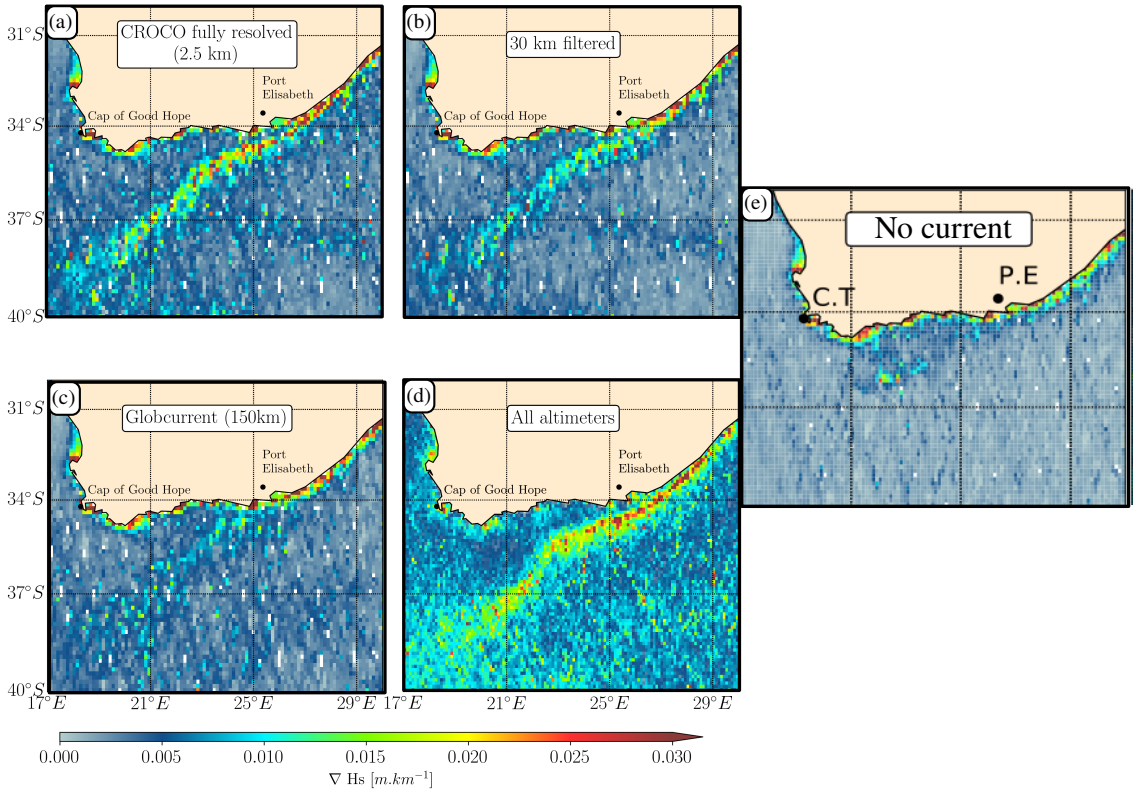

FIGURE 7.5 : Cartes des moyennes des gradients de hauteurs significatives (∇H_s) dans le courant des Aiguilles : (a) pour le modèle de vagues forcé avec des courants hautement résolus issus d'une simulation statistiquement réaliste (CROCO), (b) pour le modèle forcé par ces mêmes courants mais dégradés à une résolution de 30km, (c) pour le modèle forcé par des courants issus de l'altimétrie, (d) pour les mesures altimétriques et (e) pour une simulation numérique sans forcage de courant.

7.4.2 Quelques éléments supplémentaires sur la variabilité des H_s dans le courant des Aiguilles

J'ai également souhaité vérifier l'égalité proposée par VILLAS BÔAS et al. (2020) dans l'approximation de l'optique géométrique (égalité donnée sous une autre forme dans l'Eq.7.4). La principale différence entre mes simulations et celles des auteur.e.s précédent.e.s est que dans notre cas nous avons considéré les termes sources de l.Eq.1.21. Pour se rapprocher du cadre de l'étude faite par VILLAS BÔAS et al. (2020) nous avons également effectué une décomposition de Helmotz sur le champ de courant afin de séparer la contribution divergente et rotationnelle du courant de surface. Cette séparation faite, j'ai observé que la contribution divergente dans la gamme de la mésoéchelle est nettement plus faible que la contribution rotationnelle. j'ai réécrit l'équation de VILLAS BÔAS et al. (2020) dans sa forme spectrale ce qui donne,

$$\sqrt{\int_{k1}^{k2} k^{*2} PSD_{Hs}(k^*)dk^*} \sim \frac{2}{S \times C_g} \sqrt{\int_{k1}^{k2} k^{*2} PSD_{KE^\psi}(k^*)dk^*} \langle H_s \rangle, \tag{7.5}$$

les bornes d'intégration considérées étant : $k1$=2π/116km et $k2$=2π/15km, S la pente du spectre d'énergie cinétique et C_g et $\langle H_s \rangle$ sont la vitesse de groupe et le H_s moyen du domaine respectivement. PSD_{KE^ψ} est le spectre en puissance de l'énergie cinétique du courant (de la contribution rotationnelle) de surface et PSD_{Hs} le spectre en puissance des hauteurs significatives. k* sont les nombres d'ondes associés à l'analyse spectrale. ARDHUIN et al. (2017) et MARECHAL et ARDHUIN (2021) ont montré numériquement la proportionnalité entre les spectres d'énergies cinétiques et le spectre de H_s dans la gamme de la méso- et de la sousmésoéchelle (Fig.7.6a,b). L'Eq. 7.5 montre cette proportionnalité explicitement. Pour chaque temps d'intégration du modèle de vagues j'ai vérifié cette égalité (pendant un mois d'intégration, soit 720 égalités au total). Les PSDs ont été estimées à partir d'une transformée de Fourier discrète 2D du champ de vagues projeté le long des latitudes (à partir de la direction moyenne des vagues) et intégrées ensuite suivant l'axe-x ce qui donne un spectre directionnel le long de k_y. Ce spectre directionnel est ensuite intégré entre $k1$ et $k2$. Pour chaque champ instantanné on a donc une valeur pour le membre de droite et pour le membre de gauche de l'Eq.7.5. Le résultat final est donné Fig.7.6 dans le cas où le champ de vagues a été projeté le long des méridiens et dans le cas sans projection. Bien que dans notre cas, les vagues simulées étaient bien plus réalistes que dans VILLAS BÔAS et al. (2020), l'Eq.7.5 est cependant consistante avec un étalement des données autour de la droite $y = x$ un peu plus conséquent dans nos simulations.

Dans ce chapitre, j'ai montré dans un cadre réaliste que l'intensité des gradients spatiaux de H_s dépendent fortement de la nature et de l'intensité du courant sous-jacent. Egalement, les paramètres des vagues, c'est à dire leurs directions d'incidences, leurs longueurs d'ondes et leur étalements directionnelles sont des paramètres clefs dans l'intensité des ∇H_s. De plus, le courant lui même affect ces paramètres. Ainsi, pour essayer de mieux comprendre la variabilité du courant sur les propriétés des vagues et la contribution des paramètres des vagues sur l'intensité des ∇H_s, je regarde dans le prochain chapitre les propriétés directionnelles et en longueurs des vagues lors du passage de fronts océaniques. Ces observations viennent du nouveau diffusiomètre/spectromètre de vagues SWIM appareillé sur CFOSAT.

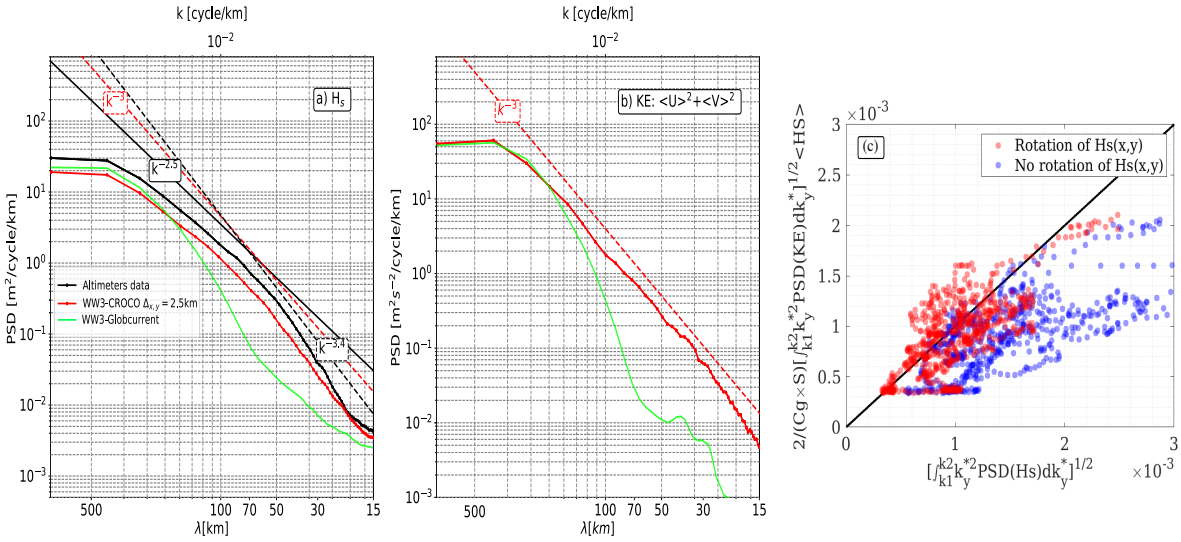

FIGURE 7.6 : Les figures (a) et (b) représentent les spectres moyens sur une période de 3 ans de H_s et d'énergie cinétique de surface (KE) pour les courants hautement résolus issue de simulation numériques avec le modèle CROCO (en rouge) et du produit altimétrique Globcurrent (en vert). Le spectre de H_s est également tracé pour les données altimétriques. La figure (c) est la représentation graphique de l'Eq.7.5, l'axe x est le terme de gauche de l'Eq.7.5 et l'axe y le terme de droite. Chaque point représente une analyse spectrale du champ de H_s et de courant. Les points rouges sont pour les champs de H_s reprojetés le long de l'axe des longitudes et les points bleus pour les champ non reprojetés.

7.5 Chapitre 4-Variabilité du spectre de vagues et de ses paramètres dans le courant des Aiguilles mesurée par l'antenne SWIM appareillée sur CFOSAT

7.5.1 Principe de la mesure

L'antenne SWIM est un spectromètre de vagues en bande Ku (13 GHz) à plateforme rotative avec 5 antennes proches nadir (à 2°, 4°, 6°, 8° et 10°) et avec un altimètre qui mesure les vagues au nadir. Le satellite mesure l'écho du signal émis qui s'est retrouvé modulé par la présence des vagues à la surface de l'océan. Un spectre de modulation est donc mesuré pour chaque incidence et azimut du satellite. Une fois que la plateforme a effectué une rotation de 360°, un spectre directionnel de vagues, $\mathrm{E}(f,\theta)$, est estimée pour chaque incidence. L'altimètre au nadir mesure les H_s le long de la trace du satellite. En général, la transformation du spectre de modulation en spectre de vagues se calcule de manière théorique (JACKSON, 1987). La fonction qui lie le spectre de modulation au spectre de vagues est appelée la Modulation Transfert Function (MTF). Dans ce manuscrit de thèse, la stratégie adoptée fut d'utiliser la mesure du H_s de l'altimètre pour estimer la MTF. L'hypothèse était de considérer que le H_s estimé à partir des données proche nadir était identique à la valeur la plus proche (géographiquement) du H_s mesuré par l'altimètre. On notera cependant que la mesure n'est pas effectuée dans la même zone. L'expression

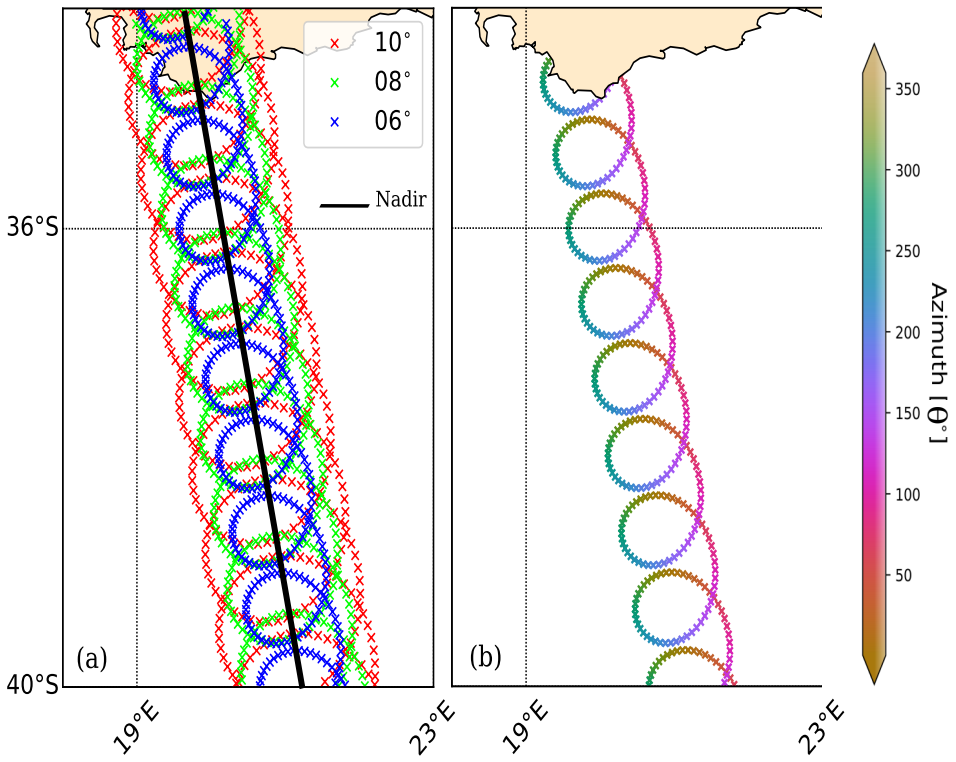

FIGURE 7.7 : On représente sur la figure (a) les empreintes au sol de 9 rotations complètes de la plateforme SWIM pour les incidences 6°, 8° et 10° ainsi que l'empreinte au sol de l'altimètre. Sur la figure (b) nous montrons l'azimute de l'antenne pour le même passage pour l'antenne 6°.

analytique de la MTF est donc,

$$MTF = \left(\frac{4}{Hs_{nadir}}\right)^2 \int_{k_0}^{k_{max}} \int_0^{2\pi} P_m(k,\theta) dk d\theta, \tag{7.6}$$

avec ϕ l'incidence de l'antenne, θ l'azimut (égal à la direction des vagues), k le nombre d'onde des vagues et $Pm(k,\theta,\phi)$ leur spectre de modulation. Le spectre de vagues est donc E(k,θ,ϕ) et est égal à : MTF$\times$ $Pm(k,\theta,\phi)$. Pour récupérer le spectre de vagues, les mesures ont été moyennées par incidence et azimut dans des boîtes de dimensions 70km $\times$ 90km de part et d'autre de l'altimètre. Dans chaque boite E(f,θ) est estimé avec $\theta \in$ [0,180°] et $f \in [0.05, 0.12]$Hz (= période de 20s à 8.3s).

J'ai tracé les empreintes au sol des incidences 6°, 8° et 10° ainsi que les azimuths de l'antenne 6° pour un passage au-dessus de la région du courant des Aiguilles Fig.7.7. De part et d'autre de l'azimute 0° (180°), dans un cône de 8°, le bruit du speckle est très important noyant le signal des vagues dans le bruit de mesure, j'ai dénomé cette zone par "cône aveugle".

7.5.2 Evolution du spectre de vagues et de ses paramètres dans le courant des Aiguilles

J'ai étudié six passages du satellite dans le courant des Aiguilles, pour des états de mer, de vent et de courant différents. Dans les cas étudiés, j'ai relevé un cas où le ∇H_s est pentu si ce n'est extrêmement pentu. En effet

l'altimètre de SWIM mesure un changement brusque de H_s entre 10 m et 6 m en moins d'un degré de latitude (soit $\sim$ 111km). On se propose de reprendre ce cas dans cette synthèse de thèse. Le 11 juin 2019 une forte tempête entre dans la région du courant des Aiguilles avec des H_s de l'ordre de 7 m. À 20°E, 37.5°S, les H_s sont renforcés et atteignent des valeurs maximales de 10 m. Cette zone coïncide avec l'ultime front du courant principal des Aiguilles (juste avant la rétroflexion). À cette date, 9 spectres de vagues sont estimés par l'antenne SWIM pour chacune de ses incidences. On décide de s'attarder sur les spectres aux alentours du très fort ∇H_s régional pour l'incidence 6° (Fig.7.8). Au fur et à mesure des spectres, la variance augmente nettement avec un maximum représenté Fig.7.8c. On peut voir que les systèmes de vagues ne sont pas symétriques de part et d'autre de l'altimètre, particulièrement pour ce qui est de la Fig.7.8a où la partie à l'est de l'altimètre est nettement moins énergétique que la partie à l'ouest. De plus, la partie ouest mesure deux systèmes de vagues, un très étalé en direction à $f = 0.08Hz$ et un très directionnel à $f = 0.06Hz$. La partie est est nettement moins énergétique surtout pour le système de vagues aux basses fréquences. La Fig.7.8c montre que les vagues ont légèrement tourné vers le nord par rapport au spectre présenté Fig.7.8a. On note qu'il y a une ambiguïté de 180° dans la direction des vagues car SWIM ne mesure pas le décalage Doppler des vagues[1], néanmoins cette ambiguité a été levée par une simulation numérique effectuée en parallèle. Pour aller plus loin que cette étude qualitative des systèmes de vagues j'ai proposé d'étudier les paramètres des vagues associés à chaque demi-spectre : la hauteur significative, la période moyenne, la direction moyenne et l'étalement en direction (H_s,$\mathrm{T}_{m0,-1}$, θ_m,σ_θ) pour chaque incidence. Leurs expressions sont données dans l'introduction de ce manuscrit (Eq.1.4,1.5,1.7,1.9). Les résultats sont présentés Fig.7.9, la zone correspondante aux spectres étudiés est surlignée en vert. Les H_s estimés par les mesures proches nadir coïncident avec les mesures de l'altimètre ce qui confirme l'Eq.7.6 (Fig.7.9a). La taille des boîtes dans lesquelles sont estimés les spectres ont une taille telle que l'on relève une sous-estimation des ∇H_s mesurés par les antennes proches nadir par rapport aux mesures de l'altimètre. Également, certains ∇H_s régionaux comme entre 40° et 39° (sûrement un tourbillon océanique ici, cf chapitre 2) sont noyés dans le signal moyen. Les périodes moyennes aux alentours du fort gradient varient entre 14 s et 15 s selon les incidences (Fig.7.9b). À l'est de l'altimètre les mesures proches nadir révèlent une augmentation de période moyenne alors qu'à l'ouest SWIM capture une décroissance des périodes. Les spectres de vagues montrent également de larges variations de la direction moyenne le long des fronts de courants, à 37.5° on observe un fort gradient de direction moyenne entre les 3 incidences pour des mesures effectuées de part et d'autre de l'altimètre. L'étalement en direction mesuré révèle un fort changement de directionnalité des vagues entre 38.25° et 37.5°, les mesures pour les 3 incidences sont consistantes entre elles et révèle un système de vagues plus étalé en direction au niveau du forts ∇H_s ce qui pourrait être expliqué par l'émergence de houles croisées dans et au voisinage de la branche du courant principal, ce système se caractérise par des vagues piégées dans le courant et d'autres vagues qui se propagent librement et de manière oblique au courant, comme discuté par KUDRYAVTSEV et al. (2017a). Si l'on fait le lien avec le chapitre 2, les gradients fortement pentus de H_s coïncident à une focalisation des rayons de vagues donc l'étalement en direction augmentent ce qui est observé ici (Fig.2.3d).

En conclusion de ce chapitre, j'ai essayé de montrer que les antennes proches nadir à 6°, 8° et 10° permettent de capturer les effets des courants sur le spectre de vagues et ses paramètres. Les résultats théoriques présentés en amont sont vérifiés par les mesures de SWIM. Les courants induisent une forte variabilité régionale sur le champ de vagues, ses hauteurs, ses longueurs d'ondes et ses directions. Cependant la taille des boîtes dans lesquelles sont estimés les spectres induit une résolution trop grossière des variabilités issues des interactions entre les vagues et

1. si les vagues s'éloignent ou se rapprochent de l'antenne

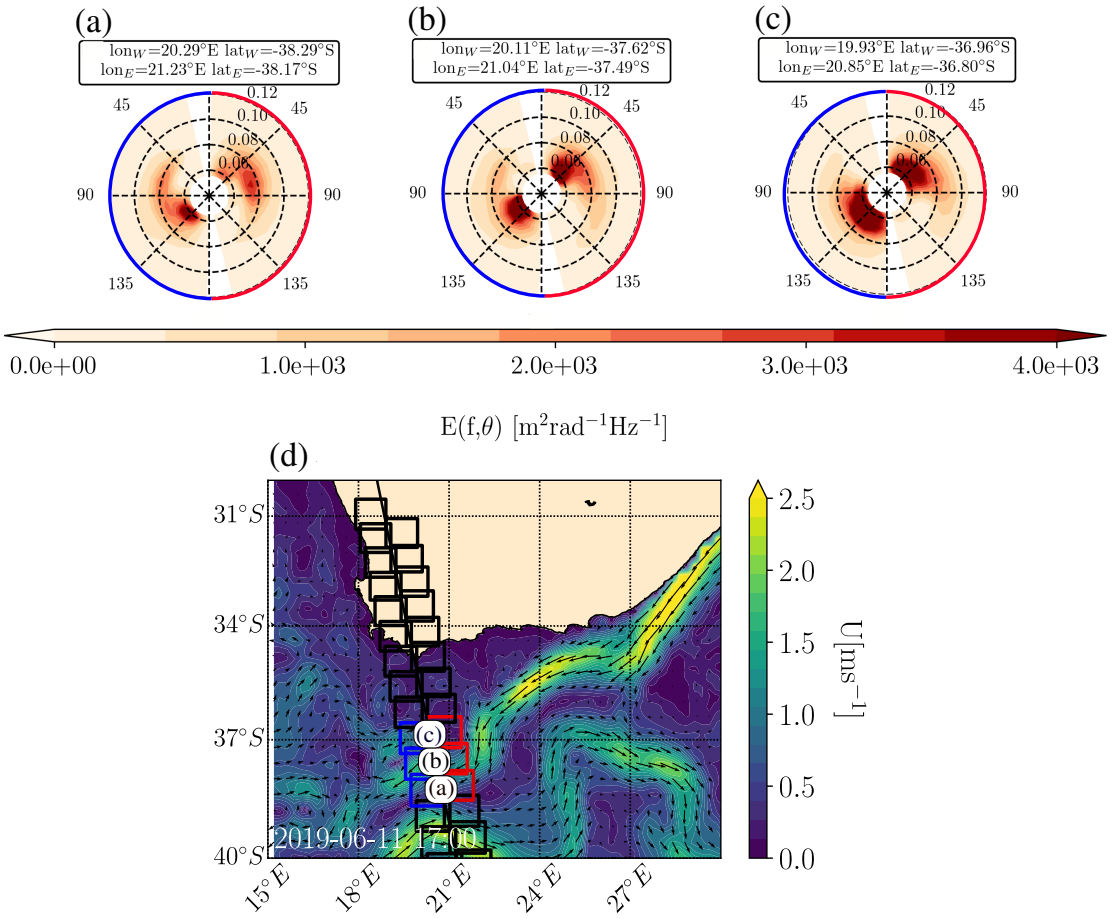

FIGURE 7.8 : Passage du satellite CFOSAT au dessus du courant des Aiguilles le 11 juin 2019 à 17 :00-UTC. Les figures (a), (b) et (c) sont 3 spectres de vagues successifs estimés de part et d'autre de l'altimètre à bord de SWIM. Les demi-cercles bleus et rouges se réfèrent aux boîtes sur la figure (d). Les boites bleues (appelées West boxes) sont pour les spectres estimés à l'ouest de l'altimètre et les boîtes rouges (appelées East boxes) pour les spectres estimés à l'est. Les positions aux-quelles les spectres sont calculés sont données sur la figure (d) par les étiquette (a,b et c). Le cône aveugle a été retiré et le spectre a été projeté de sorte que l'azimuth 0° coïncide avec le nord. Le courant représenté sur la figure (d) vient du produit altimétrique Globcurrent **rio&al.2014**.

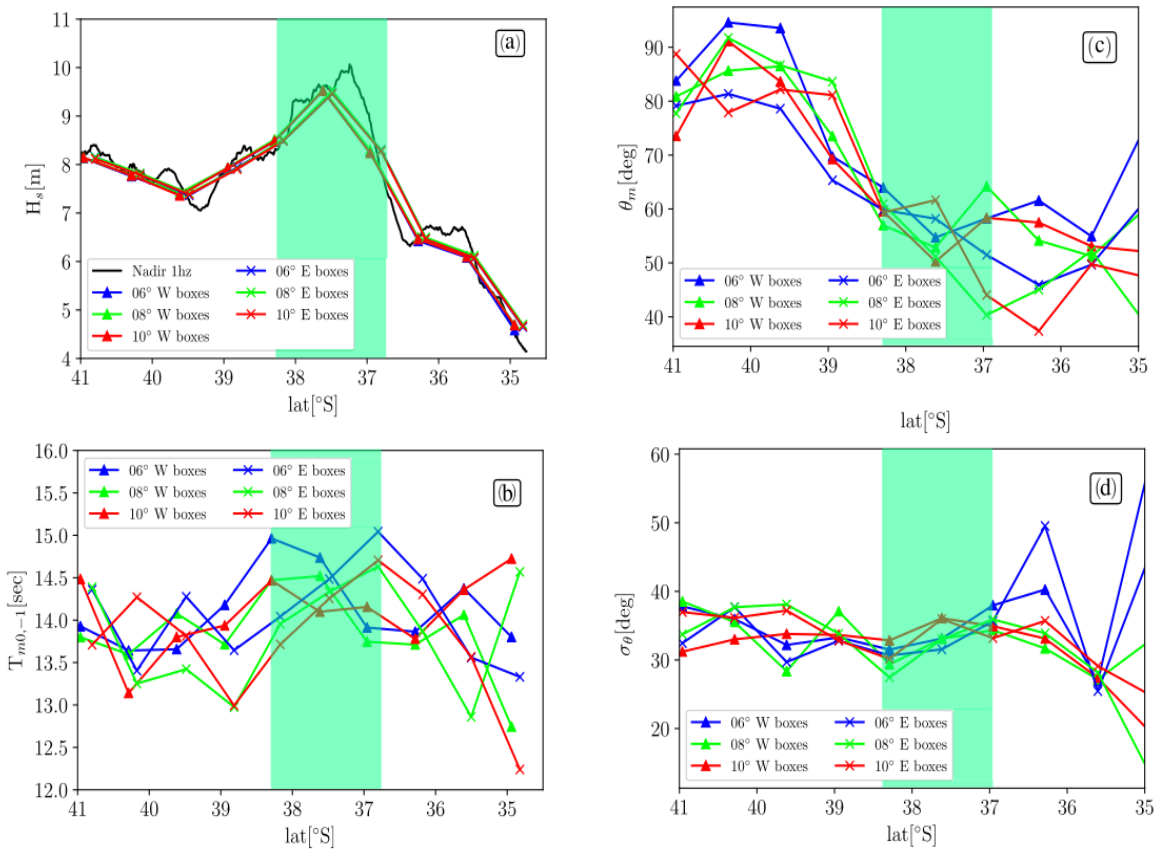

FIGURE 7.9 : La figure (a) montre l'évolution des H_s mesurés par l'altimètre et estimés à partir des spectres obtenus par les mesures proches nadir. La figure (b), (c) et (d) montre l'évolution de la période moyenne, de la direction moyenne et de l'étalement en direction des vagues respectivement. Les paramètres ont été calculés pour les incidences de 6° (en bleu), 8° (en vert) et 10° (en rouge). Les paramètres estimés pour les boîtes à l'ouest de l'altimètre (W) et pour celles à l'est (E) sont donnés par les triangles et les croix respectivement.

les courants. Ce manque de résolution est d'autant plus mis en évidence si l'on s'attarde sur les H_s estimés par l'altimètre[2]. En effet toutes les variabilités à des échelles inférieures de 90 km sont cachées dans le signal moyenné. La description de l'effet des courants sur les vagues pourrait gagner en résolution en étudiant individuellement les spectres à la position où le spectre est mesuré. Cette stratégie permettra d'étudier les changements rapides des paramètres directionnels et de longueurs d'onde et de remonter aux propriétés des courants en approximant la cinématique des vagues dans un champ de courant par les équations de l'optique géométrique (PHILLIPS, 1977) comme proposé.e.s par VILLAS BÔAS et al. (2020).

7.6 Conlusion finale et perspectives

Tout au long du manuscrit nous avons étudié au moyen de simulations numériques et de données de télédétections l'évolution du champ de vagues dans des courants fortement rotationnels à méso- et à sousmésoéchelle. Les premières études numériques idéalisées ont (re)montré que le champ de vagues est fortement dépendant du champ de vorticité sous-jacent dû à la réfraction que celui-ci induit sur les vagues. Aussi, les gradients spatiaux de hauteurs significatives des vagues sont proportionnels aux gradients spatiaux des courants dû à la dépendance des échelles des courants dans la redistribution spatiales de l'énergie des vagues. J'ai pu également montré que plus les vagues incidentes sont courtes plus les zones d'augmentations des H_s (associé aux zones de focalisation de rayons) émergent proche de la bordure gauche du domaine avec des valeurs extrêmes similaires. Dans l'approximation de l'optique géométrique, les gradients des hauteurs significatives des vagues peuvent être statistiquement estimés (et seulement statistiquement) en fonction de la longueur d'onde des vagues incidentes et des gradients de courants traversés. Il est important de noter que le tourbillon réaliste présenté ne peut pas être dérivé à partir des mesures altimétriques traditionnelles du fait du manque de résolution spatiale et temporelle de ces dernières (voir discussion section 12 de DE MAREZ et al. (2020b)). C'est pourquoi, si l'on décline cette étude à l'échelle globale, on peut noter qu'une grande partie des ∇H_s (ou raideurs de pentes) ainsi que les flux air-mer associés sont fortement sous-évalué du fait du manque de résolution des modèles opérationnels de vagues où plutôt du manque de résolutions spatiales des courants utilisés en forçage.

Dans des cas plus réalistes, comme dans le courant des Aiguilles, les altimètres mesurent des ∇H_s très pentus qui coïncident avec les zones de forts fronts océaniques du courant des Aiguilles ainsi qu'avec les zones de formation d'états de mer croisés. Les modèles de vagues forcés avec des courants trop faiblement résolus spatialement ne reproduisent pas les gradients pentus mesurés par les altimètres. Ce n'est qu'avec des modèles de courants statistiquement réalistes que les modèles arrivent à reconstituer les valeurs moyennes de ces gradients ainsi que leurs extrêmes. Il a donc été souligné que les gradients fines échelles des courants ont une grande influence sur l'intensité des ∇H_s dans des cas réalistes.

Pour ajouter une description directionnelle et en longueur d'onde aux résultats obtenus par les altimètres dans le courant des Aiguilles j'ai proposé de suivre l'évolution du spectre de vagues et de ses paramètres au moyen des nouvelles données du satellite franco-chinois CFOSAT et de son antenne SWIM avec ses multiples incidences. Les différentes incidences arrivent à capturer les variabilités caractéristiques des modulations induites par les courants sur le signal de vagues. Néanmoins, il sera nécessaire d'ouvrir l'étude jusqu'à présent menée à des données un peu plus bruts (et non moyenné dans des boîtes) pour essayer de raffiner les actions des fines échelles océaniques sur les vagues.

2. les données ont été validées auprès de la mission Jason-3 HAUSER et al. (2020)

Grâce aux quatre premiers chapitres, j'ai pu diagnostiquer comment les courants de surfaces induisent des variabilités dans le champ de H_s et quantifier ces variabilités. Bien que je n'apporte pas une réponse unique à la problématique exposée en introduction, les travaux décrit dans cette thèse confirment et apportent un regard complémentaire aux études passées des effets des courants sur les vagues. Les résultats présentés auront certainement des applications dans le domaine de la télédétections, ainsi que dans la modélisation des flux à l'interface air-mer pour les modèles océaniques et atmosphériques grandes échelles.

Finalement, des études supplémentaires pourront venir compléter ce travail de thèse en étudiant les effets d'autres régimes de courants sur le champ de vagues. En effet une large gamme de régime de courant de méso- et de sousmésoéchelle n'ont pas été appréhendés dans les 4 premiers chapitres du manuscrit. Des travaux complémentaires comme GEMMRICH et GARRETT (2012) sur les interactions des vagues avec les oscillations inertielles et proche-inertielles[3] ou comme LENAIN et PIZZO (2021) sur les interactions entre vagues et signatures en surface d'ondes internes pourront être menés. Ceux-ci pourront reposer sur des études numériques idéalisées et/ou réalistes grâce à l'augmentation permanente des moyens de calculs, mais aussi sur des techniques d'imagerie spatiale qui ont prouvé leur robustesse dans la capture des effets des courants sur les vagues à très fine résolution (KUDRYAVTSEV et al., 2017b) et même dans la reconstruction du champ de courant (YUROVSKAYA et al., 2019). Combiner les résultats présentés dans cette thèse et les perspectives proposées ici, permettront d'améliorer encore davantage nos connaissances sur les effets des courants de méso- et de sousmésoéchelles sur les caractéristiques des vagues.

3. qui représentent les courants les plus énergétiques de l'océan mondial

APPENDIX A

EFFECTS ON BROADER BANDED INCIDENT SPECTRA AND NONLINEAR WAVE-WAVE INTERACTIONS ON WAVE-CURRENT INTERACTIONS

Here we present an additional work performed in the same current field that was presented in chapter 3-*Idealized wave simulations in an isolated mesoscale oceanic eddy*. The aim of this appendix is to highlight that wave-wave interactions have an effect on the intensity of the ∇H_s.

A.0.1 New model setup

In the previous analysis, the incident waves have been simulated via wave spectra gaussian in frequency with a frequency spreading (σ_f) equal to 0.03 Hz. For a time scale much larger than the wave period and a gaussian surface, nonlinear wave-wave interactions lead to a change of the wave energy in the wave field (Hasselmann, 1962). Here we wanted to quantify the effects of nonlinear wave-wave interactions on the wave parameter gradients in the eddy field. To study the cross-spectral energy flux between frequencies we activate the nonlinear source term (S_{nl}). The right-hand side of Eq.(1.21) was thus not equal to 0 any more but to S_{nl}. Because simulations initialized with very narrow banded spectrum do not show a clear difference between simulations with and without S_{nl} (not shown), we extended the frequency spreading of the incident wave trains to σ_f=0.1 Hz. For sufficiently steep waves, nonlinear wave-wave interactions redistribute wave energy between frequencies over the spectrum which strongly modify the shape of the spectrum (Komen et al., 1984). As ∇H_s is a function of the wave steepness (kH_s, Eq.3.3) we expected that nonlinear wave-wave interactions would have an impact on the intensity of the wave parameter gradients. Nonlinear wave-wave interactions have been modeled using the discrete interaction approximation (Hasselmann et al., 1985b). The wave simulation has been run for a sufficiently long time to capture the long-term effect of nonlinear wave-wave interactions on the wave parameters. Wave simulation has been performed only for 7 sec incident waves over the fully developed eddy field. This appendix is a simple introduction of how both wave-wave interactions and wave-current interactions could induce inhomogeneities in the wave field still in a very idealized framework. Further investigations will be required.

A.0.2 Results

For a given wave parameter (H_s or $T_{m0,-1}$), the relative difference has been computed between simulations where nonlinear source term was activated and deactivated (Eq.A.1),

$$\Delta X = \frac{X_{S_{nl}} - X_{noS_{nl}}}{X_{noS_{nl}}} \times 100. \tag{A.1}$$

The nonlinear wave-wave interactions have a large effect on the spatial gradients of wave parameters studied before. H_s are globally enhanced whereas $T_{m0,-1}$ are decreased (Fig.A.1). The spatial variability of the H_s can reach +80$\%$ for X>250 km at Y$\sim$200 km when S_{nl} is activated. It has been shown that at the same location, wave-current interactions alone showed a strong decrease of H_s (Fig.3.2). One can see that simulation with wave-wave interactions enhance the H_s at the periphery of the eddy core of the fully developed eddy, in the submesoscale eddy field area. Globally, we see that H_s increases where wave-currents interactions have decreased the H_s. One can see that areas, where enhancement of H_s have been noticed in Fig.3.2, are very slightly modified in Fig.A.1a. Please note that we cannot quantitatively compare Fig.A.1a and Fig.3.2d because the incident waves from the gaussian spectra have a different spread in frequency. Nonlinear wave-wave interactions also highlight a change in the $T_{m0,-1}$ field. $\Delta T_{m0,-1}$ shows the opposite spatial variation of Δ H_s. Indeed, where Δ H_s values are (strongly) positive, $\Delta T_{m0,-1}$ values are (strongly) negative and vice versa. A transect at X=300 km shows the values of H_s and $T_{m0,-1}$ along the Y-axis (Fig.A.1c,d). One can see that ∇ H_s are globally reduced due to nonlinear wave-wave interactions especially in the core of the central eddy (Y between 200 km and 350 km). At location of submesoscale eddies, ∇H_s is also sharper for simulation without S_{nl} but the difference between the two simulations are less pronounced. $\nabla T_{m0,-1}$ show a much more striking difference between simulations with and without nonlinear wave-wave interactions. $\nabla T_{m0,-1}$ are the most pronounced in the core of the eddy where $T_{m0,-1}$ values can reach a maximum of 14 sec for simulation without nonlinear forcing. The simulation with S_{nl} reveals a maximum value of $T_{m0,-1}$ of 12 sec. Whether for H_s or $T_{m0,-1}$, in current field, wave-wave interactions have the tendency to decrease spatial gradients of the wave parameters leaded by wave-current interactions. Here the choice of the parametrization of the nonlinear wave-wave interactions was arbitrary (Hasselmann et al., 1985b), it would be interesting to expand this study to other parameterizations of S_{nl} to better describe how nonlinear wave-wave processes modify regional wave parameter gradients.

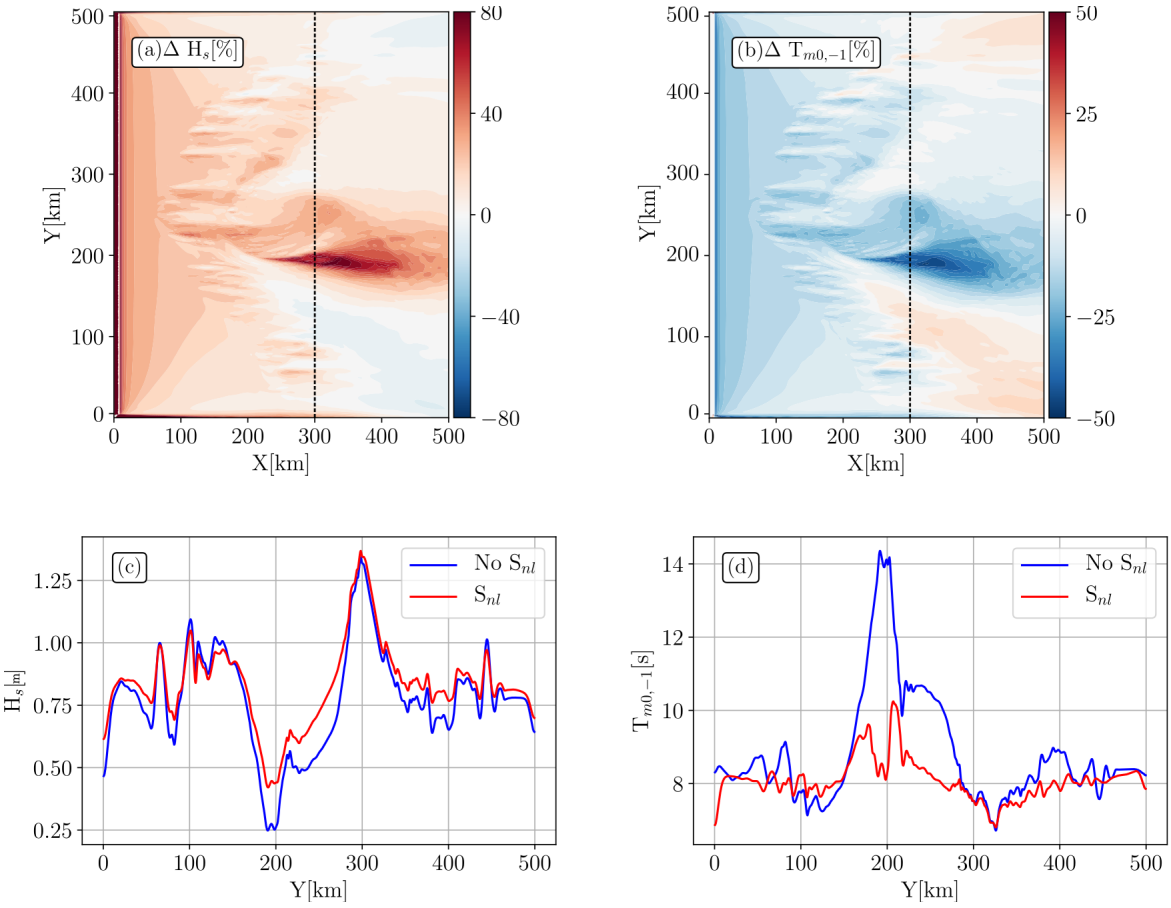

Figure A.1: Model difference between solutions with and without nonlinear wave-wave interactions. Panel (a) and (b) show the relative difference in percent of the significant wave height and the mean wave period. Panel (c) and (d) show a transect at X=300 km for simulations without (solid blue line) and with (solid red line) nonlinear source term (S_{nl}) for H_s and $T_{m0,-1}$ respectively. Waves are initialized at 7 sec.

BIBLIOGRAPHY

Airy, G. B. (1841), "Tides and waves", *in*: *Encyclopedia metropolitana (1817–1845)*, ed. by H. J. Rose et al., London.

Alpers, Werner (1985), "Theory of radar imaging of internal waves", *in*: *Nature* 314(*6008*), pp. 245–247.

Ardhuin, Fabrice, Matias Alday, and Maria Yurovskaya (2021), "Total Surface Current Vector and Shear from a Sequence of Satellite images: Effect of Waves in Opposite Directions", *in*: *Journal of Geophysical Research: Oceans*, e2021JC017342.

Ardhuin, Fabrice, Bertrand Chapron, Christophe Maes, Roland Romeiser, Christine Gommenginger, Sophie Cravatte, Rosemary Morrow, Craig Donlon, and Mark Bourassa (2019a), "Satellite Doppler observations for the motions of the oceans", *in*: *Bull. Amer. Meterol. Soc.* 100, DOI: 10.1175/BAMS-D-19-0039.1.

Ardhuin, Fabrice, Nicolas Rascle, Bertrand Chapron, Jonathan Gula, Jeroen Molemaker, Sarah T. Gille, Dimitris Menemenlis, and Cesar Rocha (2017), "Small scale currents have large effects on wind wave heights", *in*: *J. Geophys. Res.* 122(*C6*), pp. 4500–4517, DOI: 10.1002/2016JC012413.

Ardhuin, Fabrice et al. (2012), "Numerical wave modeling in conditions with strong currents: Dissipation, refraction, and relative wind", *in*: *Journal of Physical Oceanography* 42(*12*), pp. 2101–2120.

Ardhuin, Fabrice et al. (2018), "Measuring currents, ice drift, and waves from space: the Sea Surface KInematics Multiscale monitoring (SKIM) concept", *in*: *Ocean Sci.* 14, pp. 337–354, DOI: 10.5194/os-2017-65.

Ardhuin, Fabrice et al. (2019b), "Observing sea states", *in*: *Frontiers in Marine Science* 6, p. 124.

Ayet, Alex and Bertrand Chapron (2021), "The dynamical coupling of wind-waves and atmospheric turbulence: a review of theoretical and phenomenological models", *in*: *Earth and Space Science Open Archive ESSOAr*.

Bache, Alexander Dallas (1860), *Lecture on the Gulf Stream: Prepared at the Request of the American Association for the Advancement of Science*.

Ballarotta, Maxime et al. (2019), "On the resolutions of ocean altimetry maps", *in*: *Ocean Science Discussions*, DOI: 10.5194/os-2018-156.

Bates, Charles C (1949), "Utilization of wave forecasting in the invasions of Normandy, Burma, and Japan", *in*: *Annals of the New York Academy of Sciences* 51(*3*), pp. 545–572.

Belibassakis, K. A. (2007), "A coupled-mode model for the scattering of water waves by shearing currents in variable bathymetry", *in*: *J. Fluid Mech.* 578, pp. 413–434, DOI: 10.1017/S0022112007005125.

Bennis, Anne-Claire, Fabrice Ardhuin, and Franck Dumas (2011), "On the coupling of wave and three-dimensional circulation models: Choice of theoretical framework, practical implementation and adiabatic tests", *in*: *Ocean Modelling* 40(*3-4*), pp. 260–272.

Bertin, Xavier, Nicolas Bruneau, Jean-François Breilh, André B Fortunato, and Mikhail Karpytchev (2012), "Importance of wave age and resonance in storm surges: The case Xynthia, Bay of Biscay", *in*: *Ocean Modelling* 42, pp. 16–30.

Bretherton, Francis P and Christopher John Raymond Garrett (1968), "Wavetrains in inhomogeneous moving media", *in*: *Proceedings of the Royal Society of London. Series A. Mathematical and Physical Sciences* 302(*1471*), pp. 529–554.

Brown, Gary S. (1977), "The Average Impulse Response of a Rough Surface and Its Applications", *in*: *IEEE J. Oceanic Eng.* 2(*1*), pp. 67–63, DOI: 10.1109/JOE.1977.1145328.

Bruch, William, Jacques Piazzola, Hubert Branger, Alexander MJ van Eijk, Christopher Luneau, Denis Bourras, and Gilles Tedeschi (2021), "Sea-Spray-Generation Dependence on Wind and Wave Combinations: A Laboratory Study", *in*: *Boundary-Layer Meteorology*, pp. 1–29.

Brumer, Sophia E, Valérie Garnier, Jean-Luc Redelsperger, Marie-Noelle Bouin, Fabrice Ardhuin, and Mickael Accensi (2020), "Impacts of surface gravity waves on a tidal front: a coupled model perspective", *in*: *Ocean Modelling* 154, p. 101677.

Callies, Jörn, Raffaele Ferrari, Jody M Klymak, and Jonathan Gula (2015), "Seasonality in submesoscale turbulence", *in*: *Nature communications* 6(*1*), pp. 1–8.

Capet, X., J. C. Mcwilliams, M. J. Molemaker, and A. F. Shchepetkin (2016), "Mesoscale to Submesoscale Transition in the California Current System. Part I: Flow Structure, Eddy Flux, and Observational Test", *in*: *J. Phys. Oceanogr.* 38, pp. 29–43, DOI: 10.1175/2007JPO3671.

Cavaleri, L., B. Fox-Kemper, and M. Hemer (2012), "Wind Waves in the Coupled Climate System", *in*: *Bull. Amer. Meterol. Soc.* 78, pp. 1651–1661.

Chapron, Bertrand, Harald Johnsen, and René Garello (2001), "Wave and wind retrieval from SAR images of the ocean", *in*: 56(*11*), pp. 682–699.

Chelton, Dudley (2001), *Report of the high-resolution ocean topography science working group meeting*, Oregon State University, College of Oceanic and Atmospheric Sciences.

Chelton, Dudley B., Roland A. Deszoeke, Michael G. Schlax, Karim El Naggar, and Nicolas Siwertz (1998), "Geographical Variability of the First Baroclinic Rossby Radius of Deformation", *in*: *J. Phys. Oceanogr.* 28(*3*), pp. 433–460, DOI: 10.1175/1520-0485(1998)028<0433:gvotfb>2.0.co;2.

Chelton, Dudley B., Michael G. Schlax, and Roger M. Samelson (2011), "Global observations of nonlinear mesoscale eddies", *in*: *Progress in Oceanography* 91, pp. 167–216, DOI: 10.1016/j.pocean.2011.01.002.

Chelton, Dudley B, Michael G Schlax, Roger M Samelson, and Roland A de Szoeke (2007), "Global observations of large oceanic eddies", *in*: *Geophysical Research Letters* 34(*15*).

Chereskin, Teresa K, Cesar B Rocha, Sarah T Gille, Dimitris Menemenlis, and Marcello Passaro (2019), "Characterizing the transition from balanced to unbalanced motions in the southern California Current", *in*: *Journal of Geophysical Research: Oceans* 124(*3*), pp. 2088–2109.

Clément, L, E Frajka-Williams, KL Sheen, JA Brearley, and AC Naveira Garabato (2016), "Generation of internal waves by eddies impinging on the western boundary of the North Atlantic", *in*: *Journal of Physical Oceanography* 46(*4*), pp. 1067–1079.

Cox, Charles and Walter Munk (1954), "Measurement of the roughness of the sea surface from photographs of the sun's glitter", *in*: *Josa* 44(*11*), pp. 838–850.

Curtin, Thomas B and Christopher NK Mooers (1975), "Observation and interpretation of a high-frequency internal wave packet and surface slick pattern", *in*: *Journal of Geophysical Research* 80(*6*), pp. 882–894.

de Marez, Charly, Xavier Carton, Stéphanie Corréard, Pierre L'Hégaret, and Mathieu Morvan (2020a), "Observations of a deep submesoscale cyclonic vortex in the Arabian Sea", *in*: *Geophysical Research Letters* 47(*13*), e2020GL087881.

de Marez, Charly, Pierre L'Hégaret, Mathieu Morvan, and Xavier Carton (Aug. 2019), "On the 3D structure of eddies in the Arabian Sea", en, *in*: *Deep Sea Research Part I: Oceanographic Research Papers* 150, p. 103057, ISSN: 09670637, DOI: 10.1016/j.dsr.2019.06.003, (visited on 10/02/2019).

de Marez, Charly, Thomas Meunier, Mathieu Morvan, Pierre L'Hégaret, and Xavier Carton (Feb. 2020b), "Study of the stability of a large realistic cyclonic eddy", en, *in*: *Ocean Modelling* 146, p. 101540, ISSN: 14635003, DOI: 10.1016/j.ocemod.2019.101540, (visited on 01/06/2020).

Deane, Grant B. and M. Dale Stokes (2002), "Scale dependence of bubble creation mechanisms in breaking waves", *in*: *Nature* 418, pp. 839–844.

Dee, Dick P et al. (2011), "The ERA-Interim reanalysis: Configuration and performance of the data assimilation system", *in*: *Quarterly Journal of the royal meteorological society* 137(*656*), pp. 553–597.

Deike, Luc, W Kendall Melville, and Stéphane Popinet (2016), "Air entrainment and bubble statistics in breaking waves", *in*: *Journal of Fluid Mechanics* 801, pp. 91–129.

D.Hypolite, L. Romero, J.C. McWilliams, and D.P. Dauhajre (2021), "Surface gravity wave effects on submesoscale currents in the open ocean", *in*: *Journal of Physical Oceanography*.

Divoky, D., B. Le Mehaute, and A. Lin (1970), "Breaking waves on gentle slopes", *in*: *J. Geophys. Res.* 75, pp. 1681–1692.

Dodet, Guillaume et al. (2020), "The Sea State CCI dataset v1: towards a sea state climate data record based on satellite observations", *in*: *Earth System Sci. Data* 12, pp. 1929–1951, DOI: 10.5194/essd-12-1929-2020.

Dong, Xiaolong, Di Zhu, Jintai Zhu, and Tao Wang (2012), "Progresses of development of CFOSAT scatterometer", *in*: *2012 IEEE International Geoscience and Remote Sensing Symposium*, IEEE, pp. 237–240.

Drusch, Matthias et al. (2012), "Sentinel-2: ESA's optical high-resolution mission for GMES operational services", *in*: *Remote sensing of Environment* 120, pp. 25–36.

Dulov, VA, VN Kudryavtsev, and AN Bol shakov (2002), "A field study of whitecap coverage and its modulations by energy containing surface waves", *in*: *GEOPHYSICAL MONOGRAPH-AMERICAN GEOPHYSICAL UNION* 127, pp. 187–192.

Dysthe, Kristian B. (2001), "Refraction of gravity waves by weak current gradients", *in*: *J. Fluid Mech.* 442, pp. 157–159.

Echevarria, Emilio R, Mark A Hemer, and Neil J Holbrook (2021), "Global implications of surface current modulation of the wind-wave field", *in*: *Ocean Modelling* 161, p. 101792.

ESA (2019), *Report for Mission Selection: SKIM*, tech. rep. ESA-EOPSM-SKIM-RP-3550, European Space Agency, Noordwijk, The Netherlands, p. 264, DOI: 10.13140/RG.2.2.22907.98081/3.

Farrar, J Thomas, Christopher J Zappa, Robert A Weller, and Andrew T Jessup (2007), "Sea surface temperature signatures of oceanic internal waves in low winds", *in*: *Journal of Geophysical Research: Oceans* 112(*C6*).

Ferrari, Raffaele and Carl Wunsch (2009), "Ocean circulation kinetic energy: Reservoirs, sources, and sinks", *in*: *Annual Review of Fluid Mechanics* 41, pp. 253–282.

Fuglister, F. C. and L.V. Worthington (1951), "Some results of a multiple ship survey of the Gulf Stream", *in*: pp. 1–14.

Gallet, Basile and William R Young (2014), "Refraction of swell by surface currents", *in*: *Journal of marine research* 72(*2*), pp. 105–126.

Gemmrich, Johannes and Chris Garrett (2012), "The signature of inertial and tidal currents in offshore wave records", *in*: *Journal of physical oceanography* 42(*6*), pp. 1051–1056.

Gommenginger, Christine, Bertrand Chapron, Adrien Martin, Jose Marquez, Christopher Brownsword, and Christopher Buck (2018), "SEASTAR: a new mission for high-resolution imaging of ocean surface current and wind vectors from space", *in*: *Proceedings of EUSAR 2018, Aachen, Germany*, IEEE, pp. 1–6.

Gommenginger, CP, MA Srokosz, J Wolf, and PAEM Janssen (2003), "An investigation of altimeter sea state bias theories", *in*: *Journal of Geophysical Research: Oceans* 108(*C1*).

Guimaraes, Pedro Veras (2018), "Sea surface and energy dissipation", PhD thesis, Université Bretagne Loire; École Centrale de Nantes.

Gula, Jonathan, M. Jeroen Molemaker, and James C. Mcwilliams (2015), "Gulf Stream Dynamics along the Southeastern U.S. Seaboard", *in*: *J. Phys. Oceanogr.* 45, pp. 690–715.

Gula, Jonathan, M Jeroen Molemaker, and James C McWilliams (2016), "Submesoscale dynamics of a Gulf Stream frontal eddy in the South Atlantic Bight", *in*: *Journal of Physical Oceanography* 46(*1*), pp. 305–325.

Gulev, Sergey K and Vika Grigorieva (2006), "Variability of the winter wind waves and swell in the North Atlantic and North Pacific as revealed by the voluntary observing ship data", *in*: *Journal of Climate* 19(*21*), pp. 5667–5685.

Hasselmann, Klaus (1962), "On the non-linear energy transfer in a gravity-wave spectrum Part 1. General theory", *in*: *Journal of Fluid Mechanics* 12(*4*), pp. 481–500.

Hasselmann, Klaus, RK Raney, WJ Plant, Werner Alpers, RA Shuchman, David R Lyzenga, CL Rufenach, and MJ Tucker (1985a), "Theory of synthetic aperture radar ocean imaging: A MARSEN view", *in*: *Journal of Geophysical Research: Oceans* 90(*C3*), pp. 4659–4686.

Hasselmann, Susanne, Klaus Hasselmann, JHm Allender, and TP Barnett (1985b), "Computations and parameterizations of the nonlinear energy transfer in a gravity-wave specturm. Part II: Parameterizations of the nonlinear energy transfer for application in wave models", *in*: *Journal of Physical Oceanography* 15(*11*), pp. 1378–1391.

Hauser, Danièle et al. (2020), "New observations from the SWIM radar on board CFOSAT: instrument validation and ocean wave measurement assessment", *in*: p. 23.

Hayne, G.S. (1980), "Radar altimeter mean return waveforms from near-normal-incidence ocean surface scattering", *in*: *IEEE Trans. Antennas Propagat.* 28, pp. 687–692, DOI: 10.1109/tap.1980.1142398.

Heller, EJ, L Kaplan, and A Dahlen (2008), "Refraction of a Gaussian seaway", *in*: *Journal of Geophysical Research: Oceans* 113(*C9*).

Heller, Eric (2005), "Freak waves: just bad luck, or avoidable?", *in*: *Europhysics News* 36(*5*), pp. 159–162.

Herbers, T. H. C. and M. C. Burton (1997), "Nonlinear shoaling of directionally spread waves on a beach", *in*: *J. Geophys. Res.* 102(*C9*), pp. 21,101–21,114.

Holthuijsen, LH and HL Tolman (1991), "Effects of the Gulf Stream on ocean waves", *in*: *Journal of Geophysical Research: Oceans* 96(*C7*), pp. 12755–12771.

Hua, Bach Lien, Claire Ménesguen, Sylvie Le Gentil, Richard Schopp, Bruno Marsset, and Hidenori Aiki (2013), "Layering and turbulence surrounding an anticyclonic oceanic vortex: In situ observations and quasi-geostrophic numerical simulations", *in*: *Journal of Fluid Mechanics* 731, pp. 418–442.

Huang, Norden E, Davidson T Chen, Chi-Chao Tung, and James R Smith (1972), "Interactions between steady won-uniform currents and gravity waves with applications for current measurements", *in*: *Journal of Physical Oceanography* 2(*4*), pp. 420–431.

Irvine, D. E. and D. G. Tilley (1988), "Ocean wave directional spectra and wave-current interaction in the Agulhas from the shuttle imaging radar-B synthetic aperture radar", *in*: *J. Geophys. Res.* 93(*C12*), pp. 15389–15401.

Jackson, Christopher R, Jose CB da Silva, Gus Jeans, Werner Alpers, and Michael J Caruso (2013), "Nonlinear internal waves in synthetic aperture radar imagery", *in*: *Oceanography* 26(*2*), pp. 68–79.

Jackson, Frederick C. (1987), "The physical basis for estimating wave-energy spectra with the radar ocean-wave spectrometer", *in*: *Johns Hopkins APL Technical Digest*, vol. 8, 1, pp. 70–73.

Janssen, Peter (2004), *The interaction of ocean waves and wind*, Cambridge University Press: Cambridge, p. 300, ISBN: 0 521 46540 0.

Janssen, T. T. and T. H. C. Herbers (2009), "Nonlinear Wave Statistics in a Focal Zone", *in*: *J. Phys. Oceanogr.* 39, pp. 1948–1964.

Johnson, JW (1947), "The refraction of surface waves by currents", *in*: *Eos, Transactions American Geophysical Union* 28(*6*), pp. 867–874.

Kelly, Kathryn A, Sandipa Singh, and Rui Xin Huang (1999), "Seasonal variations of sea surface height in the Gulf Stream region", *in*: *Journal of physical oceanography* 29(*3*), pp. 313–327.

Kenyon, Kern. E. (1971), "Wave refraction in Ocean Current", *in*: *Deep Sea Res.* 18.

Kim, Sung Yong and P Michael Kosro (2013), "Observations of near-inertial surface currents off Oregon: Decorrelation time and length scales", *in*: *Journal of Geophysical Research: Oceans* 118(*7*), pp. 3723–3736.

Kirby, J. T. (1984), "A note on linear surface wave-current interaction over slowly varying topography", *in*: *J. Geophys. Res.* 89, pp. 745–747.

Kirby, James T and Tsung-Muh Chen (1989), "Surface waves on vertically sheared flows: approximate dispersion relations", *in*: *Journal of Geophysical Research: Oceans* 94(*C1*), pp. 1013–1027.

Klein, P., B.L Hua, G.Lapeyre, X.Capet, S.Le Gentil, and H.Sasaki (2008), "Upper ocean turbulence from high-resolution 3D simulations", *in*: *J. Phys. Oceanogr.* 38, pp. 1748–1763, DOI: 1http://dx.doi.org/10.1175/2007JPO3773.1.

Klein, Patrice, Guillaume Lapeyre, Guillaume Roullet, Sylvie Le Gentil, and Hideharu Sasaki (2011), "Ocean turbulence at meso and submesoscales: connection between surface and interior dynamics", *in*: *Geophysical & Astrophysical Fluid Dynamics* 105(*4-5*), pp. 421–437.

Komen, GJ, Susanne Hasselmann, and K1 Hasselmann (1984), "On the existence of a fully developed wind-sea spectrum", *in*: *Journal of physical oceanography* 14(*8*), pp. 1271–1285.

Kudryavtsev, V., M. Yurovskaya, B. Chapron, F. Collard, and C. Donlon (2017a), "Sun glitter Imagery of Surface Waves. Part 1: Directional spectrum retrieval and validation", *in*: *J. Geophys. Res.* 122, DOI: 10.1002/2016JC012425.

Kudryavtsev, V., M. Yurovskaya, B. Chapron, F. Collard, and C. Donlon (2017b), "Sun glitter Imagery of Surface Waves. Part 2: Waves Transformation on Ocean Currents", *in*: *J. Geophys. Res.* 122, DOI: 10.1002/2016JC012426.

Kudryavtsev, Vladimir, Alexander Myasoedov, Bertrand Chapron, Johnny A Johannessen, and Fabrice Collard (2012), "Imaging mesoscale upper ocean dynamics using synthetic aperture radar and optical data", *in*: *Journal of Geophysical Research: Oceans* 117(*C4*).

Kudryavtsev, VN (1994), "The coupling of wind and internal waves: modulation and friction mechanisms", *in*: *Journal of Fluid Mechanics* 278, pp. 33–62.

Kuik, A. J., Gerbrant Ph. van Vledder, and L. H. Holthuijsen (1988), "A method for the routine analysis of pitch-and-roll buoy wave data", *in*: *J. Phys. Oceanogr.* 18, pp. 1020–1034, URL: http://journals.ametsoc.org/doi/pdf/10.1175/1520-0485%281987%29017%3C0845%3ATROWDT%3E2.0.CO%3B2.

Laplace, Pierre Simon de (1776), "Suite des recherches sur plusieurs points du système du monde (XXV–XXVII)", *in*: *Mém. Présentés Acad. R. Sci. Inst. France*, pp. 542–552.

Lavrenov, IV (1998), "The wave energy concentration at the Agulhas current off South Africa", *in*: *Natural hazards* 17(*2*), pp. 117–127.

Le Vu, Briac, Alexandre Stegner, and Thomas Arsouze (Apr. 2018), "Angular Momentum Eddy Detection and Tracking Algorithm (AMEDA) and Its Application to Coastal Eddy Formation", en, *in*: *Journal of Atmospheric and Oceanic Technology* 35(*4*), pp. 739–762, ISSN: 0739-0572, 1520-0426, DOI: 10.1175/JTECH-D-17-0010.1, (visited on 12/18/2018).

LeBlond, Paul H and Lawrence A Mysak (1981), *Waves in the Ocean*, Elsevier.

Lenain, Luc and Nick Pizzo (2021), "Modulation of surface gravity waves by internal waves", *in*: *Journal of Physical Oceanography*.

León, Sonia Ponce de and C Guedes Soares (2021), "Extreme Waves in the Agulhas Current Region Inferred from SAR Wave Spectra and the SWAN Model", *in*: *Journal of Marine Science and Engineering* 9(*2*), p. 153.

Lévy, Marina, Peter J. S. Franks, and K. Shafer Smith (Dec. 2018), "The role of submesoscale currents in structuring marine ecosystems", en, *in*: *Nature Communications* 9, p. 4758, ISSN: 2041-1723, DOI: 10.1038/s41467-018-07059-3, (visited on 03/07/2019).

l'Hegaret, Pierre, R Duarte, Xavier Carton, Clement Vic, Daniele Ciani, R Baraille, and S Corréard (2015), "Mesoscale variability in the Arabian Sea from HYCOM model results and observations: impact on the Persian Gulf Water path", *in*: *Ocean Science* 11(*5*), pp. 667–693.

Li, Huimin, Daniele Hauser, Bertrand Chapron, Frederic Nouguier, Patricia Schippers, Biao Zhang, Jingsong Yang, and Yijun He (2021), "Up-to-Downwave Asymmetry of the CFOSAT SWIM Fluctuation Spectrum for Wave Direction Ambiguity Removal", *in*: *IEEE Transactions on Geoscience and Remote Sensing*, pp. 1–12, ISSN: 0196-2892, 1558-0644, DOI: 10.1109/TGRS.2021.3086483, URL: https://ieeexplore.ieee.org/document/9461406/ (visited on 07/05/2021).

Longuet-Higgins, Michael and Mitsuhiro Tanaka (1997), "On the crest instabilities of steep surface waves", *in*: *Journal of Fluid Mechanics* 336, pp. 51–68.

Longuet-Higgins, Michael S (1969), "Action of a variable stress at the surface of water waves", *in*: *The Physics of Fluids* 12(*4*), pp. 737–740.

Lutjeharms, Johann RE (2006), *The agulhas current*, vol. 329, Springer.

Lutjeharms, JRE and HR Roberts (1988), "The Natal pulse: An extreme transient on the Agulhas Current", *in*: *Journal of Geophysical Research: Oceans* 93(*C1*), pp. 631–645.

Lygre, Asle and Harald E Krogstad (1986), "Maximum entropy estimation of the directional distribution in ocean wave spectra", *in*: *Journal of Physical Oceanography* 16(*12*), pp. 2052–2060.

Mallory, John Kennaway (1974), "Abnormal waves on the south east coast of South Africa", *in*: *The International Hydrographic Review*.

Mapp, George R, Christopher S Welch, and John C Munday (1985), "Wave refraction by warm core rings", *in*: *Journal of Geophysical Research: Oceans* 90(*C4*), pp. 7153–7162.

Marechal, Gwendal and Fabrice Ardhuin (2021), "Surface Currents and Significant Wave Height Gradients: Matching Numerical Models and High-Resolution Altimeter Wave Heights in the Agulhas Current Region", *in*: *Journal of Geophysical Research: Oceans* 126(*2*), e2020JC016564.

Marez, Charly de, Noé J Lahaye, and Jonathan Gula (2020), "Interaction of the Gulf Stream with small scale topography: a focus on lee waves", *in*: *Scientific reports* 10(*1*), pp. 1–10.

Marmorino, GO, GB Smith, and GJ Lindemann (2004), "Infrared imagery of ocean internal waves", *in*: *Geophysical Research Letters* 31(*11*).

Mathiesen, Martin (1987), "Wave refraction by a current whirl", *in*: *J. Geophys. Res.* 92(*C4*), pp. 3905–3912.

McPhee, Miles G and Lakshmi H Kantha (1989), "Generation of internal waves by sea ice", *in*: *Journal of Geophysical Research: Oceans* 94(*C3*), pp. 3287–3302.

McWilliams, James C (1985), "Submesoscale, coherent vortices in the ocean", *in*: *Reviews of Geophysics* 23(*2*), pp. 165–182.

McWilliams, James C. (2016), "Submesoscale currents in the ocean", *in*: *Proc. R. Soc. A* 427, p. 20160117, DOI: 10.1098/rspa.2016.0117.

McWilliams, James C (2018), "Surface wave effects on submesoscale fronts and filaments", *in*: *Journal of Fluid Mechanics* 843, pp. 479–517.

Mei, C. C. (1989), *Applied dynamics of ocean surface waves*, second, 740 p., World Scientific: Singapore.

Melville, WK and Ronald J Rapp (1985), "Momentum flux in breaking waves", *in*: *Nature* 317(*6037*), pp. 514–516.

Mendes, R, JCB da Silva, JM Magalhaes, B St-Denis, D Bourgault, J Pinto, and JM Dias (2021), "On the generation of internal waves by river plumes in subcritical initial conditions", *in*: *Scientific reports* 11(*1*), pp. 1–12.

Mensa, Jean Alberto, Zulema Garraffo, Annalisa Griffa, Tamay Mehmet Özgökmen, Angelique Haza, and Milena Veneziani (2013), "Seasonality of the submesoscale dynamics in the Gulf Stream region", *in*: *Ocean Dynamics* 63(*8*), pp. 923–941.

Monahan, Edward C, Donald E Spiel, and Kenneth L Davidson (1986), "A model of marine aerosol generation via whitecaps and wave disruption", *in*: *Oceanic whitecaps*, Springer, pp. 167–174.

Montagne, R (1922), "Le service de prédiction de la houle au Maroc", *in*: *Ann. Hydrogr*, pp. 157–186.

Morrow, Rosemary et al. (2019), "Global observations of fine-scale ocean surface topography with the Surface Water and Ocean Topography (SWOT) Mission", *in*: 6, p. 232, DOI: 10.3389/fmars.2019.00232.

Munk, Walter (2002), "The Evolution of Physical Oceanography in the Last Hundred Years", *in*: *Oceanograohy* 15, pp. 136–141, DOI: 10.5670/oceanog.2002.45.

Munk, Walter (2009), "An inconvenient sea truth: Spread, steepness, and skewness of surface slopes", *in*: *Annual review of marine science* 1, pp. 377–415.

Munk, Walter Heinrich (1944), *roposed uniform procedure for observing waves and interpreting instrument records*, tech. rep.

Munk, Walter Heinrich, GR Miller, FE Snodgrass, and Norman F Barber (1963), "Directional recording of swell from distant storms", *in*: *Philosophical transactions of the royal society of london. series A, mathematical and physical sciences* 255(*1062*), pp. 505–584.

Osborne, AR and TL Burch (1980), "Internal solitons in the Andaman Sea", *in*: *Science* 208(*4443*), pp. 451–460.

Park, Jong Jin, Kuh Kim, and Brian A King (2005), "Global statistics of inertial motions", *in*: *Geophysical research letters* 32(*14*).

Passaro, Marcello, Luciana Fenoglio-Marc, and Paolo Cipollini (2014), "Validation of significant wave height from improved satellite altimetry in the German Bight", *in*: *IEEE Transactions on Geoscience and Remote Sensing* 53(*4*), pp. 2146–2156.

Peregrine, D Howell (1976), "Interaction of water waves and currents", *in*: *Advances in applied mechanics* 16, pp. 9–117.

Peureux, Charles (2017), "Observation et modélisation des propriétés directionnelles des ondes de gravité courtes", PhD thesis, Université de Bretagne occidentale-Brest.

Peureux, Charles, Fabrice Ardhuin, and Pedro Veras Guimarães (2021), "On the unsteady steepening of short gravity waves near the crests of longer waves in the absence of generation or dissipation", *in*: *Journal of Geophysical Research: Oceans* 126(*1*), e2020JC016735.

Phillips, O. M. (1977), *The dynamics of the upper ocean*, 336 p., Cambridge University Press: London.

Phillips, OM (1984), "On the response of short ocean wave components at a fixed wavenumber to ocean current variations", *in*: *Journal of Physical Oceanography* 14(*9*), pp. 1425–1433.

Pierson, Willard J (1972), "The loss of two British trawlers—a study in wave refraction", *in*: *The Journal of Navigation* 25(*3*), pp. 291–304.

Pierson, Willard J., Gerhard Neumann, and Richard W. James (1955), *Practical methods for observing and forecasting ocean waves by means of wave spectra and statistics*, U. S. Hydrographic Office, p. 284.

Ponte, Aurelien L and Patrice Klein (2015), "Incoherent signature of internal tides on sea level in idealized numerical simulations", *in*: *Geophysical Research Letters* 42(*5*), pp. 1520–1526.

Pouvreau, Nicolas, Belén Martin Miguez, Bernard Simon, and Guy Wöppelmann (2006), "Évolution de l'onde semi-diurne M2 de la marée à Brest de 1846 à 2005", *in*: *Comptes Rendus Geoscience* 338(*11*), pp. 802–808.

Qiu, Bo (1999), "Seasonal eddy field modulation of the North Pacific Subtropical Countercurrent: TOPEX/Poseidon observations and theory", *in*: *Journal of Physical Oceanography* 29(*10*), pp. 2471–2486.

Quilfen, Y. and B. Chapron (2019), "Ocean Surface Wave-Current Signatures From Satellite Altimeter Measurements", *in*: *Geophys. Res. Lett.* 216, pp. 253–261, DOI: 10.1029/2018GL081029.

Quilfen, Y., M. Yurovskaya, B. Chapron, and F. Ardhuin (2018), "Storm waves sharpening in the Agulhas current: satellite observations and modeling", *in*: *Remote sensing of Environment* 216, pp. 561–571, DOI: 10.1016/j.rse.2018.07.020.

Rascle, Nicolas (2007), "Impact des vagues sur la circulation océanique", PhD thesis, Brest.

Rascle, Nicolas, Bertrand Chapron, Aurélien Ponte, Fabrice Ardhuin, and Patrice Klein (2014), "Surface roughness imaging of currents shows divergence and strain in the wind direction", *in*: *Journal of Physical Oceanography* 44(*8*), pp. 2153–2163.

Rascle, Nicolas, Frédéric Nouguier, Bertrand Chapron, and Francisco J Ocampo-Torres (2018), "Sunglint images of current gradients at high resolution: Critical angle and directional observing strategy", *in*: *Remote Sensing of Environment* 216, pp. 786–797.

Ray, Richard D and Edward D Zaron (2011), "Non-stationary internal tides observed with satellite altimetry", *in*: *Geophysical Research Letters* 38(*17*).

Reul, Nicolas, Hubert Branger, and Jean-Paul Giovanangeli (2008), "Air flow structure over short-gravity breaking water waves", *in*: *Boundary-layer meteorology* 126(*3*), pp. 477–505.

Ribal, Agustinus and Ian R Young (2019), "33 years of globally calibrated wave height and wind speed data based on altimeter observations", *in*: *Scientific data* 6(*1*), pp. 1–15.

Richardson, PL (1985), "Average velocity and transport of the Gulf Stream near 55W", *in*: *Journal of Marine Research* 43(*1*), pp. 83–111.

Richardson, PL and G Reverdin (1987), "Seasonal cycle of velocity in the Atlantic North Equatorial Countercurrent as measured by surface drifters, current meters, and ship drifts", *in*: *Journal of Geophysical Research: Oceans* 92(*C4*), pp. 3691–3708.

Rio, M-H, S Mulet, and N Picot (2014), "Beyond GOCE for the ocean circulation estimate: Synergetic use of altimetry, gravimetry, and in situ data provides new insight into geostrophic and Ekman currents", *in*: *Geophysical Research Letters* 41(*24*), pp. 8918–8925.

Rocha, Cesar B., Teresa K. Chereskin, and Sarah T. Gille (2016a), "Mesoscale to Submesoscale Wavenumber Spectra in Drake Passage", *in*: *J. Phys. Oceanogr.* 46, pp. 601–620, DOI: 10.1175/JPO-D-15-0087.1.

Rocha, Cesar B, Sarah T Gille, Teresa K Chereskin, and Dimitris Menemenlis (2016b), "Seasonality of submesoscale dynamics in the Kuroshio Extension", *in*: *Geophysical Research Letters* 43(*21*), pp. 11–304.

Rocha, MVL, Hervé Michallet, and Paulo A Silva (2017), "Improving the parameterization of wave nonlinearities–The importance of wave steepness, spectral bandwidth and beach slope", *in*: *Coastal Engineering* 121, pp. 77–89.

Romero, Leonel, Delphine Hypolite, and James C McWilliams (2020), "Submesoscale current effects on surface waves", *in*: *Ocean Modelling* 153, p. 101662.

Romero, Leonel, Luc Lenain, and W. Kendall Melville (2017), "Observations of Surface Wave–Current Interaction", *in*: *J. Phys. Oceanogr.* 47, pp. 615–632, DOI: 10.1175/JPO-D-16-0108.1.

Ruban, VP (2010), "Giant waves in weakly crossing sea states", *in*: *Journal of Experimental and Theoretical Physics* 110(*3*), pp. 529–536.

Sandwell, David T and Walter HF Smith (2005), "Retracking ERS-1 altimeter waveforms for optimal gravity field recovery", *in*: *Geophysical Journal International* 163(*1*), pp. 79–89.

Shchepetkin, Alexander F. and James C. McWilliams (Jan. 2005), "The regional oceanic modeling system (ROMS): a split-explicit, free-surface, topography-following-coordinate oceanic model", en, *in*: *Ocean Modelling* 9(*4*), pp. 347–404, ISSN: 14635003, DOI: 10.1016/j.ocemod.2004.08.002, (visited on 03/07/2019).

Shchepetkin, Alexander F. and James C. McWilliams (Jan. 2011), "Accurate Boussinesq oceanic modeling with a practical, "Stiffened" Equation of State", en, *in*: *Ocean Modelling* 38(*1-2*), pp. 41–70, ISSN: 14635003, DOI: 10.1016/j.ocemod.2011.01.010, (visited on 03/07/2019).

Shcherbina, Andrey Y et al. (2015), "The LatMix summer campaign: Submesoscale stirring in the upper ocean", *in*: *Bulletin of the American Meteorological Society* 96(*8*), pp. 1257–1279.

Shea, Russell E and William W Broenkow (1982), "The role of internal tides in the nutrient enrichment of Monterey Bay, California", *in*: *Estuarine, Coastal and Shelf Science* 15(*1*), pp. 57–66.

Sheres, David, Kern E Kenyon, Robert L Bernstein, and Robert C Beardsley (1985), "Large horizontal surface velocity shears in the ocean obtained from images of refracting swell and in situ moored current data", *in*: *Journal of Geophysical Research: Oceans* 90(*C3*), pp. 4943–4950.

Smit, Pieter B and Tim T Janssen (2019), "Swell propagation through submesoscale turbulence", *in*: *Journal of Physical Oceanography* 49(*10*), pp. 2615–2630.

Snodgrass, FE, KF Hasselmann, GR Miller, Walter Heinrich Munk, and WH Powers (1966), "Propagation of ocean swell across the Pacific", *in*: *Philosophical Transactions of the Royal Society of London. Series A, Mathematical and Physical Sciences* 259(*1103*), pp. 431–497.

Stewart, Robert H and Joseph W Joy (1974), "HF radio measurements of surface currents", *in*: *Deep sea research and oceanographic abstracts*, vol. 21, 12, Elsevier, pp. 1039–1049.

Stopa, Justin E, Fabrice Ardhuin, Alexander Babanin, and Stefan Zieger (2016), "Comparison and validation of physical wave parameterizations in spectral wave models", *in*: *Ocean Modelling* 103, pp. 2–17.

Su, Zhan, Jinbo Wang, Patrice Klein, Andrew F Thompson, and Dimitris Menemenlis (2018), "Ocean submesoscales as a key component of the global heat budget", *in*: *Nature communications* 9(*1*), pp. 1–8.

Suzuki, Nobuhiro, Baylor Fox-Kemper, Peter E Hamlington, and Luke P Van Roekel (2016), "Surface waves affect frontogenesis", *in*: *Journal of Geophysical Research: Oceans* 121(*5*), pp. 3597–3624.

Team, SKIM et al. (2017), *Sea surface KInematics Multiscale monitoring, full proposal for ESA EE9*, tech. rep., Technical Report, Laboratoire d'Océanographie Physique et Spatiale, Brest ...

Tedesco, P., J. Gula, C. Ménesguen, P. Penven, and M. Krug (2019), "Generation of submesoscale frontal eddies in the Agulhas Current", *in*: *Journal of Geophysical Research* 124, pp. 7606–7625, DOI: 10.1029/2019JC015229.

The WAVEWATCH III ® Development Group (2019), *User manual and system documentation of WAVEWATCH III ® version 6.07*, Tech. Note 333, 465 pp. + Appendices, College Park, MD, USA: NOAA/NWS/NCEP/MMAB.

Thibaut, P, JC Poisson, E Bronner, and N Picot (2010), "Relative performance of the MLE3 and MLE4 retracking algorithms on Jason-2 altimeter waveforms", *in*: *Marine Geodesy* 33(*S1*), pp. 317–335.

Tran, N, Doug Vandemark, S Labroue, Hui Feng, Bertrand Chapron, HL Tolman, J Lambin, and N Picot (2010), "Sea state bias in altimeter sea level estimates determined by combining wave model and satellite data", *in*: *Journal of Geophysical Research: Oceans* 115(*C3*).

Tulloch, Ross, John Marshall, Chris Hill, and K Shafer Smith (2011), "Scales, growth rates, and spectral fluxes of baroclinic instability in the ocean", *in*: *Journal of Physical Oceanography* 41(*6*), pp. 1057–1076.

Vandemark, Douglas, Bertrand Chapron, Tanos Elfouhaily, and JW Campbell (2005), "Impact of high-frequency waves on the ocean altimeter range bias", *in*: *Journal of Geophysical Research: Oceans* 110(*C11*).

Vandemark, Douglas, Bertrand Chapron, J Sun, Graber H Crescenti, and Hans C Graber (2004), "Ocean wave slope observations using radar backscatter and laser altimeters", *in*: *Journal of Physical Oceanography* 34(*12*), pp. 2825–2842.

Veron, Fabrice (2015), "Ocean spray", *in*: *Annual Review of Fluid Mechanics* 47, pp. 507–538.

Villas Bôas, A. B. et al. (2019), "Integrated observations and modeling of winds, currents, and waves: requirements and challenges for the next decade", *in*: 6, p. 425, DOI: 10.3389/fmars.2019.00425.

Villas Bôas, Ana B., Bruce. D. Cornuelle, Matthew. R. Mazloff, Sarah. T. Gille, and Fabrice Ardhuin (2020), "Wave-Current Interactions at Meso and Submesoscales: Insights fromIdealized Numerical Simulations", *in*: *J. Phys. Oceanogr.* in press, DOI: 10.1002/2016JC012413.

Villas Bôas, Ana B, Sarah T Gille, Matthew R Mazloff, and Bruce D Cornuelle (2017), "Characterization of the deep water surface wave variability in the California Current region", *in*: *Journal of Geophysical Research: Oceans* 122(*11*), pp. 8753–8769.

Villas Bôas, Ana B. and William R. Young (2020), "Directional diffusion of surface gravity wave action by ocean macroturbulence", *in*: *J. Fluid Mech.* 890, R3, DOI: 10.1017/jfm.2020.116.

Villas Bôas, Ana B., Luc Lenain, Bruce D. Cornuelle, Sarah T. Gille, and Matthew R. Mazloff (2022), "A Broadband View of the Sea Surface Height Wavenumber Spectrum", *in*: *Geophysical Research Letters* 49(*4*), e2021GL096699 2021GL096699, e2021GL096699, DOI: https://doi.org/10.1029/2021GL096699, eprint: https://agupubs.onlinelibrary.wiley.com/doi/pdf/10.1029/2021GL096699, URL: https://agupubs.onlinelibrary.wiley.com/doi/abs/10.1029/2021GL096699.

White, Benjamin S and Bengt Fornberg (1998), "On the chance of freak waves at sea", *in*: *Journal of fluid mechanics* 355, pp. 113–138.

Wineteer, Alexander, Hector S. Torres, and Ernesto Rodriguez (2020), "On the surface current measurement capabilities of spaceborne Doppler scatterometry.", *in*: *Geophys. Res. Lett.* 47, e2020GL090116, DOI: 10.1029/2020GL090116.

Wunsch, Carl (1975), "Internal tides in the ocean", *in*: *Reviews of Geophysics* 13(*1*), pp. 167–182.

Young, IR (1999), "Seasonal variability of the global ocean wind and wave climate", *in*: *International Journal of Climatology: A Journal of the Royal Meteorological Society* 19(*9*), pp. 931–950.

Yu, Xiaolong, Aurélien L Ponte, Shane Elipot, Dimitris Menemenlis, Edward D Zaron, and Ryan Abernathey (2019), "Surface kinetic energy distributions in the global oceans from a high-resolution numerical model and surface drifter observations", *in*: *Geophysical Research Letters* 46(*16*), pp. 9757–9766.

Yurovskaya, Maria, Vladimir Kudryavtsev, Bertrand Chapron, and Fabrice Collard (2019), "Ocean surface current retrieval from space: The Sentinel-2 multispectral capabilities", *in*: *Remote Sensing of Environment* 234, p. 111468.

Zhang, Zhengguang, Wei Wang, and Bo Qiu (2014), "Oceanic mass transport by mesoscale eddies", *in*: *Science* 345(*6194*), pp. 322–324.

DOCTORAT SCIENCES BRETAGNE DE LA MER LOIRE ET DU LITTORAL

Université de Bretagne Occidentale

Titre : Variabilités des hauteurs significatives des vagues et propriétés des courants de méso- et de sousmésoéchelle.

Mot clés : mésoéchelle, télédetection, sousmésoéchelle, courants de surface, vagues, interactions vagues-courants

Résumé : Dans cette thèse, nous présentons les effets des courants sur les vagues avec un intérêt particulier pour la variabilité de leurs hauteurs significatives (H_s) et comment leur gradients spatiaux sont liés aux gradients spatiaux des courants sous-jacents. Dans un premier temps, nous montrons, dans un cadre théorique et simplifié que la réfraction des vagues induite par les gradients de courants se traduit par une redistribution spatiale de l'action des vagues, conduisant à une inhomogénéité dans le champ des H_s. Ensuite, cette inhomogénéité est étudiée dans un cadre numérique idéalisé dans un tourbillon océanique isolé de mésoéchelle. Cette étude permet de souligner l'effet non local des courants sur les H_s. Aussi, dans un tourbillon dynamique à la fois à la méso- et à la sousmésoéchelle, la variabilité du champ des H_s est bien plus importante que pour un tourbillon gaussien. Comme les tourbillons ne sont pas isolés en réalité, nous étudions les gradients spatiaux des H_s dans un cadre réaliste dans le courant des Aiguilles. Les forts gradients observés par les nouvelles données altimétriques filtrées sont, en moyenne, reproductibles par les modèles de vagues si les courants de forçages sont suffisamment résolus démontrant l'importance des petites échelles dans la redistribution de l'action des vagues par les courants. La proportionalité entre les gradients d'énergie cinétique de surface et les gradients de H_s est vérifiée à la fois par les données altimétriques et le modèle sur toute la gamme de la mésoéchelle. Les mesures directionnelles du capteur SWIM ont montré de premiers résultats motivant quant à l'observation des effets des courants sur le champ de vagues et de ses paramètres.

Title: Significant wave height variability and meso- and submesoscale current properties.

Keywords: mesoscale, remote sensing, submesoscale, surface currents, surface gravity waves, wave-current interactions

Abstract: In this thesis, we show the effects of the surface current on the wave field with a particular interest in the significant wave height (H_s) variability and how H_s spatial gradients are related to the underlying current gradients. With a theoretical and idealized framework, we show that the current-induced refraction leads to a spatial redistribution of the wave action resulting in an inhomogeneity in the H_s field. Then, this inhomogeneity is described in an idealized numerical framework in an isolated mesoscale eddy. The nonlocal effects of the current in the H_s field have been highlighted in this study. Also, the variability of the H_s field is much more important in an eddy field dynamical at the meso- and the submesoscale range than in an eddy with a gaussian shape. As eddies are not isolated in the ocean, we studied H_s gradients in a realistic framework in the Agulhas current. The sharp H_s gradients monitored by the new filtered altimeter data, are, on average, reproduced by the numerical wave models if forcing currents are sufficiently resolved. It proved the importance of small scale currents in the wave action spatial redistribution. The proportionality between the spatial gradients of the surface Kinetic Energy and H_s has been verified both by the numerical outputs and altimeter data at the mesoscale range. The directional data from SWIM sensors have shown first results motivating for future studies of current effects on the waves.